Doctoral Dissertation
博士論文

Search for gluinos in final states with jets and missing transverse momentum in pp collisions at $\sqrt{s}$ =13 TeV

(重心系エネルギー13 **TeV**の陽子･陽子衝突における
終状態にジェットと横方向消失運動量をもつ
超対称性粒子グルイーノ探索)

A dissertation Submitted for the Degree of Doctor of Philosophy

令和元年12月博士（理学）申請

December 2019
Department of Physics, Graduate School of Science
東京大学大学院理学系研究科
物理学専攻

The University of Tokyo
Kenta Uno
宇野　健太

Ph.D Thesis

Search for gluinos in final states with jets and missing transverse momentum in pp collisions at $\sqrt{s}$ =13 TeV

Kenta Uno

[1]*The University of Tokyo*

Abstract

Standard Model (SM) provides a successful description in the current particle physics and it is consistent with almost all experimental results. However, there are problems such as an existence of dark matter and a hierarchy problem, which cannot be explained in the SM. Hence, the extension of the SM is needed. One of the promising extension is to introduce Supersymmetry (SUSY), which is a symmetry between fermions and bosons. When SUSY is considered, partners of all the SM particles (super-partners) are introduced and these particles have been searched. This thesis describes a search for gluino, which is the super-partner of gluon at the LHC ATLAS experiment. In the pp collision, the cross section of gluino is relatively large due to strong interaction and the gluino search is one of the most important physics programs.

The result of a search for gluinos in final states with jets and missing transverse momentum at $\sqrt{s}$ =13 TeV with the ATLAS detector is presented. This thesis uses data collected in 2015-2018 corresponding to the integrated luminosity of 139 fb^{-1}. Compared to the past search, a machine learning technique as a new approach is introduced and allows the sensitivity to heavier gluino which has not been looked into before, to be improved well. No significant excess over the background prediction is observed and the gluino mass is excluded up to 2.2 TeV and the lightest neutralino mass is excluded up to about 1.2 TeV at 95% confidence level.

This research shows the first result of the gluino search using the machine learning, which is published from ATLAS. This thesis has been proved that the machine learning technique is applicable to SUSY search.

Contents

1 Introduction

Elementary particles are the most fundamental building blocks of the universe. Figure 1.1 shows all elementary particles in the Standard Model (SM) [1]. They are composed of three types: fermions with the spin $1/2$, gauge bosons with spin 1 and Higgs boson with spin 0. The SM provides a successful description of these particles and their interactions. It is also consistent with almost all experimental results. However, the SM is not a perfect theory because it cannot explain many problems. In the next section, two representative problems are discussed: the hierarchy problem [2] and the existence of the dark matter. Then, Supersymmetry (SUSY), which solves these problems, is introduced.

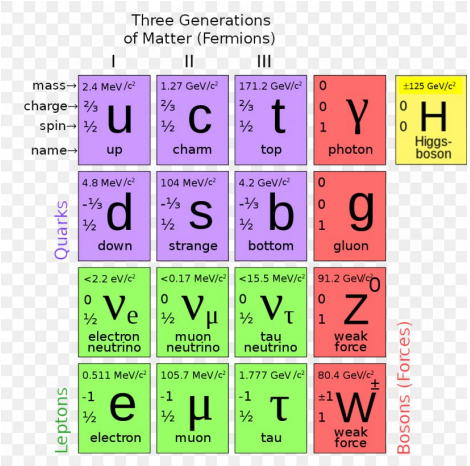

Figure 1.1: Elementary particles in the Standard Model [3]. The quarks (u, d, c, s, t and b) and leptons (e^-, ν_e, μ^-, ν_μ, τ^- and ν_τ) are spin $1/2$ particles. All matters are made up of these fermions. There are antiparticles of quarks and leptons: $\bar{u}$, $\bar{d}$, $\bar{c}$, $\bar{t}$, $\bar{b}$, e^+, $\bar{\nu}_e$, μ^+, $\bar{\nu}_\mu$, τ^+ and $\bar{\nu}_\tau$. The gauge bosons (g, Z^0, $W^\pm$ and γ) are spin 1 particles and carry interactions. The Higgs boson is a spin-zero particle and generates the masses of all particles.

1.1 Remaining problem

1.1.1 Hierarchy problem

The Higgs boson is discovered by both the ATLAS and CMS experiments at the Large Hadron Collider (LHC) in 2012 [4, 5]. They have been measuring properties of the Higgs boson. It is a particle with spin 0 and the mass of 125.09 ± 0.21 (stat) ± 0.11 (syst) GeV [4, 5], which is much lighter than Planck scale ($\sim 10^{19}$ GeV). The other particles in the SM (fermions and gauge bosons) have also light masses but the symmetries in the SM (gauge invariance and chirality conservation) allow them

to have such light masses [6, 7]. However, there is no symmetry for particles with spin 0 in the SM. Since the Higgs boson is only a particle with spin 0 as shown in Figure 1.1, it is an open question why the energy scale of the Higgs boson ($O(10^2)$ GeV) is much less than the Planck scale [2].

The mass of the Higgs boson is theoretically expressed as Eq. 1.1:

$$m^2_{h,\mathrm{obs}} = m^2_{h,\mathrm{bare}} - \frac{2y_f^2}{16\pi^2}\Lambda^2 + \frac{\lambda_S^2}{16\pi^2}\Lambda^2 + \ldots \tag{1.1}$$

where $m_{h,\mathrm{obs}}$ ($m_{h,\mathrm{bare}}$) is the observed (bare) Higgs boson mass, Λ is the cut-off scale of the loop calculation and y_f (λ_S) is the Higgs coupling with a fermion (boson) [8]. The second and third terms are the contribution of the one-loop quantum corrections from the fermion (f) and boson (S) as shown in Figure 1.2.

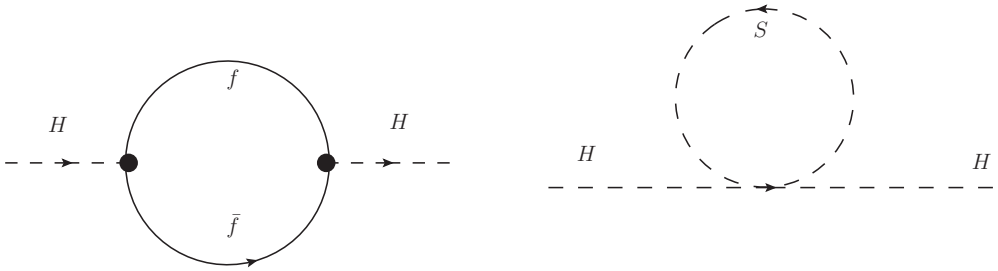

Figure 1.2: The one-loop quantum correction to the Higgs boson mass due to fermion (left) and boson (right).

If the SM is applicable to the Planck Scale, the Λ scale should be the same order. In order to be consistent with the observed Higgs boson mass, the difference between the bare Higgs boson and quantum corrections, which contain the fermion and boson loops in Eq. 1.1, has to be tuned at the level of 10^{-34}. This adjustment is quite unnatural, which is called "Fine tuning problem" [2].

1.1.2 Dark Matter problem

There are cosmological observations which indicate the existence of dark matter. An example is the measurement of the galaxy rotation curve [9]. It measures the rotational velocity, which is the orbital velocity of a star or gas in the galaxy as a function of the distance from the center of the galaxy to the orbiting object (r). Generally, the rotational velocity would expect $v(r) \propto \frac{1}{\sqrt{r}}$ in the outer side of the galaxy. However, the measured velocity is approximately constant in the large value of r as shown in Figure 1.3. It means an existence of massive material, which is not luminous. Such a massive material is called "Dark Matter" (DM).

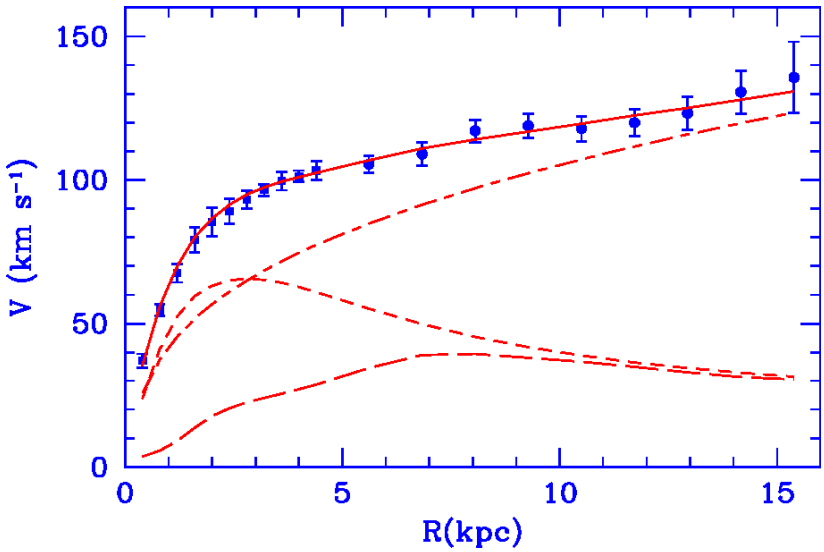

Figure 1.3: The M33 galaxy rotational curve [9]. The x-axis is the distance from the center of the galaxy to the orbiting object and y-axis is the rotational velocity. The filled circles are the measured data points. The solid line is the best fit model considered on the halo contribution (dashed line), stellar disk contribution (short dashed line) and gas contribution (long dashed line).

The DM is generally assumed to be composed of elementary particles. In order to explain observations, these particles should have the following properties:

- They do not have strong and electromagnetic interaction.
- They are stable.
- They have a finite mass.

Among the SM particles, the neutrinos have these properties. However, since the mass of the neutrinos is too light (for example, ν_e <2 eV) [10], that is, the neutrinos are so-called hot DMs, the universe would not have a large scale structure in the astronomical survey [11]. Therefore, there is no candidate in the SM to explain the dark matter.

1.2 Supersymmetry

One of the promising solution of these problems is SUSY, which is a symmetry between fermions and bosons [12–17]. There are several SUSY models, but this thesis focuses on Minimal Supersymmetric Standard Model (MSSM), which introduces minimal particle contents and degrees of freedom to SM [18, 19]. In the MSSM, two Higgs doublets model is introduced unlike the SM. This doublets model extends one Higgs boson particle to five particles: CP even neutral Higgs bosons (h and H), CP odd neutral Higgs boson (A) and charged Higgs bosons ($H^{\pm}$). In order to provide the symmetry between fermions and bosons, partners of all the SM particles (super-partners) have to be introduced as shown in Figure 1.4. The super-partners of the SM fermions are called "sfermions" and have spin 0: "squarks" are the super-partners of the quarks and "sleptons" are the super-partners of the leptons.

The super-partners of the SM gauge and higgs bosons are called "gauginos" ("winos", "binos" and "gluinos") and "higgsinos" with spin 1/2, respectively. The charged gauginos ($\tilde{W}^{\pm}$, $\tilde{H}^{\pm}$) would mix each other and give the mass eigenstates, which are called "chargino". They are denoted as $\tilde{\chi}_1^{\pm}$ and $\tilde{\chi}_2^{\pm}$ in order starting with the lightest mass. The neutral gauginos ($\tilde{Z}^0$, $\tilde{\gamma}$, $\tilde{H}_u$,$\tilde{H}_d$) are mixed as the same as the charged gauginos. They are called "neutralinos" and denoted as $\tilde{\chi}_1^0$, $\tilde{\chi}_2^0$, $\tilde{\chi}_3^0$ and $\tilde{\chi}_4^0$ in order starting with the lightest mass.

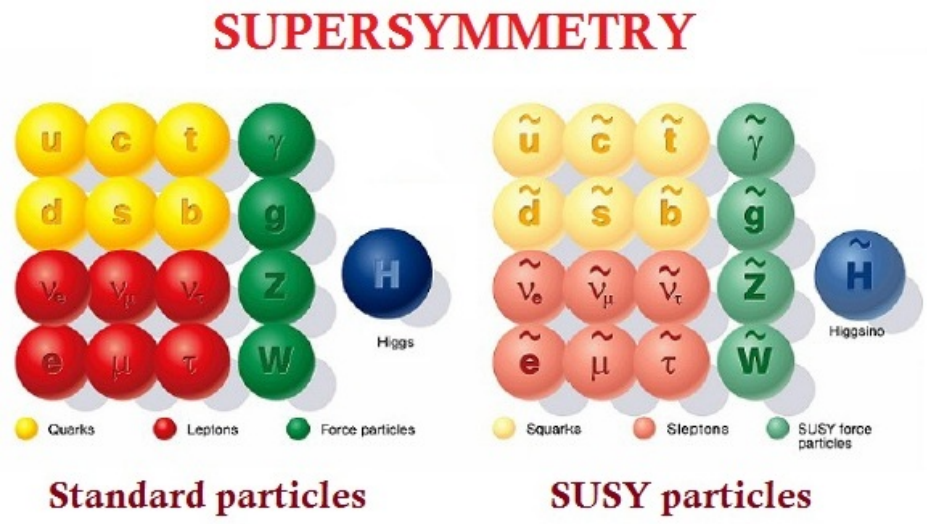

Figure 1.4: All the particles in the MSSM [20]. Two charged and neutral Higgs bosons are added in the SM particles in addition to the observed Higgs boson in this theory. Therefore, five Higgs bosons are considered in the SM particles (left figure). Furthermore, a set of the partners of the SM particles are introduced (right figure).

SUSY can provide an elegant solution to the remaining problems. For the fine tuning of the Higgs boson mass described in Sec. 1.1.1, since the super-partners of the SM fermions (bosons) are particles with spin 0 (spin 1/2), the one-loop corrections of SUSY particles are added the opposite sign to corresponding SM particles. The one-loop correction including in SUSY particles is expressed as Eq. 1.2:

$$m_{h,\mathrm{obs}} = m_{h,\mathrm{bare}}^2 - \frac{2y_f^2}{16\pi^2}\Lambda^2 + \frac{y_{\tilde{f}}^2}{16\pi^2}\Lambda^2 + \frac{\lambda_S^2}{16\pi^2}\Lambda^2 - \frac{2\lambda_{\tilde{S}}^2}{16\pi^2}\Lambda^2 \ldots \tag{1.2}$$

where $y_{\tilde{f}}$ ($\lambda_{\tilde{S}}$) is the Higgs coupling with a sfermion (gaugino). If the masses of SUSY particles are exactly the same as those of SM particles, equations of $2y_f = y_{\tilde{f}}$ and $\lambda_S = 2\lambda_{\tilde{S}}$ can be obtained [1]. It leads that the Λ contributions can be cancelled and thus the fine tuning is not needed.

[1] Since no super-partner of any SM particles has been observed, the mass of SUSY particles is not the same as SM particles. It means that SUSY must be a mechanism for breaking the symmetry at some higher energy scale [21]. In this case, some fine tuning is needed to explain the Higgs boson mass but SUSY models are still motivated because the order of the fine tuning can be significantly reduced.

1.2.1 R-parity conservation

An important conservation is introduced: R-parity conservation [18, 19, 22]. This conservation is required to explain experimental results of proton decay. The proton decays have been searched for in several experiments, but it is not observed until now. The proton decay experiments have established the upper limit of the proton lifetime, $\tau_p > 1.6 \times 10^{34}$ years [23].

SUSY can easily have proton decay, for example, via $p \rightarrow e^+\pi^0$ as shown in Figure 1.5 and in order to prohibit such a proton decay, a new quantum number, R-parity is introduced

$$R := (-1)^{3(B-L)+2S}, \tag{1.3}$$

where B (L) is the baryon (lepton) number and S is the spin. Under this definition, SM particles have R-parity of +1, while the SUSY particles have R-parity of -1. If R-parity is conserved, SUSY particles must be produced in pair from SM particles. Therefore, the process in Figure 1.5 is forbidden. R-parity-conserving SUSY is consistent with the experiment results. From the R-parity conservation, SUSY can provide a contribution of dark matter. It will be explained in the next section.

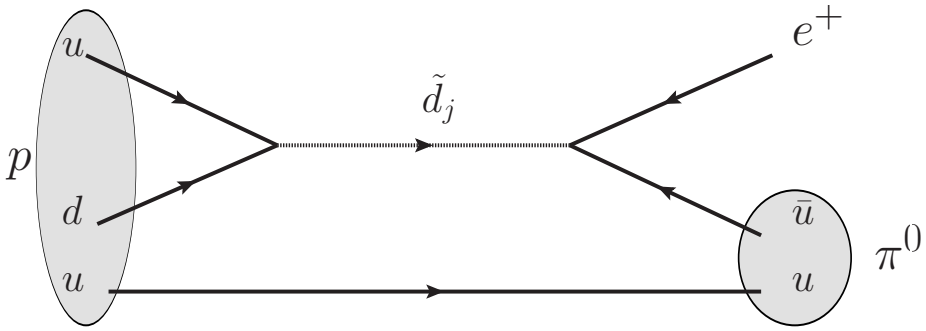

Figure 1.5: $p \rightarrow e^+\pi^0$ decay via SUSY particle, $\tilde{d}_j$.

1.3 Constraints on SUSY particles via indirect search

For the indirect search, theoretical and experimental constraints have been considered on SUSY particles. The Higgs boson mass in the MSSM can be expressed as Eq. 1.4:

$$m_h^2 = m_Z^2 \cos^2 2\beta + \delta_t^2 \tag{1.4}$$

where m_h (m_Z) is the Higgs (Z) boson mass, $\tan\beta$ is the ratio of the vacuum expectation values of up and down type Higgs boson and δ_t is the contribution from loops of top quarks and top squarks (stop) [24]. Since Z boson mass is lighter than the Higgs boson mass, a large radiation correction (δ_t) is needed to reach up to the 125 GeV. Figure 1.6 shows the Higgs boson mass as a function of the stop mass considering on up to the two-loop correction in the MSSM.

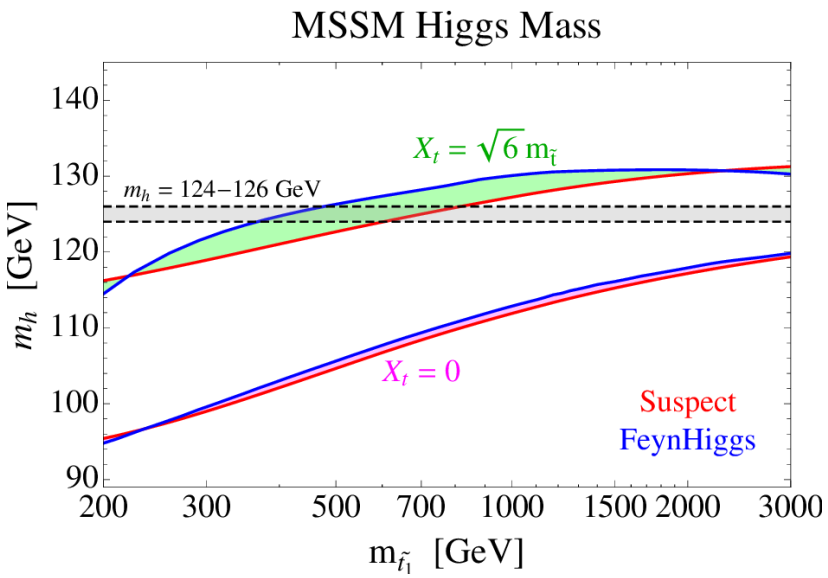

Figure 1.6: The Higgs boson as a function of the lightest stop mass in the MSSM [24]. The red (blue) lines are computed using the Suspect [25] (FeynHiggs [26]) packages, which have each renormalization prescriptions. tanβ = 20 is considered here.

This figure implies two things. First, the stop mass would be above 3 TeV in case the left- and right-handed stops do not mix with each other at all (X_t =0). In this case, a large fine tuning is necessary. Second, the stop mass would be 300∼1000 GeV with the mildly fine tuning in case the stop mixing is maximized ($X_t = \sqrt{6}\, m_{\tilde{t}}$).

The results of flavor mixing and CP violation can also set the constraints of SUSY particles. The squark masses can be estimated from $K^0 - \bar{K^0}$ oscillation; the $d\bar{s}$ and $s\bar{d}$ states can exchange into each other via weak boson as shown in Figure 1.7(a) [27]. The physical mass eigenstates are called K_s^0 and K_L^0 and there is a very small mass difference between them in the SM. However, the mass difference can be enhanced due to loop contributions of the SUSY particles as shown in Figure 1.7(b). The current measurement of the mass difference is $3.5{\times}10^{-15}$ GeV [28], so a constraint of mixing term between $\tilde{s}$ and $\tilde{d}$ is obtained [27]

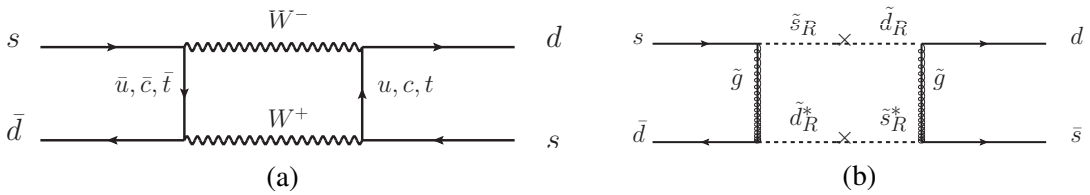

Figure 1.7: Example of the Feynman diagrams for $K^0 - \bar{K^0}$ mixing. The flavor can exchange into each other via only weak boson in the SM (a), but the oscillation can be enhanced via SUSY particles in the MSSM (b). The symbol "×" corresponds to the violation of the strangeness.

$$\frac{|\mathrm{Re}[(m^2_{\tilde{s}_R\tilde{d}_R})^2]|^{1/2}}{m_{\tilde{q}}} < \frac{m_{\tilde{q}}}{1000\ \mathrm{GeV}} \times \begin{cases} 0.04 & \text{for } m_{\tilde{g}} = 0.5 m_{\tilde{q}} \\ 0.10 & \text{for } m_{\tilde{g}} = m_{\tilde{q}} \\ 0.22 & \text{for } m_{\tilde{g}} = 2 m_{\tilde{q}} \end{cases} . \tag{1.5}$$

In the MSSM, squarks are allowed to mix between different generations. In order to suppress the $K^0 - \bar{K}^0$ oscillation, the mixing term ($\mathrm{Re}[(m^2_{\tilde{s}_R\tilde{d}_R})^2]|^{1/2}$) has to be small. From Eq. 1.5 and the current measurement, the squark masses are expected to be heavy (> 10 TeV).

In addition, the properties of neutralino can be constrained from the relic density of the DM [29]. In the early universe (thermal universe), the DM would be produced and annihilated in pair at the same rate and thus the DM particles and SM particles are balanced at the thermodynamic states. However, these processes are not occurred at the same rate and the number of the DM particles are decreased as the universe is inflating. As a result, the universe is cooled and the relic density of the DM would keep the constant due to the low rate of the processes in the current universe. Since the density depends on the cross section of the processes, the relic density can be estimated.

The recent cosmological experiments on the cosmic microwave background (CMB) radiation measure the relic density of the DM with:

$$\Omega_{\mathrm{DM}} h^2 = 0.120 \pm 0.001 \tag{1.6}$$

where Ω_{DM} is the relic density of the DM and h is the Hubble constant in units of 100 km/(s·Mpc) [30]. In the R-parity conservation, a SUSY particle should decay to a lighter SUSY particle. In the end, the lightest SUSY particle ($\tilde{\chi}^0_1$) is stable. It is called the Lightest Supersymmetric Particle (LSP) and is a candidate of the dark matter. Since each neutralino has a different cross section, the LSP type can be constrained as shown in Figure 1.8 [31]. To satisfy the measured relic density of Eq. 1.6, the upper mass bound of pure wino (higgsino) is found to be about 2 (1) TeV from Figure 1.8.

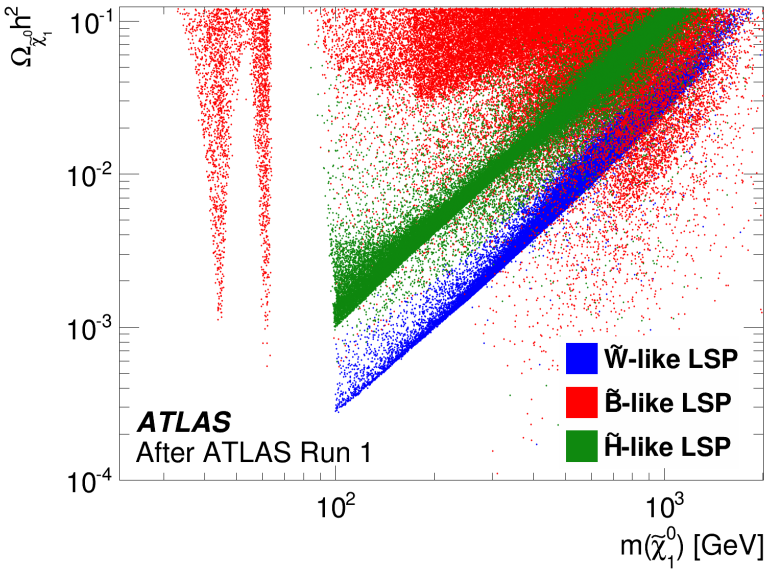

Figure 1.8: Relic density of the dark matter as a function of LSP mass in the pMSSM [32, 33], which assumes some parameters in the MSSM [31]. The colors correspond to LSP types:$\tilde{W}$ (wino), $\tilde{B}$ (bino) and $\tilde{H}$ (higgsino).

1.4 Constraints on SUSY particles via direct search

The direct search for SUSY particles has been performed in several experiments such as LEP, Tevatron, CMS or ATLAS experiments. Figures 1.9 show SUSY searches in ATLAS, which use data collected in 2015-2016 at $\sqrt{s}$ = 13 TeV corresponding to the integrated luminosity of 36.1 fb^{-1}: (a) the squark decays into quark and neutralino, (b) the gluino decays into two quarks and neutralino, (c) the stop decays into top quark and neutralino and (d) the chargino decays into two or three lepton and neutralino [34–36].

No significant excess over the SM predictions is observed and the exclusion limits for these SUSY particles (squarks, gluinos, stop and electroweak gaugino) are set. The masses of the squarks (gluinos) are excluded up to 1.6 (2.0) TeV and stop (chargino) are excluded up to 1000 (580) GeV in case of massless neutralino.

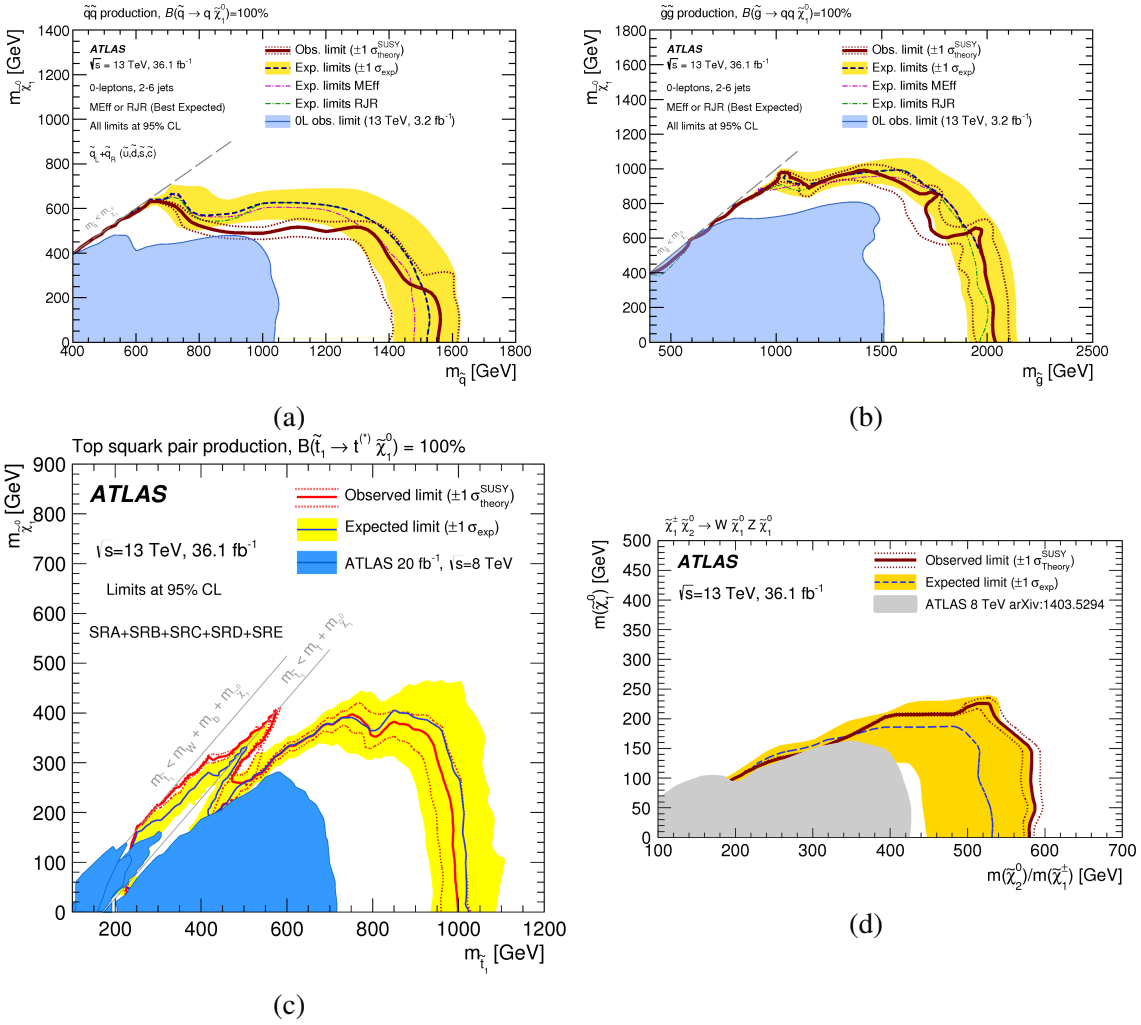

Figure 1.9: The summary of the search for SUSY particles at the ATLAS experiment. The x-axis is (a) squark mass [34], (b) gluino mass [34], (c) top squark mass [35] and (d) chargino mass [36]. The y-axis is the neutralino mass

1.5 Target SUSY particles

This thesis focuses on the gluino as a target SUSY particle. The gluino search is still one of most important physics programmes at the LHC because there are four reasons as follows.

(i) Since the stop mass is excluded up to 1 TeV as shown in Figure 1.9(c), there is a possibility that the stop mass would be heavy (>1 TeV). If the stop mixing is small, the stop mass would be a few TeV from the constraints of the Higgs boson mass calculation (Figure 1.6) and it is difficult to search for such a heavy stop in the LHC with the current center-of-mass energy.

(ii) The squark mass would be heavy (> 10 TeV) from the constraints of $K^0 - \bar{K^0}$ mixing. Therefore, it is also difficult to search for such a heavy squark in the LHC.

(iii) The cross section of slepton or electroweak production is relatively low as shown in Figure 1.10 and their searches might be difficult with the current data statistics.

(iv) The cross section of gluino production is relatively large due to strong interaction (LHC is a proton-proton machine) as shown in Figure 1.10.

Under the R-parity conserving models in the MSSM, the gluinos can be produced in pair ($\tilde{g}\tilde{g}$) as shown in Figure 1.11. In this thesis, the next two processes are considered:

(i) Gluino direct decay (GGd): the process decays through $\tilde{g} \rightarrow qq\tilde{\chi}_1^0$ to the lightest neutralino, $\tilde{\chi}_1^0$, assumed to be the LSP as shown in Figure 1.12(a). This is the simplest process in all the gluino processes and the broad search for gluinos can be performed. Hence, the process having this decay chain is the primary target in this thesis. For this purpose, the final states without leptons are required.

(ii) Gluino one-step decay (GGo): the process decays to the chargino (neutralino) through $\tilde{g} \rightarrow qq'\tilde{\chi}_1^{\pm}$ ($\tilde{g} \rightarrow qq\tilde{\chi}_2^0$) where q and q' are different flavor quark. As shown in Figure 1.12(b) and (c), the chargino (neutralino) decays to the lightest neutralino via $\tilde{\chi}_1^{\pm} \rightarrow W^{\pm}\tilde{\chi}_1^0$ ($\tilde{\chi}_2^0 \rightarrow Z\tilde{\chi}_1^0$). For this process, there are some analyses depending on the number of leptons. The final states without leptons have the highest sensitivity in a region where the gluino is heavy and thus this process is also considered in this thesis.

The search for these two processes is the main target in this thesis. Since the $\tilde{\chi}_1^0$ in Figures 1.12 cannot be detected in any detectors, an observed event topology is multiple jets and large missing transverse momentum.

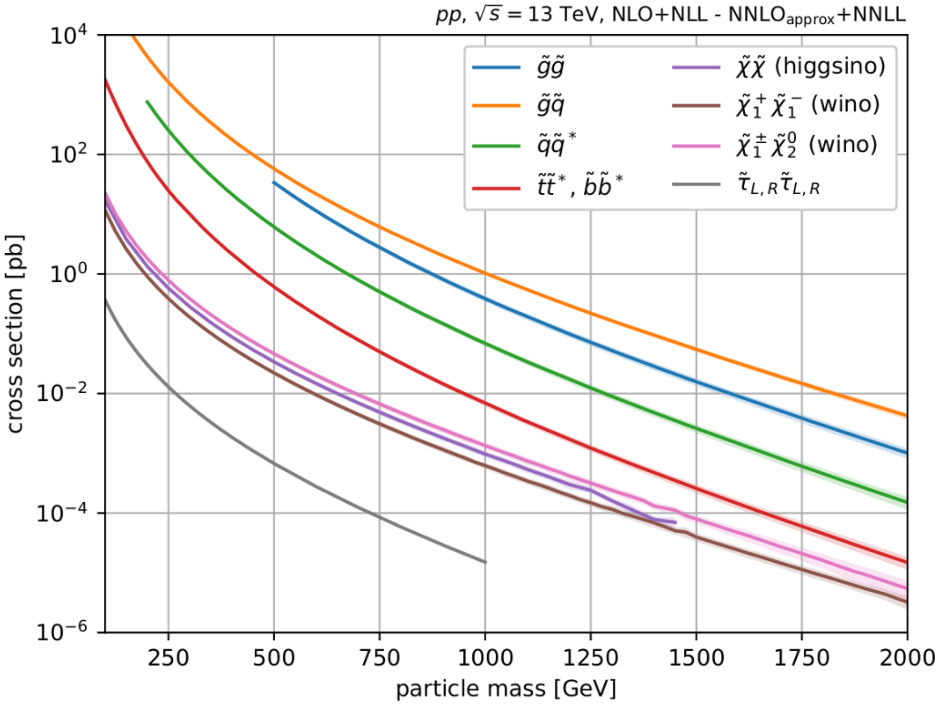

Figure 1.10: The production cross section in SUSY particles at proton-proton collider at $\sqrt{s}$ = 13 TeV [37]. The calculation includes in the resummation of soft gluon emission at the next-to-leading logarithmic accuracy.

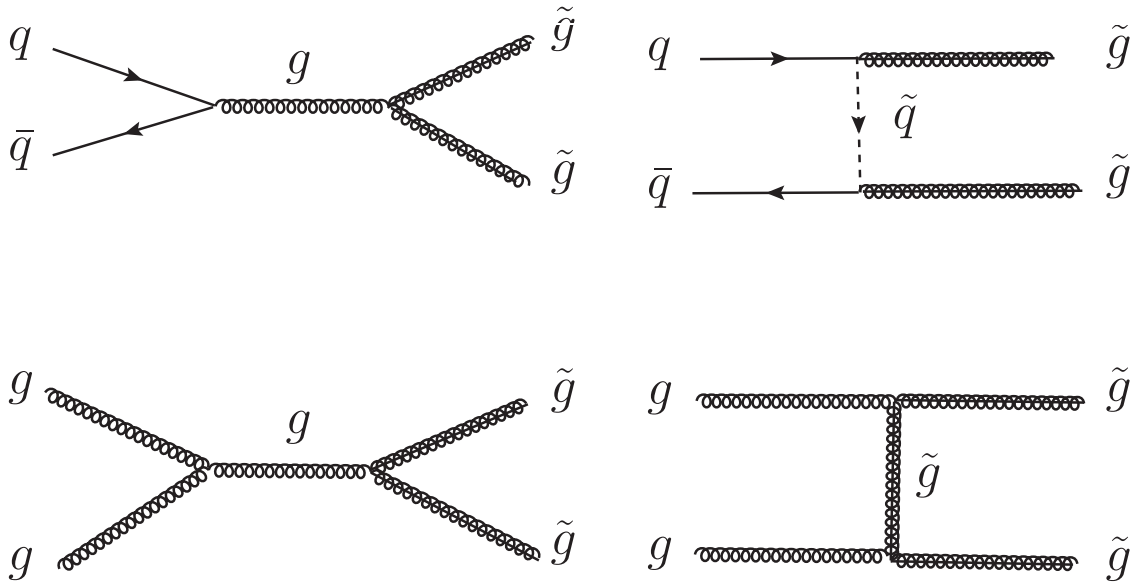

Figure 1.11: Feynmann diagrams of gluino pair production in the LHC.

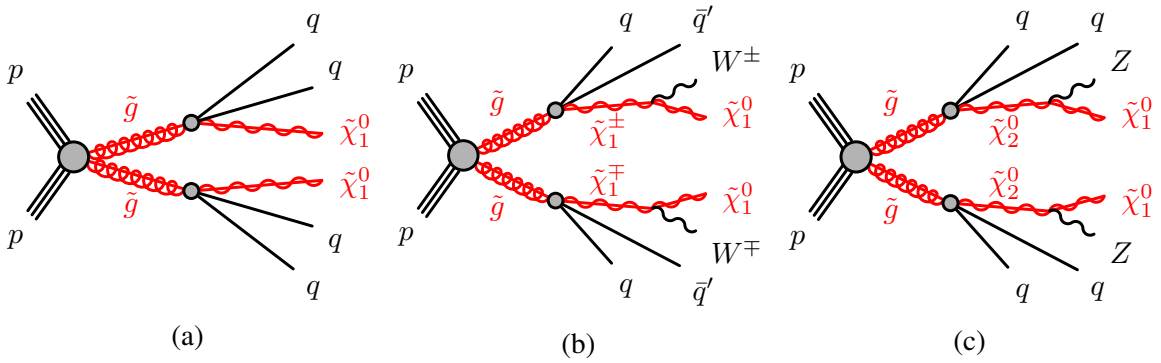

Figure 1.12: The decay topologies of gluino pair production with (a) direct decays and (b,c) one-step decay.

1.6 Strategy of gluino search

In the previous result of gluino search in final states without leptons at the ATLAS [34], more than 25 signal regions are prepared in order to search for all gluino mass points. Each signal region is determined applying cuts on discriminating variables such as the transverse momentum of jets or missing transverse momentum. The search for higher gluino mass becomes more difficult because the production of the cross section is smaller as the gluino mass is higher: the number of events is small. The sensitivity is not significantly improved if this conventional approach is used. Hence, new approach instead of the conventional approach would be needed for the gluino search.

In this thesis, a machine learning approach is introduced. It can improve the separation between signals and SM backgrounds using correlations of variables. Since the correlations are not considered explicitly in the previous result, it allows the sensitivities to be improved well. The machine learning approach has mainly two difficulties. The kinematics of signal processes depends on SUSY masses which will be explained in Section 3.3, so the determination of training samples considering kinematics is very crucial; the choice to improve the sensitivities of all mass points is required. This is first difficulty to use the machine learning in SUSY search. Second, the estimation of background is more complicated than the conventional approach because the machine learning approach utilizes correlations. The development of the background estimation considering the correlations is needed to apply the machine learning to data. Solutions of these difficulties are given in this thesis.

This thesis is organized as follows. Chapter 2 provides the overview of the experiment in this analysis. Chapter 3 explains the overview of dataset and simulation used in this analysis. Chapter 4 describes the reconstruction of objects such as jet, electron, muon or missing transverse momentum. Chapter 5 describes the analysis using the machine learning in detail. Chapter 6 describes the background estimation in detail. Chapter 7 describes the validation of the machine learning approach. Chapter 8 describes the statistical treatment in this analysis. Chapter 9 provides the result and discussion.

2 LHC-ATLAS experiment

2.1 Large Hadron Collider (LHC)

The LHC [38] is a particle accelerator of about 27 km-circumference. It is located underground between 50 m and 175 m depth from the surface in Geneva area. Figure 2.1 shows overview of the accelerator. In order to obtain accelerated protons, hydrogen atoms are first ionized. Then, the protons with 50 MeV are injected in the linear accelerator (LINAC 2). Then, they are accelerated to 1.4 GeV with the BOOSTER, Proton Synchrotron (PS) and Super Proton Synchrotron (SPS). Finally, the accelerated protons are injected in the LHC main ring. It is possible to perform direct searches for new physics at the TeV scale. In the LHC, there are four main experiments: ATLAS (A Toroidal LHC Apparatus) [39], CMS (Compact Muon Solenoid) [40], LHCb (Large Hadron Collider beauty) [41] and ALICE (A Large Ion Collider Experiment) [42]. The ATLAS and CMS experiments perform proton-proton (pp) collisions in the LHC.

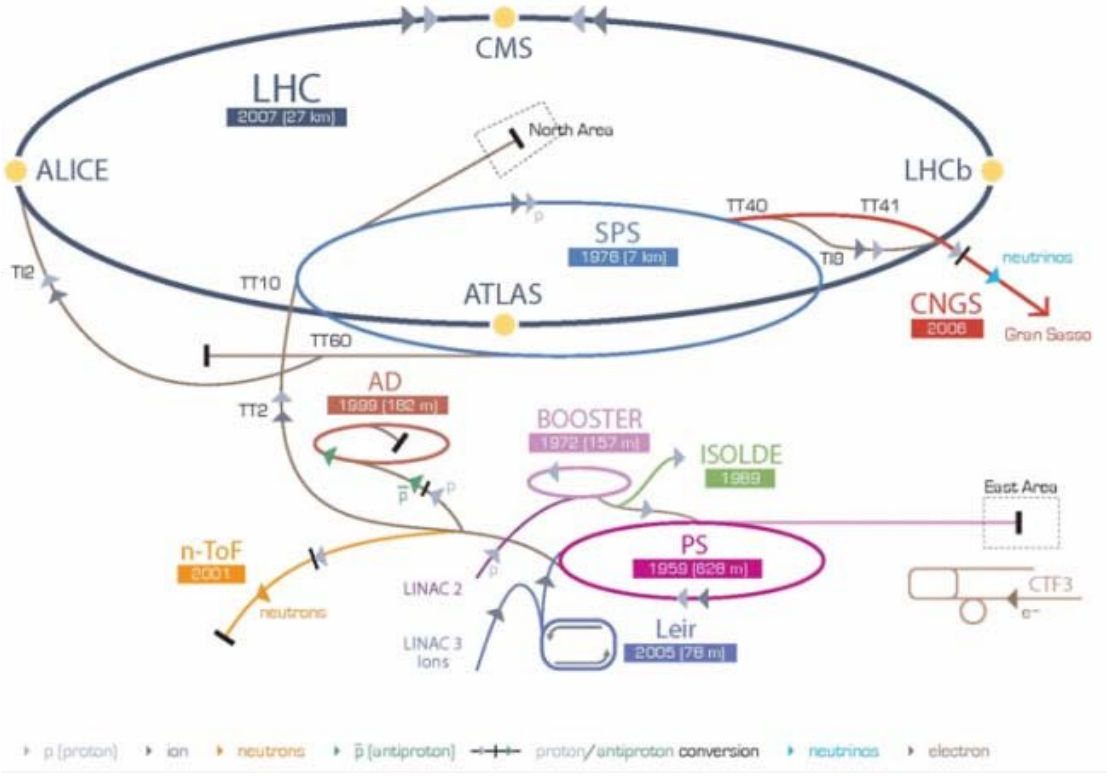

Figure 2.1: The schematic view of the CERN accelerator complex [43].

The LHC ATLAS Run 1 experiment performed pp collisions from 2010 to 2012. Its center-of-mass energy is $\sqrt{s}$ = 7, 8 TeV. The ATLAS detector has been recorded about 5 fb^{-1} for $\sqrt{s}$ = 7 TeV and 20 fb^{-1} for $\sqrt{s}$ = 8 TeV after requiring the data quality. The LHC ATLAS Run 2 experiment performed pp collisions from 2015 to 2018. Its center-of-mass energy is $\sqrt{s}$ = 13 TeV. The ATLAS detector has been recorded 147 fb^{-1} and then data of 139 fb^{-1} is used for physics analysis after requiring the data quality as shown in Figure 2.2.

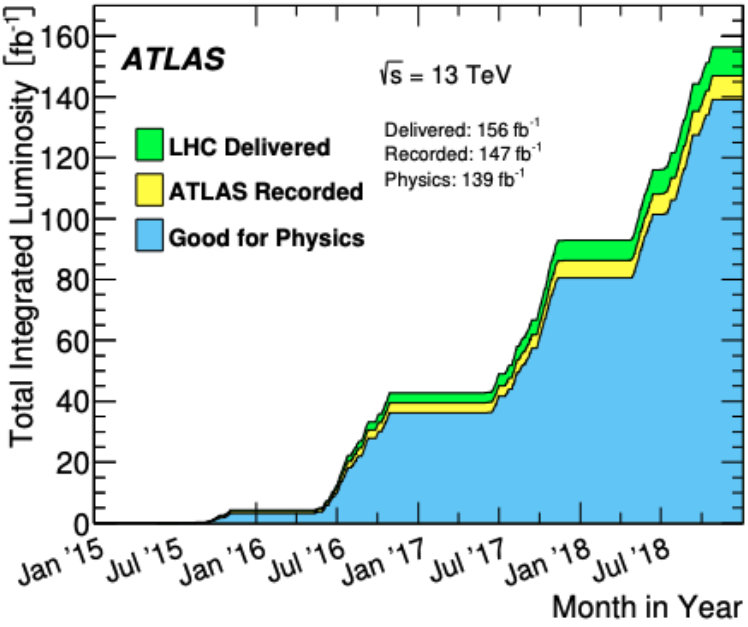

Figure 2.2: The integrated luminosity delivered to LHC (green) and ATLAS (yellow) at Run 2 experiment [44]. The blue shows the integrated luminosity after requiring the data quality and the data is used in an offline analysis.

In case of pp collision in LHC, the instantaneous luminosity is expressed as:

$$L = \frac{f_{\text{rev}} n_b {N_b}^2 \gamma_r}{4\pi\epsilon\beta_{x,y}} F \tag{2.1}$$

where f_{rev} is the revolution frequency, n_b is the number of bunches per revolution, N_b is the number of protons per bunch, ϵ is the initial geometric rms emittance, $\beta_{x,y}$ is the beam size in x-y plane and F is the geometric luminosity reduction factor. The overview of these parameters for each year is shown in Table 2.1.

Under the condition, a pileup is observed. The pileup is categorized to two types: in-time pileup and out-of-time pileup. The in-time pileup is caused by pp interactions in the same bunch crossing due to the dense proton bunches as shown in Table 2.1. In the LHC, the mean number of pp interactions per bunch crossing (μ) is 10-70 as shown in Figure 2.3 and many events with in-time pileup is occurred. The out-of-time pileup is caused by pp interactions in the different bunch crossing due to high frequency of collisions as shown in Table 2.1.

Table 2.1: Parameters for pp collisions at $\sqrt{s}$ = 13 TeV in 2015-2018 [45]. In 2017 run, the LHC runs with two conditions (n_b = 2544, N_b = 1.1×10^{11} and n_b = 1909, N_b = 1.2×10^{11})

Parameter	2015	2016	2017	2018
f_{rev} [Hz]	11253	11253	11253	11253
n_b	2232	2208	2544/1909	2544
N_b (10^{11} protons)	1.1	1.1	1.1/1.2	1.1
ϵ [m]	0.3	0.3	0.3	0.3
$\beta_{x,y}$ [μm]	0.8	0.4	0.3	0.3-0.25
F	0.94	0.94	0.94	0.94

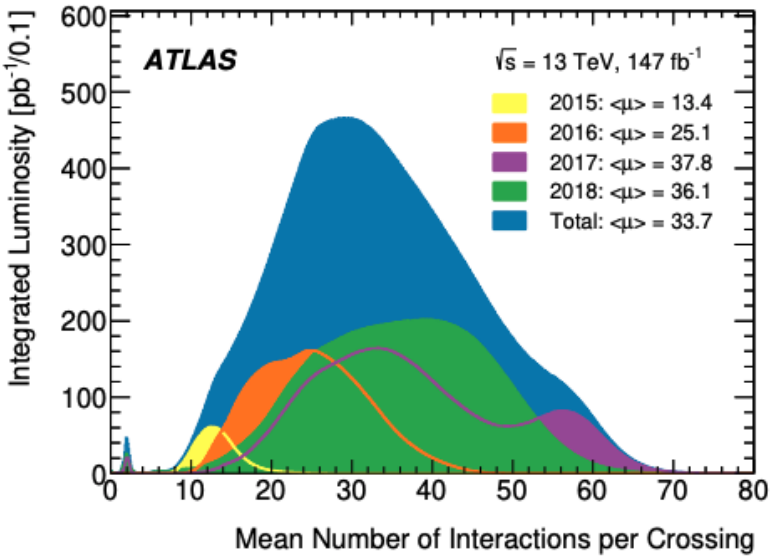

Figure 2.3: Mean number of pp interactions per bunch crossing in 2015-2018 period [44].

2.2 ATLAS detector

The ATLAS detector [39] is a general purpose detector with a symmetric cylindrical geometry on the LHC ring. It covers nearly covered 4π steradian of solid angle and has 44 m in length, 25 m in height and 7000 tons in weight.

The ATLAS uses a right-handed coordinate system with its origin at the nominal interaction point in the center of the detector. The positive x-axis is defined by the direction from the interaction point to the center of the LHC ring, with the positive y-axis pointing upwards. The z-axis is defined by the beam direction. Cylindrical coordinates (r, ϕ) are used in the transverse plane, ϕ being the azimuthal angle around the z-axis. The pseudorapidity η is defined as $\eta = -\ln\tan(\theta/2)$, where θ is the polar angle. The rapidity y is defined as $y = (1/2)\ln[(E + p_Z)/(E - p_Z)]$, where E is the energy and p_Z is the longitudinal momentum. The transverse momentum $p_T = p\sin\theta$ and transverse energy

$E_{\mathrm{T}} = E\sin\theta$ are defined in the x-y plane.

The ATLAS detector mainly consists of three subdetectors as shown in Figure 2.4: inner detector, calorimeter and muon spectrometer. In the following subsections, each subdetector is introduced.

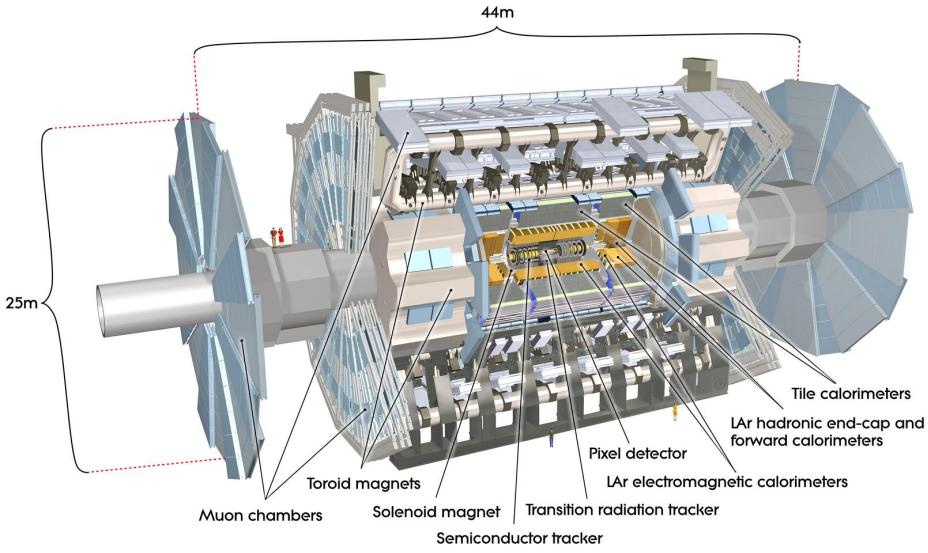

Figure 2.4: Overview of the ATLAS detector[39].

2.2.1 Inner detector

The inner detector (ID) consists of pixel, silicon microstrip and transition radiation tracker (TRT), which cover the pseudorapidity region $|\eta| < 2.5$ as shown in Figure 2.5. The aim of this subdetector is to reconstruct a track of charged particles and measure the transverse momentum (p_{T}).

Silicon pixel detector (Pixel)

Pixel detector has four layer structure and is the closest to the interaction point. The layers except the innermost layer, which is called the insertable B-layer (IBL), cover the region $|\eta| < 2.5$ [47, 48]. They are segmented in R-ϕ and z direction. All pixel sensors have 400×50 μm^2 in R-$\phi \times z$. The IBL is newly introduced since Run 2 experiment and has 250×50 μm^2 pixel sensors.

Semiconductor Tracker (SCT)

SCT detector has four layer structures at the outside of the Pixel detector. The sensors are segmented into strips a pitch of 80 μm. In order to obtain two dimensional information, two strip layers are closely laid at 40 mrad stereo angle.

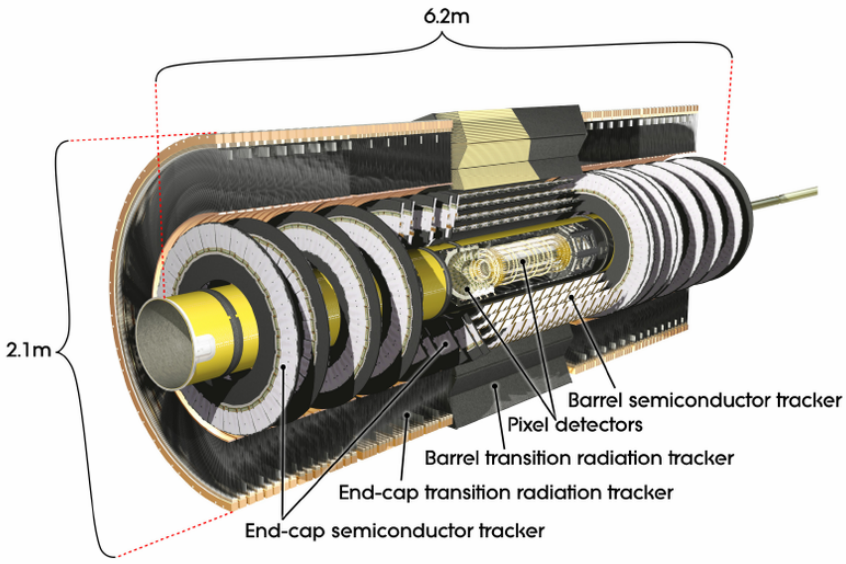

Figure 2.5: Overview of the inner detector [46].

Transition Radiation Tracker (TRT)

TRT detector [49] has a structure of straw drift tubes, which is about 150 cm long at the outside of the SCT detector. The radius of the tube is about 4 mm and operated with a gas mixture of Xe, O_2 and CO_2. This gas is ionized by incident charged particles and the ionized electrons are measured. This effect depends on the relativistic factor $\gamma = E/m$, so this detector can provide an identification between electron and charged pion.

2.2.2 Calorimeter

There are two calorimeters in the ATLAS detector as shown in Figure 2.6: electromagnetic (EM) calorimeter for an electron and a photon and hadronic calorimeter for a hadron. These calorimeters cover with the range $|\eta| < 4.9$.

Electromagnetic calorimeter (EM calorimeter)

The electromagnetic calorimeter is a sampling calorimeter with lead absorber and liquid argon (LAr) detector. The detector covers the range $|\eta| \leq 3.2$. The accordion structure is adopted in order to be continuous in azimuth direction. When an electron or a photon goes through the detector, the lead absorber induces an EM shower, which is a cascade of secondary particles. This EM shower ionizes in the LAr detector and then the ionized particles are measured. The number of ionized particles is proportional to the total energy of the incident particle.

The LAr calorimeter has four layer structures as shown in Figure 2.7. They are called presampler, front, middle and back layers, which are segmented in pseudorapidity η and azimuth ϕ directions.

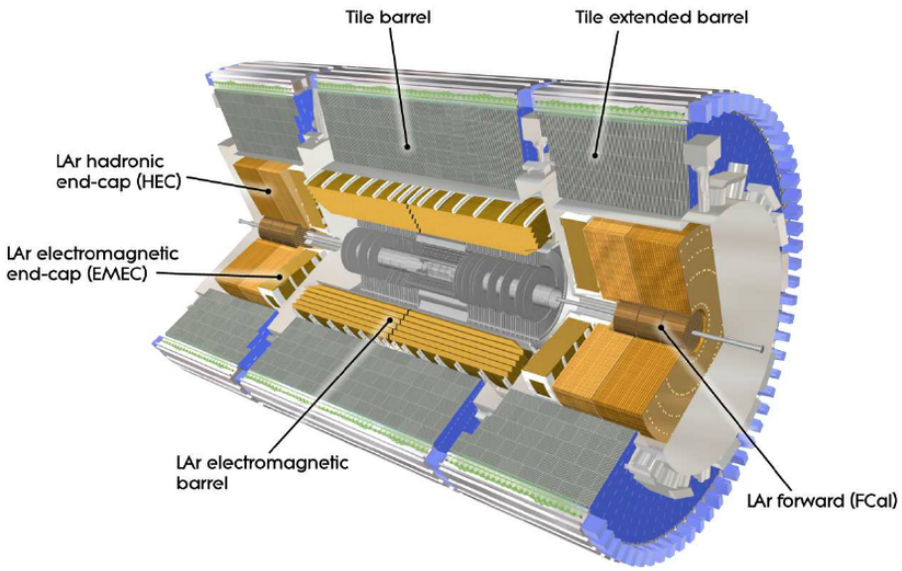

Figure 2.6: Overview of the calorimeter [50].

The presampler layers cover the range $|\eta| \leq 1.8$ and perform to correct the energy lost in front of the calorimeter. The front layer has a finer granularity in η directions ($\Delta\eta = 0.0031$) to allow for the identification between a single photon and a $\pi^0(\rightarrow \gamma\gamma)$. The middle layer is the main sampling one to measure the energy. The back layer is needed to reconstruct a high energy electron or photon ($E_{\mathrm{T}} > 50$ GeV), which traverses the outside of the middle layers.

Hadronic calorimeter

The hadron calorimeter consists of the Tile Calorimeter (TileCal), the Hadronic End-cap Calorimeter (HCAL) and the Forward Calorimter (FCAL), which are also sampling calorimeters. The TileCal covers the region $|\eta| \leq 1.7$ and has three layers with the iron absorber and the plastic scintillator detector. The HCAL covers the region $1.7 \leq |\eta| \leq 3.2$ and has four layers with the copper absorber and the LAr detector. The FCAL covers the region $3.2 \leq |\eta| \leq 4.9$ and has three layers; The front layer uses the copper absorber and the second and the third layers use the tungsten absorber. Since the FCAL is close to the beam pipe, the straw tube structures instead of the accordion structures are adopted.

2.2.3 Muon Spectrometer

The muon spectrometer (MS) is used to measure the momentum and position of muons, which pass through the calorimeters. The MS is the outermost subdetectors and consists of Monitored Drift Tube (MDT), Cathod Strip Chamber (CSC), Resistive Plate Chamber (RPC) and Thin Gap

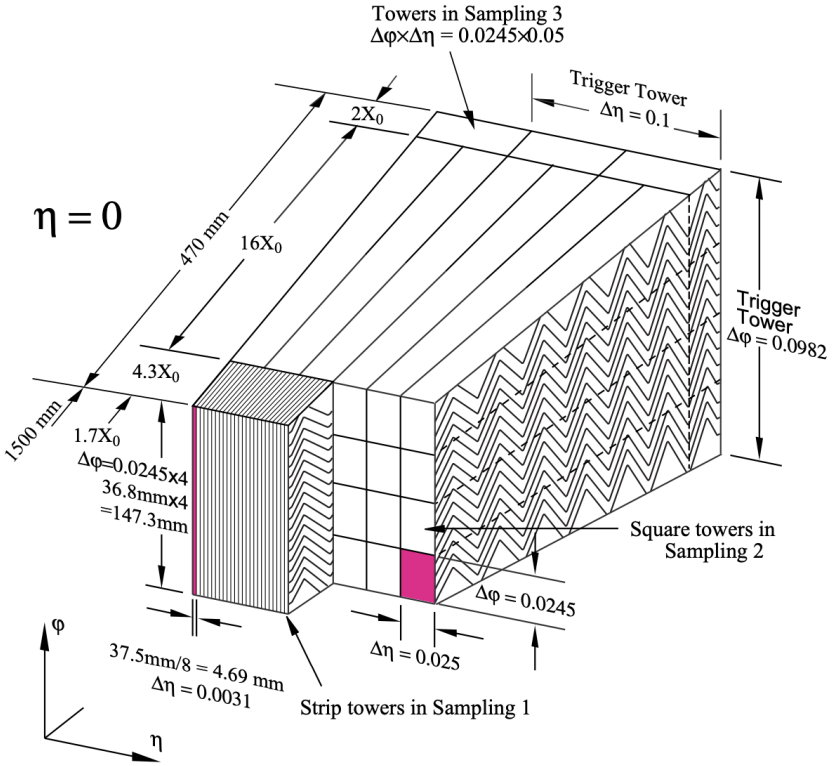

Figure 2.7: The structure of the LAr calorimeter at $\eta = 0$ region [50].

Chamber (TGC). The MDT and CSC are used for precision measurements of muons. The RPC and TGC are used for triggering muons.

Monitored Drift Tube (MDT)

The MDT has three layers, which consist of drift tubes and covers the region $\eta \leq 2.0$. The drift tubes have 30 mm diameter and use a mixture of Ar and CO_2. The position resolution is about 80 μm.

Cathod Strip Chamber (CSC)

The CSC uses multi-wire proportional chambers (MWPC) and covers the region $2.0 \leq |\eta| \leq 2.7$. They can be operated under a high occupancy. The position resolution is about 60 μm.

Resistive Plate Chamber (RPC)

The RPC covers the region $|\eta| \leq 1.05$ and consists of 2 mm gas gap with parallel electrode plates. The time resolution is about 2.0 ns and position resolution is about 10 mm.

Thin Gap Chamber (TGC)

The TGC uses the MWPC with a gas mixture of CO_2:n-C_5H_{12} and covers the region $1.05 \leq |\eta| \leq 2.4$. Since the width of the anode wire is about 1.8 mm, the better time resolution is obtained (4 ns). The position resolution is about 5 mm.

2.3 Trigger and Data Acquisition system

In the Run 2 experiment, the pp collisions are occurred at 40 MHz. Since all the events cannot be recorded, the trigger system, which judges whether each event should be recorded or not, is required. The ATLAS has two trigger systems as shown in Figure 2.8: the First Level Trigger (L1 trigger) and the High Level Trigger (HLT) [51–54].

The information of detectors are first buffered in the Readout Drivers (ROD) to wait the judgment of the L1 trigger. The L1 trigger uses the information of calorimeters and muon spectrometers. In order to process the judgment quickly, the hardware-based trigger is adopted as the L1 trigger. The event rate is reduced from 40 MHz to 100 kHz in a limited and fixed latency of 2.5 μs. An event accepted by L1 is processed in the ROD and then buffered in the Read Out System (ROS) to wait the HLT accept. The HLT is a software-based trigger so that it can perform similar selections to an offline data analysis. The HLT would recover the objects, which are not identified in the L1 trigger, by using the whole detectors. The event rate with HLT accepts is about 1 kHz and the event is transmitted to the data storage for an offline process system.

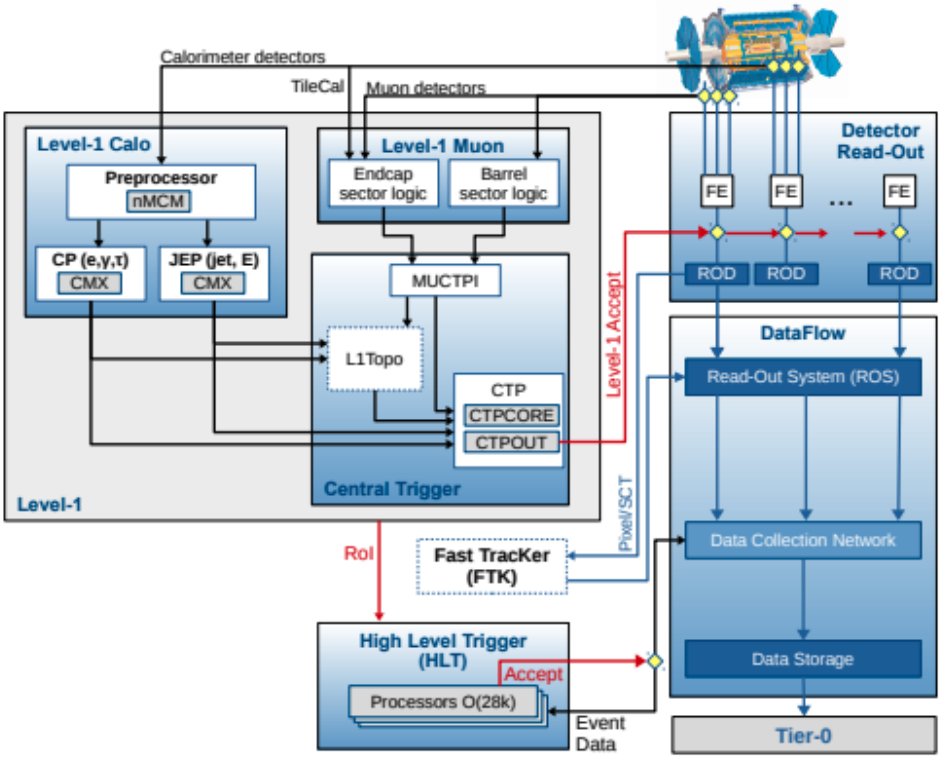

Figure 2.8: The flow of the trigger system in the Run 2 experiment [51].

3 Dataset and Monte-Calro sample

3.1 Dataset

This analysis uses data collected in 2015-2018 at $\sqrt{s}$ = 13 TeV and 25 ns collision rate. The corresponding integrated luminosities with beam and detector data-quality requirements [44] are summarized in Table 3.1. The total integrated luminosity is 139 fb^{-1}. The uncertainty in the combined 2015–2018 integrated luminosity is 1.7 % [55], obtained using the LUCID-2 detector [45] for the luminosity measurements.

Table 3.1: Summary of integrated luminosities for each period.

period	integrated luminosity [fb^{-1}]
2015	3.22
2016	33.0
2017	44.3
2018	58.5
Total	139

3.2 Trigger

Since SUSY signal events in this analysis have large missing transverse momentum, the missing transverse momentum is mainly used for triggering data. In order to maximize data statistics, the lowest unprescaled triggers ($E_{\mathrm{T}}^{\mathrm{miss}}$ trigger) in each data taking period are used as shown in Table 3.2 [51–54]. Each data taking period has the different pileup condition as shown in Figure 2.3, so the threshold of $E_{\mathrm{T}}^{\mathrm{miss}}$ triggers is changed in order to keep the same trigger rate. In addition, the electron, muon and photon triggers are used for a background estimation as discussed in Chapter 6. The single lepton (photon) trigger selects the event with at least one electron or muon (photon) satisfying the p_{T} threshold as shown in Table 3.3 [51–54].

In order to measure the $E_{\mathrm{T}}^{\mathrm{miss}}$ trigger efficiency, the tag and probe method with $W \rightarrow \mu\nu$ event is used. First, events with a single muon, which has the single lepton triggers as shown in Table 3.3, are selected. Then, the transverse mass (m_{T}) cut with 30 GeV $< m_{\mathrm{T}} <$ 100 GeV is applied in order to enhance the purity of W boson events. The remaining events are called "tag" events. The transverse mass is defined as:

$$m_{\mathrm{T}} = \sqrt{2p_{\mathrm{T}}^{\ell}E_{\mathrm{T}}^{\mathrm{miss}}(1 - \cos[\Delta\phi(\ell, \boldsymbol{E}_{\mathbf{T}}^{\mathbf{miss}})])} \tag{3.1}$$

Table 3.2: Summary of $E_{\mathrm{T}}^{\mathrm{miss}}$ triggers used in this analysis.

Year	Period	L1 threshold	HLT threshold
2015	All	50 GeV	70 GeV
2016	A-D3	50 GeV	90 GeV
2016	D4-F1	50 GeV	100 GeV
2016	F2-	50 GeV	110 GeV
2017	B	50 GeV	90 GeV
2017	C	50 GeV	100 GeV
2017	D-	50 GeV	110 GeV
2018	B	50 GeV	110 GeV
2018	C-	50 GeV	110 GeV

Table 3.3: Summary of single lepton (e, μ) and photon (γ) triggers used in this analysis.

Year	HLT threshold (e)	HLT threshold (μ)	HLT threshold (γ)
2015	26 GeV	20 GeV	120 GeV
2016 - 2018	26 GeV	24 GeV	140 GeV

where ${p_{\mathrm{T}}}^{\ell}$ is the transverse momentum of the lepton, $\Delta\phi(\ell, \boldsymbol{E}_{\mathbf{T}}^{\mathbf{miss}})$ is the angular difference between the lepton and $E_{\mathrm{T}}^{\mathrm{miss}}$. Finally, it is checked whether the tag events pass the $E_{\mathrm{T}}^{\mathrm{miss}}$ triggers or not, depending on the reconstructed $E_{\mathrm{T}}^{\mathrm{miss}}$, which is called "Probe". Figures 3.1 show the trigger efficiency as a function of $E_{\mathrm{T}}^{\mathrm{miss}}$ for each period using the tag and probe method. Since the muon momentum is not considered in L1 $E_{\mathrm{T}}^{\mathrm{miss}}$ trigger, the L1 $E_{\mathrm{T}}^{\mathrm{miss}}$ trigger can be emulated by subtracting muon contribution in offline $E_{\mathrm{T}}^{\mathrm{miss}}$ calculation. The efficiency of the $E_{\mathrm{T}}^{\mathrm{miss}}$ trigger is more increased as the $E_{\mathrm{T}}^{\mathrm{miss}}$ is larger and the efficiency reaches to 100% above 300 GeV. In this analysis, $E_{\mathrm{T}}^{\mathrm{miss}} > 300$ GeV is required as the preselection, so that the passed events are not biased due to the triggers; no corrections are needed.

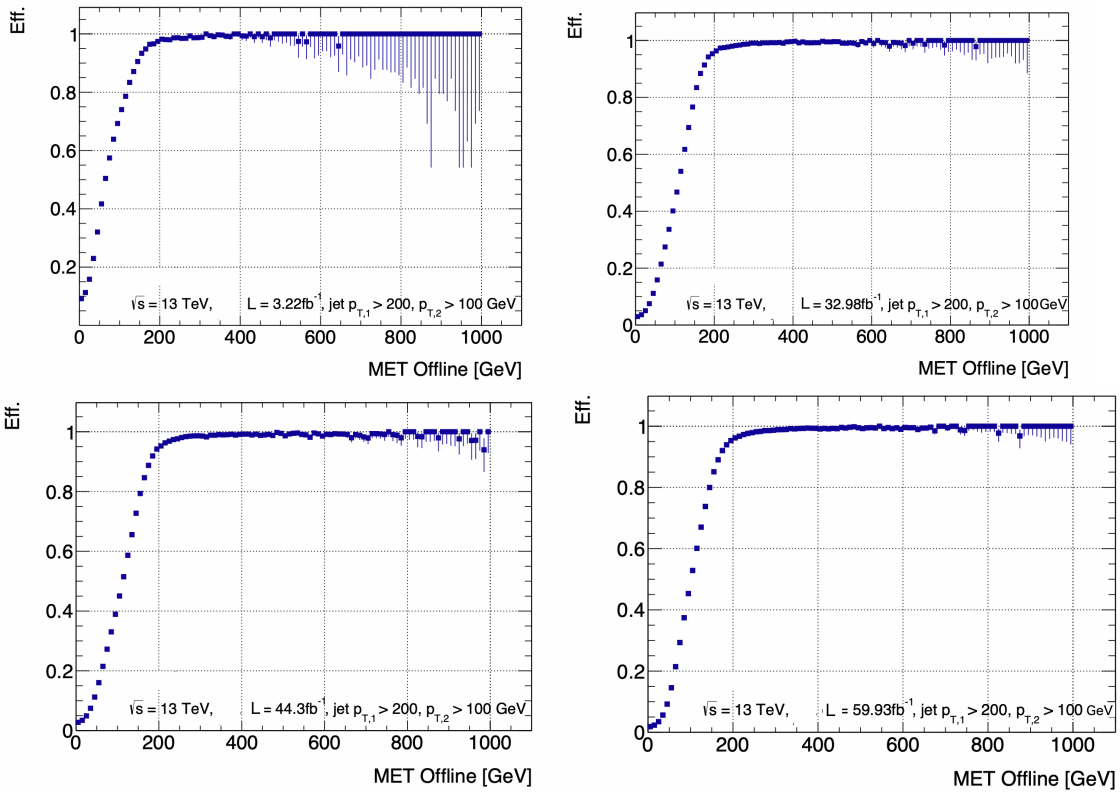

Figure 3.1: Trigger efficiencies as a function of offline $E_{\mathrm{T}}^{\mathrm{miss}}$ after subtracting the muon momentum in 2015 (left-top), 2016 (right-top), 2017 data (left-bottom) and 2018 (right-bottom). The lepton veto, a leading jet with $p_{\mathrm{T}} > 200$ GeV, a second leading jet with $p_{\mathrm{T}} > 100$ GeV and $\Delta\phi(j_{1,2,(3)}, E_{\mathrm{T}}^{\mathrm{miss}})_{\mathrm{min}} > 0.4$ selections, which are defined in Section 5.4, are applied.

3.3 Monte-Carlo sample

This analysis uses simulated samples, which are generated by Monte-Carlo (MC) method, in order to evaluate signal and background processes and to compute with the data. They are called MC samples in this thesis.

3.3.1 Background MC sample

Events of W/Z bosons associated with jets are simulated using Sherpa 2.2.1 generator, whereas γ+jets events are simulated with Sherpa 2.2.2 generator [56]. Matrix elements are calculated for up to two partons at next-to-leading order (NLO) and four partons at leading order (LO) [57, 58] using the Comix [59] and OpenLoops [60, 61] matrix element generators. Then, they are merged with the Sherpa parton shower [62] using Meps@NLOprescription [58, 63–65]. The NNPDF3.0NNLO set of parton distribution functions (PDFs) [58] is used in the Sherpa parton shower. The W/Z boson samples are normalized to the cross section at next-to-next-to-leading order (NNLO) prediction [57]. The γ+jets samples are normalized to the cross section at next-to-leading order (NLO) prediction.

For the generation of $t\bar{t}$ events, the POWHEG-BOX [66–69] v2 generator is used at NLO with NNPDF3.0NLO set of PDFs [58]. In the ATLAS, a h_{damp} parameter in POWHEG-BOX [70, 71] is set to 1.5 times the mass of the top quark (m_{top} = 172.5 GeV). The events are interfaced with PYTHIA 8.230 [72] using the A14 tune [73] and the NNPDF2.3LO set of PDFs in order to model the underlying event, parton showering and fragmentation. The samples are normalized to the cross section prediction at next-to-next-to-leading order (NNLO) in QCD including the resummation of next-to-next-to-leading logarithmic (NNLL) soft-gluon terms calculated using TOP++2.0 [74–80]. For the generation of single-top processes in the Wt, s and t-channels, the POWHEG-BOX [67–69, 81] v2 generator is used at NLO with NNPDF3.0NLO set of PDFs [58]. The events are interfaced with PYTHIA 8.230 [72] using the A14 tune [73] and the NNPDF2.3LO set of PDFs. The samples in Wt, s-channels are normalized to the cross section at NLO+NNLL prediction. The samples in s-channels are normalized to the cross section NLO prediction. For the generation of $t\bar{t}$ in association with electroweak boson ($t\bar{t}$+W/Z) or Higgs boson and four-top events, the MADGRAPH_AMC@NLO 2.3.3 generator [82] at NLO with the NNPDF3.0NLO [58] set of PDFs. The samples are normalized to the cross section prediction at NLO prediction. The events are interfaced with PYTHIA 8.210 parton-shower model, with up to two extra partons included in the matrix element. For these processes, the top quarks are decayed using MADSPIN [83, 84] to preserve spin correlations. The properties of the bottom and charm hadron decays are simulated using the EvtGen v1.2.0 program [85].

Diboson processes (WW, WZ, ZZ, $W\gamma$, $Z\gamma$) are simulated using the SHERPA 2.2.1 [56] generator with NNPDF3.0PDF set [58]. Matrix elements are calculated for no or one parton at NLO and up to three partons at LO using the COMIX and OPENLOOPS matrix element generators and merged with the SHERPA parton shower [62]. The samples are normalized to the cross section prediction at NLO prediction.

A summary of all background MC samples used in this analysis is listed in Table 3.4.

Table 3.4: All background MC samples used in this analysis. The generators, the order in α_s of cross-section calculations used for yield normalization, PDF sets for the parton shower, parton showers and tunes used for the underlying event are shown.

Physics process	Generator	Cross-section normalization	PDF set	Parton shower	Tune
$W(\rightarrow \ell\nu)$ + jets	SHERPA 2.2.1	NNLO	NNPDF3.0NNLO	SHERPA	SHERPA
$Z/\gamma^*(\rightarrow \ell\bar{\ell})$ + jets	SHERPA 2.2.1	NNLO	NNPDF3.0NNLO	SHERPA	SHERPA
γ + jets	SHERPA 2.2.2	NLO	NNPDF3.0NNLO	SHERPA	SHERPA
$t\bar{t}$	POWHEG-BOX v2	NNLO+NNLL	NNPDF2.3NLO	PYTHIA 8.230	A14
Single top (Wt-channel)	POWHEG-BOX v2	NNLO+NNLL	NNPDF2.3LO	PYTHIA 8.230	A14
Single top (s-channel)	POWHEG-BOX v2	NLO	NNPDF2.3LO	PYTHIA 8.230	A14
Single top (t-channel)	POWHEG-BOX v2	NLO	NNPDF2.3LO	PYTHIA 8.230	A14
$t\bar{t} + W/Z/H$	MADGRAPH_AMC@NLO 2.2.3	NLO	NNPDF2.3LO	PYTHIA 8.210	A14
$t\bar{t} + WW$	MADGRAPH_AMC@NLO 2.2.2	NLO	NNPDF2.3LO	PYTHIA 8.210	A14
WW, WZ, ZZ, $W\gamma$, $Z\gamma$	SHERPA 2.2.1	NLO	NNPDF3.0NNLO	SHERPA	SHERPA

3.3.2 Signal MC sample

Masses of SUSY particles are needed to prepare signal MC samples and determined from more than 100 parameters in the SUSY. However, most of parameters do not affect kinematics of the signal SUSY processes because the kinematics is mainly determined by the SUSY mass spectra. The signal MC samples are generated depending on the SUSY masses, but there are still several parameters. In order to reduce the parameters, a simplified model [86–88] are used in the SUSY search. This model assumes that the masses of all SUSY particles are set to large values except the few SUSY particles involved in the decay chain of interest. It means only one decay chain of interest is considered and all other decay chains are ignored. In this case, the kinematics of the signal SUSY processes is only determined by the production of particle masses and cross sections and the model can be described by a few parameters, which is the benefit of simplified models.

Two processes of gluino direct decay and gluino one-step decay as described in Section 1.5 are generated as signal MC samples.

Gluino direct decay The process is simulated using the MADGRAPH_AMC@NLO 2.2.3 generator [82] at NLO and interfaced with PYTHIA 8.230. In order to focus on the decay chain, gluino and lightest neutralino are only considered: other sparticles are assumed to be decoupled. The composition of the $\tilde{\chi}_1^0$ is assumed to be purely bino. The signal MC samples are generated per a gluino and neutralino mass. Figure 3.2(a) shows the generated MC sample for gluino direct decay process. 143 signal points are generated in total [1]. Since four flavour squarks ($\tilde{u}, \tilde{d}, \tilde{c}, \tilde{s}$) are nearly degenerated in the MSSM, the quarks in final states assume to be light-flavour quarks (u, d, c, s).

Gluino one-step decay The process is simulated using the MADGRAPH_AMC@NLO 2.2.3 generator at NLO and interfaced with PYTHIA 8.230. In order to focus on the decay chain, gluino, chargino and lightest neutralino are only considered for gluino one-step decay via W boson ($\tilde{\chi}_1^\pm \rightarrow W^\pm \tilde{\chi}_1^0$) and gluino, neutralino and lightest neutralino are only considered for gluino one-step decay via Z boson ($\tilde{\chi}_2^0 \rightarrow Z \tilde{\chi}_1^0$): other sparticles are assumed to be decoupled. The composition of $\tilde{\chi}_1^0$ ($\tilde{\chi}_1^\pm, \tilde{\chi}_2^0$) is assumed to be purely bino (wino). This thesis considers the following mass spectra for gluino one-step decay.

- Primary model: the chargino mass (neutralino) is fixed at $m_{\tilde{\chi}_1^\pm} = (m_{\tilde{g}} + m_{\tilde{\chi}_1^0})/2$ ($m_{\tilde{\chi}_2^0} = (m_{\tilde{g}} + m_{\tilde{\chi}_1^0})/2$).
- Secondary model: the neutralino mass is fixed at 60 GeV ($m_{\tilde{\chi}_1^0} \sim m_h/2$) in order to explain the relic density, while avoiding all the current constraints [89].

Figures 3.2(b) and 3.2(c) shows the generated MC sample for gluino one-step decay process. 73 signal points for primary model and 78 signal points for secondary model are generated in total [2]. Since four flavour squarks ($\tilde{u}, \tilde{d}, \tilde{c}, \tilde{s}$) are nearly degenerated in the MSSM, the quarks in final states assume to be light-flavour quarks (u, d, c, s).

[1] There are no signal points with a region where the gluino mass is below 1800 GeV and the neutralino mass is below 500 GeV, but the region is already excluded in the previous result of gluino search [34].

[2] The secondary model is only considered for gluino one-step decay via W boson in this thesis.

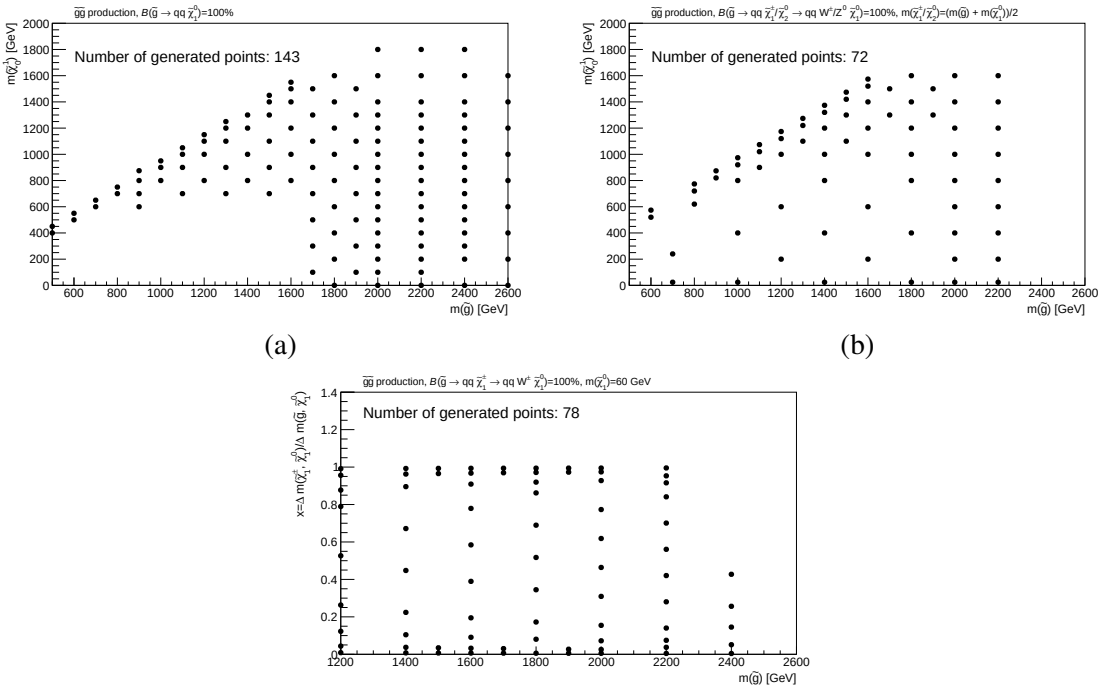

Figure 3.2: Generated MC signal points in the neutralino mass versus gluino mass for the gluino direct decay (top-left), gluino one-step decay with primary model (top-right) and gluino one-step decay with secondary model (bottom) on a simplified model.

In addition to these two processes, three signal MC samples are generated to evaluate the sensitivity discussed in Section 9.3. First, the gluino direct decay with heavy flavour (b or t) as shown in Figures 3.3 are considered. The processes are generated with the same generator as gluino direct decay. 144 signal points for $\tilde{g} \rightarrow bb\tilde{\chi}_1^0$ and 152 signal points for $\tilde{g} \rightarrow tt\tilde{\chi}_1^0$ are generated in total. Next, the models with inclusive production of squarks and gluinos are considered. Figures 3.4 show the decay topologies in the models. There are three productions in the models: gluino pair production, squark and gluino production and squark pair production. The cross section of each production depends on the squark and gluino masses. For simplicity, the neutralino mass is fixed to 0 GeV and gluino and squark masses are varied. All other supersymmetric particles, including the squarks of the third generation, have set to their masses, so the particles are effectively decoupled from the squarks, gluinos and lightest neutralinos. The processes are generated under the same generator as gluino direct decay. 42 signal points are generated in total.

3.3.3 Detector and pileup simulation

All background MC samples are passed through full ATLAS detector simulation [90] using Geant4 [91], while SUSY signal samples are passed through a fast simulation [92], which uses a parameterized simulation for response of the calorimeter systems. The generation of the simulated

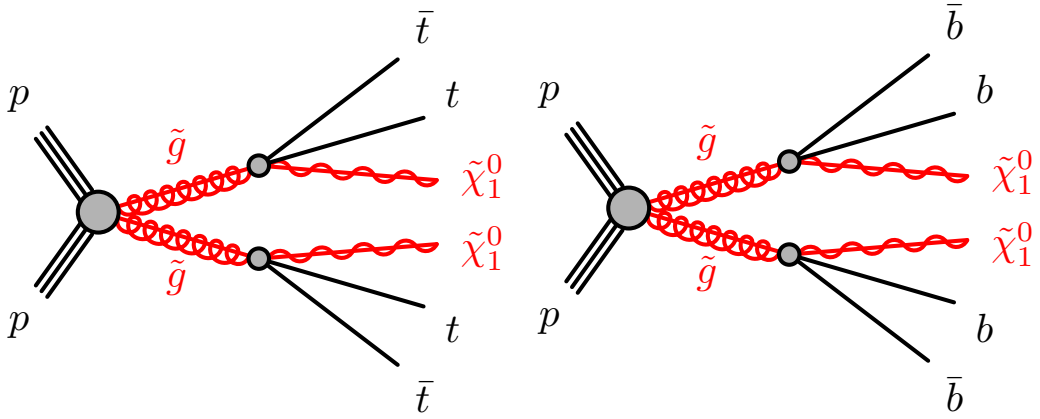

Figure 3.3: The decay topologies of gluino pair production with direct decays via t quarks (left) and b quarks (right).

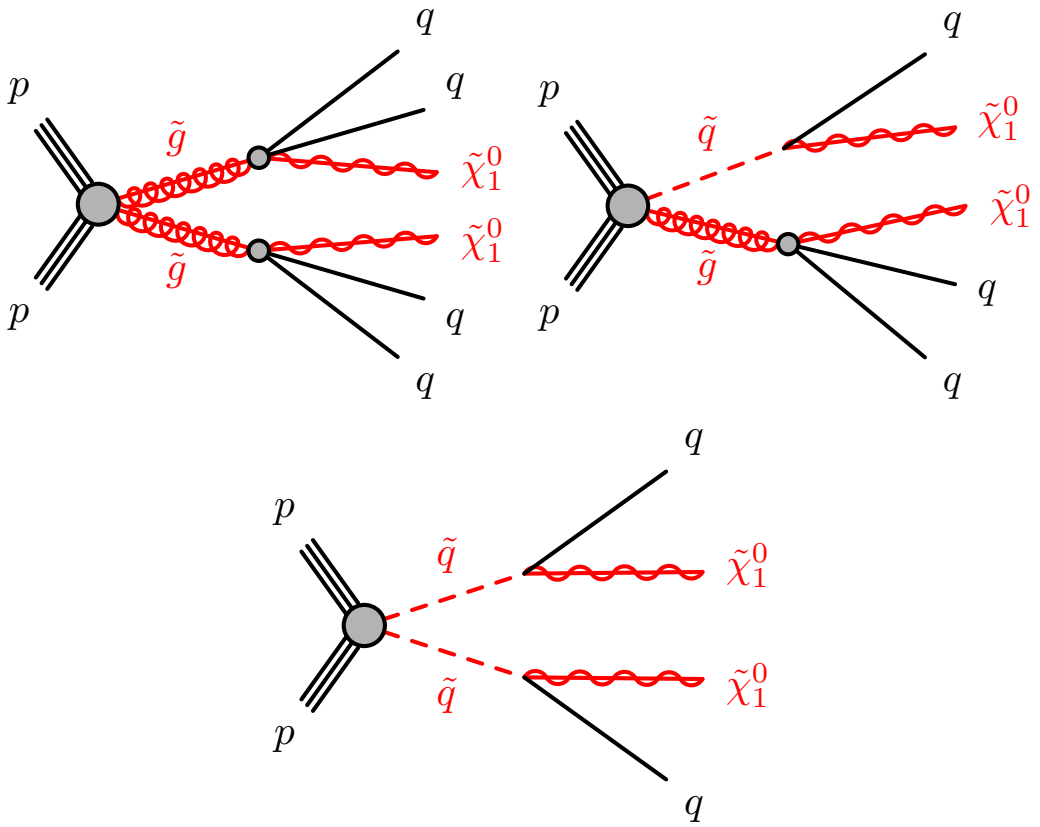

Figure 3.4: The decay topologies of the models with inclusive production of squarks and gluino for direct decays. There are three productions in the models: gluino pair production (top-left), squark and gluino production (top-right) and squark pair production (bottom). The cross section of each production depends on the squark and gluino masses.

event samples includes the effect of multiple pp interactions per bunch crossing, as well as the effect on the detector response due to pileup events. Then, reconstruction algorithms used for the data, which will be explained in Chapter 4 are applied to the MC samples. Finally, the generated MC samples are reweighted to match the observed pileup distribution. Then, a scale factor (1/0.99) is applied to MC samples to realize the observed mean number of pp interactions per bunch crossing ($\langle\mu\rangle$). However, the number of primary vertex (N_{PV}) distribution in data is not described by the MC samples in this case. If the scale factor (1/1.07) is applied to MC samples, an agreement of number of primary vertex distribution is observed. In order to take into account both distributions (N_{PV} and $\langle\mu\rangle$), the scale factor (1./1.03), which is the middle value of them is applied to MC samples as a nominal. The up-type (down-type) scale factor is 1/1.07 (1/0.99).

4 Object reconstruction and identification

This analysis uses electrons, muons, photons, jets and missing transverse momenta. This chapter describes their reconstruction, identification and calibration from the information of the ATLAS detector described in Section 2.2.

4.1 Charged tracks

When charged particles traverse the inner detectors, energy is deposited as hits on different layers in the pixel and silicon detectors. In order to reconstruct tracks there are three steps. First, clusters from the raw measurements in pixel and SCT detectors are assembled from hits using a connected component analysis [93]. Then, three-dimensional measurements referred to space-points are created from these clusters and seed tracks are formed from three space-points. Finally, track candidates are built from the seed tracks by performing a Kalman filter [94]. After applying this filter, high efficiencies of the track reconstruction are obtained. However, some track candidates have overlapping space-points or are incorrectly assigned. Hence, a track score is calculated by considering clusters assigned to a track in each track candidate. Track candidates with bad track scores are rejected. The detail of track reconstruction is found in Ref. [95].

From these tracks, vertices are reconstructed using a vertex finding algorithm [96]. This vertex finding algorithm is iterated until all tracks are associated to vertices, which have at least two tracks. Then, the sum of transverse momentum of tracks is calculated per vertex and the vertex with the largest value is used as a primary vertex (PV), which is considered as the vertex of hard scatter.

4.2 Jet

4.2.1 Reconstruction

In order to reconstruct jets, the clusters of calorimeters cells are needed. A cell with the most significant energy deposit is the start of cluster reconstruction (seed cell). Then, clusters are formed to gather neighbor cells to the seed cell. They are called "topo-clusters" [97].

Jets are reconstructed using an anti-k_t jet clustering algorithm [98, 99], which performs four-momentum recombination of the topo-clusters. The algorithm combines two topo-clusters based on the distance, $d_{i,j}$, which is defined as

$$d_{i,j} = \min({p_{\mathrm{T}i}}^{-2}, {p_{\mathrm{T}j}}^{-2}) \frac{{\Delta R_{i,j}}^2}{r^2} \tag{4.1}$$

where $p_{\mathrm{T}i}$ is the transverse energy of topo-clusters with index i and r is the distance parameter, which is set to $r = 0.4$ in this analysis. $\Delta R_{i,j}$ is the distance in η-ϕ plane defined as

$$\Delta R_{i,j} = \sqrt{(\eta_i - \eta_j)^2 + (\phi_i - \phi_j)^2}. \tag{4.2}$$

The anti-k_{T} jet algorithm first calculates the smallest $d_{i,j}$ and $d_{i,B} = p_{\mathrm{T}i}^{-2}$. Then, the two topo-clusters are merged into one cluster if $d_{i,j}$ is smaller than $d_{i,B}$ and recalculates $d_{i,j}$ and $d_{i,B}$. This iteration continues until $d_{i,B}$ becomes the smallest. Figure 4.1 shows the overview of a sample parton-level event clustered with anti-k_t jet clustering algorithm. For this algorithm, the topology of hard jets is circular with the distance parameter.

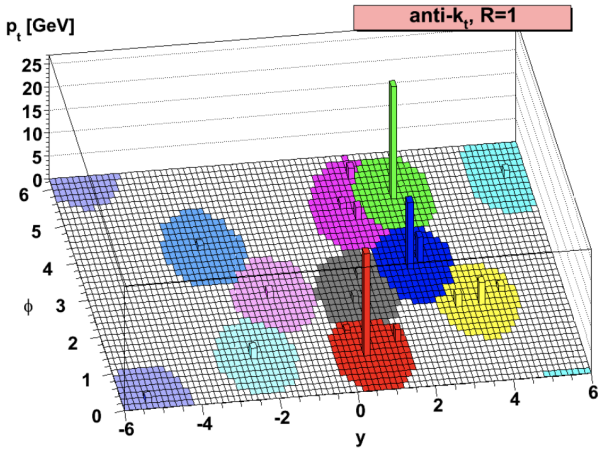

Figure 4.1: Example of a sample parton-level event clustered with anti-k_t jet clustering algorithm with the distance parameter $R = 1.0$ [98].

4.2.2 Calibration

The energy measured in the calorimeters is calibrated in EM scale, which measures the energy deposited in the calorimeter by particles produced in electromagnetic showers. Since reconstructed jets contain components of the hadronic interaction, an additional calibration should be performed to obtain their proper energy. It is called jet energy scale (JES) calibration [100]. A series of calibrations is derived from MC simulation and data as shown in Figure 4.2. The details of each calibration stage are explained below.

Origin correction

The four-momentum of jets is defined with respect to a center of the detector. The "origin correction" recalculates their four-momentum to point to a hard scatter vertex keeping the jet energy. This correction improves the η resolution of jets: the difference between reconstructed jets and truth jets would be small.

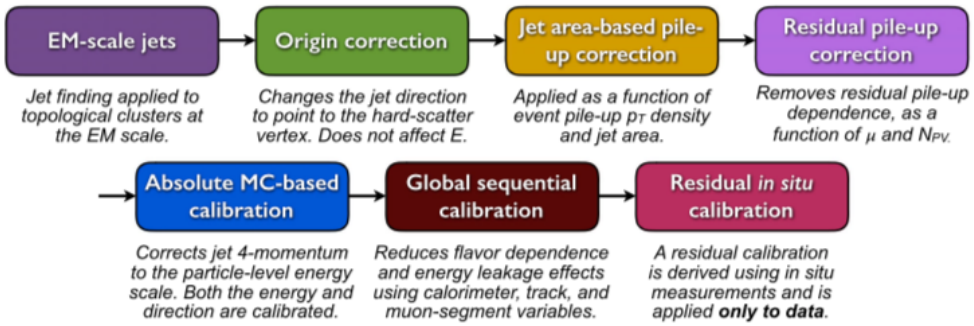

Figure 4.2: Calibration stages for jets measured in the calorimeters [100]. Corrections except "Residual in situ calibration" are performed using MC simulation. The Residual in situ calibration is performed using the data.

Pileup corrections: Jet area-based pileup correction

The contributions of in-time and out-time pileup are removed using two corrections: jet area-based correction and residual pileup correction. The jet area-based correction subtracts pileup contributions event by event. The residual pileup correction subtracts pileup contributions using the number of reconstructed primary vertex (N_{PV}) and the average number of interactions per bunch crossings (μ_{pileup}). The momenta corrected by two corrections (${p_{\mathrm{T}}}^{\mathrm{reco}}$) are expressed as:

$$ {p_{\mathrm{T}}}^{\mathrm{corr}} = {p_{\mathrm{T}}}^{\mathrm{reco}} - \rho \times A - \alpha \times (N_{\mathrm{PV}} - 1) - \beta \times \mu_{\mathrm{pileup}} \tag{4.3} $$

where ${p_{\mathrm{T}}}^{\mathrm{reco}}$ is transverse momentum of a reconstructed jet before pileup corrections and ρ is the mean of transverse momentum density of jets in the η-ϕ plane. A is jet area calculated using ghost association [101]. The α and β parameters depend on the truth jet p_{T} and η in MC simulation and are determined by linear fits.

Absolute MC-based calibration

Since the ATLAS detector has the inactive region such as the transition between calorimeters, reconstructed jets are biased; there is a difference between reconstructed jets and truth jets. The "absolute MC-based calibration" accounts the bias and corrects the four-momentum of jets using MC sample. The bias is corrected using an average energy response in MC simulation. It is defined as the ratio of reconstructed jets and truth jets ($E_{\mathrm{T}}^{\mathrm{reco}}/E_{\mathrm{T}}^{\mathrm{truth}}$). The difference between reconstructed jets and truth jets is appeared in the detector gap and transitions between calorimeters as shown in Figure 4.3(a). The η bias of jets is also corrected using the relative difference as a function of reconstructed jet $|\eta|$ as shown in Figure 4.3(b).

Global sequential calibration

Even though the calibrations described above have been applied, the residual dependencies of the jet energy scale on longitudinal and transverse features of the jets are still observed. They are related

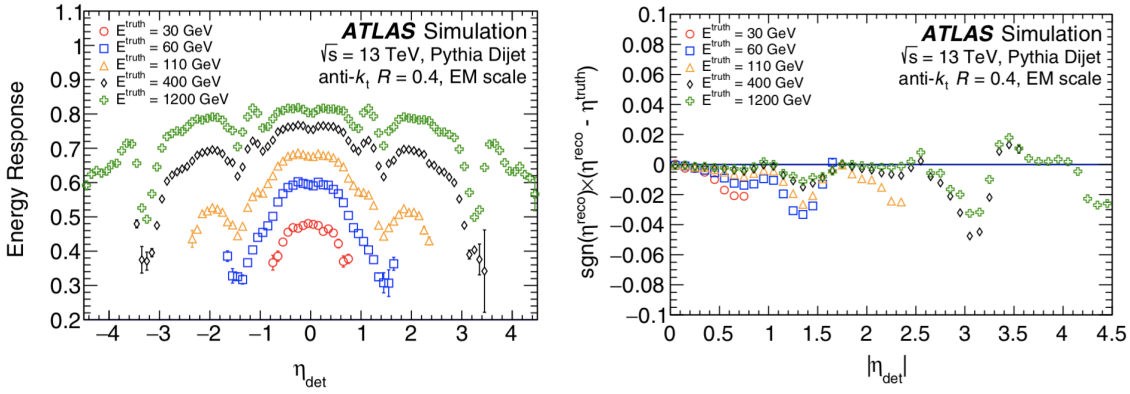

(a) (b)

Figure 4.3: (a) Average energy response as a function of reconstructed jet η for jets of $E_{\mathrm{T}}^{\mathrm{truth}} = 30, 60, 110, 400$ and 1200 GeV [100]. (b) Relative difference between truth jet η^{truth} and reconstructed jet η^{reco} as a function of reconstructed jet $|\eta_{\mathrm{det}}|$ [100].

to the particle composition and the shower shape of a jet. In order to correct such differences, the correction for five independent observables are sequentially applied to the jets: f_{Tile0}, f_{LAr3}, n_{trk}, W_{trk} and n_{segments}. f_{Tile0} is the fraction of jet energy measured in the first layer of the Tile calorimeter. f_{LAr3} is the fraction of jet energy measured in the third layer of the LAr calorimeter. n_{trk} is the number of tracks with p_{T} >1 GeV in the jet. W_{trk} is the average p_{T}-weighted transverse distance in η-ϕ plane between the jet axis and all tracks with p_{T} >1 GeV. n_{segments} is the number of muon track segments in the jet. Figures 4.4 show an average transverse momentum response in MC simulation. It is defined as the ratio of reconstructed jets and truth jets ($p_{\mathrm{T}}^{\mathrm{reco}}/p_{\mathrm{T}}^{\mathrm{truth}}$). Small deviations in these variables are observed, so the calibration is applied to correct the deviations. This procedure is called "Global sequential calibration".

In situ calibration

Since MC simulation does not describe the detector response perfectly, there are differences between data and simulation. "In situ calibration" corrects the differences. Difference between data and MC simulation is quantified by balancing the p_{T} of a jet against other well-measured reference objects such as Z boson, photon and multi-jet.

Systematic uncertainty in calibration

The final calibration includes more than 100 systematic uncertainties on the energy scale and resolution. All systematic uncertainties are listed in Ref [100]. The majority of uncertainties come from in situ calibrations as shown in Figure 4.5.

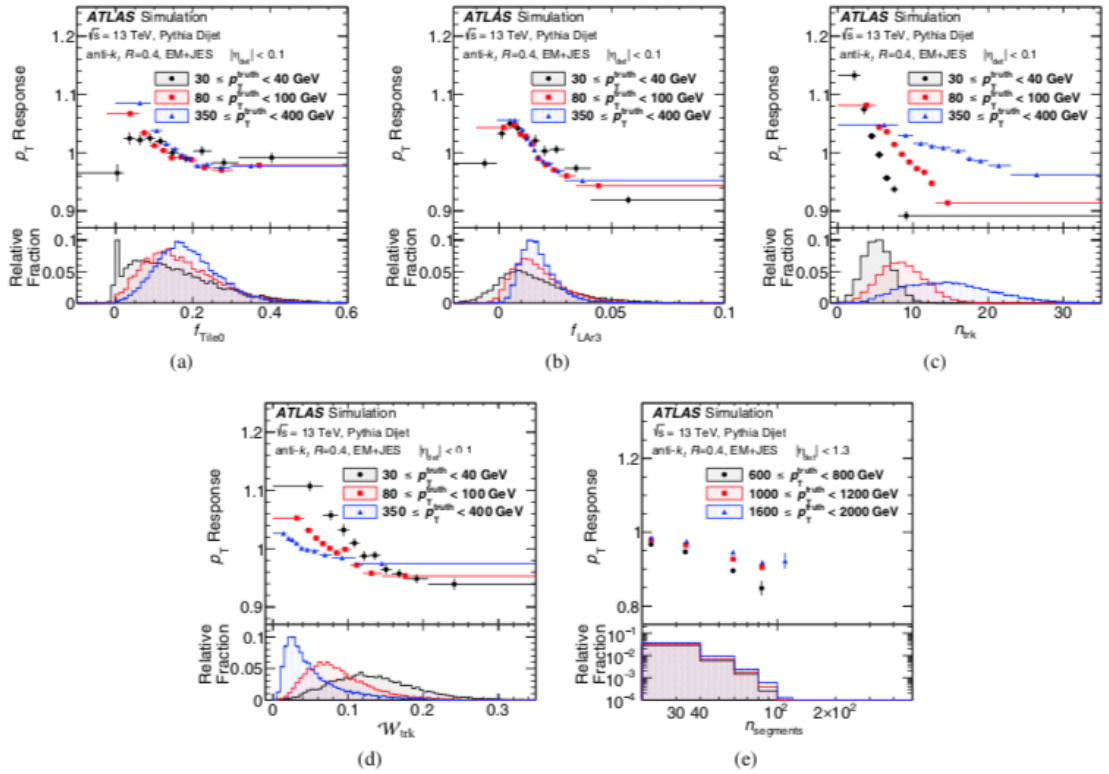

Figure 4.4: The average transverse momentum response as a function of the five independent observables for three ranges of the transverse momentum of truth jet: (a)f_{Tile0}, (b)f_{LAr3}, (c)n_{trk}, (d)W_{trk} and (e)n_{segments} [100].

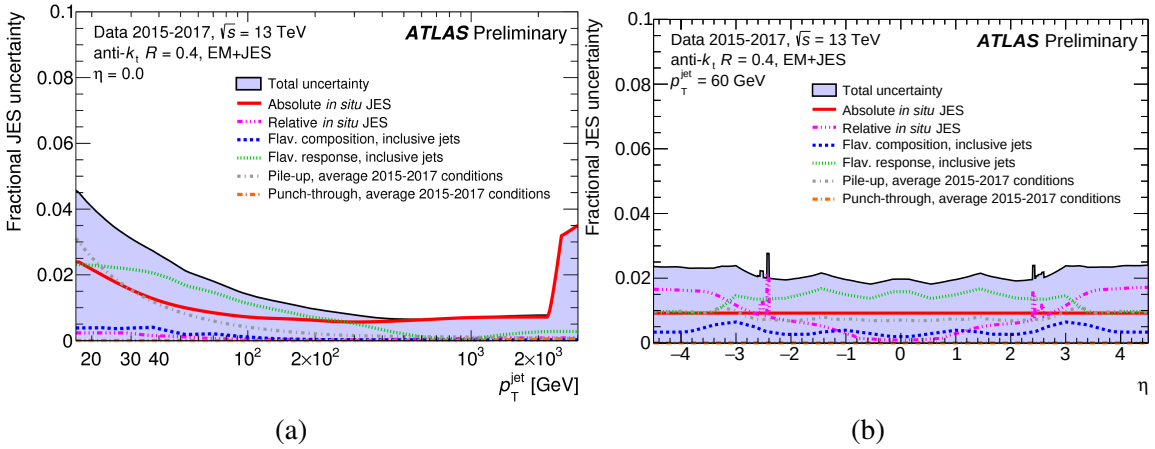

Figure 4.5: Fractional jet energy scale uncertainty components as a function of transverse momentum of jets at η=0.0 (a) and η of jets at p_{T}=60 GeV (b) [102].

4.2.3 Jet Vertex Tagging

The subtraction of pileup jets, which does not come from the primary vertex, is crucial to focus on only a hard scatter event. In order to suppress the contribution of pileup jets, two variables are introduced: a corrected Jet Vertex Fraction (corr.JVF) and R_{p_T} [103]. The corr.JVF variable is defined as

$$\text{corr.JVF} = \frac{\sum_k {p_T}^{\text{trk}_k}(\text{PV}_0)}{\sum_i {p_T}^{\text{trk}_i}(\text{PV}_0) + \sum_{n\geq 1}\sum_k {p_T}^{\text{trk}_k}(\text{PV}_n)/(\kappa \cdot n_{\text{ntrk}}^{\text{PU}})} \tag{4.4}$$

where $\sum_k {p_T}^{\text{trk}_k}(\text{PV}_0)$ is the scalar p_T sum of the tracks, which are associated with a jets in all hard scatter event (PV) [103]. The term $\sum_{n\geq 1}\sum_k {p_T}^{\text{trk}_k}(\text{PV}_n)$ is the scalar p_T sum of the associated tracks originating from any of the pileup interactions. This term depends on the total number of pileup tracks $n_{\text{trk}}^{\text{PU}}$ and thus the factor $\kappa \cdot n_{\text{ntrk}}^{\text{PU}}$ with $\kappa = 0.01$ are applied. The R_{p_T} is defined as

$$R_{p_T} = \frac{\sum_k {p_T}^{\text{trk}_k}(\text{PV}_0)}{{p_T}^{\text{jet}}} \tag{4.5}$$

where ${p_T}^{\text{jet}}$ is the fully calibrated jet p_T [103].

Figures 4.6 show the distributions of these two variables for hard scatter and pileup jets with $20 < p_T < 30$ GeV. In order to utilize these variables, the Jet Vertex Tagger (JVT), which combines them by a multivariate techniques, is made. The JVT has the strong separation power between the hard scatter and pileup jets as shown in Figure 4.7. In this analysis, the JVT cut is applied to all jets:

- JVT>0.59 with p_T <120 GeV and $|\eta|$ <2.4
- JVT>0.11 with jet p_T <120 GeV and 2.4< $|\eta|$ <2.5.

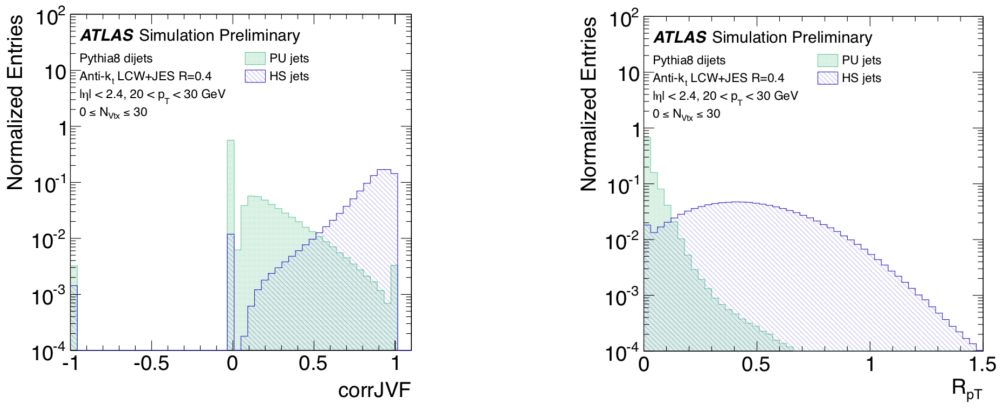

(a) (b)

Figure 4.6: Distributions of corr.JVF (a) and R_{p_T} (b) for hard scatter and pileup jets with $20 < p_T < 30$ GeV [103].

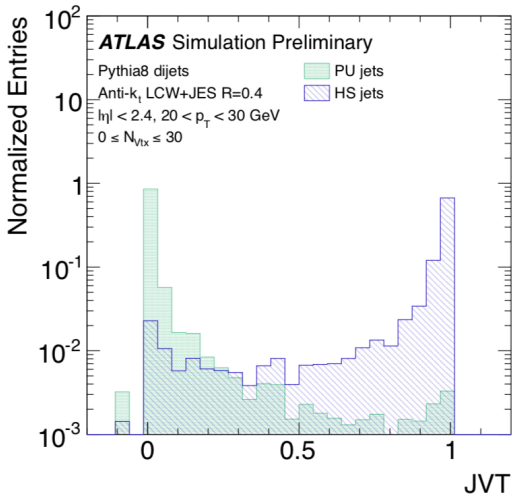

Figure 4.7: Distribution of JVT for hard scatter and pileup jets with $20 < p_{\mathrm{T}} < 30$ GeV [103].

4.2.4 Flavor Tagging

Jets containing b-hadrons can be identified by a b-tagging algorithm, which uses the tracks of charged particles [104, 105]. There are three sub-algorithms to identify b-jets in the ATLAS: the impact parameter based algorithm, the inclusive secondary vertex reconstruction algorithm and the decay chain multi-vertex reconstruction algorithm. The outputs of these algorithms are combined to one output by multivariate analysis.

Impact Parameter based algorithm

Since B-meson has a long lifetime of hadrons ($c\tau$ ~450 μm), there is at least one vertex displaced from the interaction point of the hard scatter events. It would have a large transverse impact parameter (d_0), which is defined as the closest distance of a track to the primary vertex in the r-ϕ plane. In addition, it would also have a large longitudinal impact parameter ($z_0 \sin\theta$), which is defined as the closest distance of a track to the primary vertex in longitudinal plane. In order to consider the correlation of them, a log likelihood ratio discriminant is computed as the sum of the per-track contributions.

Inclusive secondary vertex reconstruction algorithm

The secondary vertex finding algorithm explicitly reconstructs a displaced secondary vertex using tracks satisfying a quality selections. All track pairs are tested for a two track vertex hypothesis. Two track vertices, which originate from the decay of a long lived particle such as K_s or Λ, photon conversions or hadronic interactions with a detector material, are also found, but they are rejected.

Then, the remaining two track vertex candidates are required to be significantly displaced from the primary interaction vertex.

Decay chain multi-vertex reconstruction algorithm

The decay chain multi-vertex reconstruction algorithm exploits the topological structure of weak b- and c-hadron decays within a jet. In order to reconstruct a full b-hadron decay chain, a Kalman filter is used. This algorithm finds a common line on which the primary vertex and the bottom and charm vertices approximating the b-hadron flight path and their positions.

Multivariate algorithm (MV2)

Outputs of these three algorithms are combined into one output by a Boosted Decision Tree (BDT), which is explained in Section 5.5. A large statistics of $t\bar{t}$ sample is used for the training in BDT. In order to consider the rejection power of c-quark, the c-jet fraction in the training sample is composed of 10%: the light-flavour fraction is composed of 90%. The produced output by the BDT classifier is called "MV2c10 BDT Output" and it has the strong separation between b jets and light-flavour jets or c jets as shown in Figure 4.8. This analysis uses the working point at 77% b jet efficiency.

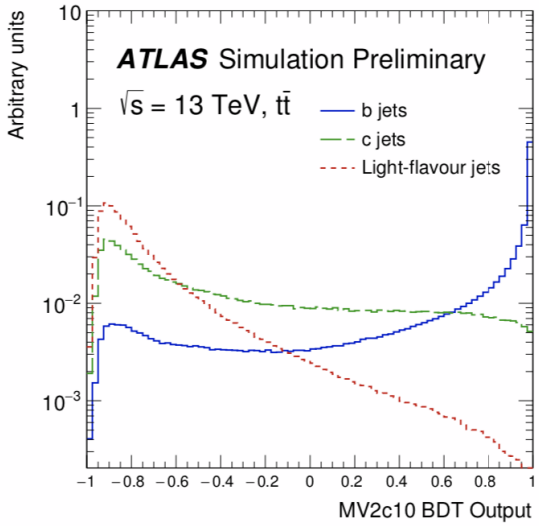

Figure 4.8: MV2c10 BDT output distribution for b jets (blue), c jets (green) and light-flavour jets (light-flavour) [104, 105].

4.2.5 Jet in this analysis

This analysis uses the following selections for jets as below.

- p_{T} >20 GeV and $|\eta|$ <2.8 for inputs to a missing transverse momentum calculation and overlap removal.
- p_{T} >50 GeV, $|\eta|$ <2.8 and the JVT cut for requiring a jet.

The additional requirement of b-tagging is performed to identify b jets.

4.3 Electron

Electrons mainly deposit their energy due to bremsstrahlung. Then, radiated photons may convert into electron-positron pairs. By continuing the processes, electromagnetic showers are constructed. The reconstruction of electrons can use three algorithms, which utilize the information of the inner detectors and calorimeters [106, 107].

The reconstruction efficiency of electrons is measured by $Z \rightarrow ee$ events. Figure 4.9 shows the reconstruction efficiency as a function of the reconstructed electron transverse energy. The efficiency is more than 97% for $E_{\mathrm{T}} > 20$ GeV and a good agreement between data and MC simulation is observed. In the reconstruction, pions in the jets are reconstructed as electrons. In order to suppress

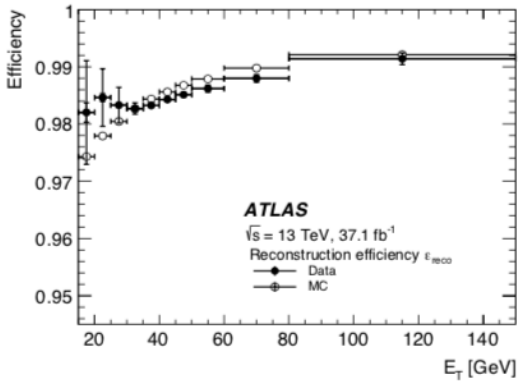

Figure 4.9: The reconstruction efficiency as a function of reconstructed electron transverse energy E_{T} obtained from $Z \rightarrow ee$ events. The black dot (white) line is data (MC simulation) [106].

the fake electrons, a likelihood based (LH) identification is performed [106, 107]. Inputs to the LH identification is measurements from the inner detectors and calorimeters such as electron leakage in the hadronic calorimeters. Depending on the electron efficiency, three working points are prepared: Loose, Medium and Tight as shown in Figures 4.10 [106]. This analysis was Loose (Tight) working point, corresponding to 93% (80%) efficiency at $E_{\mathrm{T}} = 40$ GeV.

This analysis uses two selections for an electron, which are defined as below.

- Loose working point with $p_{\mathrm{T}} > 7$ GeV, $|\eta| < 2.47$ in case of vetoing electron and input to overlap removal.
- Tight working point with $p_{\mathrm{T}} > 7$ GeV, $|\eta| < 2.47$ in case of requiring electron in order to suppress fake electrons.

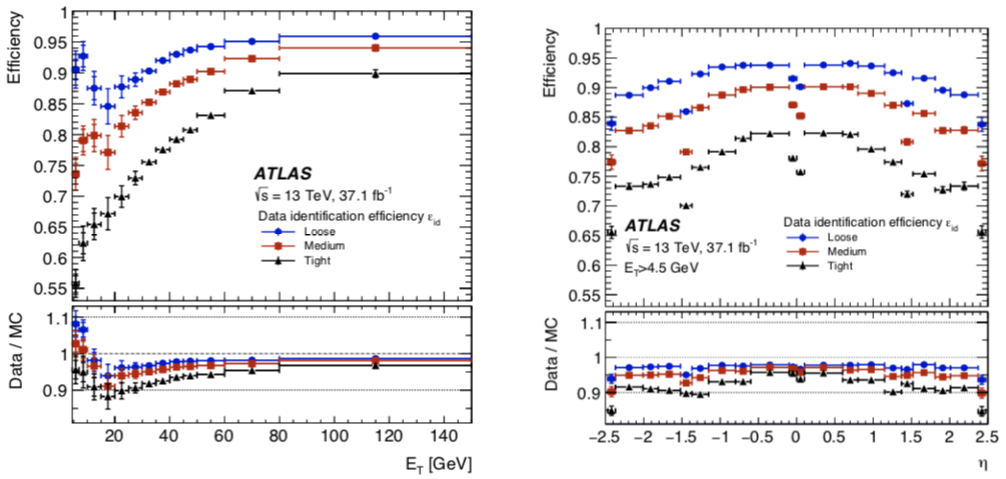

Figure 4.10: Identification efficiencies in $Z \rightarrow ee$ events for Loose (blue), Medium (red) and Tight (black) working points as a function of the reconstructed electron E_{T} (left) and η (right). The data of 37.1 fb^{-1} is used in this measurement [106, 107].

4.4 Muon

Muon reconstruction is performed in the inner detector and muon spectrometer independently and then, muon tracks are formed by combining them [108]. In order to keep the muon efficiency and reject fake muon from pion and kaon, a muon identification is applied. There are four working points in the muon identification: Loose, Medium, Tight and High-p_{T}. This analysis uses Medium working point, which minimizes the systematic uncertainties associated with muon reconstruction and calibration.

The reconstructed efficiency is measured by $Z \rightarrow \mu\mu$ events. Figure 4.11 shows the reconstruction efficiency as a function of muon η. The efficiency is more than 98% except $|\eta| < 0.1$. In this η region, the reconstruction efficiency is low due to instruments of the muon spectrometers.

This analysis uses two selections for an muon, which are defined as below.

- Medium working point with $p_{\mathrm{T}} > 6$ GeV, $|\eta| < 2.7$ in case of vetoing electron and input to overlap removal.
- Medium working point with $p_{\mathrm{T}} > 6$ GeV, $|\eta| < 2.47$ and track quality in case of requiring electron in order to suppress fake muons.
  - Track quality: $|z_0^{PV} \cdot \sin\theta| < 0.5$mm and $|d_0^{PV}|/\sigma(d_0^{PV}) < 3$

4.5 Missing transverse momentum

Since the transverse momentum of initial states is zero in the LHC, the conservation of the transverse momentum can be used. The energy and direction of each particle such as neutrinos cannot be directly

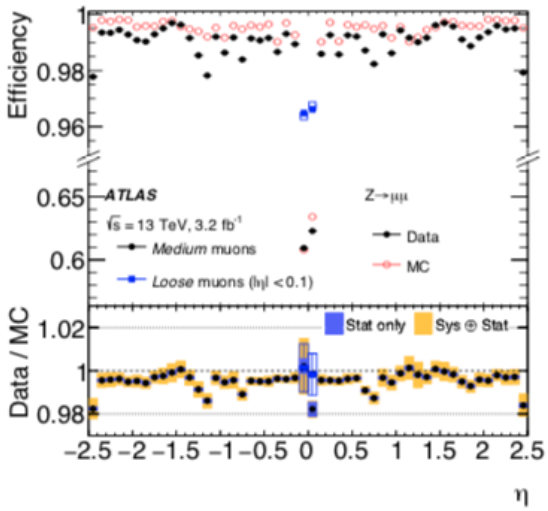

Figure 4.11: Muon reconstruction efficiency as a function of muon η using $Z \rightarrow \mu\mu$ events at the Medium working point [108].

measured, but a vector sum of these particles can be estimated from this conservation. Missing transverse momentum ($E_{\mathrm{T}}^{\mathrm{miss}}$) is defined as the negative vectorial sum of transverse momenta of all physics objects and all tracks, which are not associated with these objects (soft term):

$$\mathbf{E}_{\mathrm{T}}^{\mathrm{miss}} = -\sum \mathbf{E}_{\mathrm{T}}^{\mathrm{jet}} - \sum \mathbf{E}_{\mathrm{T}}^{e} - \sum \mathbf{E}_{\mathrm{T}}^{\gamma} - \sum \mathbf{E}_{\mathrm{T}}^{\mu} - \sum \mathbf{E}_{\mathrm{T}}^{\text{soft term}} \tag{4.6}$$

where $\mathbf{E}_{\mathrm{T}}^{\mathrm{jet}}$, $\mathbf{E}_{\mathrm{T}}^{e}$, $\mathbf{E}_{\mathrm{T}}^{\gamma}$ and $\mathbf{E}_{\mathrm{T}}^{\mu}$ are the transverse momentum of jet, electron, photon and muon. The soft term $\mathbf{E}_{\mathrm{T}}^{\text{soft term}}$ is calculated from tracks in the inner detector, which are not reconstructed in objects, but matched to the primary vertex [109]. By considering soft term, the pileup contamination of $E_{\mathrm{T}}^{\mathrm{miss}}$ can be minimized and thus the resolution is not sensitive to the number of primary vertex as shown in Figure 4.12.

The systematic uncertainties on the missing transverse momentum considers the energy response and resolution. In the ATLAS, the systematic uncertainties for the hard terms such as jet, electron, photon and muon entering $E_{\mathrm{T}}^{\mathrm{miss}}$ reconstruction are assumed to be uncorrelated [109]. Hence, the systematic uncertainties of the soft term are evaluated in this case. In order to evaluate the systematic uncertainties, the parallel ($\mathrm{E}_{\parallel}$) and perpendicular ($\mathrm{E}_{\perp}$) projections of $\mathbf{E}_{\mathrm{T}}^{\text{soft term}}$ are defined as shown in Figure 4.13 Two projections between data and MC simulation as a function of the transverse momentum of the hard terms are compared and the systematic uncertainties are assigned in order to cover all differences between data and MC simulation [109].

4.6 Overlap removal

Since each object reconstruction is performed in parallel, there is a possibility to reconstruct single particle as multiple objects. For example, electrons and jets are calorimetric objects so that it is not

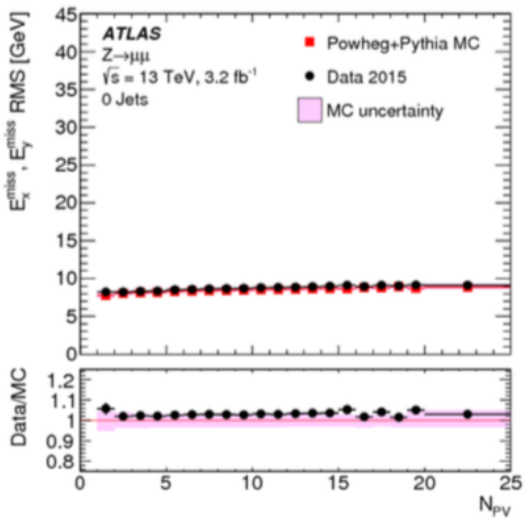

Figure 4.12: $E_{\mathrm{T}}^{\mathrm{miss}}$ resolution RMS in x-direction and y-direction using $Z \rightarrow \mu\mu$ sample as a function of number of primary vertex without jets with p_{T} >20 GeV [109].

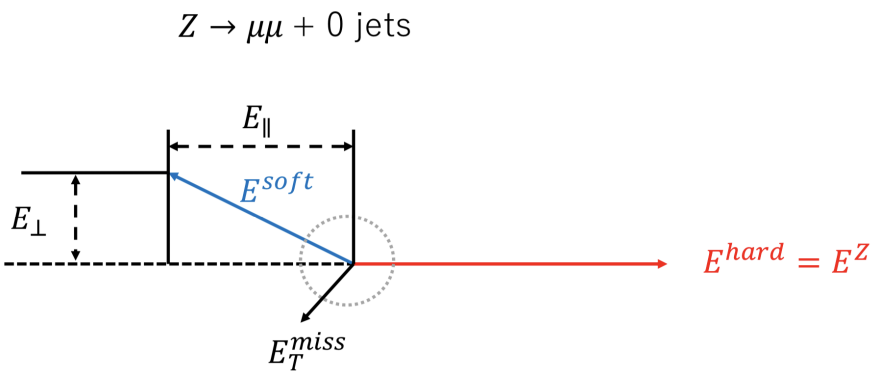

Figure 4.13: Schematic view of the parallel ($\mathrm{E}_{\parallel}$) and perpendicular ($\mathrm{E}_{\perp}$ projections of $\mathbf{E}_{\mathrm{T}}^{\text{soft term}}$ for $Z \rightarrow \mu\mu$ events without genuine $E_{\mathrm{T}}^{\mathrm{miss}}$ for a final state without any jets. If there is no mismeasurement of reconstruction, the $\mathrm{E}_{\parallel}$ is zero and the $\mathrm{E}_{\perp}$ is transverse momentum of Z boson ($p_{\mathrm{T}}{}^{Z}$).

uncommon for an electron to be also reconstructed as a jet or vice versa. In order to avoid double counts of single particle, an "overlap removal" procedure is applied. Most of the criteria in the procedure are based on a simple geometric $\Delta R = \sqrt{\Delta\phi^2 + \Delta\eta^2}$ variable.

First, the overlap removal between the electron and muon is performed. If a baseline electron and baseline muon share the same ID track, the electron is ignored. Then, if a baseline electron and a jet are found within $\Delta R < 0.2$, the object is interpreted as an electron. The overlapping jet is ignored. Then, if they are found within $\Delta R < \min(0.4, 0.04 + 10[\mathrm{GeV}]/p_{\mathrm{T}}^{e})[\mathrm{GeV}]$, the object is interpreted as a jet. The nearby electron is ignored. Then, if a muon and a jet are found within $\Delta R < 0.2$, the object is treated as a muon. In case that the number of tracks with p_{T} >500 MeV associated to the overlapping jet is less than three, the jet is ignored. Finally, if a muon and a jet are found within

$\Delta R < \min(0.4, 0.04 + 10[\text{GeV}]/p_{\text{T}}^{\mu}[\text{GeV}])$, the object is treated as a jet and the overlapping muon is removed.

5 Event selection with machine learning

First, this chapter discusses a jet cleaning and a treatment of the dead tile module. Then, this chapter discusses a search strategy of this analysis and explains selections in detail. Since the SUSY particles are not found in the search, the strategy which covers all mass ranges of the SUSY particles is described.

5.1 Jet cleaning

This search should be performed with well understood "good" data, which do not contain bad events such as noise bursts or beam-induced background (BIB). The noise bursts are the bursts of coherent noise over a large region of subdetectors. The detector response may not be normal and the measurement performed over this period would not be reliable. The BIB is observed due to proton losses upstream of the interaction point. They induce secondary particles (muon) and reach to the ATLAS detector. The energy depositions created by them in the ATLAS detector would be measured and reconstructed as fake jets. In addition, muons from non-collision would be observed when cosmic-ray showers overlap with collision events.

Since these events, which contain noise bursts and the BIB, would have high jet p_{T} and $E_{\mathrm{T}}^{\mathrm{miss}}$, those are potentially signal like events and not included in MC samples. In order to eliminate these effects, an event cleaning criterion is introduced. The summary of the criteria and efficiencies for the event cleaning is shown in Table 5.1.

Table 5.1: Summary of event cleaning efficiencies for data and Z+jets MC sample.

Selection	Efficiency [%]	
	Data	MC sample (Z+jets)
Loose bad jet veto	99.0	99.8
Tight bad jet veto for 1^{st}&2^{nd} jets	92.7	99.5
Jet timing cut	97.7	100

There are two selections using the information from calorimeters, which are described in Ref. [110]: "Loose bad jet" and "Tight bad jet". In order to identify bad jet in this analysis, the selection of tight bad jet is applied to leading and subleading jets and loose bad jet is used for other jets. The events which have any bad jets are vetoed to reject event contaminated by noise burst. The jet timing measurement, which is relative timing difference of jet and pp collision, is also used to reduce the BIBs. Figures 5.1 show the jet timing distributions for collision events and non-collision events, which is affected by BIBs. In order to visualize these events, a special criterion is applied. The collision

events are selected by single jet triggers and the selection of tight bad for the leading and subleading jets is required. The non-collision events are selected by the $E_{\mathrm{T}}^{\mathrm{miss}}$ trigger and requiring that at least one of the first two leading jets has the tight bad jet. The jet distribution has a peak around 0 ns for collision events, whereas the broad distribution is observed in the non-collision events as shown in Figures 5.1. The BIBs can be reduced by applying the jet timing cut (4 ns).

Most of event cleaning criteria have small loss of events (below 1%) in both data and Z+jets MC as shown in Table 5.1. No efficiency loss on the SUSY signal event due to these criteria is also observed.

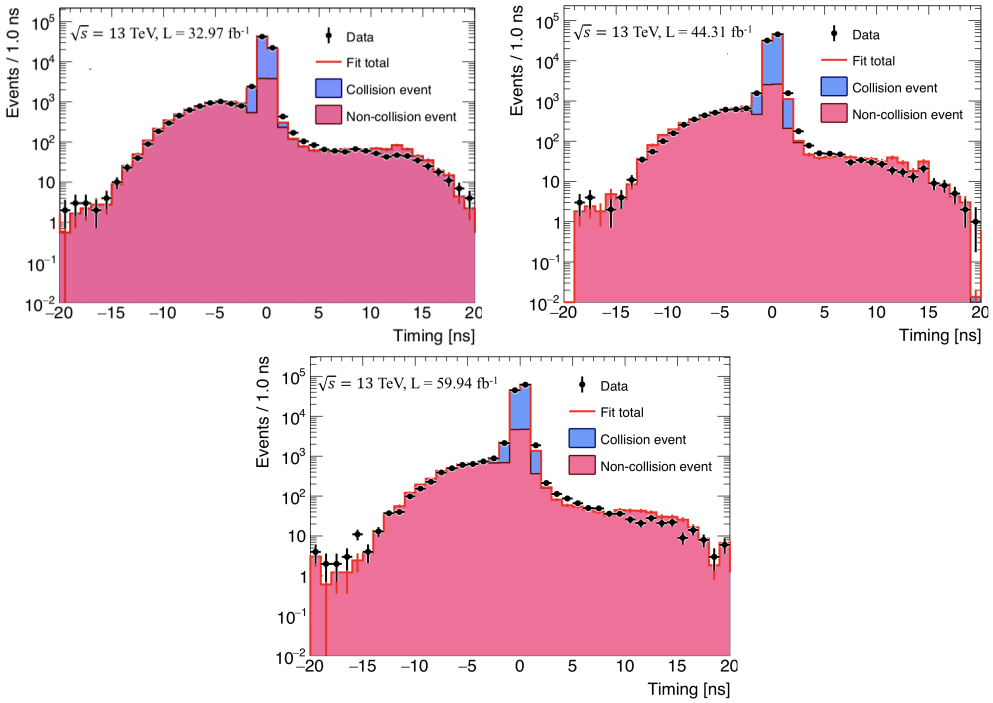

Figure 5.1: Jet timing distributions for 2016 (top-left), 2017 (top-right) and 2018 (bottom) data period. The selection, $E_{\mathrm{T}}^{\mathrm{miss}}$ ≥300 GeV ($E_{\mathrm{T}}^{\mathrm{miss}}$ ≤300) GeV is applied to collision events (non-collision events) in order to increase purity of the event.

5.2 Treatment of dead tile modules

Some modules in the tile calorimeters were having issues in data periods accidentally. These modules are called dead tile modules. If the jets point close to the dead tile modules, part of the energy of the jets cannot be measured, which is added to the missing transverse momentum. In these events, both the jet and the missing transverse momentum would be mismeasured. Since the dead tile modules are not implemented in the MC simulation, such a event has to be vetoed in data for signal and background estimations.

Since period and location of the dead tile modules are recorded, the following approach is adopted in this analysis. If jets point to a region around dead tile modules, the energy of jets would be lost. Therefore, jet p_{T} ordering would be changed. Figures 5.2 show two dimensional distribution of subleading jet ϕ and η. Because of the dead tile module, leading jet would become subleading jet, which makes clear excess in the plots. The missing transverse momentum is increased by the mismeasurement of the energy of jets, so the azimuth direction of the missing transverse momentum (ϕ ($E_{\mathrm{T}}^{\mathrm{miss}}$)) becomes to be correlated with the dead tile module as shown in Figure 5.3(a). In order to minimize the effect due to the dead tile module, the events, which have the jets around the dead tile modules, are treated as follows. If an angular difference between jets and $E_{\mathrm{T}}^{\mathrm{miss}}$ is small (<0.3), events are affected by the dead tile modules and vetoed. Fiducial cuts of the dead tile module listed in Table 5.2 are applied in this analysis. By applying the cuts to data and all MC samples, the ϕ ($E_{\mathrm{T}}^{\mathrm{miss}}$) distribution does not have any peaks correlated with the dead tile modules as shown in Figure 5.3(b).

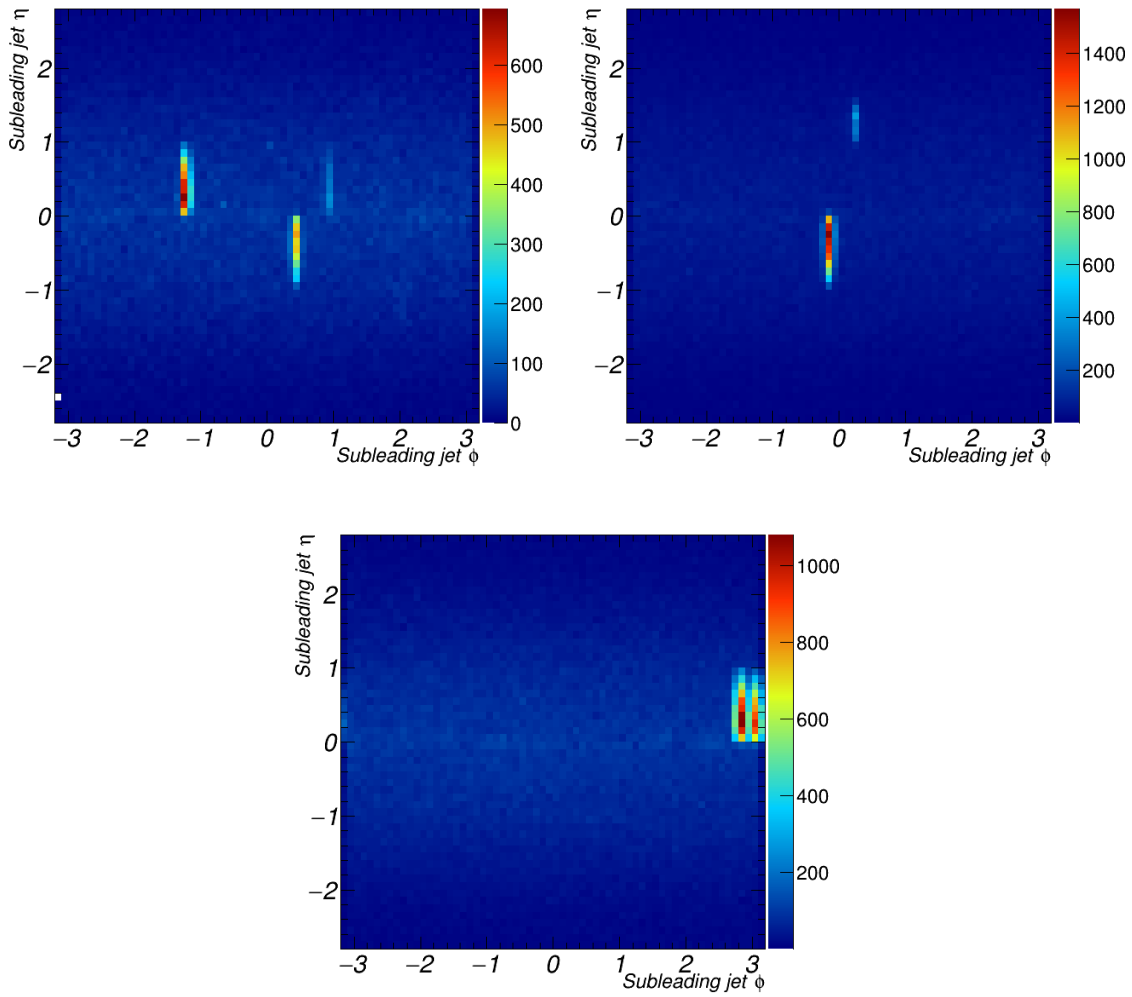

Figure 5.2: The two dimensional distribution of the subleading jet ϕ (x-axis) and subleading jet η (y-axis) for 2015-2016 (top-left), 2017 (top-right) and 2018 (bottom) data period. The z-axis indicates the number of events. The energy of the jet around the dead tile modules would be decreased compared to the original one, so the number of the subleading jet in the region is significantly increased.

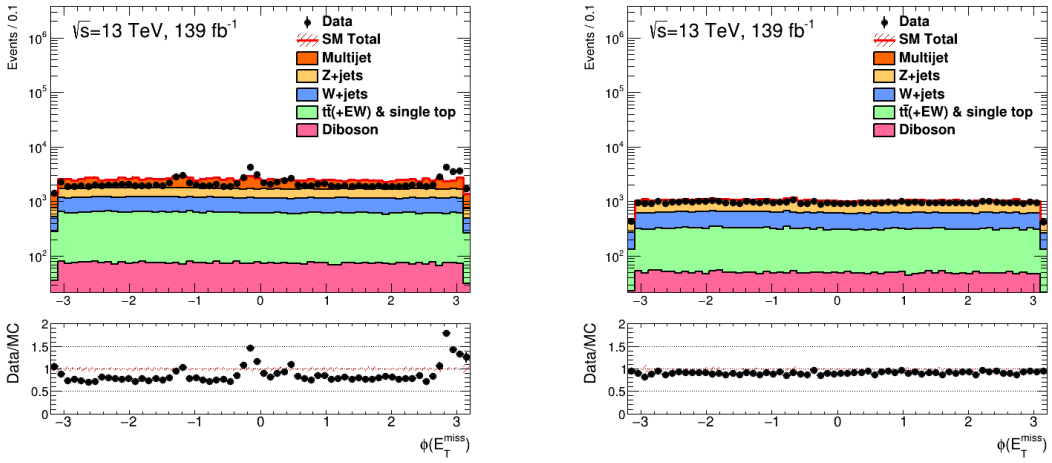

(a) (b)

Figure 5.3: Distribution of the azimuth direction of the missing transverse momentum ($\phi(E_{\mathrm{T}}^{\mathrm{miss}})$) before (a) and after (b) applying the dead tile module cuts in the data and MC simulation. The dead tile module cuts are applied to both data and MC simulation. The MC samples are normalized to cross section times integrated luminosity of 139 fb^{-1}. The bottom panel is the ratio of the observed data and the sum of SM backgrounds from simulation. The hatched red error bands indicate the statistical uncertainties of background prediction based on MC samples.

Table 5.2: The definition of the dead tile module cut.

Data period	The cuts of all jets for the dead tile module
2015	($0 < \eta < 0.9$ and $0.8 < \phi < 1.0$) or ($-1.6 < \eta < -0.9$ and $1.9 < \phi < 2.1$)
2016	($0 < \eta < 0.9$ and $-1.33 < \phi < -1.13$) or ($-0.9 < \eta < 0.$ and $0.34 < \phi < 0.54$)
2017	($-0.9 < \eta < 0.$ and $-0.25 < \phi < -0.05$) or ($0.8 < \eta < 1.7$ and $0.14 < \phi < 0.34$)
2018	($0 < \eta < 0.9$ and $2.7 < \phi < 3.0$ for 350310 $\leq$ Run number $\leq$ 352514 ($0. < \eta < 0.9$ and ($\phi > 3.0$ or $\phi < -3.0$) for 355261 $\leq$ Run number $\leq$ 364292
kinematic cuts	
jet p_{T}	$\geq$ 50 GeV
$\Delta\phi(\mathrm{jet}, E_{\mathrm{T}}^{\mathrm{miss}})$	< 0.3

5.3 Preselection

A preselection, which is defined as Table 5.3, is applied to all signal regions (SRs). The preselection is applied in distributions which is shown in this chapter. The preselection except the number of leptons is applied for control regions (CRs) and validation regions (VRs), which will be explained later. Figures 5.4 show the distribution of the leading jet p_{T} and $E_{\mathrm{T}}^{\mathrm{miss}}$ after applying the preselection. Since the target signals as shown in Figures 1.12 would have the high energy scales compared to the SM backgrounds, the large leading jet p_{T} and $E_{\mathrm{T}}^{\mathrm{miss}}$ is expected as shown in Figures 5.4.

Table 5.3: Preselection using $E_{\mathrm{T}}^{\mathrm{miss}}$, $\mathrm{N_j}$ (number of jet with p_{T} ≥50 GeV), leading jet p_{T} and number of leptons.

Jet cleaning	See Section 5.1
Dead Tile Module cut	See Section 5.2
$E_{\mathrm{T}}^{\mathrm{miss}}$ [GeV]	≥ 300
N_{j}	≥ 4
Leading jet p_{T} [GeV]	≥ 200
Number of leptons	= 0

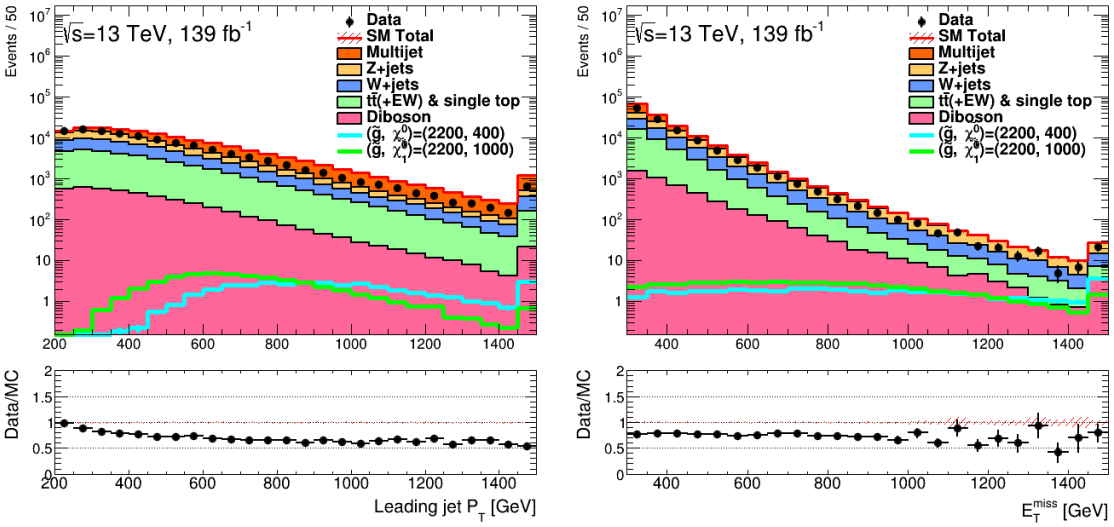

Figure 5.4: Distribution of the leading jet p_{T} (left) and $E_{\mathrm{T}}^{\mathrm{miss}}$ (right) with the preselection. The signals in the plot are gluino direct decay. The last bin includes the overflow. The MC samples are normalized to cross section times integrated luminosity of 139 fb^{-1}. The bottom panel is the ratio of the data and the sum of SM backgrounds. The hatched red error bands indicate the statistical uncertainties of background prediction based on MC samples.

After applying the preselection, the remaining backgrounds are Z+jets, W+jets, $t\bar{t}$, single top, diboson and multi-jets. As discussed in Section 3.3, the cross section is computed at the NLO or NNLO level. Even if the NLO or NNLO cross section is used for normalizing SM backgrounds, the MC samples do not describe data well. This causes the mismodelling on the description of the objects,

such as the leading jet p_{T} or $E_{\mathrm{T}}^{\mathrm{miss}}$ as shown in Figures 5.4. In this analysis, dedicated corrections are applied on the MC samples based on the data as discussed in Chapter 6.

5.4 Discriminating variables

Before going to the search strategy, the discriminating variables between SUSY signals and SM backgrounds are listed as follows.

- **$\mathbf{H_T}$**: $\mathrm{H_T}$ is defined as the scalar sum of p_{T} of all jets with $p_{\mathrm{T}} \geq$50 GeV.
- **Effective mass ($\boldsymbol{m_{\mathrm{eff}}}$)**: Effective mass ($m_{\mathrm{eff}}$) is defined as the scalar sum of $E_{\mathrm{T}}^{\mathrm{miss}}$ and p_{T} of all jets with $p_{\mathrm{T}} \geq$50 GeV (H_{T}):

$$m_{\mathrm{eff}} \equiv \sum_{i=1}^{n} |\mathbf{p}_{\mathrm{T}^{(i)}}| + E_{\mathrm{T}}^{\mathrm{miss}} = \mathrm{H_T} + E_{\mathrm{T}}^{\mathrm{miss}}. \tag{5.1}$$

  It approximately corresponds to the gluino mass. The distribution of the effective mass in the signals has a broad peak, while the backgrounds are smoothly decreasing as shown in Figure 5.5.

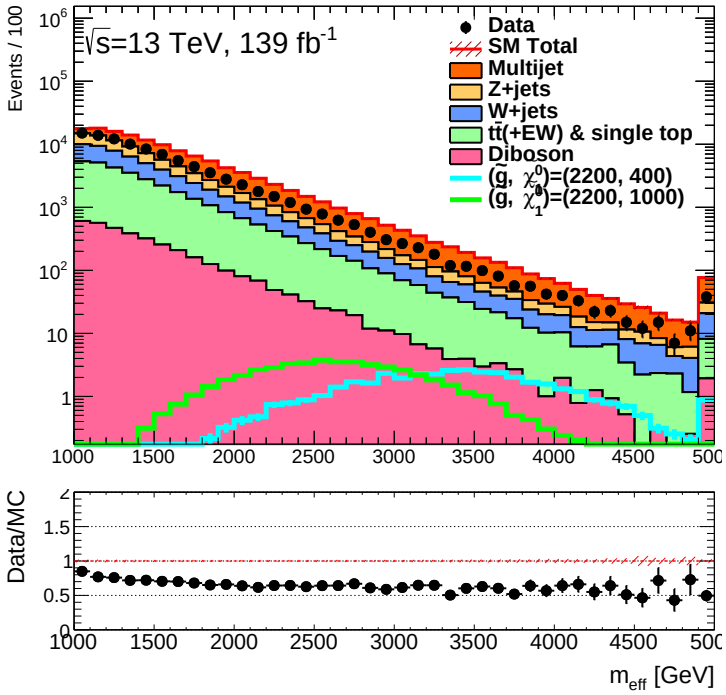

Figure 5.5: Distribution of the effective mass with the preselection. The signals in the plot are gluino direct decay. The last bin includes the overflow. The MC samples are normalized to cross section times integrated luminosity of 139 fb^{-1}. The bottom panel is the ratio of the data and the sum of SM backgrounds. The hatched red error bands indicate the statistical uncertainties of background prediction based on MC samples.

- **$\Delta\phi(\text{jet}_{1,2,(3)}, \vec{E}_{\text{T}}^{\text{miss}})_{\text{min}}$ and $\Delta\phi(\text{jet}_{i>3}, \vec{E}_{\text{T}}^{\text{miss}})_{\text{min}}$**: The variables of $\Delta\phi(\text{jet}_{1,2,(3)}, \vec{E}_{\text{T}}^{\text{miss}})_{\text{min}}$ and $\Delta\phi(\text{jet}_{i>3}, \vec{E}_{\text{T}}^{\text{miss}})_{\text{min}}$ are introduced in order to suppress multi-jet events. They are defined as the smallest azimuthal difference between the missing transverse momentum and the momentum of the jets. Up to three leading jets are considered in case of $\Delta\phi(\text{jet}_{1,2,(3)}, \vec{E}_{\text{T}}^{\text{miss}})_{\text{min}}$. Other jets with p_{T} ≥50 GeV are considered in case of $\Delta\phi(\text{jet}_{i>3}, \vec{E}_{\text{T}}^{\text{miss}})_{\text{min}}$. The requirements of $\Delta\phi(\text{jet}_{1,2,(3)}, \vec{E}_{\text{T}}^{\text{miss}})_{\text{min}}$ and $\Delta\phi(\text{jet}_{i>3}, \vec{E}_{\text{T}}^{\text{miss}})_{\text{min}}$ can suppress the multi-jet background in which a mismeasurement of the jet energy generates the missing transverse momentum. The distributions of $\Delta\phi(\text{jet}_{1,2,(3)}, \vec{E}_{\text{T}}^{\text{miss}})_{\text{min}}$ and $\Delta\phi(\text{jet}_{i>3}, \vec{E}_{\text{T}}^{\text{miss}})_{\text{min}}$ are shown in Figures 5.6.

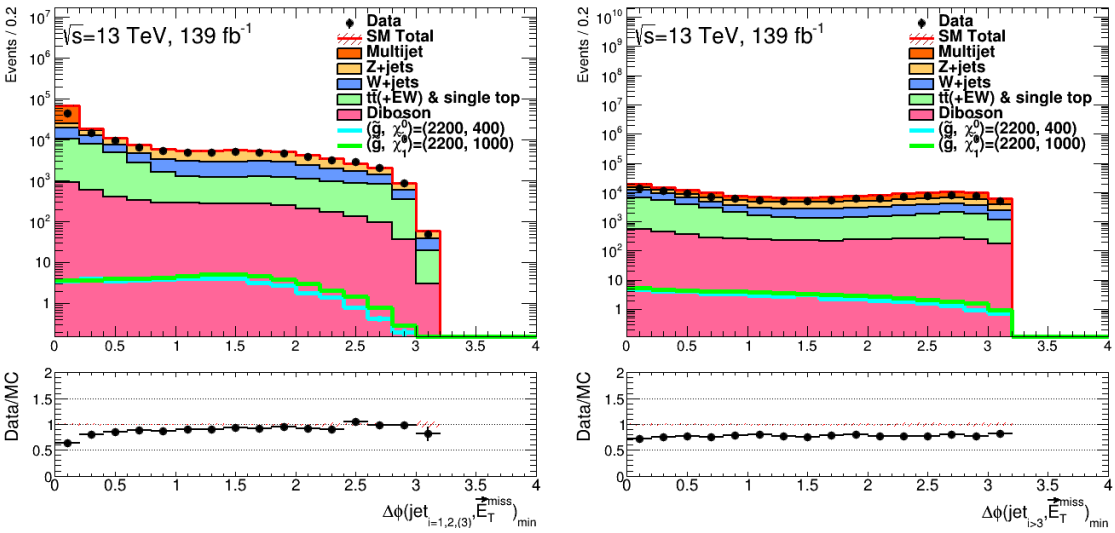

Figure 5.6: Distribution of the smallest azimuthal difference between the missing transverse momentum and the momentum of the jets: $\Delta\phi(\text{jet}_{1,2,(3)}, \vec{E}_{\text{T}}^{\text{miss}})_{\text{min}}$ considers up to three leading jets (left) and $\Delta\phi(\text{jet}_{i>3}, \vec{E}_{\text{T}}^{\text{miss}})_{\text{min}}$ considers other jets with p_{T} ≥50 GeV (right). The signals in the plot are gluino direct decay. The MC samples are normalized to cross section times integrated luminosity of 139 fb^{-1}. The bottom panel is the ratio of the data and the sum of SM backgrounds. The hatched red error bands indicate the statistical uncertainties of background prediction based on MC samples.

- **Aplanarity**: The information of event topology is also useful to separate the signal from backgrounds. An aplanarity is a variable designed to provide event topological information about the full momentum tensor of an event. It is defined as $3/2\lambda_3$, where λ_3 is the smallest eigenvalue of the normalized momentum tensor calculated using the momenta of the jets with p_{T} ≥50 GeV in an event [111]. The values near zero indicate relatively planar event shape, which is background-like events. Signal events tend to have high aplanarity values because they are more spherical event shape than background events. This is because multiple objects have high momentum emitted in the heavy SUSY particle decays. In case of Z+jets background, the selected Z boson is boosted since the large missing transverse momentum is required as shown in Table 5.3. There are several jets via initial state radiation, which are at the opposite direction of the Z boson. The event topology is a planar rather than spherical and the distribution of the aplanarity is different from the signal as shown in Figure 5.8.

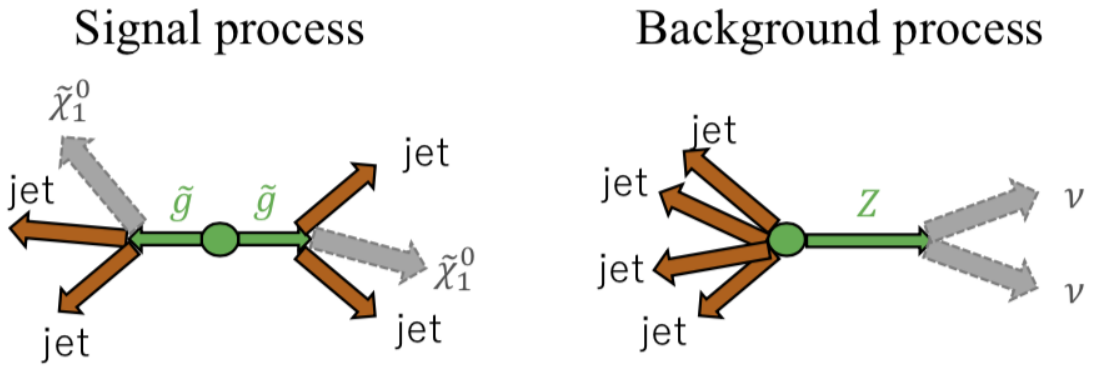

Figure 5.7: The event topology between the gluino decay (left) and Z+jets (right).

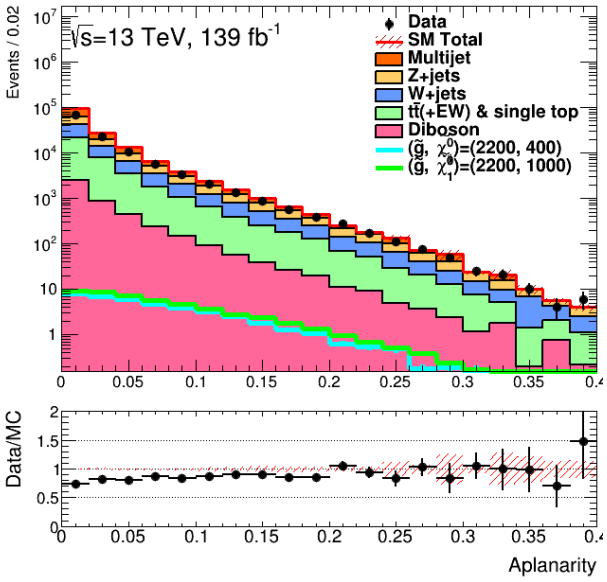

Figure 5.8: Distribution of the aplanarity with the preselection. The signals in the plot are gluino direct decay. The last bin includes the overflow. The MC samples are normalized to cross section times integrated luminosity of 139 fb^{-1}. The bottom panel is the ratio of the data and the sum of SM backgrounds. The hatched red error bands indicate the statistical uncertainties of background prediction based on MC samples.

In these discriminating variables, the effective mass has the strongest separation power between the signals and backgrounds. However, it gets weaker as the mass difference between gluino and neutralino ($\Delta m(\tilde{g},\tilde{\chi}_1^0)$) is smaller. If the mass difference is small, the transverse momentum of the jet in the final state is small. As a result, the effective mass is also small and the distribution is shifted to the low energy scale as shown in Figure 5.5. It is difficult to extract the signal from the background for the small $\Delta m(\tilde{g},\tilde{\chi}_1^0)$ as far as this analysis relies on the effective mass. The new discriminating variable is needed for the further improvement.

In order to utilize the feature of the discriminating variables, the variable correlation is newly considered. Figure 5.9 shows the two dimensional distribution of the leading jet p_{T} and subleading jet p_{T} with the preselection. Since the gluino is produced in a pair and decays to the jets and the neutralino, the properties of the leading jet and subleading jet are similar. On the other hand, the background does not have the correlation between them and the obvious difference is observed. The two dimensional distribution between the effective mass and the aplanarity can also separate the signal from the background as shown in Figure 5.10. If the effective mass is large for the signals, the signal events also have jets from initial state radiations and are close to planar event shape. Hence, the broad aplanarity distribution is obtained for large missing transverse momentum as shown in Figure 5.10. If the non-linear cut can be performed to these distribution, the separation between the signal and background would be efficiently improved. Therefore, the non-linear cut considered on the variable correlation (non-linear correlation) is introduced in this analysis. In order to obtain the cut, the machine learning is adopted. This thesis focuses on the Boosted Decision Tree (BDT) in the machine learning.

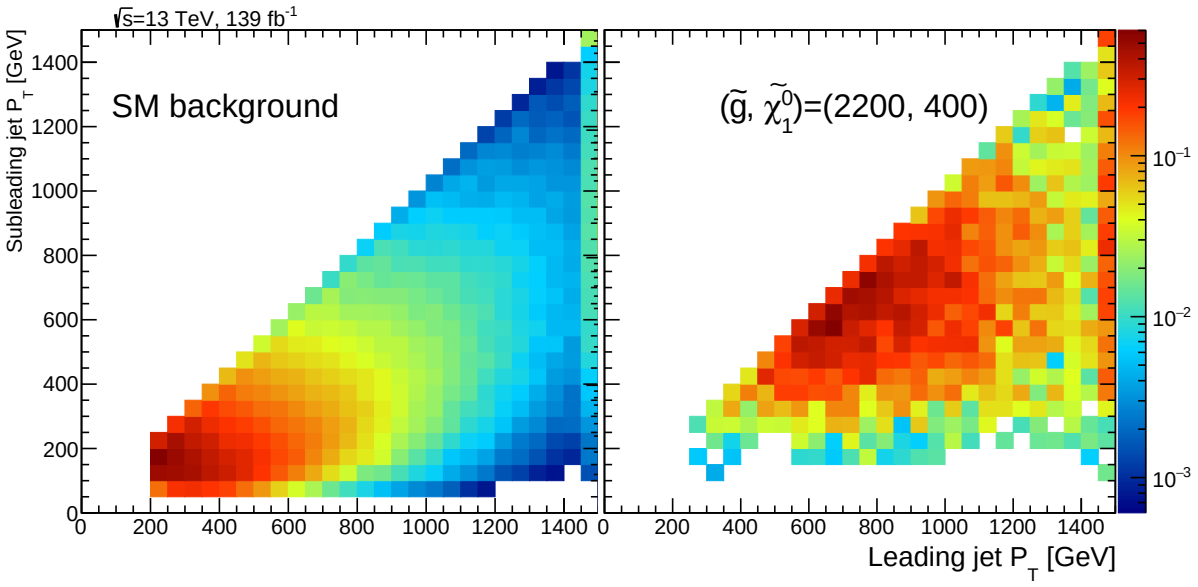

Figure 5.9: Two dimensional distribution of the leading jet p_{T} and subleading jet p_{T} with the preselection. The last bin includes the overflow. The left figure shows the distribution in the SM background and the right figure shows the distribution in the gluino direct decay signal with ($m_{\tilde{g}}$, $m_{\tilde{\chi}_0^1}$)=(2200, 400) GeV.

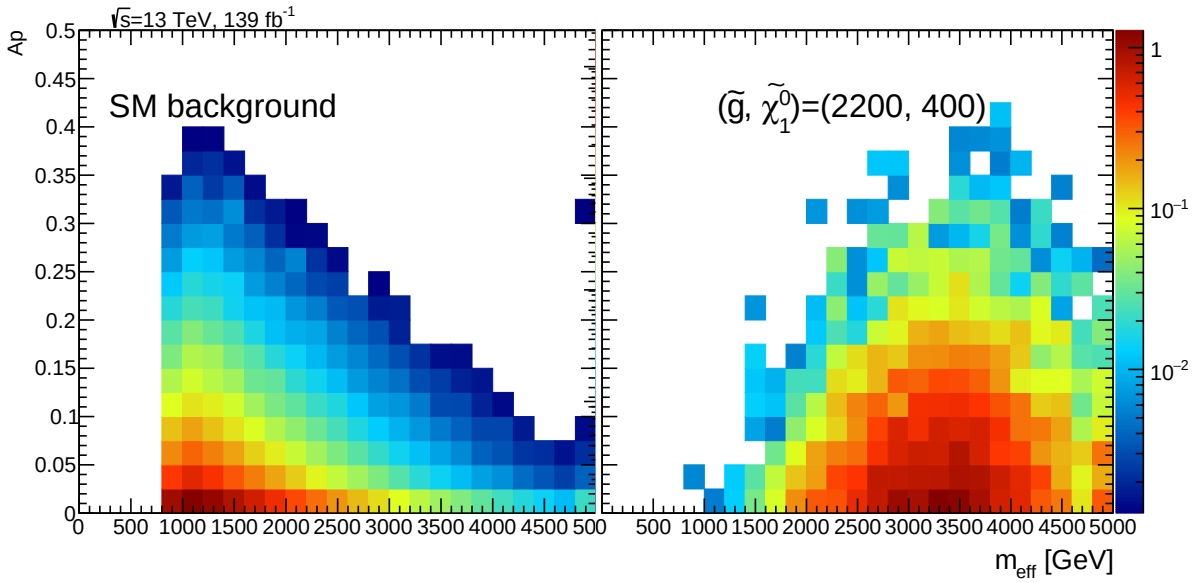

Figure 5.10: Two dimensional distribution of the effective mass and the aplanarity with the preselection. The last bin includes the overflow. The left figure shows the distribution in the SM background and the right figure shows the distribution in the gluino direct decay signal with ($m_{\tilde{g}}$, $m_{\tilde{\chi}^1_0}$)=(2200, 400) GeV.

5.5 Boosted Decision Tree (BDT)

BDT is one of the most famous multivariate analysis (MVA) methods in particle physics [112, 113]. This is a binary tree structured classifier and one of ensemble learnings. The ensemble learning is composed of many "weak" learners and constructs one learner, which is called "strong learner". Outputs of the strong learner are obtained from majority vote of weak learners considering weights. In the BDT, a decision tree as shown in Figure 5.11 is used as the weak learners and the weights are updated by "Boosting" algorithm. A classification criteria of the decision trees is determined by residual sum of squares, entropy information or Gini coefficient: this analysis uses entropy information to determine a classification criteria of the decision trees. By using many decision trees, the phase space can be split into several regions and each region is classified as signal or background. This analysis uses 800 decision trees in order to make strong learner. The considering weights are determined by "Gradient Boosting" algorithm.

The two orthogonal samples are needed in the BDT: training and testing samples. The training sample is provided to calculate the entropy information and determine the classification criteria of decision trees. The strong learner produced by the training samples is called "BDT classifier" and considers the non-linear correlation as shown in Figure 5.12. The output of the BDT classifier is called "BDT score". This BDT score is applied to the testing sample and used in the analysis.

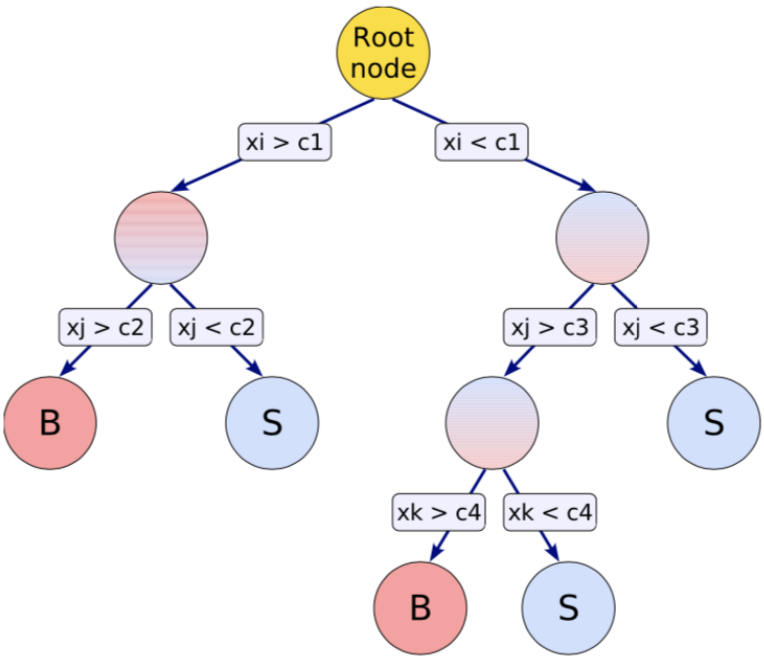

Figure 5.11: Schematic view of one decision tree [113]. In a decision tree, there is a sequence of binary splits using the discriminating variables (x_i, x_j and x_k) starting from the root node. The discriminating variables are determined to give the best separation between signal and background at each node. The final nodes in the decision tree are labelled as "S" for signal and "B" for background. They are determined from the majority events in the final node.

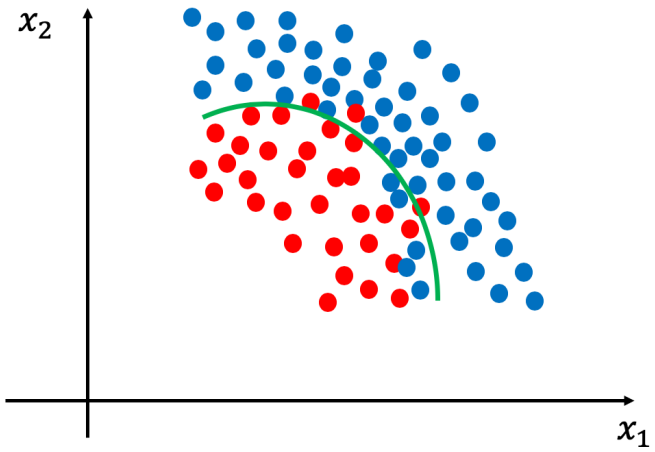

Figure 5.12: The illustration of the non-linear correlation between variable x_1 and x_2. The red point corresponds to the signal and the blue point corresponds to the background. The most appropriate cut is the green line and it can be produced by using BDT classifier.

5.6 Approach of BDT analysis

5.6.1 BDT classifier training

Since all mass points of the target signals have to be probed, it is not evident how the training of the BDT classifier is performed. The simplest approach is to prepare all the signal samples and perform the training per signal point. It means the infinite training samples would be needed and this approach is not realistic.

In order to avoid the training per the mass point, the signals with the similar kinematics are mixed in the training. The jet activity in final states depends on $\Delta m(\tilde{g},\tilde{\chi}_1^0)$ as shown in Figure 5.13. Therefore, the approach of mixing signals in the training with a similar $\Delta m(\tilde{g},\tilde{\chi}_1^0)$ is adopted. Similar kinematic distribution in these signals is observed as shown in Figure 5.14. In this analysis, eight training categories are prepared such that they can cover the signals with $\Delta m(\tilde{g},\tilde{\chi}_1^0) \geq$ 200 GeV[1]: four training categories each for the gluino direct decay (indicated as GGdi, $i = 1 \sim 4$) and the gluino one-step decay (GGoi, $i = 1 \sim 4$) as shown in Figure 5.15. For gluino one-step decay, the primary model with $m_{\tilde{\chi}_1^\pm} = (m_{\tilde{g}} + m_{\tilde{\chi}_1^0})/2$, as discussed in Section 1.5, is used in the training sample. In addition, the gluino one-step decay via W boson as shown in Figure 1.11(b) has the similar kinematics to the gluino one-step decay via Z boson as shown in Figure 1.12(c), and thus the gluino one-step decay via W boson is only used.[2] The training of BDT uses all background components of Z+jets, W+jets, $t\bar{t}$, single top and diboson except multi-jet in this analysis.

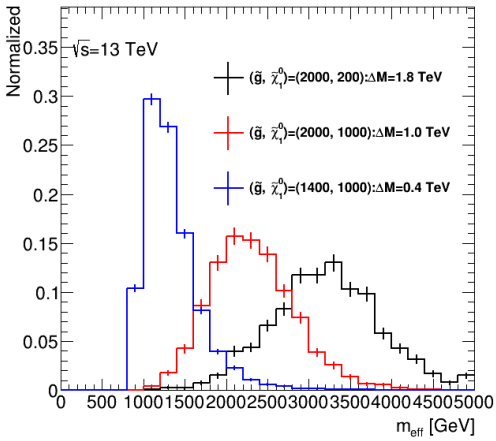

Figure 5.13: Normalized distribution of the effective mass applying the preselection for gluino direct decay signals with $(m_{\tilde{g}},m_{\tilde{\chi}_1^0})$=(2000, 200) (black line), (2000, 1000) (red line) and (1400, 100) (blue line) GeV. The last bin includes the overflow.

[1] This thesis does not focus on the signals with $\Delta m(\tilde{g},\tilde{\chi}_1^0) \leq$ 200 GeV. In Ref. [114], another approach is adopted to search for this region.

[2] There is an idea to mix two signal models for the training, but this thesis uses one signal models in order to simplify the training.

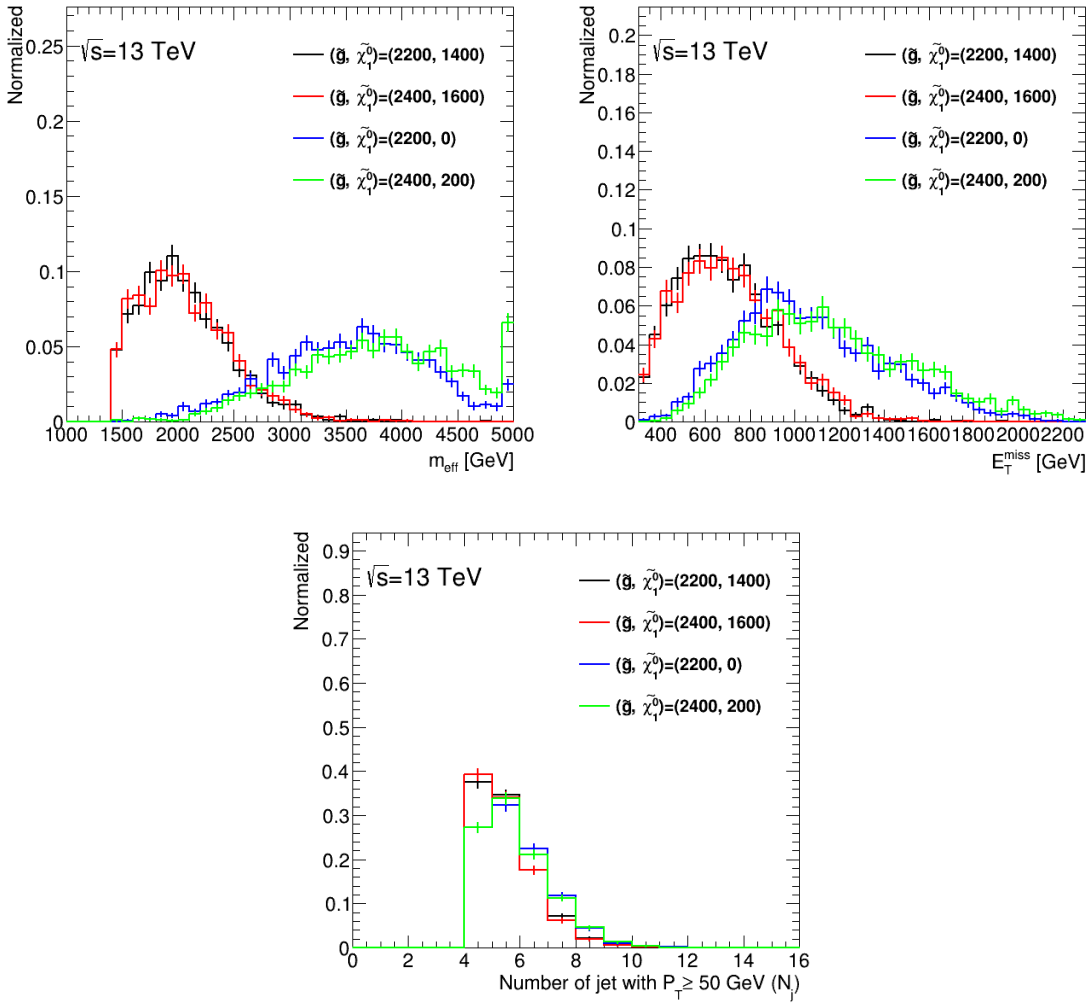

Figure 5.14: Distribution of the effective mass (top-left), the missing transverse momentum (top right) and N_j (bottom) in four gluino direct decay signals with ($m_{\tilde{g}}$,$m_{\tilde{\chi}_1^0}$)=(2200, 1400) (black line), (2400, 1600) (red line), (2200, 0) (blue line) and (2400, 200) (green line) GeV. The last bin includes the overflow.

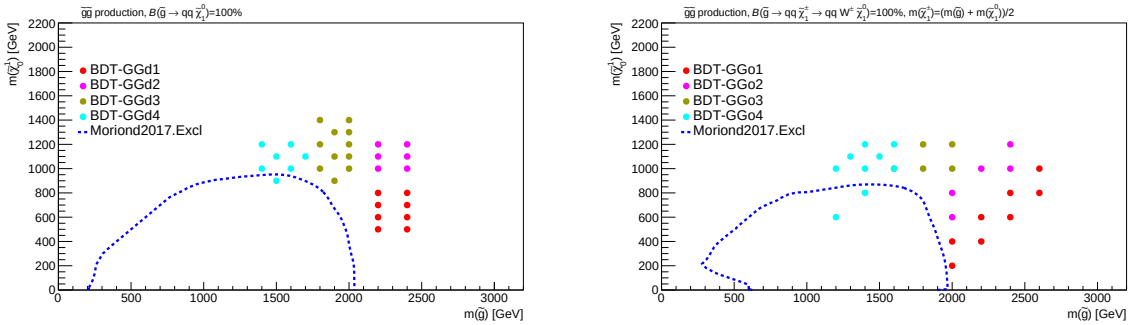

(a) GG direct (b) GG one-step

Figure 5.15: Illustration of training categories for gluino direct decay (a) and gluino one-step decay (b). For gluino direct decay (gluino one-step decay), the red point corresponds to GGd1 (GGo1), the magenta point corresponds to GGd2 (GGo2), the gold point corresponds to GGd3 (GGo3) and the light blue point corresponds to GGd4 (GGo4) training category. The blue dotted line shows the expected exclusion limit on the previous ATLAS result with the data of 36.1 fb^{-1} [34].

5.6.2 Application of BDT classifier

The training samples should not be used for the evaluation of signal and background events. This is because a BDT score is built from the training sample and there is a possibility that the BDT score obtained from the training sample can be biased. Therefore, each sample is normally divided into two samples (training sample and testing sample) and the testing sample is only used to evaluate the performance and to obtain the BDT score. However, it would decrease MC statistics to the half in the final fit. In order to avoid it, a method as shown in Figure 5.16 is adopted:

- MC samples are randomly divided into two data sets: the former set (half sample 1) is used as training sample and the latter set (half sample 2) is used as input for signal and background estimations.
- The training is also performed using the half sample 2 as well. In total, two kinds of BDT score are produced.
- The BDT classifier, which is obtained using the half sample 1, is applied to the half sample 2, and vice versa.
- Both half sample 1 and half sample 2 are used for the background estimation discussed in Chapter 6 (No loose of MC statistics).

This method is also applied to the data. Events in the data are divided in half and the BDT score is obtained from one of BDT classifiers. The validation of this method is discussed in Chapter 7.

5.6.3 Optimization of BDT classifier

With the preselection as listed in Table 5.3, the additional cuts are applied before the training to reduce background contributions beforehand and focus on the separation between the signal and the

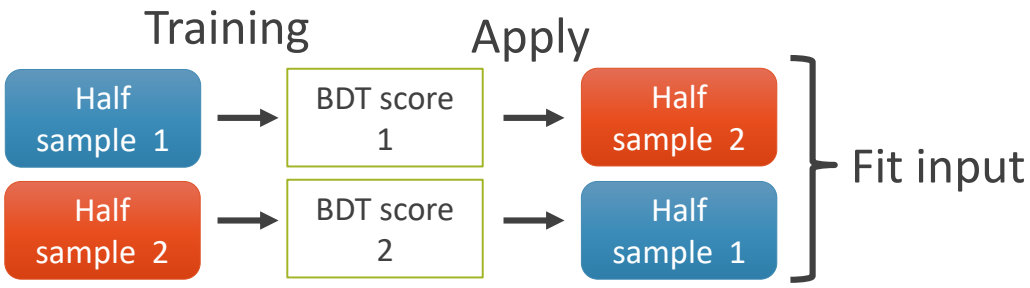

Figure 5.16: A schematic view of sample division into two sets randomly: for BDT training and for score usage, respectively. Half sample 1 is the first half of all MC events and half sample 2 is the second half.

background in the training. Table 5.4 show the cuts applied in the training samples.

Table 5.4: The definition of cuts per each training category for gluino direct decays (top) and gluino one-step decays (bottom), respectively.

	GGd1	GGd2	GGd3	GGd4
N_{j}	≥4	≥4	≥4	≥4
$\Delta\phi(j_{1,2,(3)}, \boldsymbol{p}_{\mathrm{T}}^{\mathrm{miss}})_{\mathrm{min}}$	≥0.4	≥0.4	≥0.4	≥0.4
$\Delta\phi(j_{i>3}, \boldsymbol{p}_{\mathrm{T}}^{\mathrm{miss}})_{\mathrm{min}}$	≥0.4	≥0.4	≥0.4	≥0.4
$E_{\mathrm{T}}^{\mathrm{miss}}/m_{\mathrm{eff}}$	≥0.2	≥0.2	≥0.2	≥0.2
m_{eff} [GeV]	≥1400	≥1400	≥800	≥800
$\Delta m(\tilde{g}, \tilde{\chi}_1^0)$ [GeV]	1600 – 1900	1000 – 1400	600 – 1000	200 – 600

	GGo1	GGo2	GGo3	GGo4
N_{j}	≥6	≥6	≥5	≥5
$\Delta\phi(j_{1,2,(3)}, \boldsymbol{p}_{\mathrm{T}}^{\mathrm{miss}})_{\mathrm{min}}$	≥0.4	≥0.4	≥0.4	≥0.2
$\Delta\phi(j_{i>3}, \boldsymbol{p}_{\mathrm{T}}^{\mathrm{miss}})_{\mathrm{min}}$	≥0.4	≥0.4	≥0.4	≥0.2
$E_{\mathrm{T}}^{\mathrm{miss}}/m_{\mathrm{eff}}$	≥0.2	≥0.2	≥0.2	≥0.2
m_{eff} [GeV]	≥1400	≥1400	≥800	≥800
$\Delta m(\tilde{g}, \tilde{\chi}_1^0)$ [GeV]	1400 – 2000	1200 – 1400	600 – 1000	200 – 400

5.6.4 Determination of input variables

In order to maximize the sensitivity, the following variables are checked as the candidate of input variables.

- Information of each jet: 1st - 6th jet p_{T}, η and ϕ.
- Information of event scale: m_{eff} and $E_{\mathrm{T}}^{\mathrm{miss}}$
- Information of event topology: Aplanarity, $\Delta\phi(\mathrm{jet}_{1,2,(3)}, \vec{E}_{\mathrm{T}}^{\mathrm{miss}})_{\mathrm{min}}$ and $\Delta\phi(\mathrm{jet}_{i>3}, \vec{E}_{\mathrm{T}}^{\mathrm{miss}})_{\mathrm{min}}$

The variable N_{j} is not the candidate of input variables in this analysis. Figures 5.17 show N_{j} distributions and the mismodeling is observed in CR, which will be explained in Section 6.2. When this variable is used, the background estimation is difficult. Therefore, this variable is not used in the candidate of input variables.

As the number of input variables is larger, the BDT classifier is more complicated. It causes that the validation of variable correlations discussed in Section 7.3 is difficult. Hence, if there is no impact on the sensitivities by adding the variables, the variables are not used in input variables. Under the decision criteria, the variables, which have the improvement of sensitivity, are selected. The determination of the input variables are based on the best sensitivity reach. The sensitivity (Z_n) is defined as below:

$$Z_n = \begin{cases} +\sqrt{2\left[n\ln\left\{\frac{n(b+\sigma)^2}{b^2+n\sigma^2}\right\} - \frac{b^2}{\sigma^2}\ln\left\{1+\frac{\sigma^2(n-b)}{b(b+\sigma^2)}\right\}\right]} & n > b \\ -\sqrt{2\left[n\ln\left\{\frac{n(b+\sigma)^2}{b^2+n\sigma^2}\right\} - \frac{b^2}{\sigma^2}\ln\left\{1+\frac{\sigma^2(n-b)}{b(b+\sigma^2)}\right\}\right]} & n < b \end{cases} \tag{5.2}$$

where n is the number of signal and background and $b \pm \sigma$ is the number of background events with statistic and systematic errors [115]. Following the previous publication [34], 20% systematic uncertainties are also assumed in this study. The sensitivity for all the signal points is calculated by applying the BDT score cut. In order to check impacts on input variables, 3σ sensitivity contour is evaluated by adding the variable one by one.

Figure 5.18(a) shows the 3σ sensitivity contours in the GGd1 category to check the impact on 1st-4th jets p_{T}. The black line corresponds to the contour when 1st-4th jets η, effective mass, missing transverse momentum and aplanarity (default variables) are used in input variables. The red line corresponds to the contour with the default variables and 1st jet p_{T}, the blue line corresponds to the contour with the default variables and 1st-2nd jets p_{T}, the green line corresponds to the contour with the default variables and 1st-3rd jets p_{T}, and the magenta line corresponds to the contour with the default variables and 1st-4th jets p_{T}. By adding the the variable one by one, the 3σ sensitivity contours are improved as shown in Figure 5.18(a). Figure 5.18(b) shows the breakdown of the sensitivities with four signal points in the GGd1 training category: ($m_{\tilde{g}}$,$m_{\tilde{\chi}_1^0}$)=(2200, 600), (2200, 0), (2200, 700) and (2000, 800) GeV. The correlations between jet p_{T} are effective as shown in Figure 5.9 and the sensitivity for gluino direct signal with ($m_{\tilde{g}}$,$m_{\tilde{\chi}_1^0}$)=(2000, 800) GeV is improved by ~50% when 1st-4th jets p_{T} are used.

Figure 5.19(a) shows the 3σ contours in GGd1 category to check the impact on the variables of aplanarity, $\Delta\phi(\mathrm{jet}_{1,2,(3)}, \vec{E}_{\mathrm{T}}^{\mathrm{miss}})_{\mathrm{min}}$, $\Delta\phi(\mathrm{jet}_{i>3}, \vec{E}_{\mathrm{T}}^{\mathrm{miss}})_{\mathrm{min}}$ and 1st-4th jets ϕ. The black line corresponds

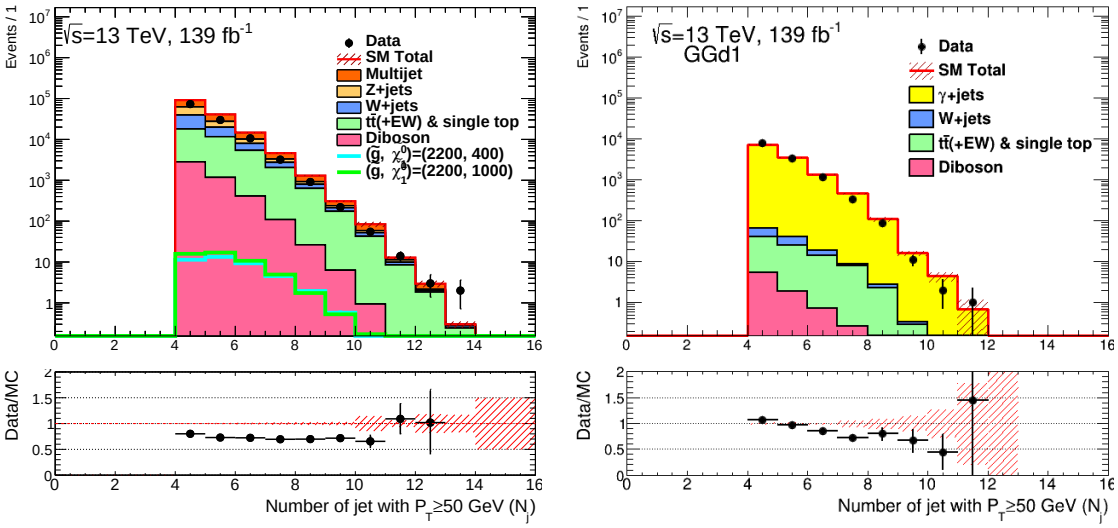

Figure 5.17: Left figure shows the distribution of the number of jet with p_{T} ≥50 GeV (N_{j}) with the preselection. Right figures shows the N_{j} with the preselection in CR, which will be explained in Section 6.2. The signals in the plot are gluino direct decay. The MC samples are normalized to cross section times integrated luminosity of 139 fb^{-1}. The bottom panel is the ratio of the data and the sum of SM backgrounds. The hatched red error bands indicate the statistical uncertainties of background prediction based on MC samples.

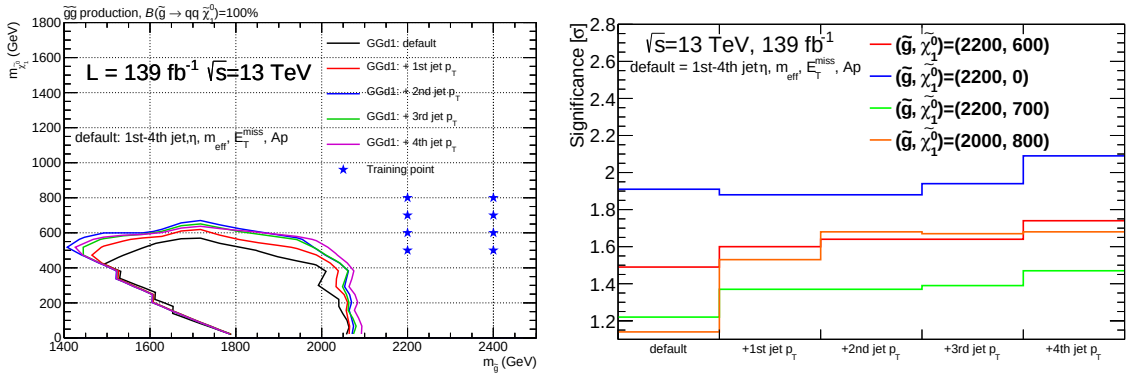

(a) (b)

Figure 5.18: The left figure is 3σ sensitivity contours in the GGd1 training category. The x-axis indicates the gluino mass and y-axis indicates the lightest neutralino mass. Each line corresponds to the contours with the different sets of input variables (see the text). The right figure is the breakdown of the sensitivities with four signal points in the GGd1 training category: ($m_{\tilde{g}}$,$m_{\tilde{\chi}^0_1}$)=(2000, 800), (2200, 0), (2200, 700) and (2000, 800) GeV. The x-axis indicates the used input variables and y-axis indicates the significance. By adding the variable of jet p_{T}, the sensitivity can be improved and these variables are used.

to the contour when 1st-4th jets p_{T}, η, effective mass and missing transverse momentum (default variables) and aplanarity are used in input variables. The red line corresponds to the contour with the default variables and $\Delta\phi(\mathrm{jet}_{1,2,(3)}, \vec{E}_{\mathrm{T}}^{\mathrm{miss}})_{\mathrm{min}}$, the blue line corresponds to the contour with the default variables and $\Delta\phi(\mathrm{jet}_{i>3}, \vec{E}_{\mathrm{T}}^{\mathrm{miss}})_{\mathrm{min}}$, and the green line corresponds to the contour with the default variables and 1st-4th jets ϕ. Since the aplanarity uses the information of the jets ϕ efficiently, the impact on $\Delta\phi(\mathrm{jet}_{i>3}, \vec{E}_{\mathrm{T}}^{\mathrm{miss}})_{\mathrm{min}}$ and jet ϕ is smaller than the aplanarity. The impact on $\Delta\phi(\mathrm{jet}_{1,2,(3)}, \vec{E}_{\mathrm{T}}^{\mathrm{miss}})_{\mathrm{min}}$ is almost same as the aplanarity as shown in Figure 5.19(b), so it is enough to add either $\Delta\phi(\mathrm{jet}_{1,2,(3)}, \vec{E}_{\mathrm{T}}^{\mathrm{miss}})_{\mathrm{min}}$ or aplanarity. The aplanarity is only used in this analysis.

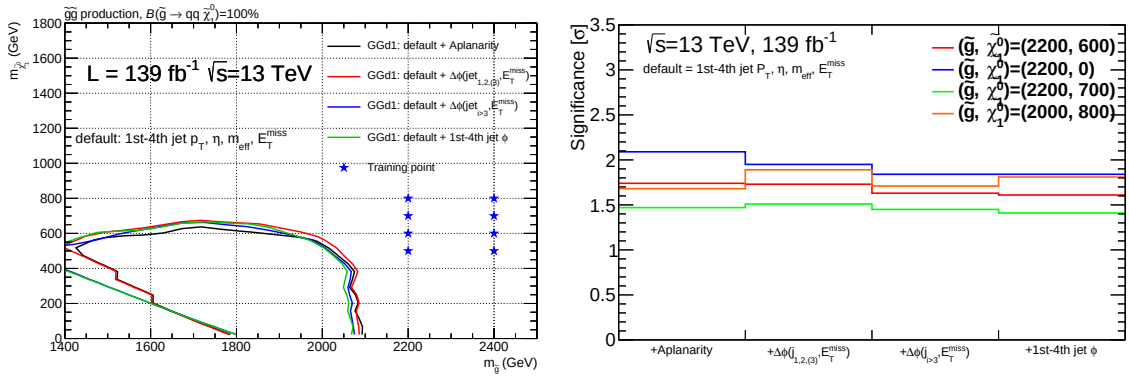

(a) (b)

Figure 5.19: The left figure is 3σ sensitivity contours in the GGd1 training category. The x-axis indicates the gluino Mass and y-axis indicates the lightest neutralino mass. Each line corresponds to the contours with the different sets of input variables (see the text). The right figure is the breakdown of the sensitivities with four signal points in the GGd1 training category: $(m_{\tilde{g}}, m_{\tilde{\chi}_1^0})$=(2200, 600), (2200, 0), (2200, 700) and (2000, 800) GeV. The x-axis indicates the used input variables and y-axis indicates the significance. For GGd1 category, the apalanarity is only used.

Figure 5.20(a) shows the 3σ contours in GGd1 category to check the impact on jet η. The black line corresponds to the contour when 1st-4th jets p_{T}, effective mass, missing transverse momentum and aplanarity (default variables) is used in input variables. The red line corresponds to the contour with the default variables and 1st-4th jets η. The 3σ sensitivity contour with 1st-4th jets ϕ are similar to the contour without 1st-4th jets ϕ. However, the sensitivity for the heavy gluino ($m_{\tilde{g}}$ >2400 GeV) is improved by ∼15% when 1st-4th jets η are used as shown in Figure 5.20(b). Therefore, the variables of jets η are kept in this analysis.

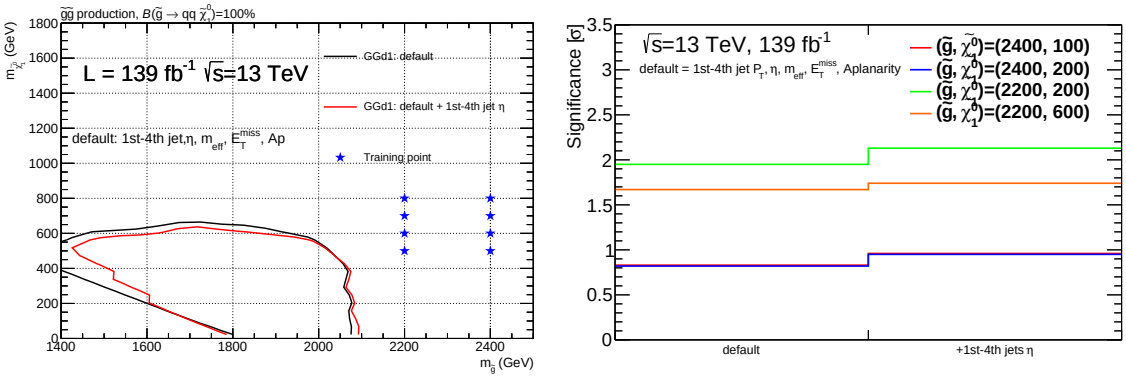

(a) (b)

Figure 5.20: 3σ sensitivity contours in the GGd1 training category with different sets of input variables. The x-axis indicates the gluino Mass and y-axis indicates the lightest neutralino mass. Each line corresponds to the contours with the different sets of input variables (see the text). The right figure is the breakdown of the sensitivities with four signal points in the GGd1 training category: $(m_{\tilde{g}}, m_{\tilde{\chi}_1^0})$=(2400, 800), (2200, 0), (2200, 700) and (2000, 800) GeV. The x-axis indicates the used input variables and y-axis indicates the significance. For GGd1 category, 1st-4th jets η are used.

Tables 5.5 and 5.6 are the summary of input variables in all the training categories. For GGd2, GGo1, GGo2 and GGo3, the impact on the missing transverse momentum is small (< 10%), so it is removed from input variables to reduce the number of input variables. For GGd4 and GGo4, the impact on the aplanarity is small (< 10%) because the signals in these categories have a planar event shape. Up to 12 variables are selected among $E_{\mathrm{T}}^{\mathrm{miss}}$, m_{eff}, aplanarity, p_{T} and η of selected jets, and used in the training for the eight categories.

Table 5.5: Input variables for the gluino direct decay. Circle (◯) indicates the variable is used in input variables. The hyphen (-) indicates the variable is not used in input variables.

Input variables	GGd1	GGd2	GGd3	GGd4
$E_{\mathrm{T}}^{\mathrm{miss}}$ [GeV]	◯	-	◯	◯
p_{T}(j) [GeV]	1st-4th	1st-4th	1st-4th	1st-4th
η(j)	1st-4th	1st-4th	1st-4th	1st-4th
Aplanarity	◯	◯	◯	-
m_{eff} [GeV]	◯	◯	◯	◯
Total number of input variables	11	10	11	10

Table 5.6: Input variables for the gluino one-step decay. Circle (◯) indicates the variable is used in input variables. The hyphen (-) indicates the variable is not used in input variables.

Input variables	GGo1	GGo2	GGo3	GGo4
$E_{\mathrm{T}}^{\mathrm{miss}}$ [GeV]	-	-	-	◯
p_{T}(j) [GeV]	1st -5th	1st - 4th	1st - 3rd, 5th - 6th	1st - 4th
η(j)	1st - 5th	1st - 4th	1st - 3rd, 5th - 6th	1st - 4th
Aplanarity	◯	◯	◯	-
m_{eff} [GeV]	◯	◯	◯	◯
Total number of input variables	12	10	12	10

5.7 Signal region (SR) definition

The BDT scores are close to -1 for background-like events, while they are close to 1 for signal-like events. As shown in Figure 5.21, BDT scores have a good separation power between the target signals and backgrounds. The BDT score cut is required to define signal regions (SRs) This cut is the final discriminating variable. The SRs are defined for each training category to cover all gluino and neutralino masses. In order to determine the optimized BDT score cut per each training category, the expected significance defined in Eq. 5.2 is calculated for each SR as shown in Figure 5.22. The optimized cut is chosen to maximize the significance but some of the BDT cuts are loosened from the optimal cuts to have enough background statistics in terms of background estimation as discussed in Chapter 6. The summary of all SRs are listed in the Table 5.7.

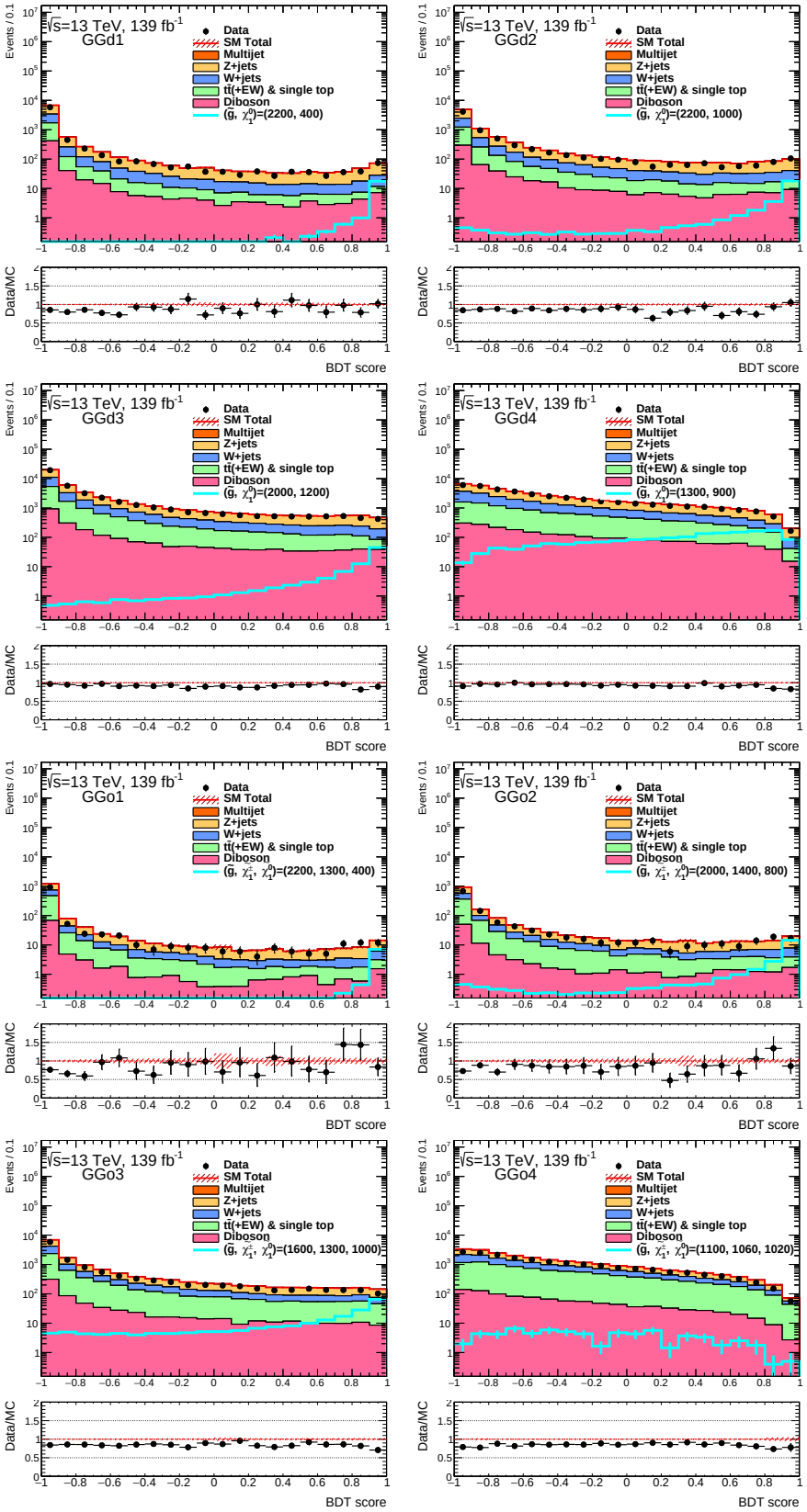

Figure 5.21: BDT score distributions for all categories. The signals in the plot are gluino direct decay for GGd1-4 and gluino one-step decay via W boson for GGo1-4. The MC samples are normalized to cross section times integrated luminosity of 139 fb^{-1}. The bottom panel is the ratio of the data and the sum of SM backgrounds. The hatched red error bands indicate the statistical uncertainties of the MC samples.

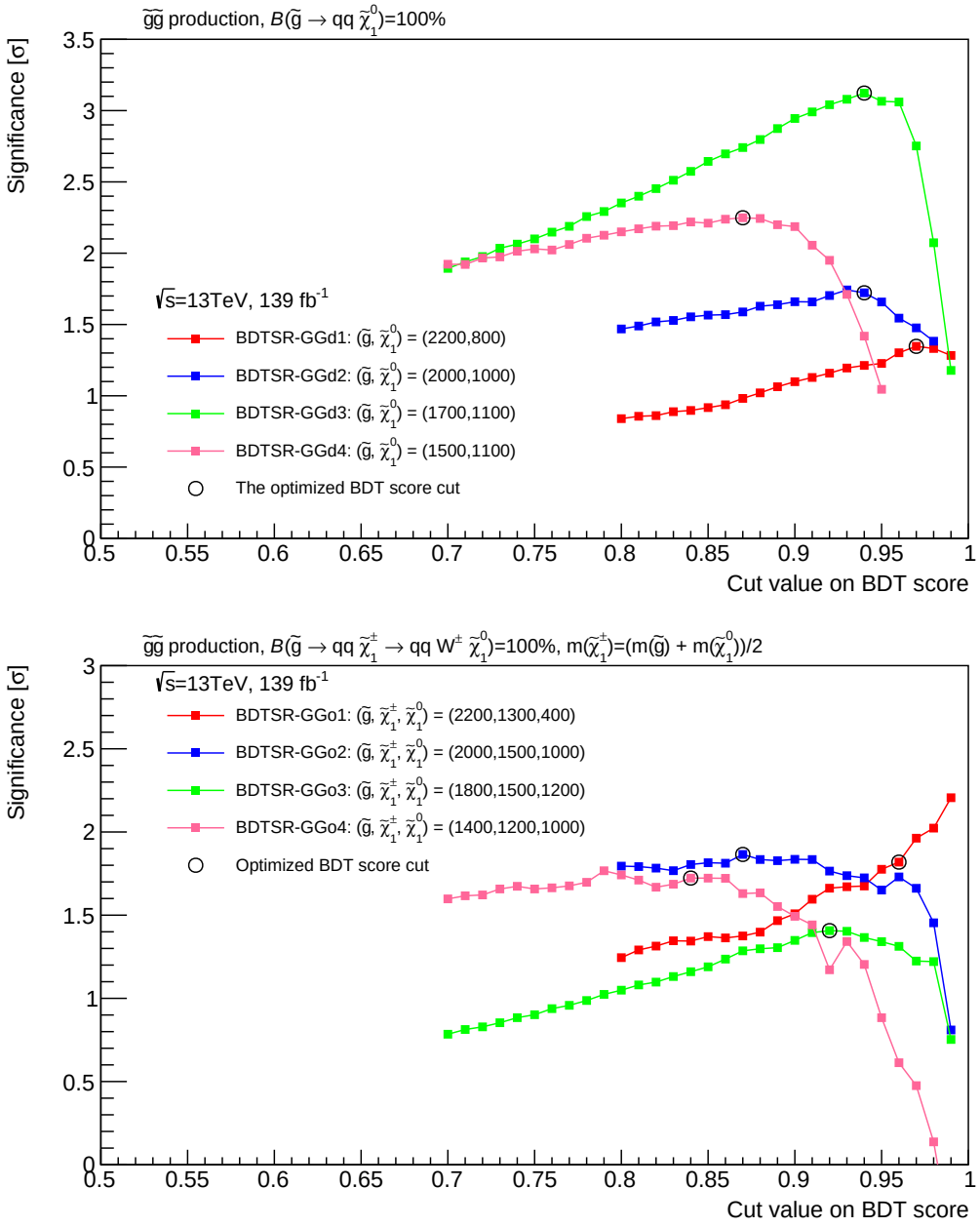

Figure 5.22: The expected sensitivities as a function of BDT score cut in all categories for gluino direct (top) and one-step (bottom) decay signals, respectively. These signal masses are one of the target masses for each training category. The final optimized BDT score cuts are highlighted by large solid circles per the categories.

Table 5.7: Definition of signal region with the benchmark signal model parameters ($\Delta m(\tilde{g}, \tilde{\chi}_1^0)$) for gluino direct decays (top) and gluino one-step decays (bottom), respectively.

	GGd1	GGd2	GGd3	GGd4
N_{j}	≥4	≥4	≥4	≥4
$\Delta\phi(j_{1,2,(3)}, \boldsymbol{p}_{\text{T}}^{\text{miss}})_{\text{min}}$	≥0.4	≥0.4	≥0.4	≥0.4
$\Delta\phi(j_{i>3}, \boldsymbol{p}_{\text{T}}^{\text{miss}})_{\text{min}}$	≥0.4	≥0.4	≥0.4	≥0.4
$E_{\text{T}}^{\text{miss}}/m_{\text{eff}}$	≥0.2	≥0.2	≥0.2	≥0.2
m_{eff} [GeV]	≥1400	≥1400	≥800	≥800
BDT score	≥ 0.97	≥ 0.94	≥ 0.94	≥ 0.87
$\Delta m(\tilde{g}, \tilde{\chi}_1^0)$ [GeV]	1600 – 1900	1000 – 1400	600 – 1000	200 – 600

	GGo1	GGo2	GGo3	GGo4
N_{j}	≥6	≥6	≥5	≥5
$\Delta\phi(j_{1,2,(3)}, \boldsymbol{p}_{\text{T}}^{\text{miss}})_{\text{min}}$	≥0.4	≥0.4	≥0.4	≥0.2
$\Delta\phi(j_{i>3}, \boldsymbol{p}_{\text{T}}^{\text{miss}})_{\text{min}}$	≥0.4	≥0.4	≥0.4	≥0.2
$E_{\text{T}}^{\text{miss}}/m_{\text{eff}}$	≥0.2	≥0.2	≥0.2	≥0.2
m_{eff} [GeV]	≥1400	≥1400	≥800	≥800
BDT score	≥ 0.96	≥ 0.87	≥ 0.92	≥ 0.84
$\Delta m(\tilde{g}, \tilde{\chi}_1^0)$ [GeV]	1400 – 2000	1200 – 1400	600 – 1000	200 – 400

6 Background estimation

The SRs in this analysis are defined in corners of phase space with large m_{eff}, leading jet p_{T} and $E_{\text{T}}^{\text{miss}}$. In addition, the variable correlations are used in this analysis. Therefore, background estimation is challenging. The MC simulation is not modeled well as described in Section 5.4, thus MC samples need to be corrected properly. This chapter discusses the data driven MC sample correction for each SM background.

6.1 Background composition

The following SM processes are considered to be background processes in this analysis:

- **Z+jets**: Since large missing transverse momentum is required as shown in Table 5.3, the remaining process of Z boson is $Z(\rightarrow\nu\bar{\nu})$+jets as shown in Figure 6.1.

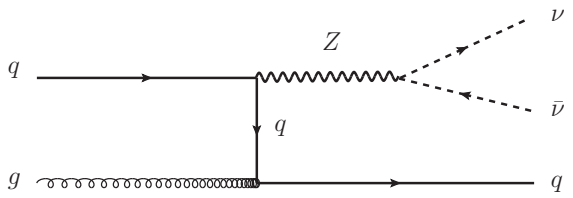

Figure 6.1: Feynman diagram of $Z + q$, $Z \rightarrow\nu\bar{\nu}$.

- **W+jets**: Events of W+jets with the leptonic decay $W \rightarrow e\nu$, $\mu\nu$ and $\tau\nu$ remain in SRs as shown in Figure 6.2. Figures 6.3 show the composition of W+jets background as a function of BDT score. The majority of the remaining events from W+jets is $W \rightarrow\tau\nu$ with $\sim$ 70% and others are $W \rightarrow\mu\nu$ with $\sim$ 25% and $W \rightarrow e\nu$ with $\sim$ 5%. There are two reasons why the leptonic decays of W+jets remain in SRs. One is that the lepton is misidentified and reconstructed as a jet. The other is that the lepton is not selected due to low p_{T} or out of η acceptance. The detail is discussed in Section 6.4.

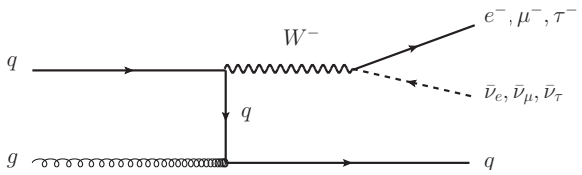

Figure 6.2: Feynman diagram of leptonic decays of W boson.

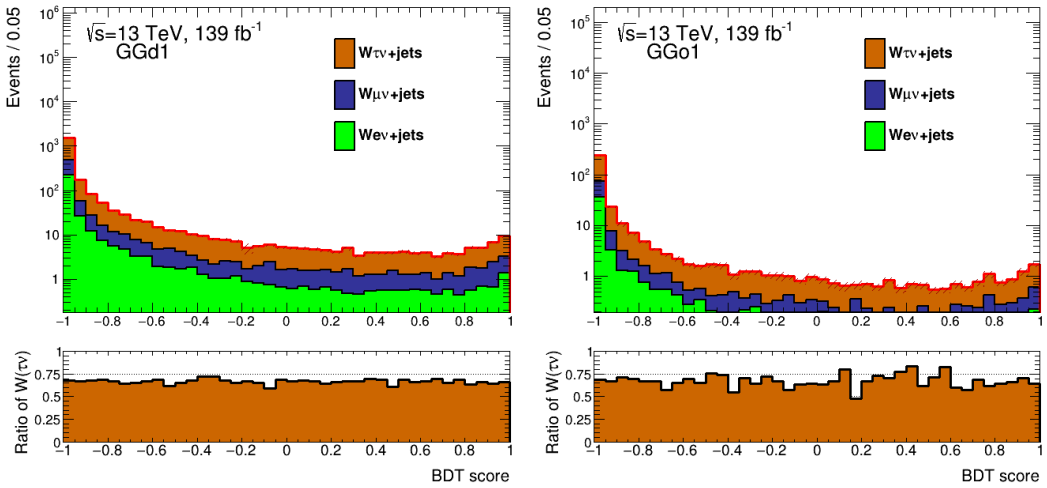

Figure 6.3: The composition of W+jets background in GGd1 and GGo1 as a function of BDT score. The bottom panel of the plots shows the relative fraction of $W \rightarrow \tau\nu$ events.

- **Top**: The dominant production process with top quark of this analysis is top and anti-top pair production ($t\bar{t}$) as shown in Figure 6.4. A top (anti-top) quark decays to a b ($\bar{b}$) quark with W^+ (W^-) boson, which are called "$t\bar{t}$+EW". In order to obtain a large missing transverse momentum, the two W bosons have different decays: one is the leptonic decay $W \rightarrow \ell\nu$ and the other is the hadronic decay $W \rightarrow qq$ The events remain in SRs by failing one lepton. The subdominant process is the single top production as shown in Figure 6.5. The fraction in the top background processes are $\sim$ 85% with the $t\bar{t}$ and $\sim$ 15% with the single top.

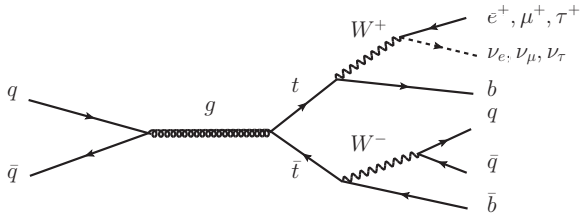

Figure 6.4: Feynman diagram of $t\bar{t}$ production.

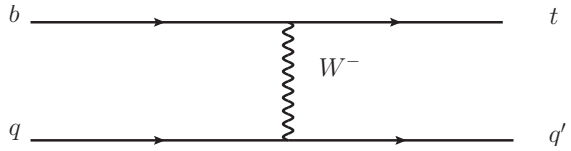

Figure 6.5: Feynman diagram of single top production.

- **Diboson**: The diboson production has two bosons as shown in Figure 6.6. Considered on the requirement of large missing transverse momentum, the dominant remaining process in the diboson production is $W(\rightarrow\ell\nu)Z(\rightarrow\nu\nu)$ with additional jets.

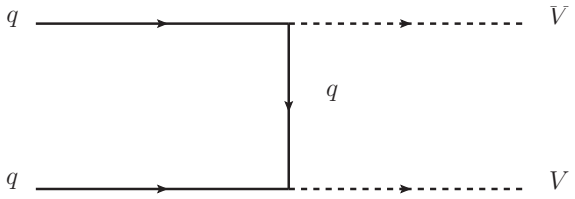

Figure 6.6: Feynman diagram of diboson production. V indicates the boson (Z, W, γ)

- **Multi-jet**: The multi-jet production has multi jets in the final states as shown in Figure 6.7 and the cross section is larger than other background processes. When the energy of these jets is mismeasured, a fake missing transverse momentum is generated and the multi-jet events remain in the SRs. As discussed in Section 5.4, these events are suppressed by $\Delta\phi(\text{jet}_{1,2,(3)}, \vec{E}_{\text{T}}^{\text{miss}})_{\text{min}}$ and $\Delta\phi(\text{jet}_{i>3}, \vec{E}_{\text{T}}^{\text{miss}})_{\text{min}}$ cuts.

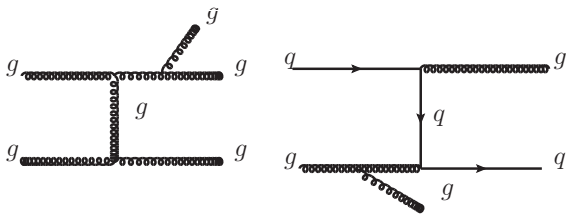

Figure 6.7: Main Feynman diagram of multi-jet production.

Figure 6.8 shows the breakdown of expected background components in each SR after applying selections as shown in Table 5.7. The most dominant component is Z+jets except GGo4 SR because of the requirement of large missing transverse momentum. For GGo4 SR, $t\bar{t}$ and single top components are dominated. The W+jets component is subdominated in all SRs. The diboson contribution is less than 15%. The multi-jet contribution is negligible (<1%) by applying $\Delta\phi(\text{jet}_{1,2,(3)}, \vec{E}_{\text{T}}^{\text{miss}})_{\text{min}}$ and $\Delta\phi(\text{jet}_{i>3}, \vec{E}_{\text{T}}^{\text{miss}})_{\text{min}}$ cuts.

6.2 Background estimation strategy

Since MC simulation cannot perfectly describe the data, it should be corrected by using the data. This analysis[1] uses control regions (CRs) to make correction for each background as follows. First, CRs for each background are designed to be kinematically close but orthogonal to corresponding SRs. Then, MC samples are normalized to data in CRs. Finally, their normalization factors are applied to MC samples in their corresponding SR. With this procedure, the number of background events in SR (N_{SR}) is expressed as:

$$\text{N}_{\text{SR}} = {\text{N}_{\text{SR}}}^{\text{MC}} \times \left[\frac{{\text{N}_{\text{CR}}}^{\text{data}}}{{\text{N}_{\text{CR}}}^{\text{MC}}} \right], \tag{6.1}$$

where ${\text{N}_{\text{CR}}}^{\text{data}}$ is the number of the observed events in CR and ${\text{N}_{\text{SR}}}^{\text{MC}}$ (${\text{N}_{\text{CR}}}^{\text{MC}}$) is the number of the events from MC samples in SR (CR). This approach assumes the mismodeling in CRs is the same as

[1] Each SR has a single-bin.

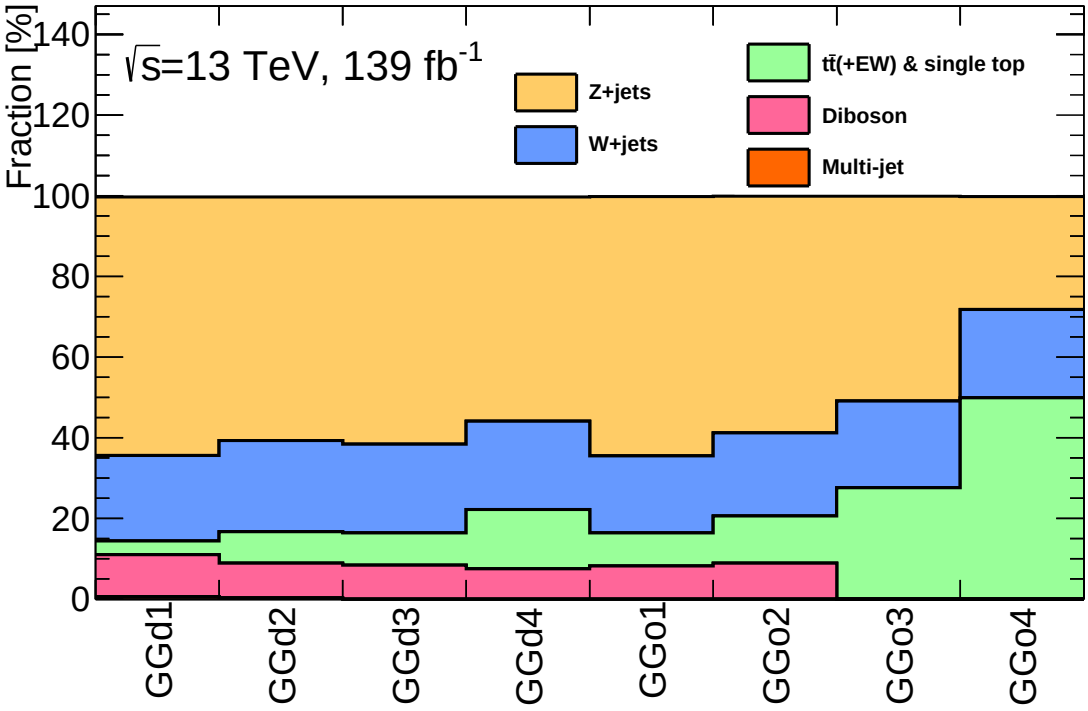

Figure 6.8: Breakdown of the SM components in each SR.

their SRs and it means that differences between the data and MC samples are the same in both SRs and CRs. This assumption is tested using a validation regions (VRs) as discussed in Section 6.6. CRs for Z+jets, W+jets and top ($t\bar{t}$ and single top) components are prepared and discussed below. The MC samples of diboson and multi-jet are used for the estimation without any corrections. The validity of these MC samples are checked by the VRs.

6.3 Z+jets background estimation

In order to control the Z+jets background, the γ+jets event is used as CR, which is called CRY. The kinematics is expected to closely resemble those of $Z(\rightarrow\nu\bar{\nu})$+jets events in case the transverse momentum of Z boson is significantly greater than $m(Z) = 91.2$ GeV as shown in Figure 6.9. Therefore, a cut on the high transverse momentum of the reconstructed photon, ${p_{\mathrm{T}}}^{\gamma} > 150$ GeV is applied in CRY. A vector of ${p_{\mathrm{T}}}^{\gamma}$ is added to the $E_{\mathrm{T}}^{\mathrm{miss}}$ vector ($E_{\mathrm{T}}^{\mathrm{miss}\prime} = |\mathbf{E}_{\mathrm{T}}^{\mathrm{miss}} + \mathbf{p}_{\mathrm{T}}^{\gamma}|$) because a photon is considered to be a Z boson and the transverse momentum of the neutrinos from Z boson is measured as $E_{\mathrm{T}}^{\mathrm{miss}}$. After the modification, the $E_{\mathrm{T}}^{\mathrm{miss}}$ in CRY is similar to corresponding SR as shown in Figure 6.10 and CRY can provide an estimation of the p_{T} of the Z boson decaying to neutrinos in SRs.

By using the events, the kinematic selections in CRY are a little bit optimized in order to obtain the similar BDT score distribution to SR. The selections are same with SRs except GGo1 and GGo2. For GGo1 and GGo2, the number of remaining data events in the CRY is very

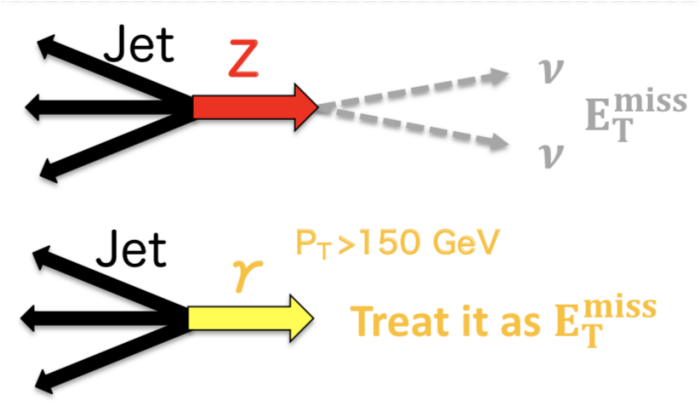

Figure 6.9: The schematic view of $Z(\rightarrow \nu\bar{\nu})$ and γ+jets events

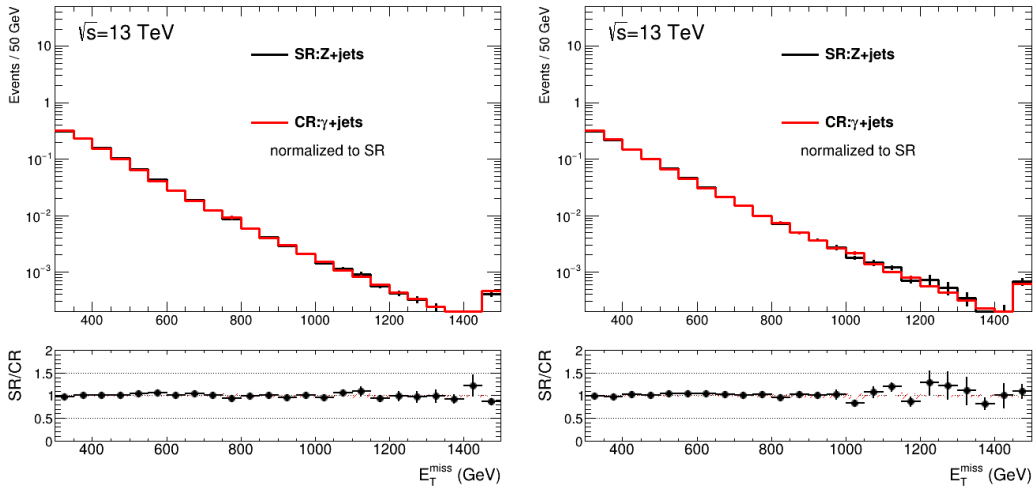

Figure 6.10: Comparison of the distribution between $E_{\mathrm{T}}^{\mathrm{miss}}$ of Z+jets in SR and $E_{\mathrm{T}}^{\mathrm{miss}\prime} = |\mathbf{E}_{\mathrm{T}}^{\mathrm{miss}} + \mathbf{p}_{\mathrm{T}}^{\gamma}|$ of γ+jets in CRY. The selection, $N_{\mathrm{jet}} \geq 4$ is applied in the left figure and $N_{\mathrm{jet}} \geq 6$ is applied in the right figure. The last bin includes the overflow. The bottom panel is the ratio of the MC sample in SR and CRY. The total number of events in each CRY is normalized to that in the SR in each plot. The black error bar is the relative statistical uncertainty in SR. The hatched red error bands indicate the statistical uncertainties of background prediction based on MC samples in CRY.

lows due to the tight selection. It causes large statistical uncertainties of the normalization factor and the precise estimation would not be performed despite the main background in the SR. Therefore, the selections in the CRY are changed. Figures 6.11 show the distributions of three variables ($\Delta\phi(\text{jet}_{1,2,(3)}, \vec{E}_{\text{T}}^{\text{miss}})_{\text{min}}$,$\Delta\phi(\text{jet}_{i>3}, \vec{E}_{\text{T}}^{\text{miss}})_{\text{min}}$,$E_{\text{T}}^{\text{miss}}/m_{\text{eff}}$). These variables do not have any slope in the ratio of data and MC samples so that the normalization factor would not be biased even if the selections of these variables are removed. In GGo1 and GGo2, the cuts on these variables are not required in CRY.

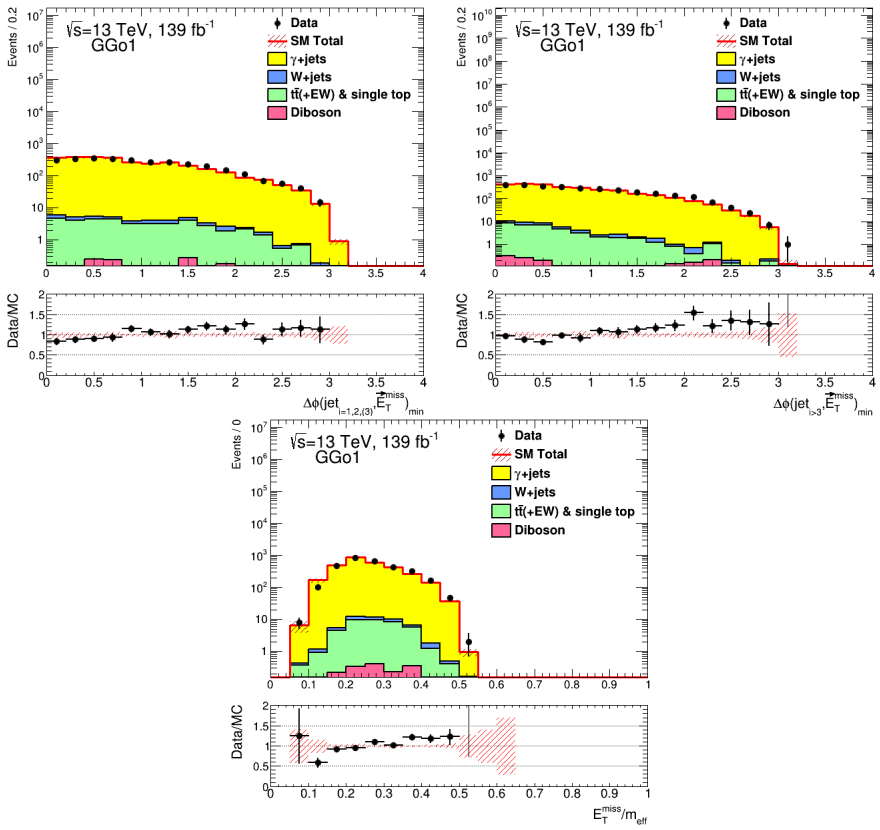

Figure 6.11: $\Delta\phi(\text{jet}_{1,2,(3)}, \vec{E}_{\text{T}}^{\text{miss}})_{\text{min}}$, $\Delta\phi(\text{jet}_{i>3}, \vec{E}_{\text{T}}^{\text{miss}})_{\text{min}}$ and $E_{\text{T}}^{\text{miss}}/m_{\text{eff}}$ distributions in the CRY. The same selections as GGo1 SR except $\Delta\phi(\text{jet}_{1,2,(3)}, \vec{E}_{\text{T}}^{\text{miss}})_{\text{min}}$, $\Delta\phi(\text{jet}_{i>3}, \vec{E}_{\text{T}}^{\text{miss}})_{\text{min}}$, $E_{\text{T}}^{\text{miss}}/m_{\text{eff}}$ and BDT score are applied. The MC samples are normalized to data in order to visualize the shape of distribution. The bottom panel is the ratio of the observed data and the MC simulation. The black bar is the relative statistical uncertainty in data. The hatched red error bands indicate the statistical uncertainties of background prediction based on MC samples.

Figures 6.12 show the comparison of BDT score distribution between SRs and CRYs in MC simulation and the shape in CRY is similar to the corresponding SR within the statistical uncertainty of MC samples. Therefore, the designed CRYs are suitable for the estimation of Z+jets background.

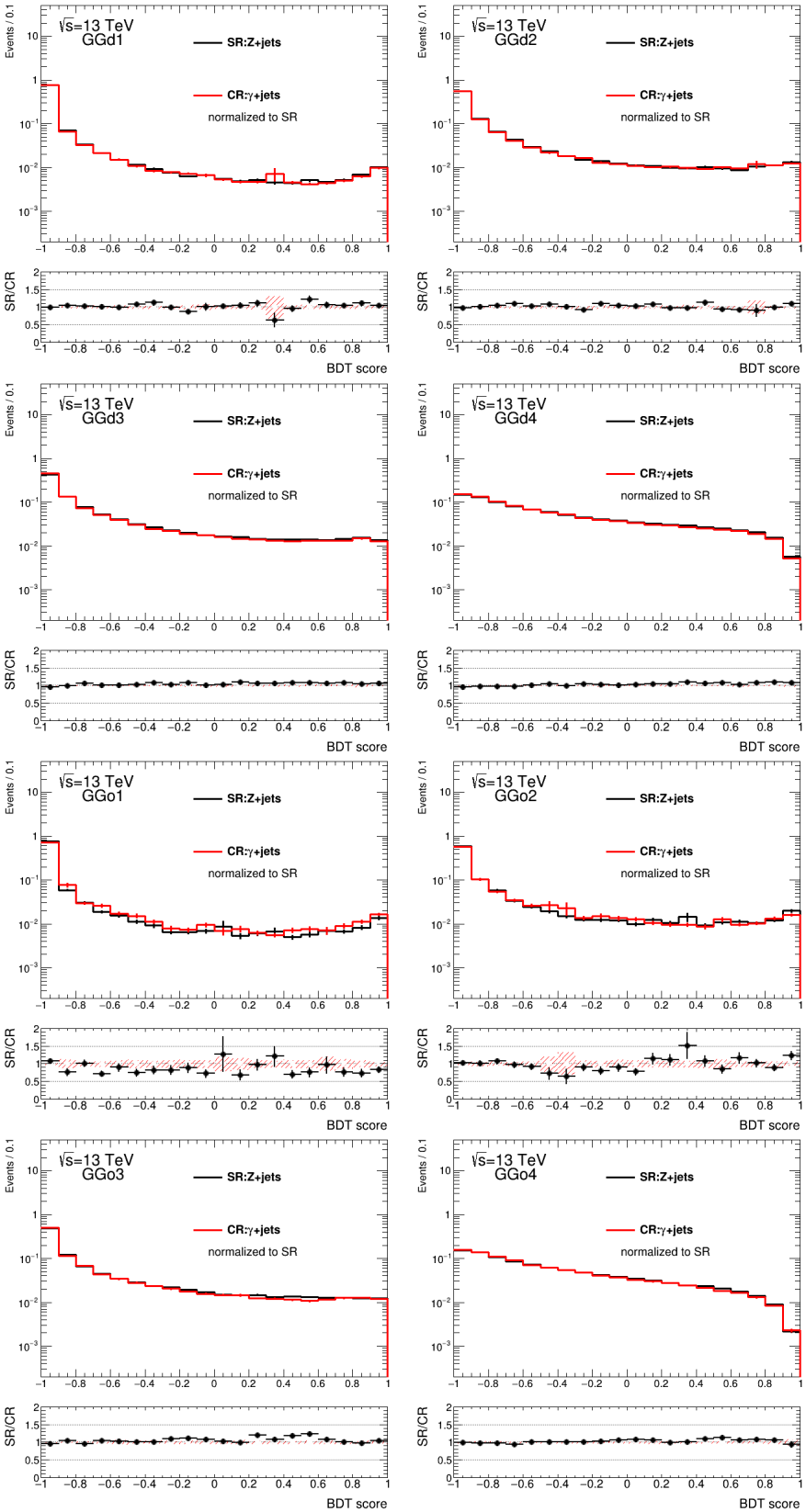

Figure 6.12: Comparison of BDT score distribution between Z+jets in SRs (black lines) and γ+jets in CRYs (red lines) in MC simulation. The bottom panel is the ratio of the MC sample in SR and CRY. The total number of events in each CRY is normalized to that in the SR in each plot. The black error bar is the relative statistical uncertainty in SR. The hatched red error bands indicate the statistical uncertainties of the MC samples in CRY.

6.4 W+jets background estimation

As explained in Section 6.1, events of W+jets with the leptonic decay $W \to e\nu$, $\mu\nu$ and $\tau\nu$ remain in SRs. For $W \to e\nu$ events, the electron is misidentified and reconstructed as a jet in SRs. For $W \to \mu\nu$ events, the muon is not selected due to low p_{T}, out of η acceptance ($|\eta| > 2.5$) and low efficiencies at $|\eta| \sim 0$ as shown in Figure 4.11. For $W \to \tau\nu$ events, the tau decays hadronically so that this tau is reconstructed as a jet. When a tau decays leptonically ($\tau \to e\nu_e\nu_\tau, \mu\nu_\mu\nu_\tau$), events having such a tau are considered in $W \to e\nu$ or $W \to \mu\nu$.

6.4.1 Definition of CR

In order to estimate the W+jets background in SRs, $W(\to \ell\nu)$+jets events by requiring an electron or a muon are used as CR, which is called CRW. The event topology in $W \to e\nu$ in SRs is similar to $W \to \tau\nu$ in SRs because the electron and tau are reconstructed as a jet. $W \to e\nu$ events are CRs for $W \to e\nu$ and $W \to \tau\nu$, and $W \to \mu\nu$ events are a CR for $W \to \mu\nu$ but they are combined and considered as one CR because all the event topologies are similar after a procedure explained below is applied.

The same $E_{\mathrm{T}}^{\mathrm{miss}}$ trigger as SRs is used to select the CRW events. This makes it possible to access a low p_{T} muon region, which is closer to the SR phase space for $W \to \mu\nu$ events. Additionally, a requirement of the transverse mass defined in Eq. 3.1, 30 GeV$< m_{\mathrm{T}} <$ 100 GeV is applied and the b quark is vetoed to enhance the purity of W+jets events against $t\bar{t}$ events. Figures 6.13 show the comparison of the $E_{\mathrm{T}}^{\mathrm{miss}}$ distribution between SRs and CRWs in MC sample for each decay mode. Good agreement is already observed in $W \to e\nu$ and $\tau\nu$ but disagreement is observed in $W \to \mu\nu$. In order to have similar event topologies in SR, the following procedure for electron and muon in CRW is performed.

- A lepton is treated as a jet if the lepton is identified as an electron.
- A lepton is treated as a jet if the lepton is identified as a muon with $|\eta| > 0.2$.
- A lepton is added to the $E_{\mathrm{T}}^{\mathrm{miss}}$ vector ($E_{\mathrm{T}}^{\mathrm{miss}\prime} = |\mathbf{E}_{\mathrm{T}}^{\mathrm{miss}} + \mathbf{p}_{\mathrm{T}}^{\ell}|$) if the lepton is identified as a muon with $|\eta| < 0.2$.

Using this procedure, good agreement of $E_{\mathrm{T}}^{\mathrm{miss}}$ distributions for each decay mode between SRs and CRWs is observed within the statistical uncertainties as shown in Figure 6.14. In the next subsection, the third bullet is explained in details.

6.4.2 Properties of $W \to \mu\nu$ events

Figures 6.15 show the truth kinematic distribution of muons in SR. First, the truth muon p_{T} distribution has a sharp peak at low values, so the majority of the muons is failed due to lepton p_{T} threshold cut. Figure 6.16 is the distribution of the difference between truth and reconstructed $E_{\mathrm{T}}^{\mathrm{miss}}$ for the events where the muon p_{T} is failed due to the lepton p_{T} threshold cut. The difference is small, so the reconstructed $E_{\mathrm{T}}^{\mathrm{miss}}$ is hardly affected when the muon p_{T} is low.

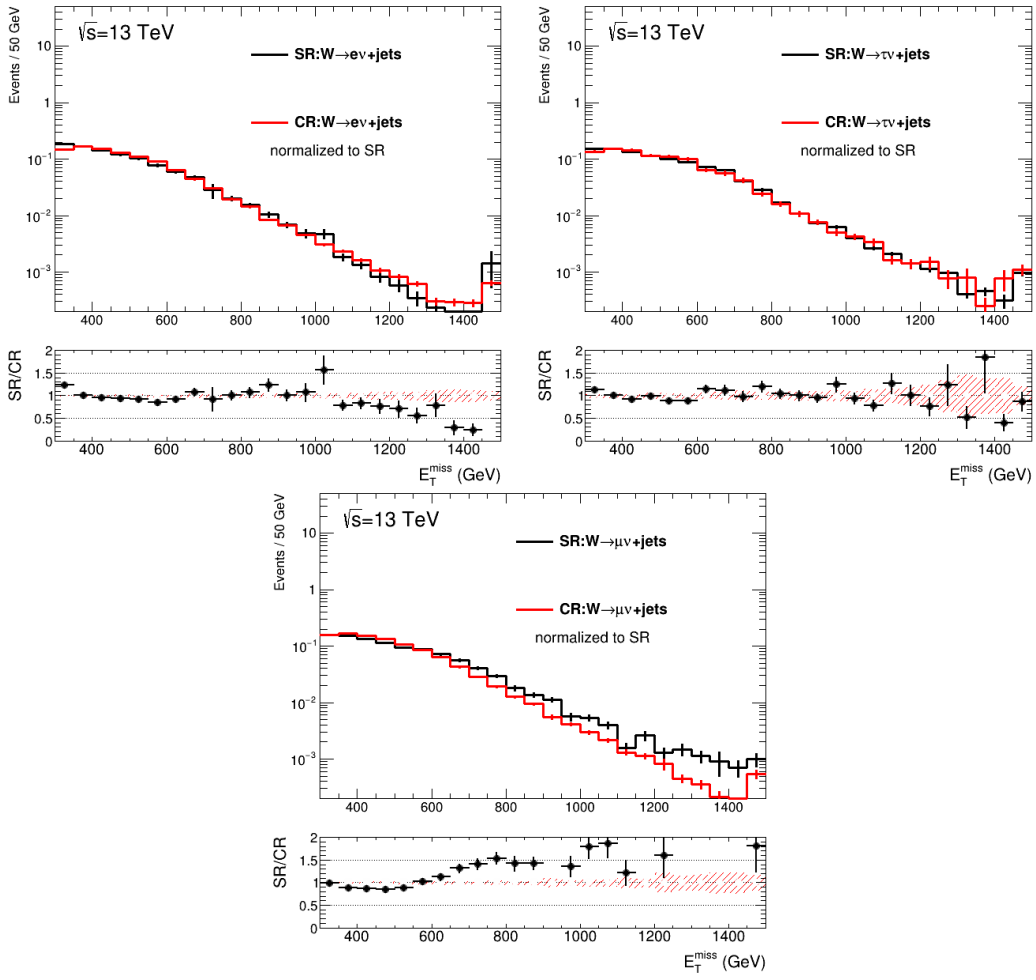

Figure 6.13: Comparison of the $E_{\mathrm{T}}^{\mathrm{miss}}$ distribution between $W(\rightarrow e\nu)$+jets in SR and CRW (top-left), $W(\rightarrow \tau\nu)$+jets in SR and CRW (top-right) and $W(\rightarrow \mu\nu)$+jets in SR and CRW (bottom). $N_{\mathrm{jet}} \geq 4$ is applied in all the figures. The last bin includes the overflow. The bottom panel is the ratio of the MC sample in SR and CRW. The total number of events in each CRW is normalized to that in SR in each plot. The black error bar is the relative statistical uncertainty in SR.T he hatched red error bands indicate MC statistical uncertainties in CRW.

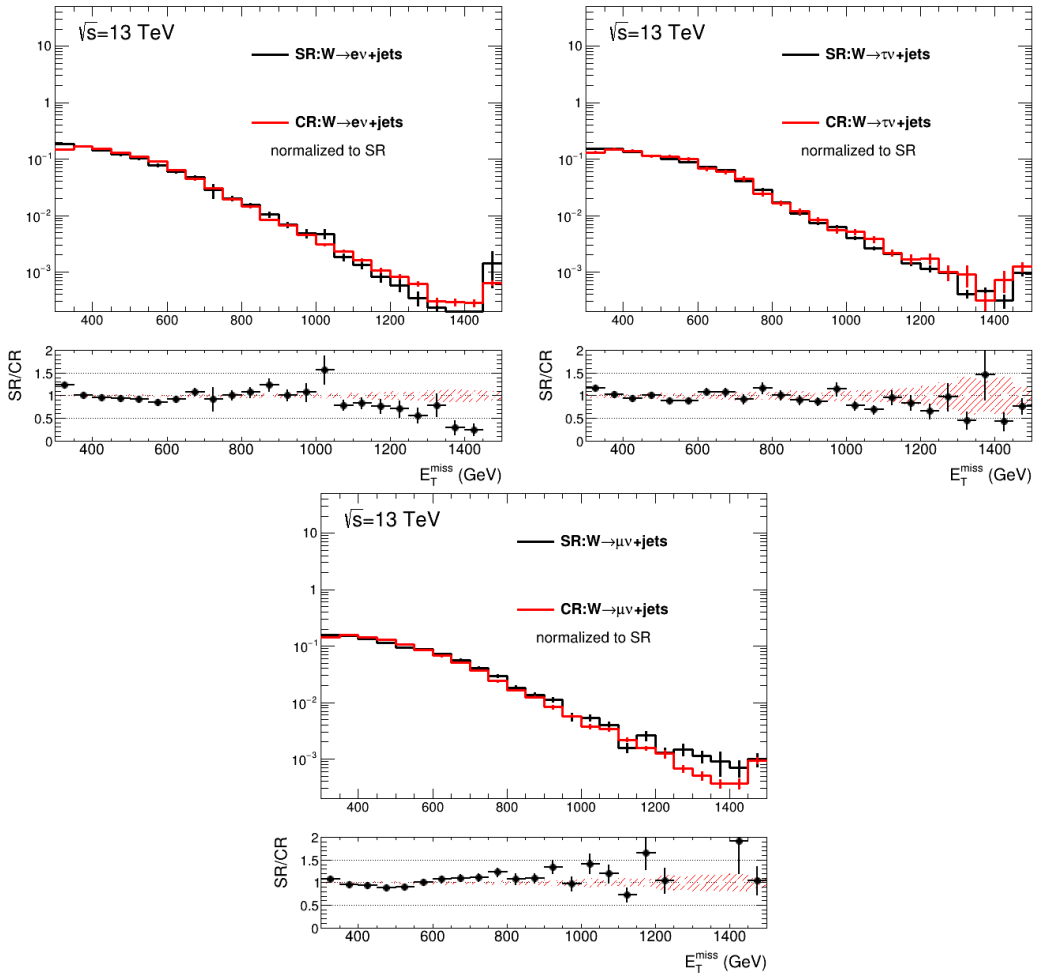

Figure 6.14: Comparison of the $E_{\mathrm{T}}^{\mathrm{miss}}$ distribution between $W(\rightarrow e\nu)$+jets in SR and CRW (top-left), $W(\rightarrow \mu\nu)$+jets in SR and CRW (top-right) and $W(\rightarrow \tau\nu)$+jets in SR and CRW (bottom). The selection, $N_{\mathrm{jet}} \geq 4$ is applied to all the figures and the missing transverse momentum is modified under the treatment. The last bin includes the overflow. The bottom panel is the ratio of the MC simulation in SR and CRW. The total number of events in each CRW is normalized to that in the SR in each plot. The black error bar is the relative statistical uncertainty in SR. The hatched red error bands indicate the statistical uncertainties of background prediction based on MC samples in CRW.

Next, the truth muon η distribution has three peaks : $\eta > 2.5$, $\eta < -2.5$ and $\eta \sim 0$. When the muon traverses the region of $\eta > 2.5$ or $\eta < -2.5$, the muon is not reconstructed due to the out of η acceptance in the muon spectrometer. Such a muon causes the difference between the truth and reconstructed $E_{\mathrm{T}}^{\mathrm{miss}}$ as shown in Figures 6.17. However, since this contribution in the SRs is small (less than 15%) in $W \rightarrow \mu\nu$+jets events, there is almost no impact in the $E_{\mathrm{T}}^{\mathrm{miss}}$ distribution in CRWs. When the muon traverses the region with $\eta \approx 0$, the muon identification efficiency is rather low ($\sim 60\%$) compared to other regions as shown in Figure 4.11. Since such an undetected muon would have very high p_{T}, it makes a large difference between the truth and reconstructed $E_{\mathrm{T}}^{\mathrm{miss}}$ as shown in Figures 6.18. This is the reason why a muon at $|\eta| \sim 0$ is added to the missing transverse momentum instead of being treated as a jet.

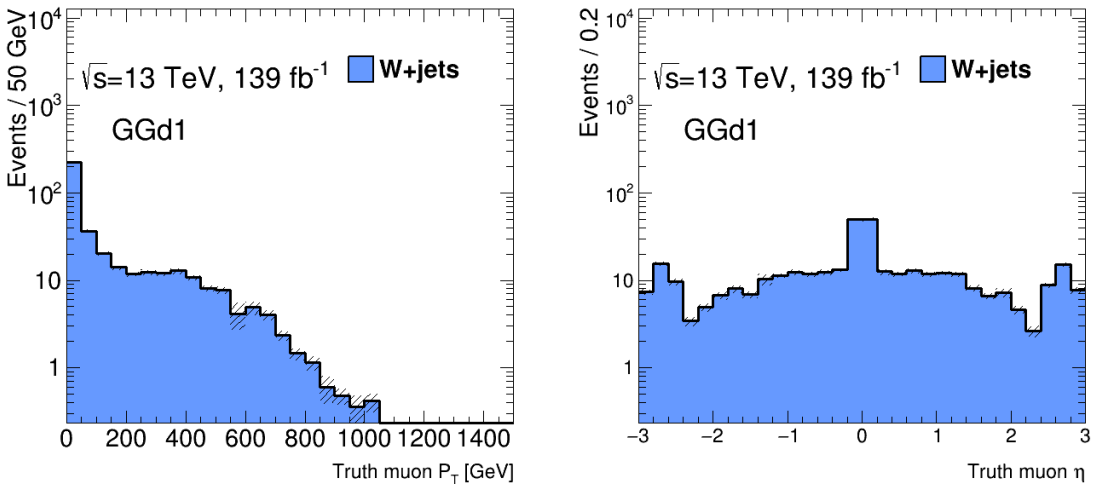

Figure 6.15: Distributions of the truth muon p_{T} (left) and η (right) in GGd1 SR. The hatched black error bands indicate the statistical uncertainties of background prediction based on MC samples.

6.4.3 Adjustment of cut in CRW

In order to pass the requirement of large missing transverse momentum, a large momentum of the neutrino from W boson is needed. In this case, the W boson must be boosted. As a result, the lepton from the W boson has large momentum and the direction of the lepton and the neutrino is similar. Therefore, the variable of $\Delta\phi(\mathrm{jet}_{1,2,(3)}, \vec{E}_{\mathrm{T}}^{\mathrm{miss}})_{\mathrm{min}}$ is small for the lepton which is treated as a jet and such events would be rejected due to the selection of this variable. In other words, W boson with very high p_{T} would have small $\Delta\phi(\mathrm{jet}_{1,2,(3)}, \vec{E}_{\mathrm{T}}^{\mathrm{miss}})_{\mathrm{min}}$ in CRW. If these events are rejected, the kinematics of remaining events in CRWs is biased and the difference of BDT score distribution between W+jets in SRs and W+jets in CRWs becomes large as shown in Figure 6.19(a). In order to avoid this bias, the cut of $\Delta\phi(\mathrm{jet}_{1,2,(3)}, \vec{E}_{\mathrm{T}}^{\mathrm{miss}})_{\mathrm{min}}$ is not required in CRWs, so good agreement of BDT score distribution between W+jets in SRs and W+jets in CRWs is observed as shown in Figure 6.19(b). The same biases are observed in all other CRWs. For GGo1, GGo2, GGo3 and GGo4, the number of remaining data events in the CRW is very low due to the tight selection. Like the CRY, it causes the large statistical uncertainties of the normalization factor. Therefore, the cut on $\Delta\phi(\mathrm{jet}_{i>3}, \vec{E}_{\mathrm{T}}^{\mathrm{miss}})_{\mathrm{min}}$ is not required.

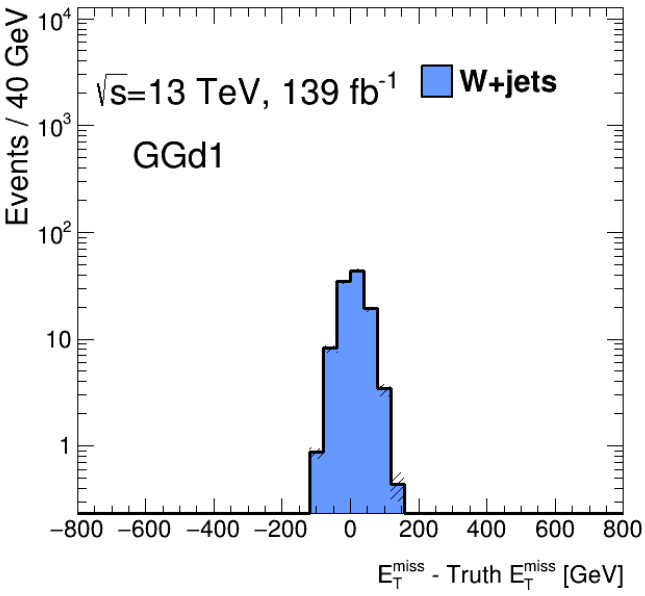

Figure 6.16: Distribution of the difference between truth and reconstructed $E_{\mathrm{T}}^{\mathrm{miss}}$ for events where the muon p_{T} is below the muon p_{T} threshold (<6 GeV) in GGd1 SR. The hatched black error bands indicate the statistical uncertainties of background prediction based on MC samples.

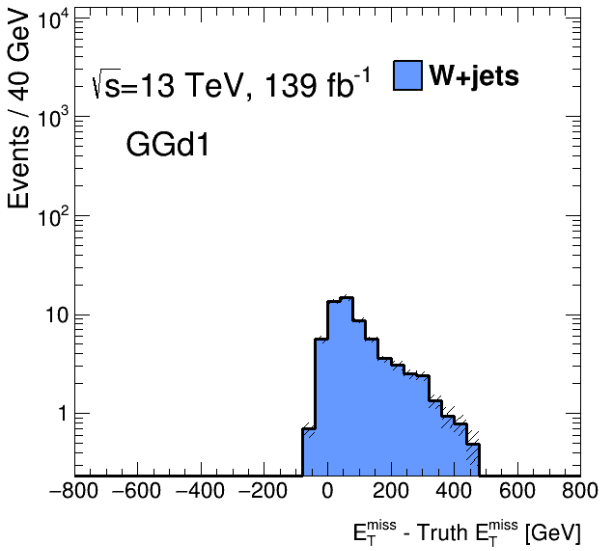

Figure 6.17: Distribution of the difference between truth and reconstructed $E_{\mathrm{T}}^{\mathrm{miss}}$ in case of the outside of η acceptance ($|\eta| > 2.5$). The hatched black error bands indicate the statistical uncertainties of background prediction based on MC samples.

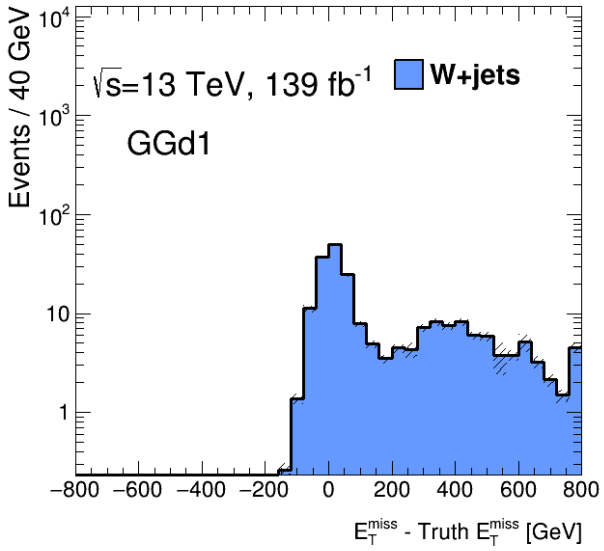

Figure 6.18: Distribution of the difference between truth and reconstructed $E_{\mathrm{T}}^{\mathrm{miss}}$ in case of the region with $\eta \approx 0$. The hatched black error bands indicate the statistical uncertainties of background prediction based on MC samples.

Figure 6.20 show distributions of $\Delta\phi(\mathrm{jet}_{i>3}, \vec{E}_{\mathrm{T}}^{\mathrm{miss}})_{\mathrm{min}}$. This variable does not have any slope in the ratio of data and MC samples so that the normalization factor would not be biased. Figures 6.21 show the comparison of BDT score distributions between SRs and CRWs in MC simulation after applying these procedures. The distributions in CRs are well modeled to describe those in SRs within the statistical uncertainty of MC samples.

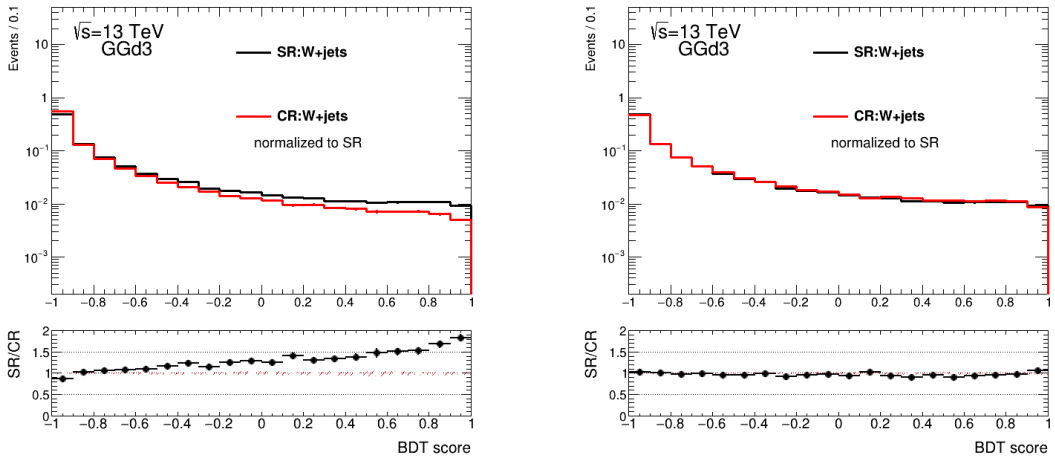

Figure 6.19: Comparison of BDT score distribution in GGd3 between W+jets in SR (black lines) and CRW (red lines). $\Delta\phi(\text{jet}_{1,2,(3)}, \vec{E}_{\text{T}}^{\text{miss}})_{\text{min}}$ >0.4 is applied in the left figure, but is not applied in the right figure. The bottom panel is the ratio of the MC simulation in SR and CRW. The total number of events in each CRW is normalized to that in the SR in each plot. The black error bar is the relative statistical uncertainty in SR. The hatched red error bands indicate the statistical uncertainties of background prediction based on MC samples in CRW.

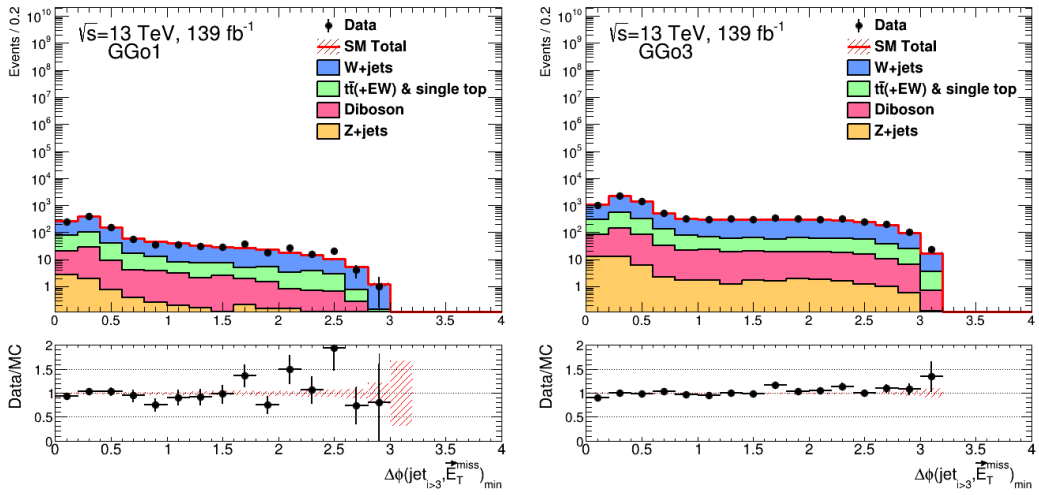

Figure 6.20: Distribution of $\Delta\phi(\text{jet}_{i>3}, \vec{E}_{\text{T}}^{\text{miss}})_{\text{min}}$ in the CRW. The same selections as GGo1 (GGo3) SR except $\Delta\phi(\text{jet}_{1,2,(3)}, \vec{E}_{\text{T}}^{\text{miss}})_{\text{min}}$, $\Delta\phi(\text{jet}_{i>3}, \vec{E}_{\text{T}}^{\text{miss}})_{\text{min}}$ and BDT score are applied to left figure (right figure). The MC samples are normalized to data in order to visualize the shape of distribution. The bottom panel is the ratio of the observed data and the MC simulation. The black bar is the relative statistical uncertainty in data. The hatched red error bands indicate the statistical uncertainties of background prediction based on MC samples.

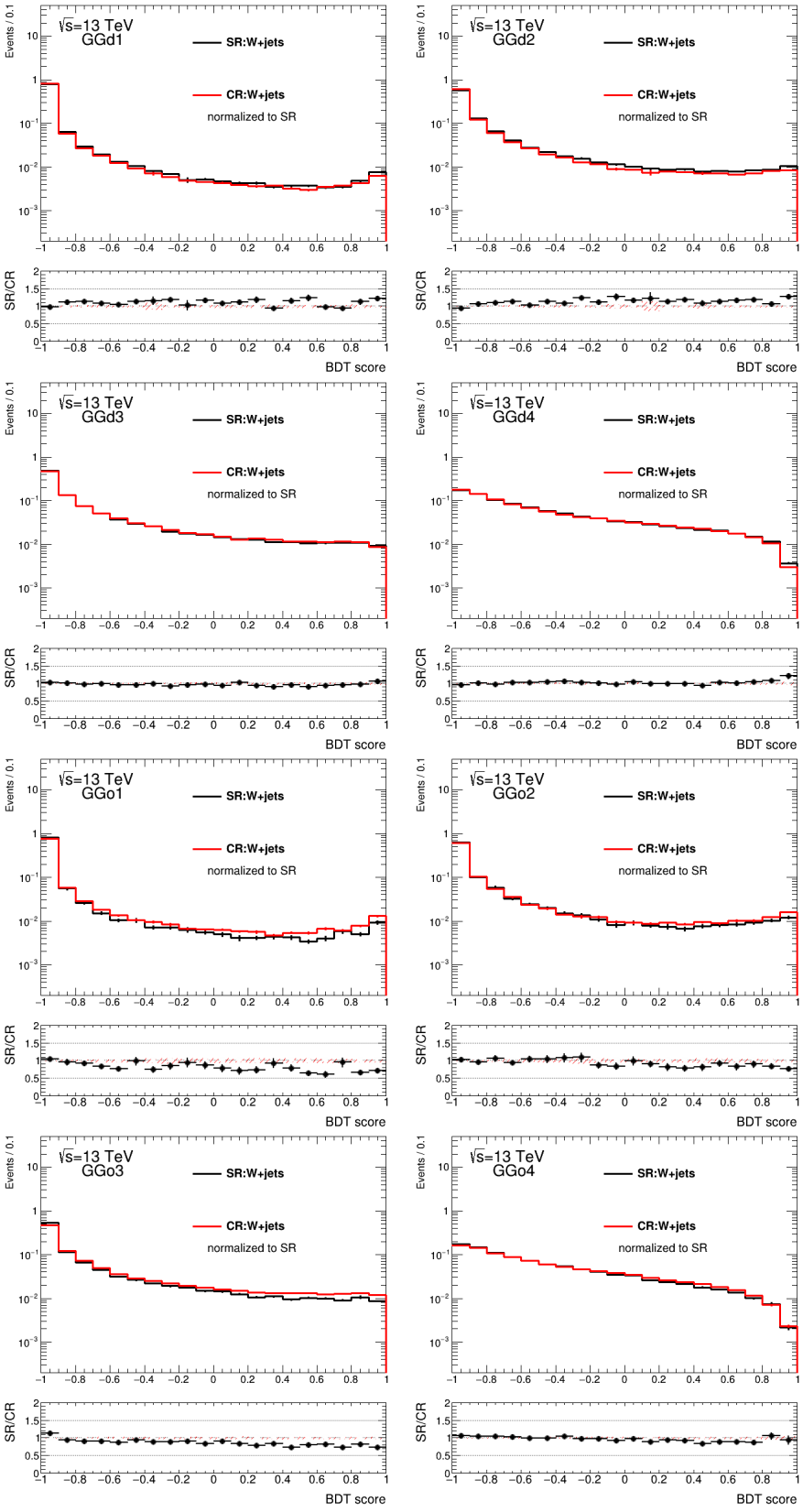

Figure 6.21: Comparison of all the BDT score distributions between W+jets in SR (black lines) and CRW (red lines). The bottom panel is the ratio of the MC simulation in SR and CRW. The total number of events in each CRW is normalized to that in the SR in each plot. The black error bar is the relative statistical uncertainty in SR. The hatched red error bands indicate the statistical uncertainties of MC samples in CRW.

6.5 Top background estimation

In order to estimate the top ($t\bar{t}$ and single top) background in SRs, the top events are selected as CR (called CRT) as follows. Like CRW, the same $E_{\mathrm{T}}^{\mathrm{miss}}$ triggers as SRs are applied, an electron or a muon is required and a requirement of the transverse mass defined in Eq. 3.1 is applied to enhance the purity of W boson (30 GeV$< m_{\mathrm{T}} <$ 100 GeV). Since an event from top background should have at least one b quark, an additional criteria of at least one b-jet is required. The treatment of the electron and the muon in CRTs is the same as CRWs.

The cut of $\Delta\phi(\mathrm{jet}_{1,2,(3)}, \vec{E}_{\mathrm{T}}^{\mathrm{miss}})_{\mathrm{min}}$ is removed from the selection as discussed in Section 6.4.3. In addition to the variable, the cut of $\Delta\phi(\mathrm{jet}_{i>3}, \vec{E}_{\mathrm{T}}^{\mathrm{miss}})_{\mathrm{min}}$ is removed in order to increase the statistics of CRTs. Figures 6.22 show the comparison of all the BDT score distributions between top events in SRs and CRTs. For GGo1 and GGo2, the visible difference is appeared. The observed differences are 50% for GGo1 and GGo2. Therefore, the systematic uncertainties are assigned so that the differences are corrected. However, the contribution of the top events is relatively small (9% for GGd1 and 12% for GGo2) as shown in Figure 6.8, thus the total background estimation is almost unchanged.

There are known mismodeling on the $t\bar{t}$ background [116]. This effect is observed in some variables in this analysis, such as m_{eff} and leading jet p_{T} as shown in Figures 6.23. In order to avoid the effect in the background estimation, the cuts of these variables in CR are designed to be same as SR. This background estimation is checked by using validation region (VR), which is explained in next section.

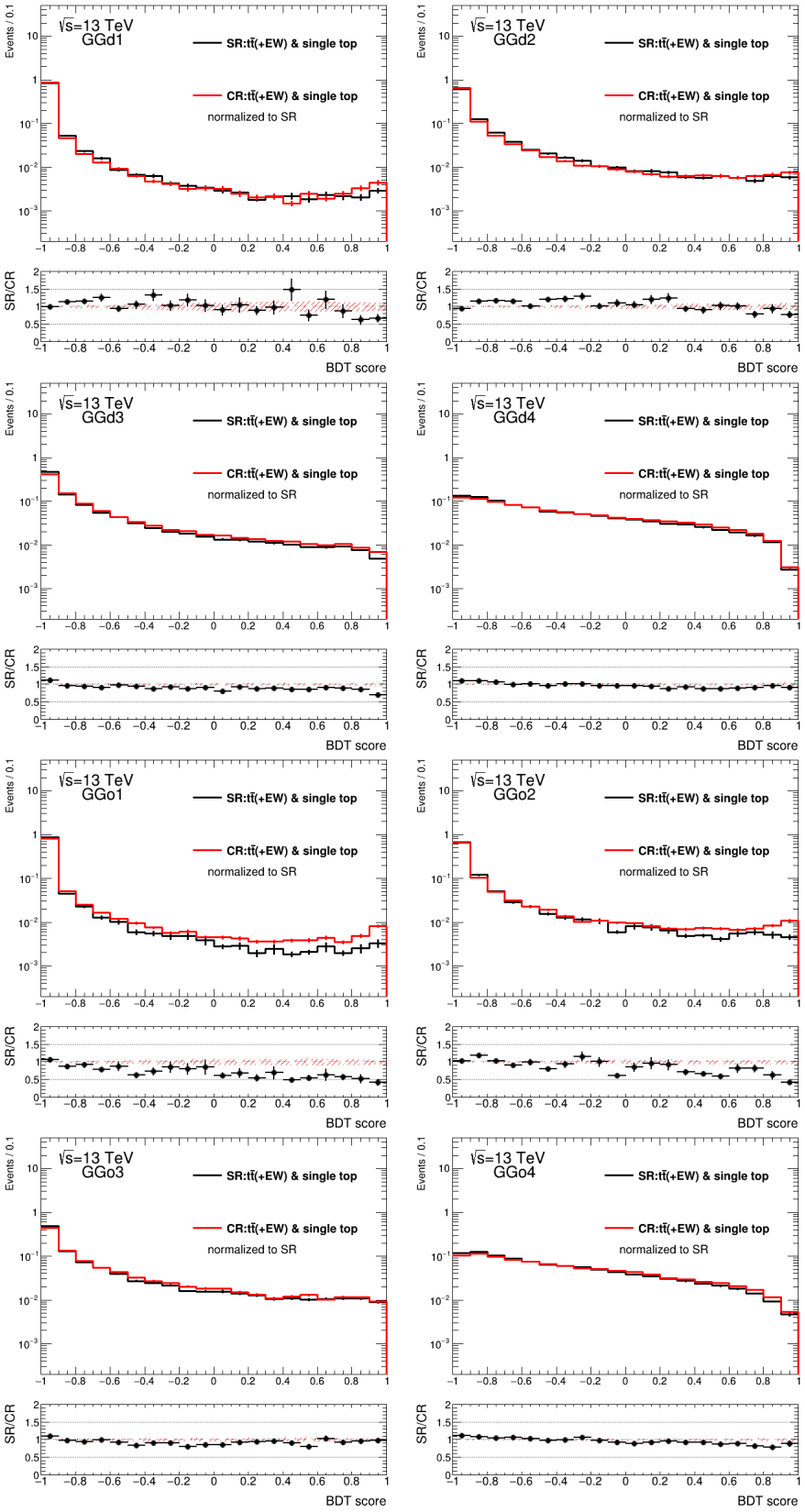

Figure 6.22: Comparison of all the BDT score distributions between top events in SR (black lines) and CRT (red lines). The bottom panel is the ratio of the MC simulation in SR and CRT. The total number of events in each CRT is normalized to that in the SR in each plot. The black error bar is the relative statistical uncertainty in SR. The hatched red error bands indicate the statistical uncertainties of background prediction based on MC samples in CRT.

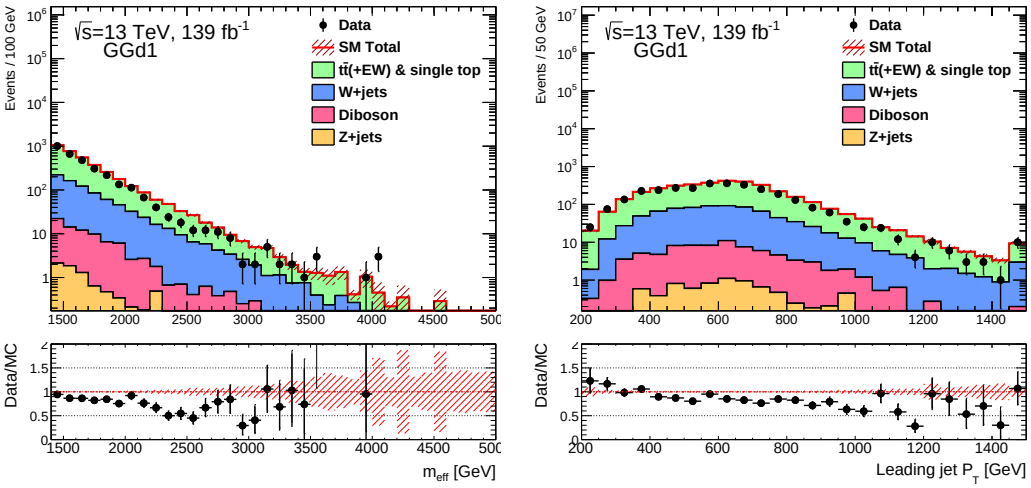

Figure 6.23: Distribution of the effective mass m_{eff} (left) and the leading jet p_{T} (right) with the GGd1 cut except BDT score cut in CRT. The last bin includes the overflow. The bottom panel is the ratio of the observed data and the MC simulation. The black error bar is the relative statistical uncertainty in the data. The hatched red error bands indicate the statistical uncertainties of background prediction based on MC samples.

6.6 Validation region

In order to check the results of these background estimation, a further set of regions, called Validation Region (VR), is designed. They are determined with the same strategy as the CR. In this analysis, five VRs are introduced.

***Z*+jets validation region** Z+jets events with two electrons or muons are used as VR, which is called VRZ as orthogonal region to SRs and CRYs. In order to emulate the transverse momentum of neutrinos from Z boson, the reconstructed p_{T} from two leptons is added to the $E_{\mathrm{T}}^{\mathrm{miss}}$ vector ($E_{\mathrm{T}}^{\mathrm{miss}\prime} = |\mathbf{E}_{\mathrm{T}}^{miss} + \mathbf{p}_{\mathrm{T}}^{Z\to\ell\ell}|$). After the modification, the missing transverse momentum distribution in VRZ can be similar to the corresponding SR. The $Z(\to\ell\ell)$ events do not have the large $E_{\mathrm{T}}^{\mathrm{miss}}$, so the $E_{\mathrm{T}}^{\mathrm{miss}}$ triggers cannot be used. Hence, the events are selected by lowest unprescaled single lepton triggers instead of the $E_{\mathrm{T}}^{\mathrm{miss}}$ triggers. In order to enhance the purity of the events, two leptons of the same flavour and opposite sign with $p_{\mathrm{T}}(\ell_1) > 27$ GeV and $p_{\mathrm{T}}(\ell_2) > 7$ GeV, are required. Furthermore, the cut of invariant mass in the dilepton system, 66 GeV $< m_{\ell\ell} <$116 GeV is applied. Depending on the selection criteria, three VRZs are prepared:

- VRZf is defined with the exact same cuts as the SRs.
- VRZLdPhi is defined with the same cuts as the SR, but the cuts of $\Delta\phi(\mathrm{jet}_{1,2,(3)}, \vec{E}_{\mathrm{T}}^{\mathrm{miss}})_{\mathrm{min}}$ and $\Delta\phi(\mathrm{jet}_{i>3}, \vec{E}_{\mathrm{T}}^{\mathrm{miss}})_{\mathrm{min}}$ are loosened.
- VRZLBDT is defined with the same cuts as the SR, but the cut of BDT score is loosened.

***W*+jets and top validation region** Events of VRs for W+jets and top events (VRW and VRT) are the same as CRW and CRT but the requirements on the variables $\Delta\phi(\mathrm{jet}_{1,2,(3)}, \vec{E}_{\mathrm{T}}^{\mathrm{miss}})_{\mathrm{min}}$, $\Delta\phi(\mathrm{jet}_{i>3}, \vec{E}_{\mathrm{T}}^{\mathrm{miss}})_{\mathrm{min}}$ and BDT score are changed.

- VRWf, VRTf: In addition to the CRW and CRT selection criteria, the same cut values are used for $\Delta\phi(\mathrm{jet}_{1,2,(3)}, \vec{E}_{\mathrm{T}}^{\mathrm{miss}})_{\mathrm{min}}$ and $\Delta\phi(\mathrm{jet}_{i>3}, \vec{E}_{\mathrm{T}}^{\mathrm{miss}})_{\mathrm{min}}$ as SR.
- VRWLBDT, VRTLBDT use the same criteria as the CR, but cut on BDT score is loosened.

Diboson validation region There is no CR for the diboson background, but one VR is prepared as orthogonal region to SRs to check if the MC simulation can model the data well. For this purpose, the process of $W(\to\ell\nu)Z(\to\ell\ell)$ is used as VR, which is called VR3L. The events are selected by lowest unprescaled single lepton triggers and three leptons with $p_{\mathrm{T}}(\ell_1) > 27$ GeV, $p_{\mathrm{T}}(\ell_2) > 7$ GeV and $p_{\mathrm{T}}(\ell_3) > 7$ GeV are required. In order to enhance the purity of the event, the cuts about W boson and Z boson are required: invariant mass in the dilepton system with 66 GeV $< m_{\ell\ell} <$116 GeV and transverse mass with 30 GeV$< m_{\mathrm{T}} <$ 100 GeV and vetoing the b quark. In the VR3L, the transverse momentum of the leptons from the Z boson is added to the $E_{\mathrm{T}}^{\mathrm{miss}}$ vector. The lepton from the W boson is treated as a jet. The VR3L is defined as follows.

- VR3LBDT is defined with the same cuts as the SR, but cuts on BDT score are removed.

0 lepton validation region Unlike other VRs, a VR0L is prepared as orthogonal region to SRs in order to test all backgrounds in 0 lepton channel. Two VR0Ls are defined as follow.

- VR0Lmetmeff is defined with the same cuts as the SR, but the cut on $E_{\mathrm{T}}^{\mathrm{miss}}/m_{\mathrm{eff}}$ is inverted ($E_{\mathrm{T}}^{\mathrm{miss}}/m_{\mathrm{eff}}$ <0.2).
- VR0LdPhi is defined with the same cuts as the SR, but the cut on $\Delta\phi(\mathrm{jet}_{1,2,(3)}, \vec{E}_{\mathrm{T}}^{\mathrm{miss}})_{\mathrm{min}}$ is inverted ($\Delta\phi(\mathrm{jet}_{1,2,(3)}, \vec{E}_{\mathrm{T}}^{\mathrm{miss}})_{\mathrm{min}}$ <0.4).

Table 6.1 shows the list of selection criteria which is different from SR (Table 5.7). The selection of $\Delta\phi(\mathrm{jet}_{1,2,(3)}, \vec{E}_{\mathrm{T}}^{\mathrm{miss}})_{\mathrm{min}}$, $\Delta\phi(\mathrm{jet}_{i>3}, \vec{E}_{\mathrm{T}}^{\mathrm{miss}})_{\mathrm{min}}$, $E_{\mathrm{T}}^{\mathrm{miss}}/m_{\mathrm{eff}}$ and BDT score are changed, depending on the VRs. These results are discussed in Section 9.1. In VRXLBDT (X=Z,W,T,3), the BDT score cuts are loosened to obtain enough statistics.

Table 6.1: Summary of the validation regions for all the categories. The selection criteria which is different from SR is only listed. The selection criteria which is not listed is the same as SR.

$\Delta\phi(\mathrm{jet}_{1,2,(3)}, \vec{E}_{\mathrm{T}}^{\mathrm{miss}})_{\mathrm{min}}$	≥ 0.2 : VRXLdPhi (X=Z)
	< 0.4 : VR0LdPhi
$\Delta\phi(\mathrm{jet}_{i>3}, \vec{E}_{\mathrm{T}}^{\mathrm{miss}})_{\mathrm{min}}$	≥ 0.2 : VRXLdPhi (X=Z)
$E_{\mathrm{T}}^{\mathrm{miss}}/m_{\mathrm{eff}}$	< 0.2 : VR0Lmetmeff
Loosened BDT score	≥ 0.6 : VRXLBDT (X=Z,W,T) for GGd1-GGd4
	≥ 0.0 : VRXLBDT (X=Z,W,T) for GGo1
	≥ 0.2 : VRXLBDT (X=Z,W,T) for GGo2
	≥ 0.4 : VRXLBDT (X=Z,W,T) for GGo3
	≥ 0.5 : VRXLBDT (X=Z,W,T) for GGo4
	$\geq$-1.0 : VR3LBDT

7 BDT validation

The BDT score is not a quantity directly related to measurements, but an output value from a machine learning technique explained in Section 5.5. The BDT score is a useful variable to efficiently separate signal and background events. It is important to check carefully if the BDT score has the expected response in both data and MC samples. This chapter discusses several checks in order to validate the response.

7.1 Overtraining

If the statistics in the training sample is low or the number of the training parameters is large, BDT classifiers could extract the local information of the sample in the training. This is called overtraining. If the overtraining is observed, the BDT score cut for the testing sample is not optimal. Figure 7.1 shows the signal and background distributions for training and testing samples, respectively. Since a difference between the training and testing samples is observed in the signals, the optimal BDT score cuts would be different from training and testing samples. If two distributions are similar, the BDT score cut which is optimized to testing sample is optimal and thus "no overtraining" is very important.

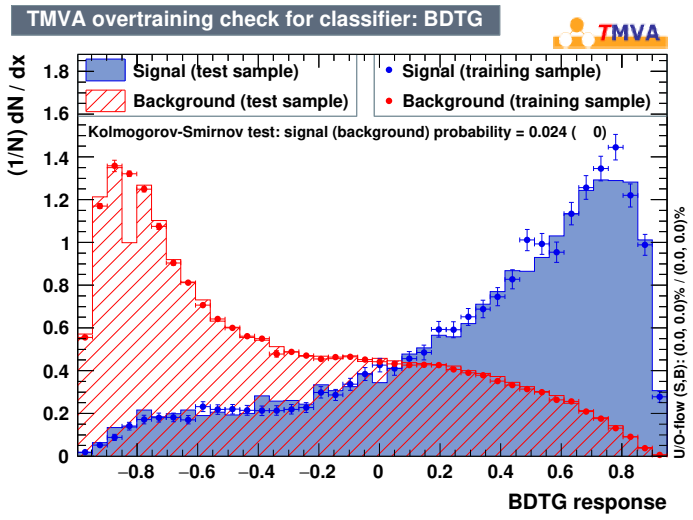

Figure 7.1: BDT score distribution for signals (blue) and backgrounds (red). The dot (filled) histograms are for the training (testing) samples [113]. Since a difference between the training and testing samples is observed in the signals, the different sensitivities are obtained when the same BDT score cut is applied.

In order to check the overtraining, the comparison of BDT score distribution between the training sample and testing sample in each SR is performed as shown in Figures 7.2. A ratio of training and testing samples is checked to quantify the level of a consistency between two distributions. For the background, the BDT score distributions in the training sample are similar to the testing sample because the ratio is almost 1 within the MC statistical uncertainty. For the signal, disagreement of BDT score distributions is appeared with low BDT score (< -0.5) due to the MC statistics in training sample. They are slightly affected by the overtraining. However, the optimal BDT score cut in the training sample is similar to the testing sample because there are following reason. As shown in Figures 7.2, these signals are almost have the positive BDT score and the ratio in the positive BDT score is almost 1. It means that the signal efficiency of testing sample is almost same as training sample until the BDT score cut is more than 0.0. In this analysis, all the regions only use the high BDT scores, so the optimal BDT score cut in the training sample is similar to testing sample.

From the check, the sensitivity of target signals are maximized by the optimized BDT score cuts as defined in Table 5.7.

7.2 Difference of two BDT score distribution

The training method illustrated in Figure 5.16 assumes that there are no differences between two BDT classifiers If the statistics in the training is large enough, both BDT score distributions should be statistically the same and the sensitivity is maximized. In order to validate this, the comparison of BDT score distributions between first- and second-half training samples is performed on signal and background components, respectively. The BDT score in the first-half sample shows good agreement with that in second-half sample for both signal and background components because the ratio of training and testing is almost 1 within the MC statistical uncertainty as shown in Figure 7.3.

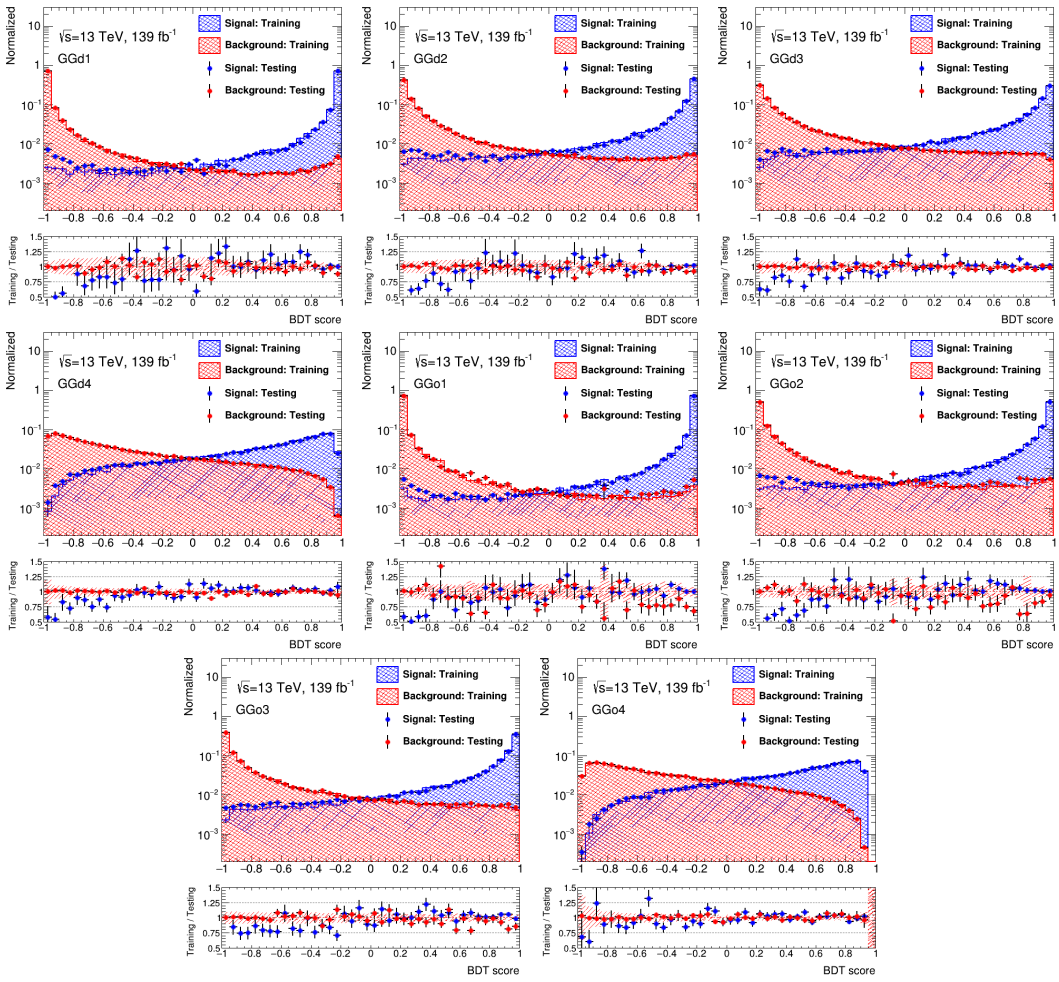

Figure 7.2: Normalized BDT score distributions between the signal (blue) and background (red) component. The histogram indicates the training sample and the dot point indicates the testing sample. The bottom panel is the ratio of the training and testing sample.

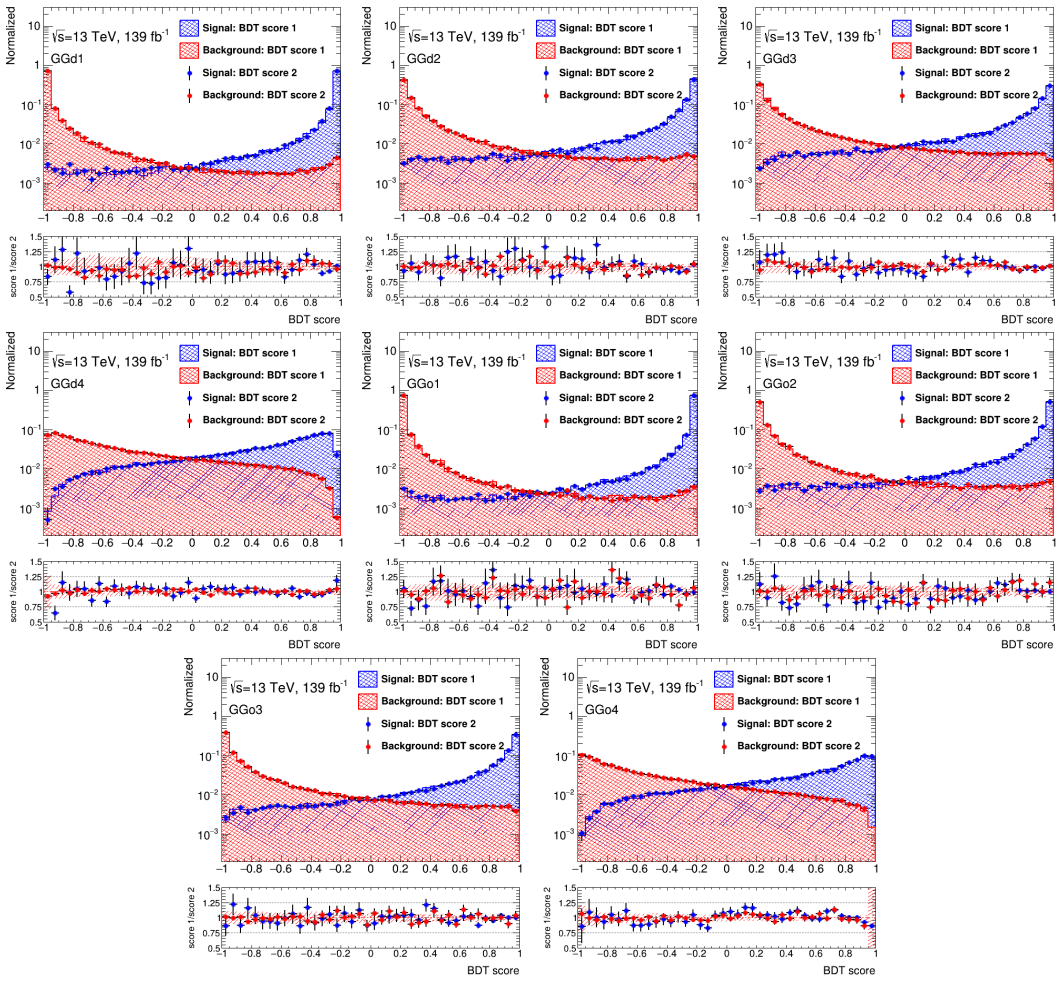

Figure 7.3: Normalized BDT score distributions in the signal (blue) and background (red) component. The histogram indicates the first-half sample and the dot point indicates the second-half sample. The bottom panel is the ratio of the first-half and second-half sample.

7.3 Correlation of input variables

The BDT scores are produced by taking into account the correlation of variables. Hence, the variable correlations in the MC samples need to be described by the data in order to use BDT scores build by MC simulation to data. Additionally, since the normalization factors calculated in CRs is applied to SRs, the correlations in CRs should have similar tendencies as SRs.

In order to check them, the correlation coefficient values are calculated for the input variables. The correlation coefficients of two variables, x, y are defined as:

$$\mathrm{corr}(x,y)_i = \frac{(x_i - \langle x \rangle) \cdot (y_i - \langle y \rangle)}{\sigma_x \sigma_y} \tag{7.1}$$

$$\langle x \rangle = \frac{\sum_i^N x_i}{N}, \quad \langle y \rangle = \frac{\sum_i^N y_i}{N} \tag{7.2}$$

$$\sigma_x = \sqrt{\frac{1}{N}\sum_i^N {x_i}^2}, \quad \sigma_y = \sqrt{\frac{1}{N}\sum_i^N {y_i}^2} \tag{7.3}$$

where N is the total number of events, $\langle x \rangle, \langle y \rangle$ are the mean of the variable and σ_x, σ_y are the RMS. If two variables are uncorrelated, the distribution of correlation coefficient becomes a gaussian distribution centered at zero. This distribution would be distorted if there is the correlation of two variables. The features of the correlations can be extracted from the distribution. Figures 7.4-7.5 show the distributions of correlation coefficients between m_{eff} and leading jet p_{T} for SRs. Since m_{eff} is defined as Eq. 5.1, they are positively correlated so that the positive tails in the distribution are observed. Good agreement of data and MC samples is observed within the MC statistical uncertainty. Figures 7.6 show the mean of the distributions of correlation coefficients as a matrix ($\langle \mathrm{corr}(x,y)_i \rangle$) for the signals, MC samples and data in GGd1 SR. Compared to the signals and SM backgrounds, the clear difference between the leading jet p_{T} and subleading jet p_{T} (0.49 for signals and 0.24 for SM backgrounds) as explained in Section 5.4. The matrix of the data has similar tendency. Figure 7.7 shows the difference of correlation coefficients between the data and MC samples and The value corresponds to the difference. All the correlations in MC samples show agreement with those of the data within 10% level and all correlations are modeled well by MC samples The similar tendencies are also observed in CRY, CRW and CRT as shown in Figures 7.8.

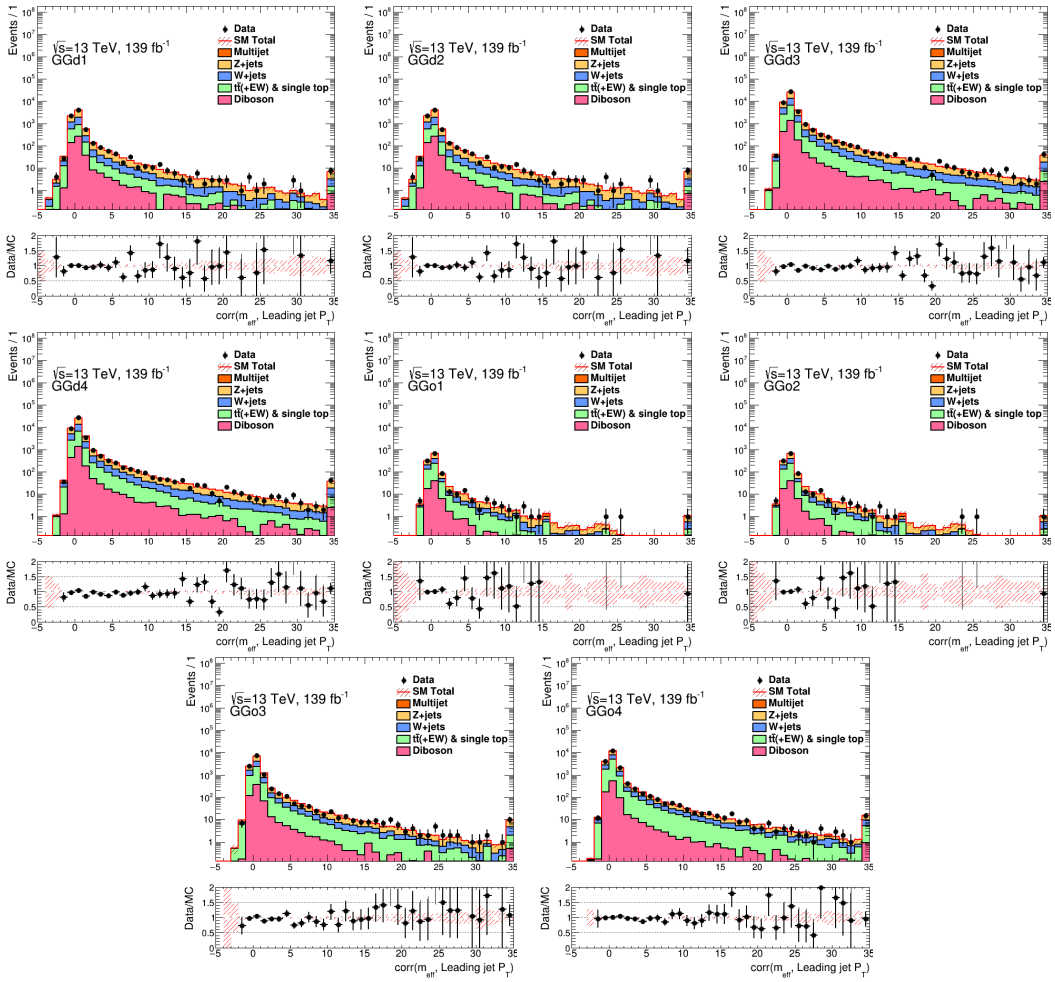

Figure 7.4: Correlation coefficients of m_{eff} and leading jet p_{T} with the selection criteria in all SRs except BDT score cut. All MC samples are normalized to the data of 139 fb^{-1}. The last bin includes the overflow. The bottom panel is the ratio of the data and the MC simulation. The black error bar is statistical uncertainty in the data. The hatched red error bands indicate MC statistical uncertainties.

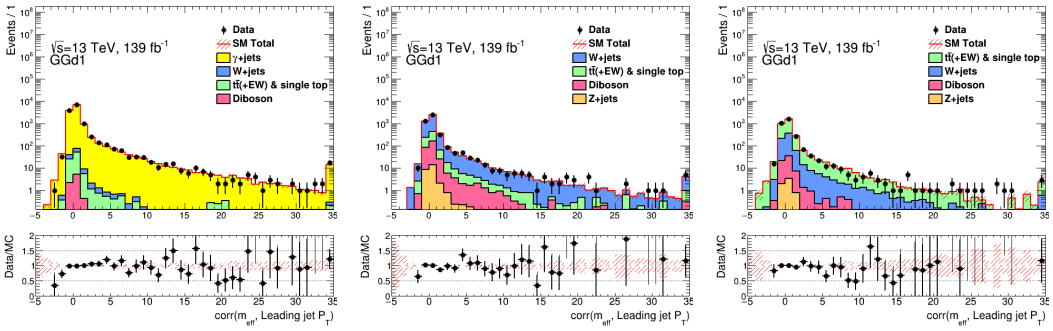

Figure 7.5: Correlation coefficients of m_{eff} and leading jet p_{T} with the selection criteria in GGd1 CRY (left), CRW (center) and CRT (right) except BDT score cut. All MC samples are normalized to the data of 139 fb^{-1}. The last bin includes the overflow. The bottom panel is the ratio of the data and the MC simulation. The black error bar is statistical uncertainty in the data. The hatched red error bands indicate MC statistical uncertainties.

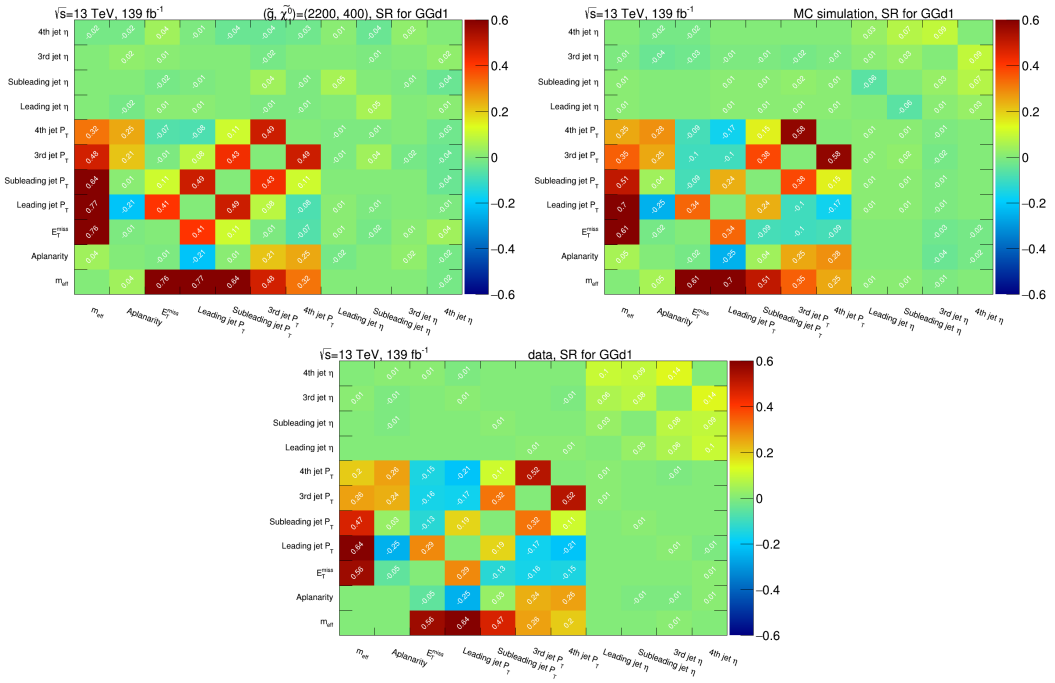

Figure 7.6: Matrix of all correlations in gluino direct decay signals with ($m_{\tilde{g}}$,$m_{\tilde{\chi}_1^0}$)=(2000, 400) (top-left), MC samples (top-right) and data (bottom) applying the selection criteria in GGd1 SR without BDT score cut. The value corresponds to the mean of each correlation coefficient. The x- and y-axes indicate input variables.

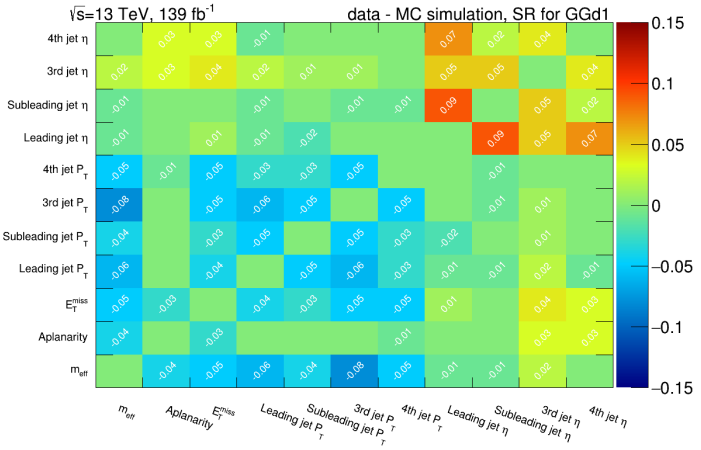

Figure 7.7: Matrix of the difference of the mean correlation coefficients between the data and MC samples applying the selection criteria in GGd1 SR without BDT score cut. The value corresponds to the difference of each correlation coefficient between the data and MC simulation. The x- and y-axes indicate input variables.

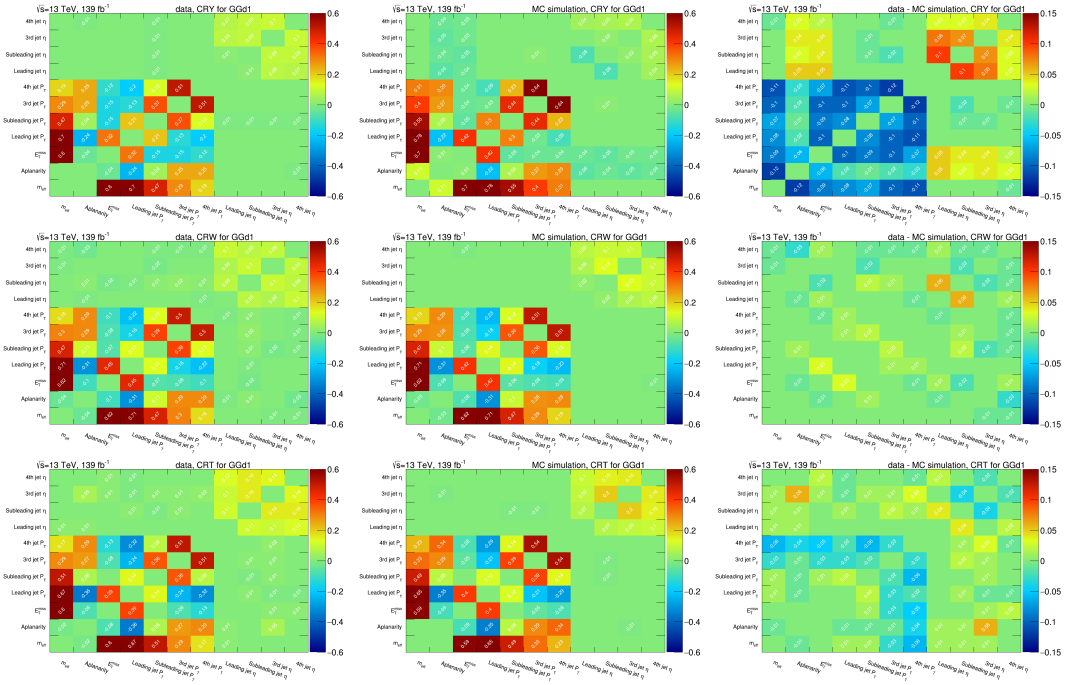

Figure 7.8: Matrix of all correlations in data (left) and MC simulation (center) for GGd1 CRY (top), CRW (center) and CRT (bottom) without BDT score cut. The value corresponds to the mean of each correlation coefficient. The difference of the correlation coefficient between the data and MC simulation is shown in the right figures. The x- and y-axes indicate input variables.

7.4 Profile distribution in BDT score

As discussed in Section 7.3, the correlations of input variables are modeled by MC simulation. If the BDT classifier utilizes these correlations in the separation between signal and background, the produced BDT scores should have the expected dependence of input variables. For example, BDT score should become larger as the effective mass is larger if the feature of signals is extracted correctly. For this purpose, the dependence on each input variable to the BDT score is checked by calculating the mean value of input variables per BDT score bin (profile). Figures 7.9 show profile distributions for the effective mass. It is observed that the effective mass is larger as the BDT score is larger. Since the effective mass of the signals is large as discussed in Section 5.4, the signals can be survived with the tight BDT score cuts. It implies that the signals remain in SRs even though the signals are different from the training samples. Additionally, an agreement of the profile distribution between the data and MC simulation is observed within 10% in SR, CRY and CRW as shown in Figures 7.9 and 7.10. Since there is the mismodeling on the $t\bar{t}$ background, an agreement within 15% in CRT is observed. The behavior of the BDT score distributions are well modeled.

7.5 Summary of BDT validation

Three validations discussed in this Chapter are summarized.

- **Overtraining**: The produced BDT scores are not biased as shown in Figures 7.2 and 7.3 and the cuts on BDT score in the Table 5.7 are optimal cuts, which allows the sensitivity of the target signals to maximize.
- **Correlation of input variables**: The correlation of input variables in the MC samples, which the BDT classifier takes into account, is described by the data within 10% level as shown in Figures 7.4-7.8. It implies that the BDT scores are the well-understood variables.
- **Profile distribution in BDT score**: The produced BDT scores have the expected behavior as shown in Figures 7.9 and 7.10. The effective mass is larger as the BDT scores are larger and signals having large effective mass are selected. It means that even if the properties of events are different from the signals used as training sample, the BDT scores can catch the events up to large effective mass is large. Hence, the search for the general signal like events having large effective mass can be performed.

It has been proved that the BDT classifiers are applicable to both data and MC samples from these results. In addition to the method of designing CRs as discussed in Section 6.2, the background estimation using the machine learning has been established in gluino search. It is the important and unique point in this thesis. Based on the framework, the first preliminary result of the gluino search using the machine learning was published from ATLAS[1], which is shown in next chapter.

[1] It is the preliminary results in a public note of the ATLAS Collaboration, prepared for conferences in 2019. It will be submitted to a journal in early 2020.

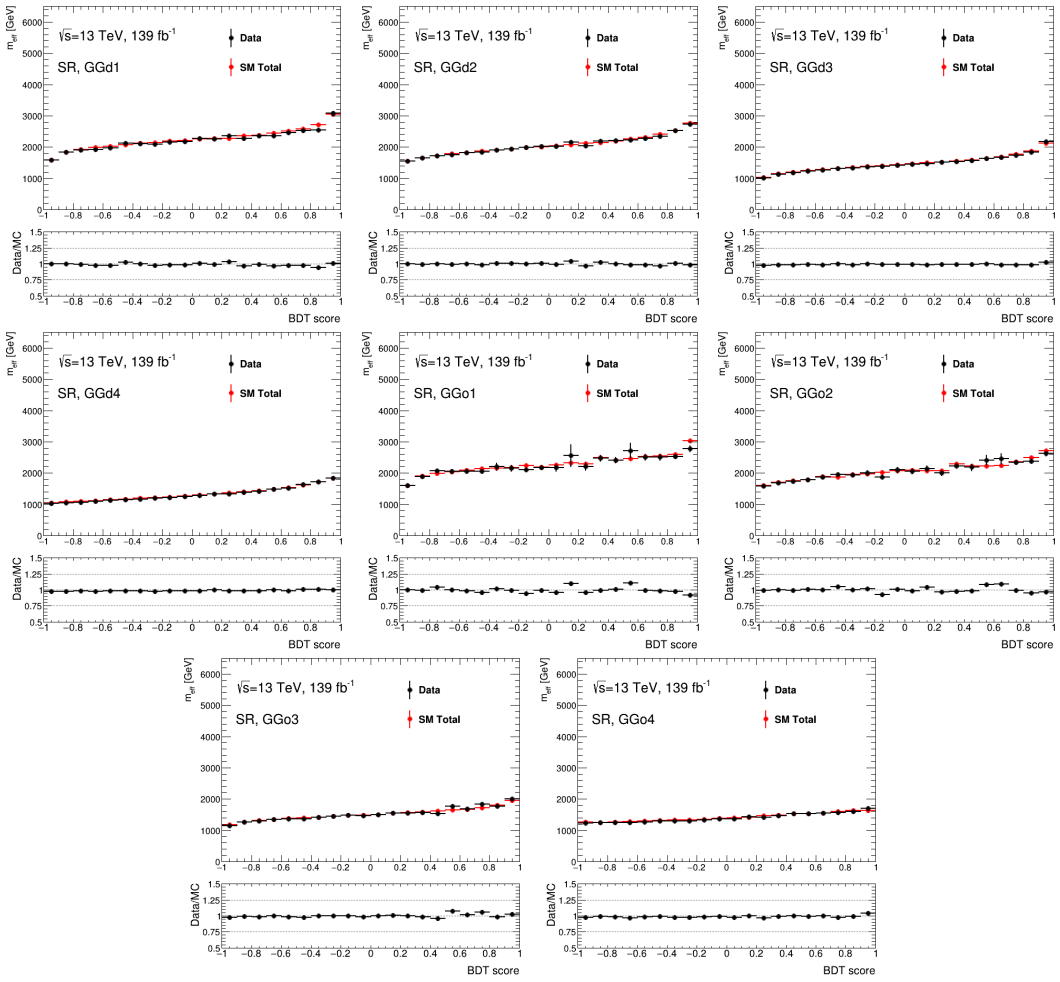

Figure 7.9: Average of m_{eff} value in each BDT score bin in all SRs without BDT score cut. The black dot indicates the data and the red dot indicates the MC simulation. The bottom panel is the ratio of the data and the MC simulation.

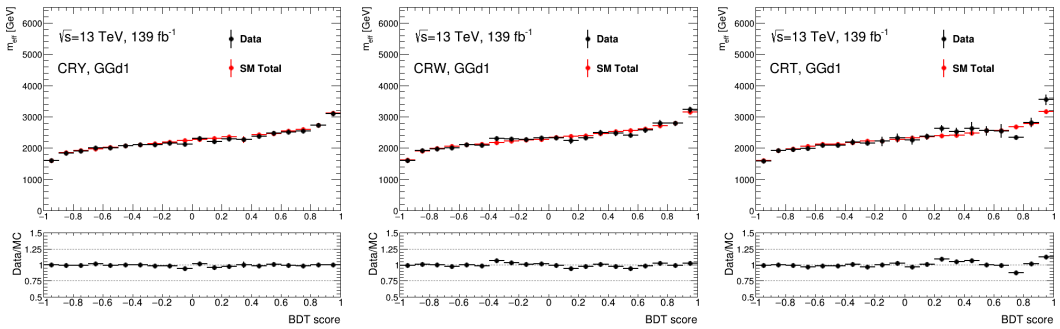

Figure 7.10: Average of m_{eff} value in each BDT score bin for GGd1 CRY (left), CRW (center) and CRT (right). The black dot indicates the data and the red dot indicates the MC simulation. The bottom panel is the ratio of the data and the MC simulation.

8 Statistical analysis

A fit to estimate the expected number of events in the SR is performed under a given hypothesis using a profile Log Likelihood Ratio (LLR) approach. The profile LLR is computed a SR and a set of CRs in three kind of fits: background only fit, model-dependent fit and model-independent fit [117]. This chapter describes the definition of the likelihood function and the treatment of systematic uncertainties.

8.1 Likelihood function

The likelihood function is defined as a product of Poisson probability density for SR, and all considered CRs and the Gaussian probability density for the systematic uncertainties:

$$L(\boldsymbol{n}|\boldsymbol{\mu}, \boldsymbol{s}, \boldsymbol{b}, \boldsymbol{\theta}) \quad = \quad P_{\mathrm{SR}} \times P_{\mathrm{CRW}} \times P_{\mathrm{CRT}} \times P_{\mathrm{CRY}} \times C_{\mathrm{Syst}} \tag{8.1}$$

where P_{SR}, P_{CRY}, P_{CRW} and P_{CRT} are Poisson probability distributions in each region. C_{Syst} is the product of Gaussian probability distributions of systematic uncertainties. Each Poisson probability density distribution P_i uses the observed number of events n_i and the expected number of events λ_i in a given region:

$$P_k = P(n_k|\lambda_k) = \frac{\lambda_k^{n_k}}{n_k!} e^{-\lambda_k} \tag{8.2}$$

The λ_k is expressed as:

$$\lambda_k(\boldsymbol{\mu}, s_k, \mathbf{b}, \boldsymbol{\theta}) \quad = \quad s_k(\boldsymbol{\theta}) \cdot \mu_s + (\sum_j b_{k,j}(\boldsymbol{\theta}) \cdot \mu_j) + b_{k,\text{Diboson}}(\boldsymbol{\theta}) + b_{k,\text{Multi-jet}}(\boldsymbol{\theta}) \tag{8.3}$$

where each parameter is defined as followings:

- k refers to a region (SR, CRY, CRW, CRT).
- j refers to a physics process (Z+jets, W+jets or Top).
- s_k is the expected number of signal events from MC simulation in a region k.
- $b_{k,j}$ is the expected number of background events of physics process j from MC simulation in a region k.
- $b_{k,\text{Diboson}}$ is the expected number of background events of diboson process from MC simulation, which does not have a dedicated CR.
- $b_{k,\text{Multi-jet}}$ is the expected number of background events of multi-jet process from MC simulation, which does not have a dedicated CR.

- μ_s is the free normalization factor of a signal process and called signal strength.
- μ_j is the free normalization factor of a background process j. These are set to the normalization factors calculated from each CR: $N_{\text{data,CR}}/N_{\text{MC,CR}}$
- $\boldsymbol{\theta}$ is a set of the nuisance parameters, which parametrizes systematic uncertainties.

The systematic uncertainties C_{syst} is expressed as:

$$C_{\text{syst}} = \prod_{i \in \text{SU}} G(\theta_i) \tag{8.4}$$

where SU is a set of systematic uncertainties and G is the standard gaussian probability with the nuisance parameter θ_i. The mean of standard deviation of all probability density distributions is set to 0 and thus $\theta = +1$ ($\theta = -1$) corresponds to $+1\sigma$ (-1σ) variations. Since $\boldsymbol{s}$ and $\boldsymbol{b}$ are a function of $\boldsymbol{\theta}$, the likelihood function is denoted as $L(\mu, \boldsymbol{\theta})$ from next section.

8.2 Hypothesis test

The profile likelihood ratio [118] is defined as:

$$\text{LLR}(\mu_s) = \frac{L(\boldsymbol{n}|\mu_s, \hat{\hat{\boldsymbol{\theta}}})}{L(\boldsymbol{n}|\hat{\mu}_s, \hat{\boldsymbol{\theta}})} \tag{8.5}$$

where $L(\boldsymbol{n}|\mu_s, \hat{\hat{\boldsymbol{\theta}}})$ is the maximized likelihood function for a given parameter μ_s (conditional maximum-likelihood function). $\hat{\hat{\boldsymbol{\theta}}}$ corresponds to $\boldsymbol{\theta}$ for the conditional maximum-likelihood function. On the other hand, $L(\boldsymbol{n}|\hat{\mu}_s, \hat{\boldsymbol{\theta}})$ is the maximized likelihood function (unconditional maximum-likelihood function). The parameters of ($\hat{\mu}_s$, $\hat{\boldsymbol{\theta}}$) correspond to the parameters of (μ_s, $\boldsymbol{\theta}$) for the unconditional maximum-likelihood function.

A test statistics q_{μ_s} [118] is defined as

$$q_{\mu_s} = -2\log(\text{LLR}(\mu_s)) = \begin{cases} -2\log(\text{LLR}(\mu_s)) = -2\log\frac{L(\mu_s, \hat{\hat{\boldsymbol{\theta}}})}{L(\hat{\mu}_s, \hat{\boldsymbol{\theta}})} & \mu_s \geq \hat{\mu}_s \\ 0 & 0 < \mu_s < \hat{\mu}_s \end{cases} \tag{8.6}$$

Then, a p-value is defined as

$$p_{\mu_s} = \int_{q_{\mu_s,\text{obs}}}^{\infty} f(q_{\mu_s}|\mu_s) dq_{\mu_s} \tag{8.7}$$

where $q_{\mu_s,\text{obs}}$ is the observed value q_{μ_s} and $f(q_{\mu_s}|\mu_s)$ is the probability density function of the q_{μ_s} under the signal strength μ_s [118]. The probability density function is defined as

$$f(q_{\mu_s}|\mu_s) = \frac{1}{2\sqrt{q_{\mu_s}}} \frac{1}{\sqrt{2\pi}} \left[\exp\left\{ -\frac{1}{2}(\sqrt{q_{\mu_s}} + \frac{\mu_s - \hat{\mu}_s}{\sigma})^2 \right\} + \exp\left\{ -\frac{1}{2}(\sqrt{q_{\mu}} - \frac{\mu_s - \hat{\mu}_s}{\sigma})^2 \right\} \right] \tag{8.8}$$

where σ is the standard deviation of $\hat{\mu}_s$ [118]. Under the assumption of the signal plus background case, the probability density function is obtained with $\mu_s = 1$: $f(q_{\mu_s}|\mu_s = 1)$. On the other hand,

under the assumption of the background only case, the probability density function is obtained with $\mu_s = 0$: $f(q_{\mu_s}|\mu_s = 0)$.

In order to claim the exclusion of a signal hypothesis, CL_{s+b}, CL_b and CL_s, which are defined as below, are used [119].

$$CL_{s+b} = \int_{q_{\mu,\mathrm{obs}}}^{\infty} f(q_\mu|\mu_s = 1)dq_\mu = p_1 \tag{8.9}$$

$$CL_b = \int_{q_{\mu,\mathrm{obs}}}^{\infty} f(q_\mu|\mu_s = 0)dq_\mu = p_0 \tag{8.10}$$

$$CL_s = \frac{p_1}{p_0} \tag{8.11}$$

When a CL_s value is less than 0.05, its signal hypothesis is considered to be excluded at the 95% confidence level.

In this analysis, the fit without the contribution of signal process is first performed to obtain the number of background events in SRs: the fit with the signal strength $\mu_s = 0$ is performed. This fit is called background-only fit. Then, when there is no excess in SRs over the number of predicted background events, the model-independent and model-dependent fits are performed. The aim of the model-independent fit is to set upper limits on the number of the events Beyond Standard Model (BSM event) in SRs using asymptotic formulae [118]. The fit is performed in SR and CRs simultaneously. Under the fit condition, the p-value defined in Eq. 8.7 is calculated, varying the signal strength. Then, the number of expected signal events and observed signal events on the p-value at 0.05 is interpreted. They are called S^{95}_{exp} and S^{95}_{obs}. The visible cross section ($\langle\epsilon\sigma\rangle^{95}_{obs}$) which is defined Eq. 8.12 is also calculated [119].

$$\langle\epsilon\sigma^{95}_{obs}\rangle = \frac{S^{95}_{obs}}{\int Ldt} \tag{8.12}$$

The aim of the model-dependent fit is to set upper limits for the dedicated signal models at the 95% confidence level [118]. The fit is performed in SR and CRs simultaneously like model-independent fit. Under the fit condition, the CL_s value defined in Eq. 8.11 is calculated at the fixed signal strength $\mu_s = 1.0$ for all signal points. Then, the upper limit on the CL_s value at 0.05 is evaluated. These results are discussed in Section 9.2 and 9.3.

8.3 Systematic uncertainty

There are four types of systematic uncertainties in background prediction: experimental uncertainty, theoretical uncertainty, MC statistical uncertainty and CR statistical uncertainty. In addition, the SUSY signal uncertainties are considered. The details of all the uncertainties are explained in this section.

8.3.1 Experimental uncertainty

The following experimental uncertainties are considered.

Jet As discussed in Section 4.2, the uncertainties in JES calibration are assigned on the jet energy scale and resolution [100]. More than 100 independent uncertainties are prepared, but the uncertainties with the similar behavior can be combined [100]. This analysis takes 20 nuisance parameters. Since this analysis focuses on the kinematic edge of jets, the shift of the jet energy would become large effect in all SRs. The uncertainty of JES calibration is the most dominant in all experimental uncertainties.

$E_{\mathrm{T}}^{\mathrm{miss}}$ soft term As discussed in Section 4.5, the scale and resolutions of the objects are propagated to the soft term in the missing transverse momentum. Hence, the uncertainties of the energy scale and resolution with the soft term in the missing transverse momentum are considered [109].

Lepton, photon and *b*-tagging The uncertainties of calibration and identification of electrons, muons and photons and the efficiency correction of the *b*-tagging algorithm are assigned [104–108]. Since the effect of these objects is not sensitive in the SRs, these uncertainties are small in this analysis.

Luminosity The uncertainty in the combined 2015–2018 integrated luminosity is 1.7 % [55], obtained using the LUCID-2 detector [45] for the primary luminosity measurements.

Pileup Reweight As discussed in Section 3.3, the up-type (down-type) scale factor is 1/1.07 (1/0.99). If the scale factor is varied from down-type to up-type scale factor, the impact on the event yield is assigned as the systematic uncertainties. Since this analysis requires the large jet p_{T} and missing transverse momentum, the effect of the pileup is relative small. It means that this analysis is not sensitive for the pileup and the systematic uncertainty is negligible level.

When these systematic sources are varied, the difference of background events from the nominal is evaluated. The systematic uncertainties are calculated to cover the difference. The evaluated relative uncertainties of each experimental uncertainty on the background prediction are summarized in Figure 8.1. The uncertainties related to jets are dominant in the experimental uncertainties and raise up to $\sim$ 15% for GGo1 region. The kinematic selection in GGo1 region is tightest in all regions and a shift in jet energy has the impact of the background prediction. The effects of uncertainties related to $E_{\mathrm{T}}^{\mathrm{miss}}$ soft terms and pileup reweight are a few percent level. The lepton, photon, *b*-tagging and luminosity uncertainties are negligible (<1%).

8.3.2 Theoretical uncertainty

The theoretical uncertainties of V+jets, top and diboson components are considered. There are CRs for the V+jets and top components and all the uncertainties are assigned on the transfer factors, which are $\mathrm{N}_{\mathrm{SR}}^{\mathrm{MC}}/\mathrm{N}_{\mathrm{CR}}^{\mathrm{MC}}$ in Eq. 6.1. For the diboson components, there is no dedicated CR, so the uncertainties were determined not only on shape, but also on the cross-section. The treatment of systematic uncertainties are based on Refs. [120, 121].

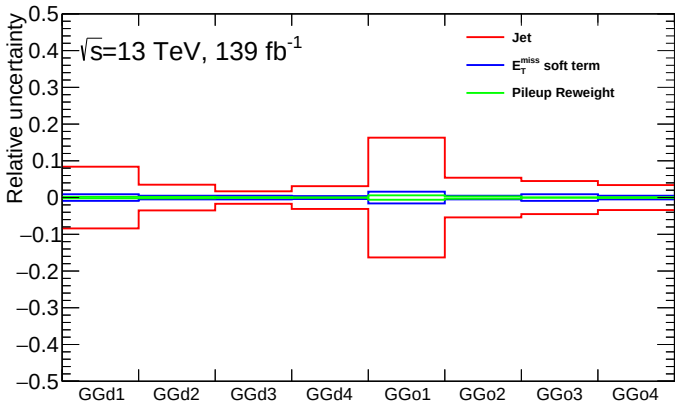

Figure 8.1: Calculated relative theoretical uncertainties on the background prediction for all the experimental uncertainties. The red line corresponds to the uncertainties related to jets and the blue line corresponds to the uncertainties related to $E_{\mathrm{T}}^{\mathrm{miss}}$ soft terms. The green line corresponds to pileup reweight uncertainty. The uncertainties of lepton, photon, b-tagging and luminosity are less than 0.01 and they are not displayed in the plot.

***V*+jets** Since the dominant background is V+jets component, the theoretical uncertainties of V+jets is crucial. The V+jets components are simulated using Sherpa 2.2.1 generator as shown in Table 3.4 and the scale variations are performed to evaluate systematic uncertainties. There are four considering scale variations for the used samples: renormalization, factorization, resummation (qsf) and CKKW[1] [65, 122]. In order to estimate these uncertainties, the impact on the shift of the envelope with respect to the nominal samples is evaluated as up-type and down-type. The renormalization, factorization and qsf scales in up-type (down-type) samples are four (one fourth) times as the nominal sample. The CKKW scale in nominal sample uses 20 GeV and it varies from 15 GeV (down-type variation) to 30 GeV (up-type variation). Next, the parton distribution function (PDF) and strong coupling constant (α_s) uncertainties are considered [120]. The PDF uncertainties are calculated using the corresponding error sets and taking the standard deviation. α_s uncertainties are estimated by using the same PDF set evaluated at different α_s values ($\alpha_s^{\mathrm{up}} = 0.119$, $\alpha_s^{\mathrm{down}} = 0.117$).

The evaluated relative uncertainties of V+jets on the background prediction are summarized in Figures 8.2. The dominant theoretical uncertainty is the scale variation and it typically varies from 2% to 10%, depending on the region. If the region with softer kinematic cuts, the PDF and α_s uncertainties are negligible, but they raise up to 4% for tight kinematic region (GGo1).

Diboson The diboson process is also simulated using Sherpa 2.2.1 generator as shown in Table 3.4 and the scale variations are considered as similar approach as V+jet samples. The evaluated relative uncertainties on the background estimation are summarized in Figure 8.3. The dominant uncertainty in the scale uncertainties is the renormalization and factorization scale variations. They raise up to $\sim$ 30% for GGd4 region.

[1] CKKW indicates the boundary of transverse momentum between tree-level matrix elements and parton showers.

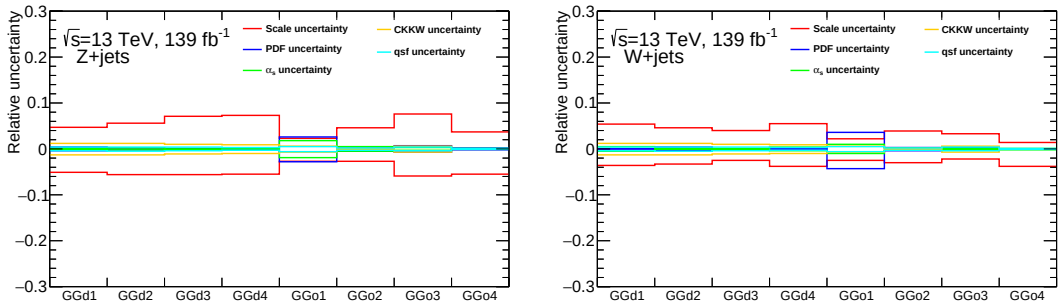

Figure 8.2: Calculated relative theoretical uncertainties on the background prediction for Z+jets samples (left) and for W+jets samples (right). The red line corresponds to renormalization, factorization scale uncertainties and the blue line corresponds to PDF uncertainties. The green line corresponds to α_s uncertainties, the orange line corresponds to CKKW uncertainties and the pink line corresponds to resummation (qsf) uncertainties.

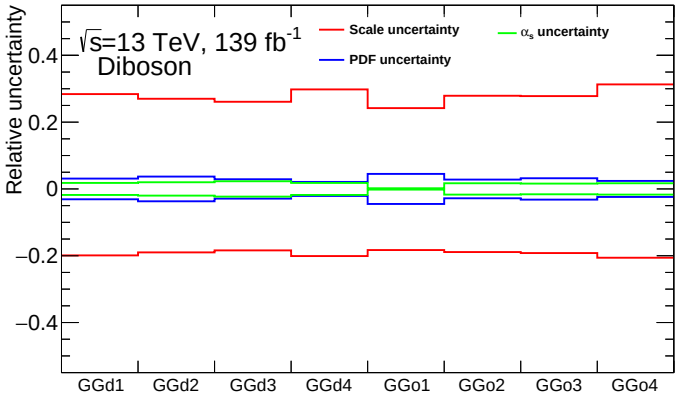

Figure 8.3: Calculated relative theoretical uncertainties on the background prediction for diboson samples. The red line corresponds to renormalization, factorization scale uncertainties, the blue line corresponds to PDF uncertainties and the green line corresponds to α_s uncertainties.

Top As discussed in Section 6.1, the dominant process in the production which includes top quarks is $t\bar{t}$ production. Hence, the uncertainties of $t\bar{t}$ sample are only considered. The modelling of the $t\bar{t}$ process is difficult and known problem [116], so the difference of generated by an alternative generators, which have different calculation of matrix elements is assigned as theoretical uncertainty. The nominal $t\bar{t}$ sample is simulated using Powheg-box and the following uncertainties are evaluated:

- Hard Scatter: difference between Powheg-box+Pythia8 and MC@NLO+Pythia8 [82].
- Hadronization, showring: difference between Powheg-box+Herwig7 [123] and Powheg-box+Pythia8.
- Radiation: difference between Powheg-box + Pythia8 and Powheg-box + Pythia8 with different shower parameters.
  - Radiation up (RadHigh): the renormalisation and factorisation scales by 0.5 and at the same time varying the Pythia8 parameter.
  - Radiation down (RadLow): the renormalisation and factorication scales by 2 and at the same time varying the Pythia8 parameter.

The evaluated relative systematic uncertainties on the background prediction are summarized in Figure 8.4. The m_{eff} distribution in MC@NLO generator is significantly softer than in the Powheg-box generator, so the hard scatter uncertainty is large when the target $\Delta m(\tilde{g}, \tilde{\chi}_1^0)$ is large. The systematic uncertainty is very large for applying the tight kinematic selection cut such as GGd1, GGd2, GGo1 and GGo2.

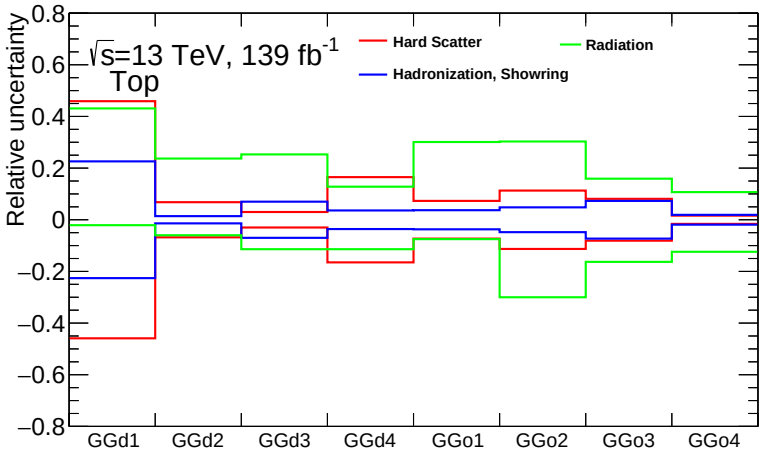

Figure 8.4: Calculated relative theoretical uncertainties on the background prediction for $t\bar{t}$ samples. The red line corresponds to hard scatter uncertainty, the blue line corresponds to hadronization, showering uncertainties and the green corresponds to radiation uncertainty.

In addition, the visible difference between SR and CRT is considered as the systematic uncertainty as discussed in Section 6.5. In order to cover the difference, 50% uncertainty to top yield is considered for GGo1 and GGo2. Since the contribution of top events is relatively small for GGo1 and GGo2, this systematic uncertainty does not affect the total background yield.

Multi-jet As discussed in Section 6.1, the multi-jet process is negligible. In this analysis, 100% uncertainty to the multi-jet yield is considered. This is a conservative uncertainty from the validation region result discussed in Section 9.1.

8.3.3 MC statistical uncertainty

The MC statistical error to the MC events in all regions is considered. Since this analysis uses the MC samples and the kinematic edge of distributions due to tight cut, the MC statistical uncertainty is important source in systematic uncertainties.

8.3.4 CR statistical uncertainty

As discussed in Chapter 6, normalization factors are obtained from the observed data in the CRs. Since all fits are performed in SR and CRs simultaneously as explained in Section 8.2, the statistical errors in CR are considered as the uncertainties of normalization factors. Only the statistical errors in CRs are taken into account as their systematic uncertainties because of single-bin counting experiment. The uncertainties of the normalization factors are most dominant in most of SRs because the statistics is very low due to tight BDT score cut.

8.3.5 SUSY signal

The cross section uncertainty is estimated by changing the renormalization, factorization, PDF and the strong coupling constant. The fraction on the cross section is varied from $\sim$ 8.6% (for 600 GeV gluino mass) to $\sim$ 30% (for 2600 GeV gluino mass) [37]. Experimental uncertainties and MC statistical uncertainties are also estimated in the same way for the backgrounds, but they are less than a few percent.

8.3.6 Summary of systematic uncertainties

In this analysis, the nuisance parameters are treated as follow.

- Experimental uncertainties are correlated across the different regions (SR, CRY, CRW and CRT) and the different physics processes (V+jets, top, diboson and multi-jet).
- Theory uncertainties are correlated across the different regions but independent per process.
- MC statistical and CR statistical uncertainties are fully uncorrelated variables.

Figure 8.5 shows the breakdown of the relative systematic uncertainties on the background prediction. The dominant systematic uncertainty is the statistical uncertainty in CRs. The theoretical uncertainty of V+jets is subdominant. The dominant experimental uncertainty is the JES uncertainty. The values of relative systematic uncertainties for all types are shown in Table 8.1. These systematic uncertainties are used in both SRs and VRs.

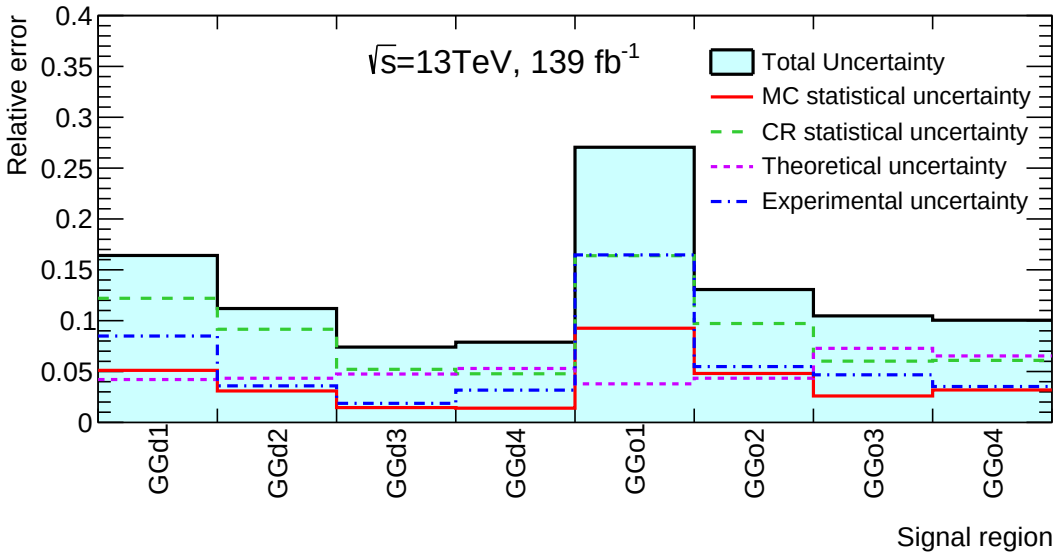

Figure 8.5: Breakdown of the relative systematic uncertainties on the background prediction. The individual uncertainties can be correlated so that the total background uncertainty is not necessarily their sum in quadrature.

Table 8.1: Relative systematic uncertainties on the background estimation.

SR	GGd1	GGd2	GGd3	GGd4	GGo1	GGo2	GGo3	GGo4
Experimental uncertainty [%]	8.5	3.6	1.9	3.2	16.5	5.5	4.7	3.5
Theoretical uncertainty [%]	4.2	4.3	4.8	5.3	3.8	4.3	7.3	6.5
MC statistical uncertainty [%]	5.1	3.1	1.5	1.4	9.3	4.9	2.6	3.2
CR statistical uncertainty [%]	12.2	9.2	5.2	4.8	16.4	9.7	6.0	6.1
Total statistical uncertainty [%]	16.4	11.2	7.4	7.9	27.1	13.1	10.5	10.0

9 Results

This chapter shows the results of the fit described in the previous Chapter and discusses the results in detail.

9.1 Results from background-only fit

The normalization factors determined in each CR of each background component from the background-only fit are shown in Figure 9.1. The normalization factors for top background (μ(Top)) are smaller than 1.0 in the SR with tight kinematic selection such as GGd1, GGd2, GGo1 or GGo2. Since there is the mismodelling of the jets at $t\bar{t}$ system as shown in Figure 6.23, the small normalization factors are expected. Since the MC simulation of V+jets samples is described well, the normalization factors for W+jets ($\mu(W)$) and Z+jets ($\mu(Z)$) are closer to 1.0.

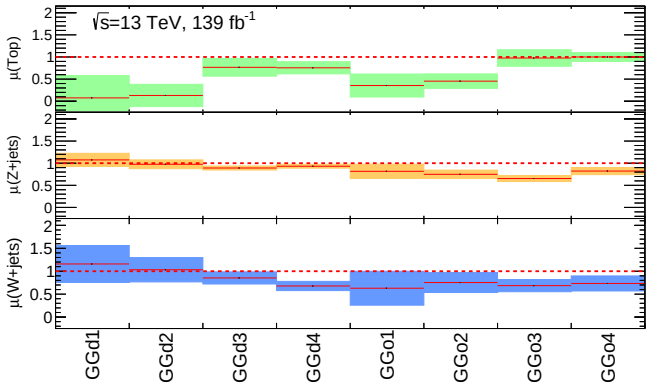

Figure 9.1: Fitted normalization factors per component for all the SRs. The vertical size of the colored region corresponds to the uncertainty of the normalization factor in each background component.

As discussed in Section 6.6, the number of the background events with background-only fit is tested by using VRs. In order to evaluate the difference between the prediction and observed data, the standard deviation (Z_n) is estimated from the p-value (p_0) defined as Eq. 8.11. Summary of the deviation in all the VRs are shown in Figure 9.2 and good agreement between the prediction and the data is observed within $Z_n < 2.0\sigma$. The comparison of the prediction and the data in each VR is shown in Figures 9.3-9.5. The background estimation discussed in Section 6.2 seems to have worked properly from these results, so all SRs were unblinded under these setup. Figure 9.6 shows the comparison of the prediction and the data in all SRs. The event yields are summarized in Tables 9.1-9.8. The MC

event yields ("MC exp.") in these Tables indicate the yields without the normalization factors (pre-fit yields) and the fitted event yields ("Fitted") indicate the yields with the normalization factors (post-fit yields). The contribution of the Z+jets component is dominant and followed by the W+jets and diboson component except GGo4. The contribution of the top background is negligible for GGd1, GGd2, GGo1 and GGo2 where the tight kinematic selections are applied and visible for GGd3, GGd4, GGo3 and GGo4 where the loose kinematic selections are applied. No significant excess over the background prediction is observed as shown in Figure 9.6 and Tables 9.1-9.8.

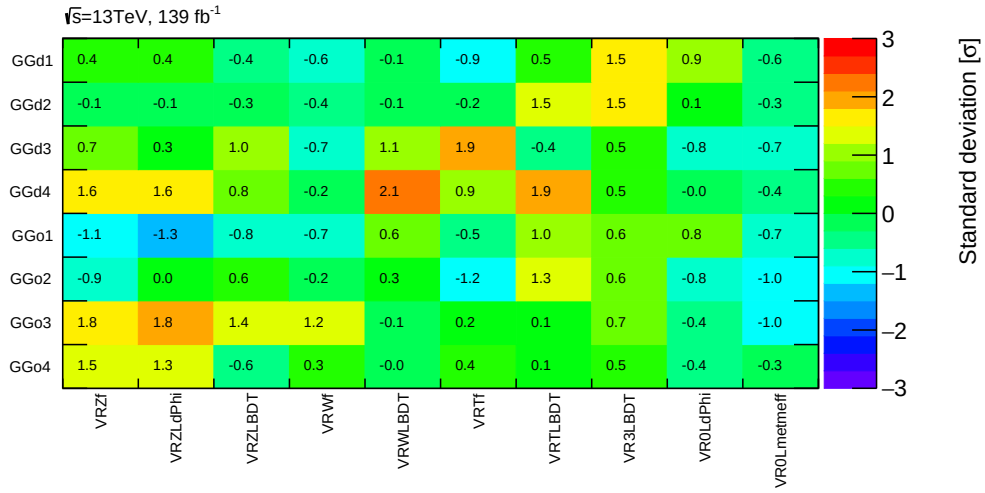

Figure 9.2: Summary of the standard deviation, which is calculated from the p-value in all the VRs (x-axis) for each SR (y-axis).

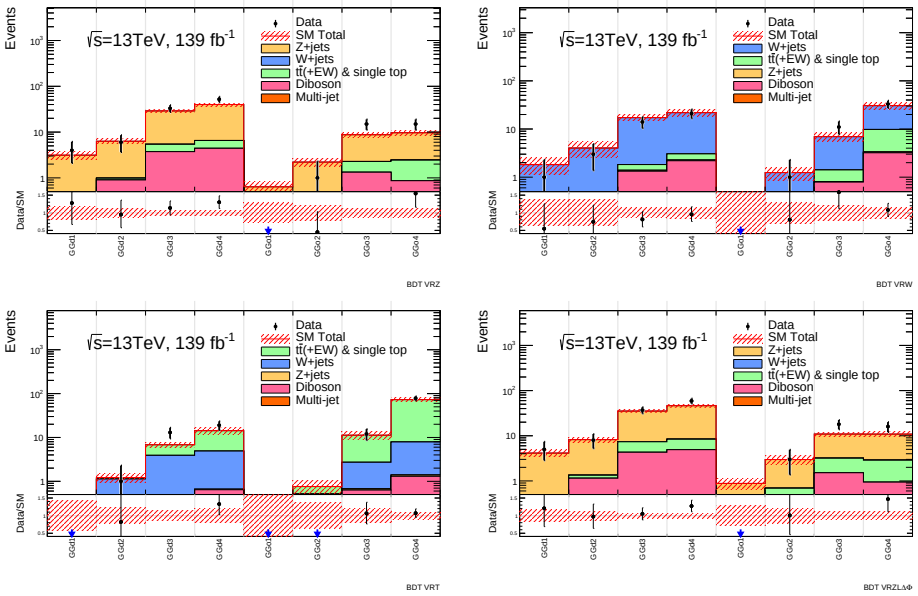

Figure 9.3: Comparison of the background prediction and observed data in VRZf (top-left), VRWf (top-right), VRTf (bottom-left) and VRZLdPhi (bottom-right) regions for each SR.

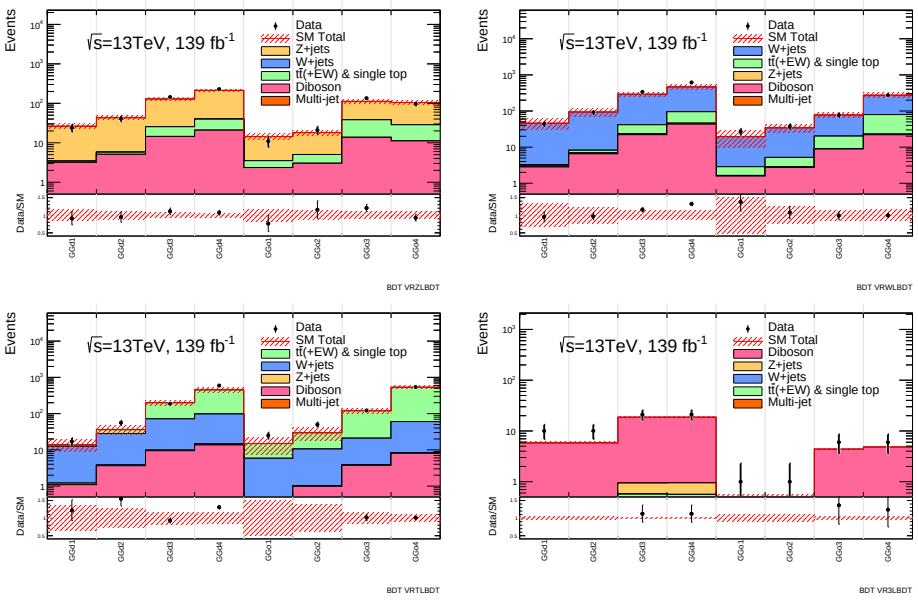

Figure 9.4: Comparison of the background prediction and observed data in VRZLBDT (top-left), VRWLBDT (top-right), VRTLBDT (bottom-left) and VR3LBDT (bottom-right) regions for each SR.

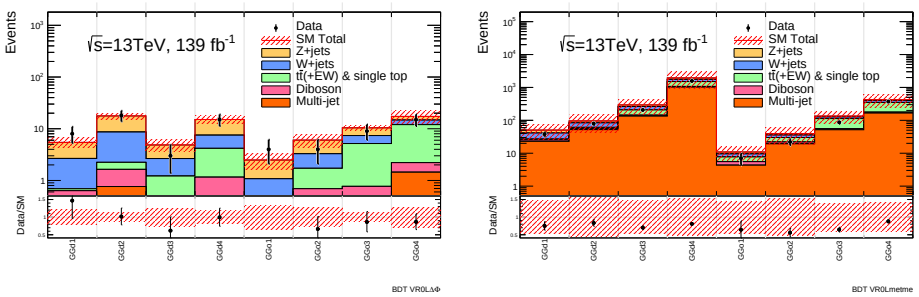

Figure 9.5: Comparison of the background prediction and observed data in VR0LdPhi (left), VR0Lmetmeff (right) regions for each SR.

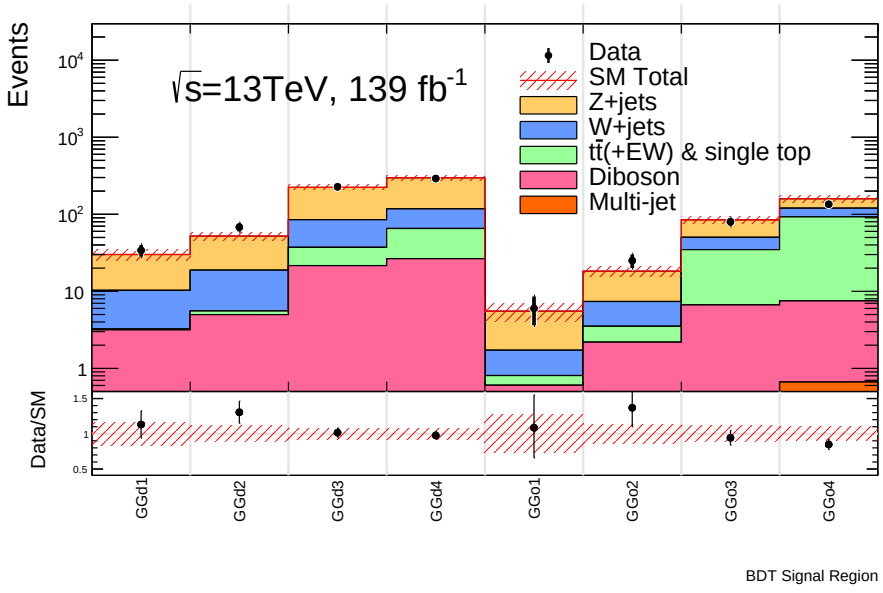

Figure 9.6: Comparison of the background prediction and observed data for all the SRs. The event yield for all the SRs are shown in Table 9.1-9.8.

Table 9.1: Observed and expected event yield in the GGd1 CRT, CRW, CRY and SR for an integrated luminosity of 139 fb^{-1}. The MC event yield ("MC exp.") indicates pre-fit yield and the the fitted event yield ("Fitted") indicates post-fit yield. The errors in the fitted event yield are the systematic uncertainties. For the MC event yield lower than 0.1, the yield is displayed as at 0.0±0.0.

GGd1	CRT	CRW	CRY	SR
Observed	4	13	62	34
Fitted	4.0 ± 1.6	13.0 ± 3.7	62.0 ± 7.9	30.0 ± 4.9
Fitted Multijets	0.0 ± 0.0	0.0 ± 0.0	0.0 ± 0.0	$0.1^{+0.1}_{-0.1}$
Fitted Wjets	3.4 ± 1.5	11.8 ± 3.9	0.6 ± 0.2	7.1 ± 2.6
Fitted Zjets	0.1 ± 0.0	0.0 ± 0.0	$0.0^{+0.0}_{-0.0}$	19.8 ± 3.8
Fitted GAMMAjets	0.0 ± 0.0	0.0 ± 0.0	61.3 ± 7.9	0.0 ± 0.0
Fitted Top	$0.5^{+1.9}_{-0.5}$	$0.1^{+0.5}_{-0.1}$	$0.1^{+0.2}_{-0.1}$	$0.1^{+0.3}_{-0.1}$
Fitted Diboson	$0.1^{+0.8}_{-0.1}$	1.0 ± 0.3	$0.0^{+0.0}_{-0.0}$	3.0 ± 0.9
MC exp.	9.6	13.0	58.4	28.6

Table 9.2: Observed and expected event yield in the GGd2 CRT, CRW, CRY and SR for an integrated luminosity of 139 fb^{-1}. The MC event yield ("MC exp.") indicates pre-fit yield and the the fitted event yield ("Fitted") indicates post-fit yield. The errors in the fitted event yield are the systematic uncertainties. For the MC event yield lower than 0.1, the yield is displaced as at 0.0±0.0.

GGd2	CRT	CRW	CRY	SR
Observed	8	24	110	68
Fitted	8.0 ± 2.2	24.0 ± 5.0	110.0 ± 10.5	52.1 ± 5.8
Fitted Multijets	0.0 ± 0.0	0.0 ± 0.0	0.0 ± 0.0	$0.0^{+0.0}_{-0.0}$
Fitted Wjets	5.8 ± 1.7	21.3 ± 5.3	0.7 ± 0.2	13.2 ± 3.6
Fitted Zjets	0.1 ± 0.0	0.1 ± 0.1	0.0 ± 0.0	33.3 ± 4.5
Fitted GAMMAjets	0.0 ± 0.0	0.0 ± 0.0	109.1 ± 10.5	0.0 ± 0.0
Fitted Top	$1.8^{+2.6}_{-1.8}$	$0.3^{+0.5}_{-0.3}$	$0.1^{+0.1}_{-0.1}$	$0.6^{+0.8}_{-0.6}$
Fitted Diboson	$0.3^{+0.3}_{-0.3}$	2.3 ± 1.1	0.1 ± 0.0	4.9 ± 1.4
MC exp.	19.9	25.4	113.4	56.3

Table 9.3: Observed and expected event yield in the GGd3 CRT, CRW, CRY and SR for an integrated luminosity of 139 fb^{-1}. The MC event yield ("MC exp.") indicates pre-fit yield and the the fitted event yield ("Fitted") indicates post-fit yield. The errors in the fitted event yield are the systematic uncertainties. For the MC event yield lower than 0.1, the yield is displayed as at 0.0±0.0.

GGd3	CRT	CRW	CRY	SR
Observed	48	78	458	227
Fitted	48.1 ± 6.9	78.0 ± 8.8	458.1 ± 21.4	223.4 ± 16.6
Fitted Multijets	0.0 ± 0.0	0.0 ± 0.0	0.0 ± 0.0	$0.1^{+0.1}_{-0.1}$
Fitted Wjets	15.2 ± 2.9	65.7 ± 9.7	2.1 ± 0.4	47.7 ± 7.8
Fitted Zjets	0.1 ± 0.0	0.3 ± 0.2	0.3 ± 0.0	138.5 ± 13.6
Fitted GAMMAjets	0.0 ± 0.0	0.0 ± 0.0	452.9 ± 21.4	0.0 ± 0.0
Fitted Top	31.0 ± 7.9	5.5 ± 2.0	2.6 ± 1.1	15.6 ± 5.2
Fitted Diboson	1.7 ± 1.1	6.4 ± 2.8	0.3 ± 0.0	21.4 ± 5.0
MC exp.	60.2	90.7	514.4	253.2

Table 9.4: Observed and expected event yield in the GGd4 CRT, CRW, CRY and SR for an integrated luminosity of 139 fb^{-1}. The MC event yield ("MC exp.") indicates pre-fit yield and the the fitted event yield ("Fitted") indicates post-fit yield. The errors in the fitted event yield are the systematic uncertainties. For the MC event yield lower than 0.1, the yield is displayed as at 0.0±0.0.

GGd4	CRT	CRW	CRY	SR
Observed	70	83	595	291
Fitted	70.2 ± 8.4	82.9 ± 9.1	594.9 ± 24.4	297.8 ± 23.5
Fitted Multijets	0.0 ± 0.0	0.0 ± 0.0	0.0 ± 0.0	$0.1^{+0.1}_{-0.1}$
Fitted Wjets	15.9 ± 3.0	67.5 ± 9.6	1.9 ± 0.4	52.0 ± 8.8
Fitted Zjets	0.3 ± 0.1	0.6 ± 0.1	0.6 ± 0.1	180.4 ± 17.7
Fitted GAMMAjets	0.0 ± 0.0	0.0 ± 0.0	586.6 ± 24.4	0.0 ± 0.0
Fitted Top	52.0 ± 9.2	7.3 ± 1.8	5.6 ± 1.9	38.9 ± 11.1
Fitted Diboson	2.0 ± 0.7	7.5 ± 0.7	$0.1^{+0.3}_{-0.1}$	26.4 ± 6.8
MC exp.	94.6	117.3	641.2	348.2

Table 9.5: Observed and expected event yield in the GGo1 CRT, CRW, CRY and SR for an integrated luminosity of 139 fb^{-1}. The MC event yield ("MC exp.") indicates pre-fit yield and the the fitted event yield ("Fitted") indicates post-fit yield. The errors in the fitted event yield are the systematic uncertainties. For the MC event yield lower than 0.1, the yield is displayed as at 0.0±0.0.

GGo1	CRT	CRW	CRY	SR
Observed	6	6	34	6
Fitted	6.0 ± 2.5	6.0 ± 2.5	34.0 ± 5.8	5.5 ± 1.5
Fitted Multijets	0.0 ± 0.0	0.0 ± 0.0	0.0 ± 0.0	$0.0^{+0.0}_{-0.0}$
Fitted Wjets	1.9 ± 1.2	4.9 ± 2.8	$0.1^{+0.1}_{-0.1}$	0.9 ± 0.5
Fitted Zjets	0.0 ± 0.0	0.0 ± 0.0	0.0 ± 0.0	3.8 ± 1.3
Fitted GAMMAjets	0.0 ± 0.0	0.0 ± 0.0	33.7 ± 5.8	0.0 ± 0.0
Fitted Top	3.9 ± 2.8	0.3 ± 0.2	$0.2^{+0.3}_{-0.2}$	0.2 ± 0.2
Fitted Diboson	0.2 ± 0.1	$0.7^{+1.1}_{-0.7}$	$0.0^{+0.0}_{-0.0}$	0.6 ± 0.2
MC exp.	14.2	9.4	42.0	7.3

Table 9.6: Observed and expected event yield in the GGo2 CRT, CRW, CRY and SR for an integrated luminosity of 139 fb^{-1}. The MC event yield ("MC exp.") indicates pre-fit yield and the the fitted event yield ("Fitted") indicates post-fit yield. The errors in the fitted event yield are the systematic uncertainties. For the MC event yield lower than 0.1, the yield is displayed as at 0.0±0.0.

GGo2	CRT	CRW	CRY	SR
Observed	22	21	74	25
Fitted	22.0 ± 4.7	21.0 ± 4.6	73.9 ± 8.6	18.3 ± 2.5
Fitted Multijets	0.0 ± 0.0	0.0 ± 0.0	0.0 ± 0.0	$0.0^{+0.0}_{-0.0}$
Fitted Wjets	6.6 ± 2.1	18.2 ± 5.2	0.3 ± 0.1	3.9 ± 1.3
Fitted Zjets	0.1 ± 0.0	0.1 ± 0.0	$0.0^{+0.0}_{-0.0}$	10.9 ± 1.9
Fitted GAMMAjets	0.0 ± 0.0	0.0 ± 0.0	72.4 ± 8.6	0.0 ± 0.0
Fitted Top	14.6 ± 5.2	1.2 ± 0.5	1.1 ± 0.5	1.3 ± 1.0
Fitted Diboson	0.6 ± 0.1	$1.5^{+1.8}_{-1.5}$	0.1 ± 0.0	2.2 ± 0.6
MC exp.	41.8	28.5	99.6	24.8

Table 9.7: Observed and expected event yield in the GGo3 CRT, CRW, CRY and SR for an integrated luminosity of 139 fb^{-1}. The MC event yield ("MC exp.") indicates pre-fit yield and the the fitted event yield ("Fitted") indicates post-fit yield. The errors in the fitted event yield are the systematic uncertainties. For the MC event yield lower than 0.1, the yield is displayed as at 0.0±0.0.

GGo3	CRT	CRW	CRY	SR
Observed	46	69	120	80
Fitted	46.0 ± 6.8	68.9 ± 8.3	120.0 ± 11.0	84.9 ± 9.6
Fitted Multijets	0.0 ± 0.0	0.0 ± 0.0	0.0 ± 0.0	$0.1^{+0.1}_{-0.1}$
Fitted Wjets	5.6 ± 1.3	49.7 ± 9.3	0.4 ± 0.1	15.5 ± 3.8
Fitted Zjets	0.1 ± 0.1	0.5 ± 0.1	0.1 ± 0.0	34.7 ± 5.5
Fitted GAMMAjets	0.0 ± 0.0	0.0 ± 0.0	116.8 ± 11.0	0.0 ± 0.0
Fitted Top	39.2 ± 7.2	13.8 ± 3.6	2.7 ± 1.1	28.1 ± 7.8
Fitted Diboson	1.2 ± 0.5	4.9 ± 1.4	$0.0^{+0.1}_{-0.0}$	6.6 ± 2.2
MC exp.	49.6	92.3	182.2	110.9

Table 9.8: Observed and expected event yield in the GGo4 CRT, CRW, CRY and SR for an integrated luminosity of 139 fb^{-1}. The MC event yield ("MC exp.") indicates pre-fit yield and the the fitted event yield ("Fitted") indicates post-fit yield. The errors in the fitted event yield are the systematic uncertainties. For the MC event yield lower than 0.1, the yield is displayed as at 0.0±0.0.

GGo4	CRT	CRW	CRY	SR
Observed	138	53	140	135
Fitted	138.0 ± 11.7	53.0 ± 7.3	140.0 ± 11.8	159.1 ± 16.0
Fitted Multijets	0.0 ± 0.0	0.0 ± 0.0	0.0 ± 0.0	$0.7^{+0.7}_{-0.7}$
Fitted Wjets	10.0 ± 2.9	36.0 ± 7.8	0.8 ± 0.6	27.4 ± 6.4
Fitted Zjets	0.1 ± 0.0	0.4 ± 0.2	0.1 ± 0.0	39.3 ± 6.9
Fitted GAMMAjets	0.0 ± 0.0	0.0 ± 0.0	135.0 ± 11.9	0.0 ± 0.0
Fitted Top	125.9 ± 12.4	12.3 ± 1.8	4.1 ± 0.7	84.9 ± 14.2
Fitted Diboson	2.0 ± 0.6	4.4 ± 1.3	$0.0^{+0.1}_{-0.0}$	6.8 ± 2.1
MC exp.	141.6	66.2	169.5	177.3

9.2 Model-independent fit

In order to set the upper limits on the number of BSM events, the model-independent fit, which is discussed in Section 8.2, is performed. Figures 9.7 show the p-value as a function of the signal strength μ_s with different probability density functions ($f(q_{\mu_s}|\mu_s = 0)$ and $f(q_{\mu_s}|\mu_s = 1)$) for GGd2 and GGo2, which have a small excess over the prediction. From these results, the upper limits at 95% confidence level on the number of events from BSM events for all SRs are calculated: S^{95}_{obs} and S^{95}_{exp}. The visible cross section defined in Eq. 8.12 is also calculated as shown in Table 9.9.

In all signal regions, no significant excess over the background prediction is observed from p_0 values and any indication of SUSY signal in final states with jets and missing transverse momentum cannot be found. The constraint of the target signal-like events which have multiple jets and large missing transverse momentum has been set.

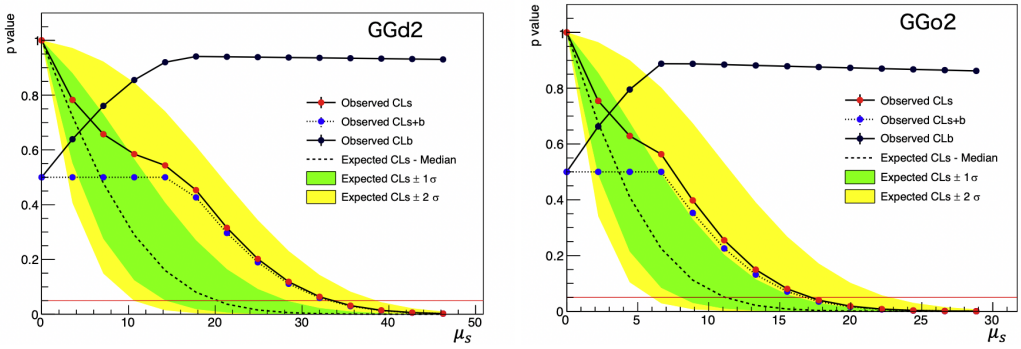

Figure 9.7: Expected and observed CL_s (red), CL_{s+b} (blue) and CL_b (black) as a function of the signal strength μ_s for GGd2 (left) and GGo2 (right). The expected CL_s value with $\pm 1\sigma$ (green band) and $\pm 2\sigma$ (yellow band) are overlaid. The red horizontal line indicates the value at 0.05.

Table 9.9: 95% CL upper limits on the visible cross section ($\langle\epsilon\sigma\rangle^{95}_{obs}$),the number of visible signal events (S^{95}_{obs}) and the number of expected signal event (S^{95}_{exp}) given the expected number of background events (and $\pm 1\sigma$ excursions of the expectation). The p-values (p_0) give the probabilities of the observations being consistent with the estimated backgrounds. For an observed number of events lower than expected, the p-value is displayed as at 0.5 in asymptotic calculation.

SR	GGd1	GGd2	GGd3	GGd4	GGo1	GGo2	GGo3	GGo4
p_0	0.30	0.05	0.44	0.50	0.43	0.12	0.50	0.50
S^{95}_{obs}	18	34	46	50	7	17	23	25
S^{95}_{exp}	15^{+6}_{-4}	20^{+8}_{-6}	43^{+17}_{-12}	54^{+21}_{-15}	$6.6^{+2.5}_{-1.8}$	11^{+5}_{-3}	26^{+10}_{-7}	36^{+14}_{-10}
$\langle\epsilon\sigma\rangle^{95}_{obs}$ [fb]	0.13	0.24	0.33	0.36	0.05	0.10	0.16	0.18

9.3 Model-dependent fit

This section shows the upper limits for the dedicated signal models at 95% confidence level using model-independent fit. First, the upper limits for the target signal models as discussed in Section 1.5 are shown. Then, the interpretation of other models is performed. Finally, cross sections of upper limits are extracted.

9.3.1 Target signal models

Figures 9.8 show the upper limits in the simplified models with gluino direct and one-step decay. The gluino mass with the direct decay is excluded up to 2.15 TeV for massless neutralino at the 95% confidence level and the exclusion limit is extended by 100 (200-300) GeV in higher gluino (neutralino) mass directions comparing to the previous publication at 36 fb^{-1} [34]. For the gluino one-step decay via W boson ($\tilde{g} \rightarrow qq'\tilde{\chi}_1^{\pm}$), the gluino mass is excluded up to 2.18 TeV and the exclusion limit is extended by 200 (300-400) GeV in higher gluino (neutralino) mass directions comparing to the previous publication at 36 fb^{-1} [34]. The signals with large $\tilde{\chi}_1^0$ mass have complicated kinematics and the improvement of sensitivities is expected by using BDT classifiers as discussed in Section 5.6. The large gain in neutralino mass, in particular on the one-step decays are observed as shown in Figure 9.8 and 9.9, For the gluino one-step decay via Z boson ($\tilde{g} \rightarrow qq'\tilde{\chi}_2^0$), the gluino mass is excluded up to 2.2 TeV as shown in Figure 9.9. In the Ref. [124], there is only exclusion limit in final states with two leptons ($Z \rightarrow \ell\ell$). Hence, the exclusion limit is highly improved in higher gluino mass direction: 500 GeV (300-400) GeV in gluino (neutralino) mass directions.

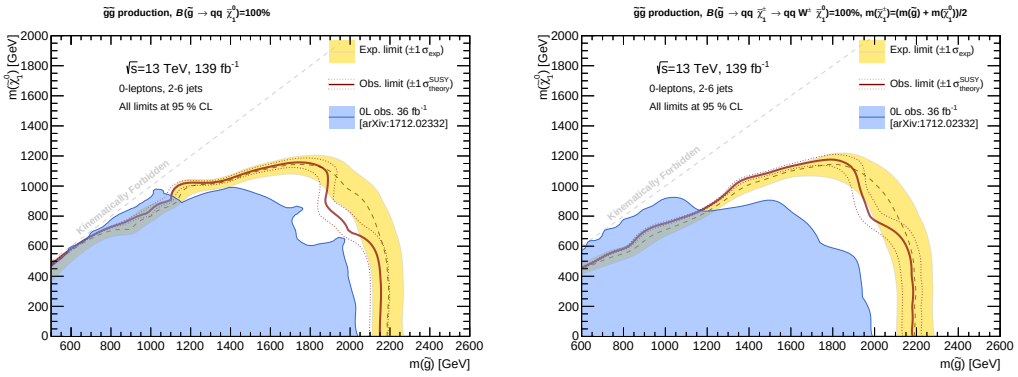

Figure 9.8: . Expected and observed limits at the 95% confidence level in the neutralino mass versus gluino mass for the gluino-pair production with direct decay (left), one-step decay with W boson (right) on a simplified model. The expected (observed) exclusion limit is denoted by the dash (solid) red line. The blue shaded area is the observed exclusion limits from the previous publication corresponding to the integrated luminosity of 36 fb^{-1} [34].

The other set of gluino one-step decay with the mass spectra with a fixed $m_{\tilde{\chi}_1^0}$=60 GeV is also motivated in term of the relic density of the dark matter as discussed in Section 3.3 [89]. Figures 9.10 show the exclusion limits for the gluino one-step decay via W boson and the gluino mass is excluded up

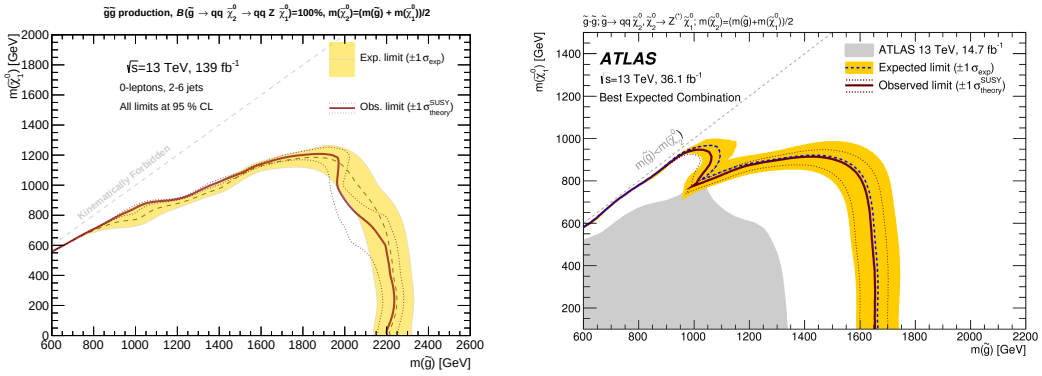

Figure 9.9: . Left: Expected and observed limits at the 95% confidence level in the neutralino mass versus gluino mass for the gluino-pair production with one-step decay with Z boson on a simplified model. The expected (observed) exclusion limit is denoted by the dash (solid) red line. Right: Expected and observed limits at the 95% confidence level in the neutralino mass versus gluino mass for the gluino-pair production with one-step decay with Z boson in final states with two leptons on a simplified model for the integrated luminosity of 36 fb^{-1} [124].

to 2.17 TeV. The exclusion limit are extended by 300 GeV in higher gluino mass directions comparing to the previous publication at 36 fb^{-1} [34].

9.3.2 Other signal models

Some other signal models are interpreted in case the event topology is similar to the target signals. First, the gluino direct decay with heavy flavour quarks (b or t) as shown in Figures 3.3 are evaluated. Unlike light-flavour squarks, the sbottoms and stops are not degenerated in the MSSM. Hence, the different upper limits from Figures 9.8 are evaluated. Figures 9.11 show the expected and observed limits for these models and the gluino mass is excluded up to 1.8 (2.15) TeV for massless neutralino at the 95% confidence level. There are dedicated analyses, which require many b-jets [125]. Since the effective mass and missing transverse momentum is large in the signals, the SRs can catch the signal events. Compared to Ref. [125], the expected exclusion limit in Figure 9.11 is improved in higher gluino mass direction for gluino decay with b quarks. The constraints on gluino decay with heavy flavour quarks can be set in this analysis.

Next, the signals of the inclusive production of squarks and gluinos with a fixed $m_{\tilde{\chi}_1^0}$ =0 GeV are considered as shown in Figure 3.4. Figures 9.12 show the expected and observed limits for this model. A upper limit of 2.15 TeV for gluino mass is set with massless $\tilde{\chi}_1^0$ if the squark is very heavy (>2 TeV). In this case, the dominant production in the signals becomes the gluino pair production and Figure 1.12(a) is dominant process. If the gluino is heavy (>3 TeV), the dominant production in the signals becomes the squark pair production. Since the observed event topology is two jets and missing transverse momentum, the exclusion limit in is not improved compared to the previous result. The constraints on inclusive production of squarks and gluinos can be set in this analysis.

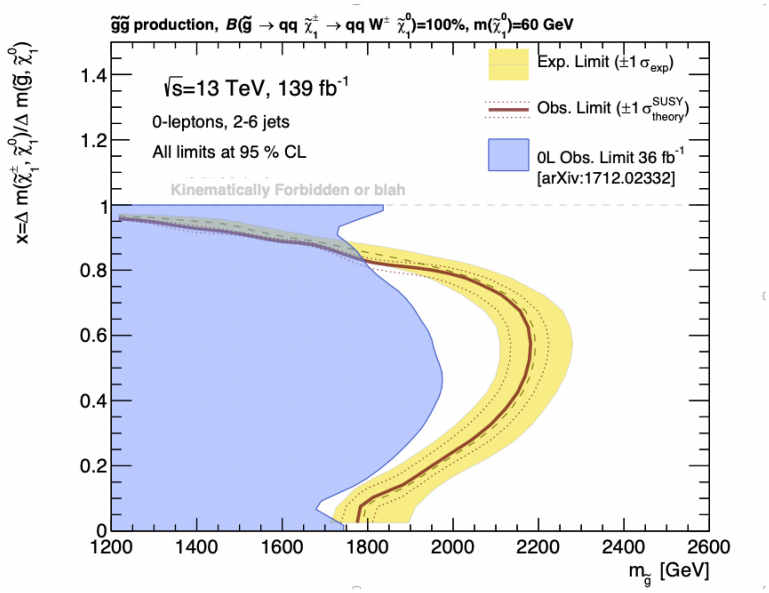

Figure 9.10: Expected and observed limits on the 95% confidence level in the gluino mass vs variable x, which is defined $x = \Delta m(\tilde{\chi}_0^{\pm} - \tilde{\chi}_i^0)/\Delta m(\tilde{g} - \tilde{\chi}_1^0)$ with fixed neutralino mass of 60 GeV for the gluino-pair production with one-step decay via W boson on a simplified model. The expected (observed) exclusion limit is denoted by the dash (solid) red line. The blue shaded area is the observed exclusion limits from the previous publication corresponding to the integrated luminosity of 36 fb^{-1} [34].

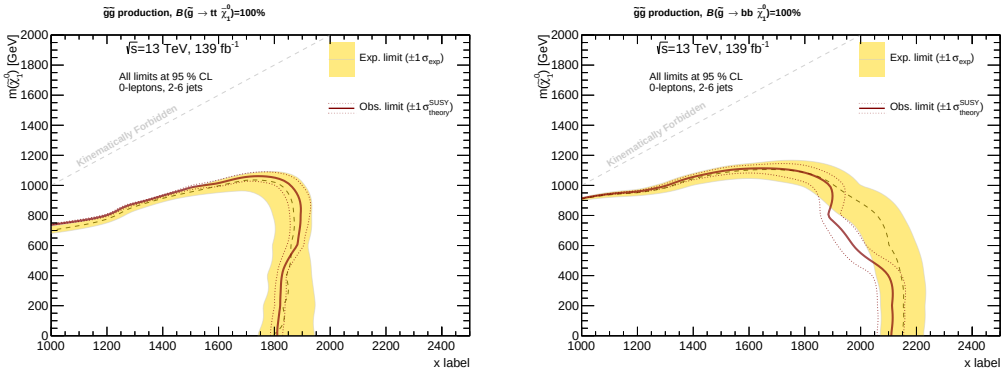

Figure 9.11: Expected and observed limits at the 95% confidence level in the neutralino mass versus gluino mass for the gluino-pair production with direct decay via t quarks (left) and b quarks (right). The expected (observed) exclusion limit is denoted by the dash (solid) red line.

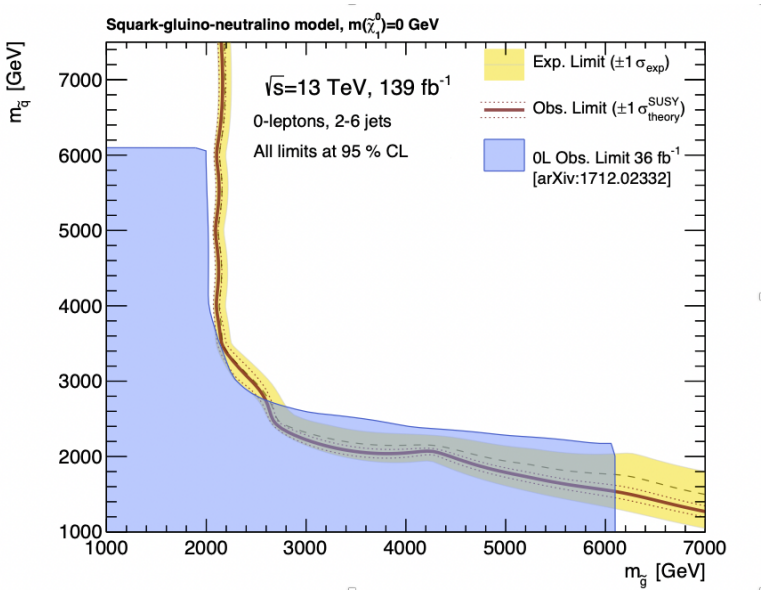

Figure 9.12: Expected and observed limits on the 95% confidence level in gluino mass vs squark mass for the phenomenological squark-gluino model with fixed neutralino mass of 0 GeV. The expected (observed) exclusion limit is denoted by the dash (solid) red line. The blue shaded area is the observed exclusion limits from the previous publication corresponding to the integrated luminosity of 36 fb^{-1} [34].

9.3.3 Cross section upper limits

In order to cover several signal models, the upper limits on the cross section for the target signals are obtained. First, the CL_s value is calculated, depending on the signal strength μ_s as discussed in Section 8.2. Then, the μ_s^{95} is obtained for a result of $CL_s = 0.05$. Finally, the upper limits on the cross section is calculated from the μ_s^{95} values. Figures 9.13 show the upper limits on the cross section for gluino direct and one-step decays.

9.4 Discussion

9.4.1 Comparison to the convensional approach

The expected signal and background events with the integrated luminosity of 36 fb^{-1} are estimated and they are compared to the previous result [34], which uses the convensional approach explained in Section 1.6. The impact on the machine learning approach is fairly evaluated in this comparison. Table 9.10 shows the number of gluino direct decay signal with ($m_{\tilde{g}}$, $m_{\tilde{\chi}_0^1}$)=(1950, 650) GeV and background events for the convensional approach and the machine learning approach. The cuts in the previous result are tunned to maximize the sensitivity with the integrated luminosity of 36 fb^{-1}. For this comparison, the cuts on BDT score is also tunned in order to maximize the sensitivity. The number of signal events in the machine learning approach is twice than the convensional approach, while the number of backgrounds is almost the same. It means that the non-linear correlation allows

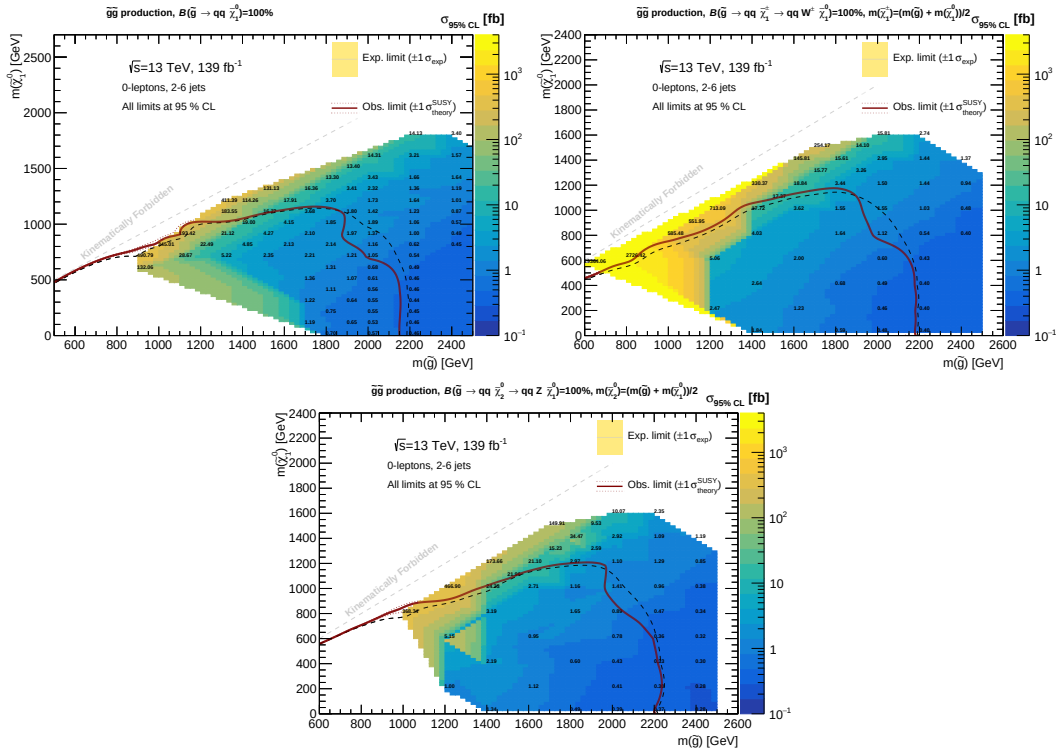

Figure 9.13: Excluded upper limits of expected and observed cross section at 95% confidence level in the neutralino mass versus gluino mass for the gluino-pair production with direct decay (top-left), one-step decay with W boson (top-right) and one-step decay with Z boson (bottom) on a simplified model. The upper limit values in all signal points are displayed in the figures.

the signals, which does not remain in the convensional approach, to be survived. This is the reason why the sensitivity in the machine learning approach is better than convensional approach.

Table 9.10: Comparison of the number of expected signal and background events with the integrated luminosity of 36 fb^{-1}. The gluino direct decay signal with ($m_{\tilde{g}}$, $m_{\tilde{\chi}_0^1}$)=(1950, 650) GeV is used in the comparison. The MC statistical uncertainty is only displayed in the table.

	Previous result [34]	The result with the method in this thesis
Number of signal	8.6 ± 1.0	16.2 ± 0.7
Number of background	16.5 ± 2.7	19.1 ± 3.0

Figures 9.14 show the comparison of expected exclusion limits with the integrated luminosity of 36 fb^{-1} at the 95% confidence level between the machine learning and the convensional approach. For gluino direct decay, the exclusion limit is extended by 100 GeV in higher gluino mass directions comparing to the convensional approach. For gluino one-step decay, the exclusion limit is extended by 200 GeV in higher neutralino mass directions comparing to the convensional approach. Since the training categories are prepared such that they can cover the signals with $\Delta m(\tilde{g},\tilde{\chi}_1^0) \geq$ 200 GeV, the exclusion limit in the regions is improved as shown in Figures 9.14. It means that the use of the

machine learning contributes to the improvement of the results shown in this thesis.

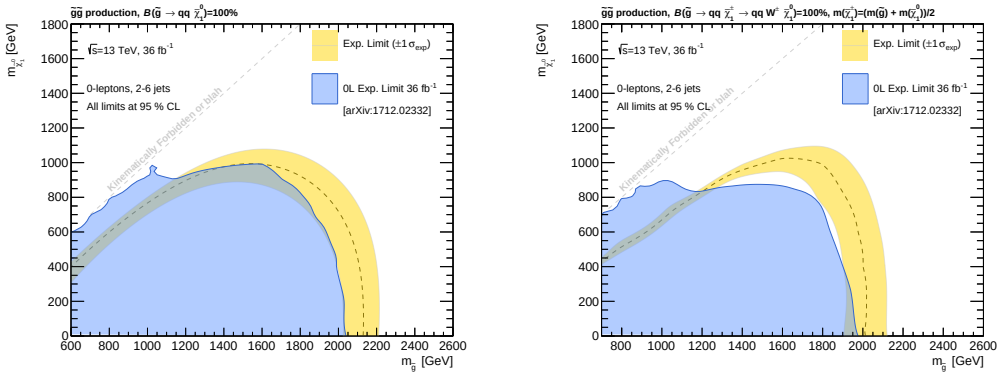

Figure 9.14: Expected exclusion limits at the 95% confidence level in the neutralino mass versus gluino mass for the gluino-pair production with direct decay (left), one-step decay with W boson (right) on a simplified model. The expected exclusion limit using machine learning approach at the integrated luminosity of 36 fb^{-1} is denoted by the dash line. The blue shaded area is the expected exclusion limits from the previous publication corresponding to the integrated luminosity of 36 fb^{-1} [34].

9.4.2 Comparison to the CMS experiment

Figures 9.15 show the exclusion limits at 95% confidence level for gluino direct and gluino one-step decay on the simplified models with the CMS detector [126]. The data collected 2016-2018 corresponding to the integrated luminosity of 137 fb^{-1} is used in the results. The analysis in the CMS adopts a multi-bin technique where the signal and background separation is performed by simultaneously fitting to multiple observables. The gluino mass is excluded up to 2.0 TeV for direct decay and 2.03 TeV for one-step decay at the CMS experiment. Compared to the CMS analysis, this research shown in this thesis clearly outperform the expected exclusion limits in a region where the gluino mass is heavy ($m_{\tilde{g}}$ >1.9 TeV). In particular, the significant superiority is observed in the gluino one-step decay and a impact of the machine learnining is very large. It implies that a machine learnining approach is superior to the multi-bin approach for gluino one-step decay, which has more complicated event topologies than gluino direct decay.

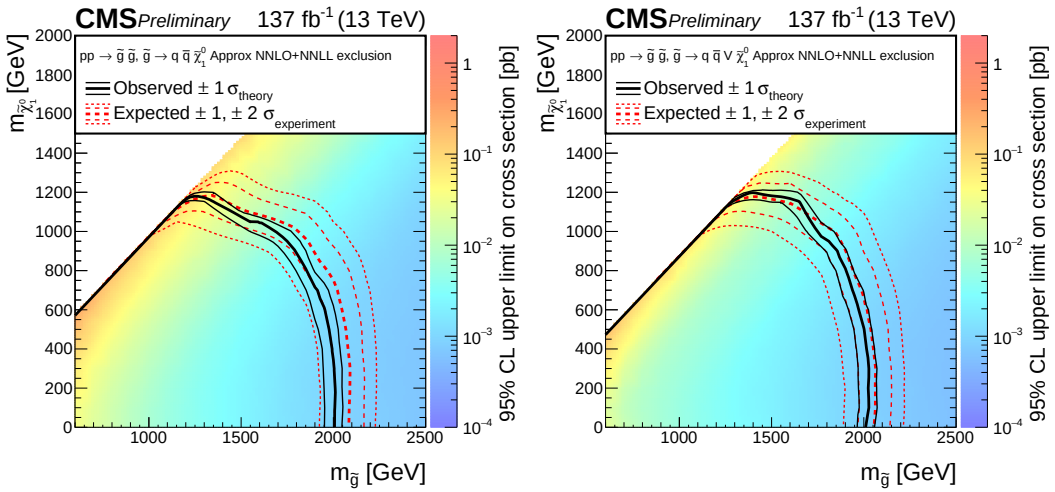

Figure 9.15: Expected and observed limits at the 95% confidence level in the neutralino mass versus gluino mass for the gluino-pair production with direct decay (left), one-step decay with bosons (right) on a simplified model [126].

9.4.3 Impact of the result to SUSY models

As explained in Section 1.5, the gluino search is one of most important physics programmes at the LHC. In addition, the result in this thesis can provide the constraints of SUSY models. For example, the ratio of gaugino mass parameters in the Anomaly mediated SUSY breaking (AMSB) [127] and minimum supergravity (mSUGRA) models [128–130] is written as

$$m_{\text{bino}} : m_{\text{wino}} : m_{\text{gluino}} \sim 3 : 1 : 8 \quad \text{for AMSB} \tag{9.1}$$

$$m_{\text{bino}} : m_{\text{wino}} : m_{\text{gluino}} \sim 1 : 2 : 7 \quad \text{for mSUGRA} \tag{9.2}$$

where m_{bino} is the bino mass, m_{wino} is the wino mass and m_{gluino} is the gluino mass. The lightest neutralino is expected to be less than a few TeV from the relic density of the dark matter as shown in Figure 1.8, so the light gluino mass (O(1-10) TeV) is preferable. The gluino mass is also expected to be light in term of the fine tuning problem [131]. The gluino mass is related to the Higgs boson mass calculation at higher order and the level of the fine tuning is smaller as the gluino mass is lighter. Therefore, the search for gluino with a few TeV mass is important considering on the level of the fine tuning problem. In this thesis, the search for this important region can be probed. The extension of the exclusion limit in this thesis has provided new constraint of the heavier gluino and neutralino for these models which have not been looked into before.

10 Conclusion

This thesis presents a search for gluinos in final states with jets and missing transverse momentum using pp collision at $\sqrt{s}$ =13 TeV with the ATLAS detector. The data is collected in 2015-2018 corresponding to the integrated luminosity of 139 fb^{-1}. A machine learning technique is introduced in this search to improve the sensitivity of heavier gluino. In order to probe all mass points of signals, eight training categories are prepared depending on the mass difference between gluino and neutralino. The sensitivities of all signal masses are improved by using the training categories. The background estimation considering the correlation is carefully performed and it is validated that the estimation is worked properly from results of the validation regions. In all signal regions, no significant excess over the background prediction is observed and any indication of SUSY signal in final states with jets and missing transverse momentum cannot be found.

The exclusion limits for some dedicated signal models at 95% confidence level are set. The gluino mass with the direct decay is excluded up to 2.15 TeV for massless neutralino. Compared to the previous results, it is extended by 100 (200-300) GeV in heavier gluino (neutralino) mass. The gluino mass with the one-step decay is excluded up to 2.2 TeV for massless neutralino and it is extended by 500 (300-400) GeV in heavier gluino (neutralino) mass compared to the previous results. Using the machine learning in this analysis allows the heavier gluino which has not been looked into before to access.

In this research, the framework using the machine learning has been established in gluino search. Based on the framework, the first preliminary result of the gluino search using the machine learning was published from ATLAS. The constraints of gluino mass are the best in the world. It has been proved that the machine learning technique is applicable to SUSY search.

Acknowledgements

First of all I would like to express my gratitude to my supervisor, Prof. Junichi Tanaka for giving me such a wonderful research theme and providing the helpful suggestions at all times. He always leads me to the right direction, so I was able to continue the research. I would like to also express my gratitude to Dr. Yuji Enari for providing the helpful suggestions and discussing the detail of research at all times. He also gave a support of the research of LAr calorimeter, which is very interested theme for me, and I was able to have a precious experience. I wouild like to appriciate an important suggestion about SUSY analysis Prof. Shoji Asai gave me. He also gave a support for the research at CERN.

I would like to thank all the members of ATLAS SUSY group. Dr. Yu Nakahama Higuchi, Dr. Zuzana Rurikova and Prof. Paul Jackson are the analysis contact in my analysis. They always gave a lot of suggestion and discussed the details in the analysis with me in order to establish this analysis. Dr. Tomoyuki Saito, Dr. Takuya Nobe, Dr. Shion Chen, Dr. Masahiko Saito and Prof. Ryu Sawada gave me a technical advice and useful comment for improvement of my analysis. Dr. Emma Sian Kuwertz, Dr. Julien Maurer, Dr. Jonathan Long and Dr. Teng Jian Khoo are the leaders in the SUSY strong production group. They gave a lot of suggestion in the meeting and approved my analysis. Prof. Zachary Lewis Marshall, Dr. Federico Meloni are the leaders in the SUSY group. They helped me to publish my analysis result in an international conference. In addition, they also gave me some advice for my new job position.

I would like to thank all the members of ATLAS Japan group and ICEPP, because I was able to enjoy my student life for their support. Prof. Masaya Ishino, Prof. Yasuyuki Okumura, Prof. Tetsuro Mashimo, Dr. Koji Terachi, Dr. Tatsuya Masubuchi, Dr. Tomoe Kishimoto and Dr. Michiru Kaneda gave me a support at CERN and maintained the computer I uses for my analysis. In particular, Prof. Masaya Ishino and Prof. Yasuyuki Okumura gave me a lot of advice for my new job position. I would like to also express my gratitude to the secretaries in ICEPP. They always supported me, so I was able to focus on my research.

Finally, I would like to thank my family and friends for their support in my life.

A Input variable distribution

Figures A.1, A.2, A.3 and A.4 show pre-fit distribution of input variables used in the BDT classifier.

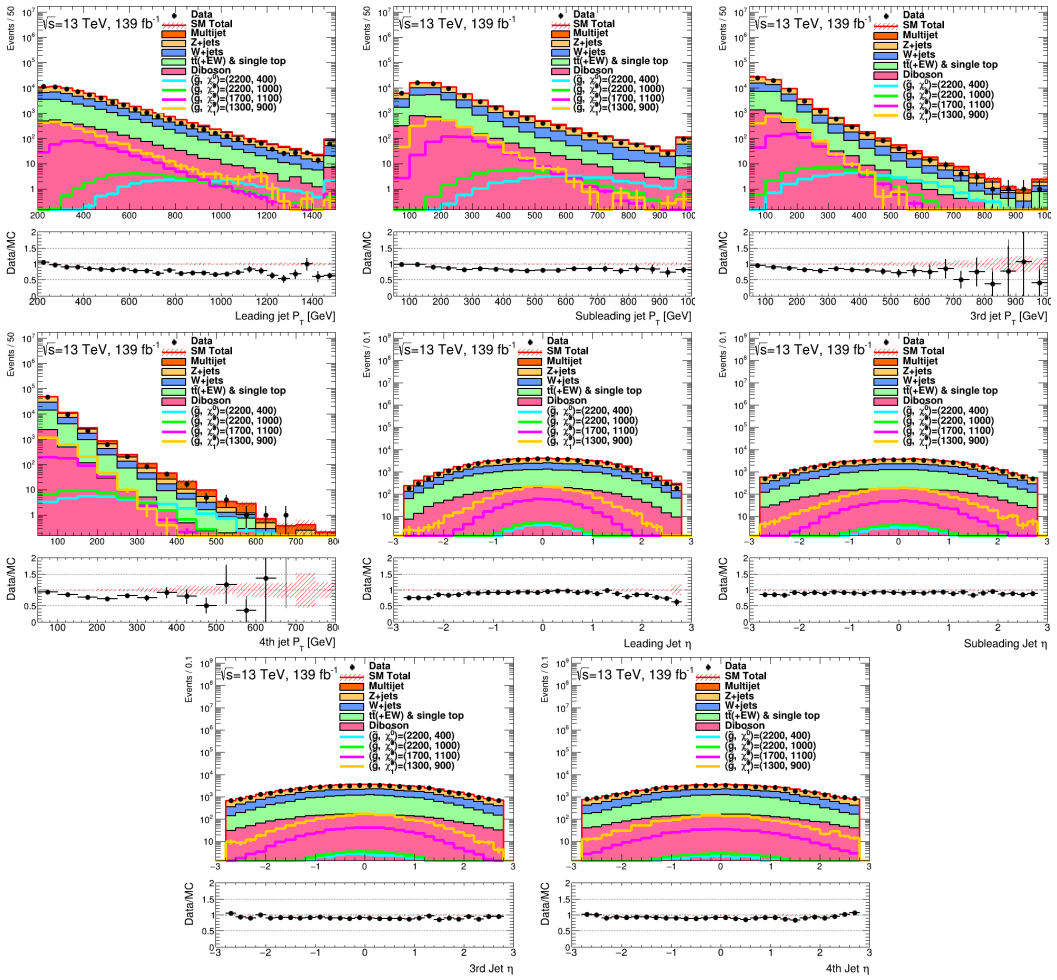

Figure A.1: Distribution of leading jet to 4th jet p_{T} and η with the preselection cut. This signals in the plot are gluino direct decay. The last bin includes the overflow. The hatched red error bands indicate the MC statistical uncertainties. The bottom panel is the ratio of the observed data and the MC simulation.

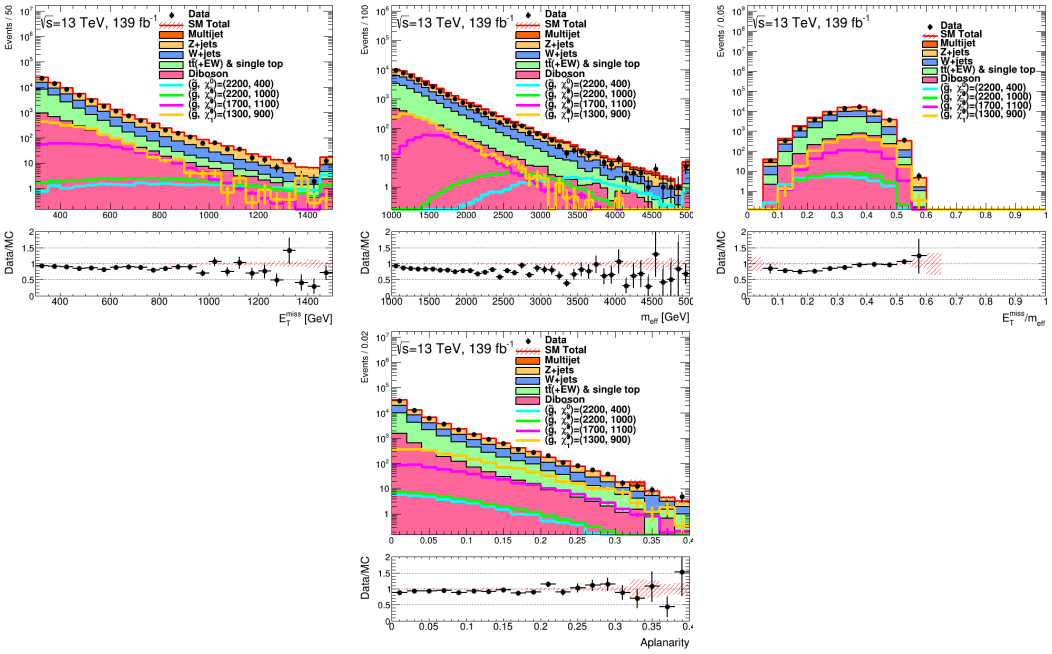

Figure A.2: Distribution of $E_{\mathrm{T}}^{\mathrm{miss}}$, m_{eff}, $E_{\mathrm{T}}^{\mathrm{miss}}/E_{\mathrm{T}}^{\mathrm{miss}}$ and aplanarity with the preselection cut. This signals in the plot are gluino direct decay. The last bin includes the overflow. The hatched red error bands indicate the MC statistical uncertainties. The bottom panel is the ratio of the observed data and the MC simulation.

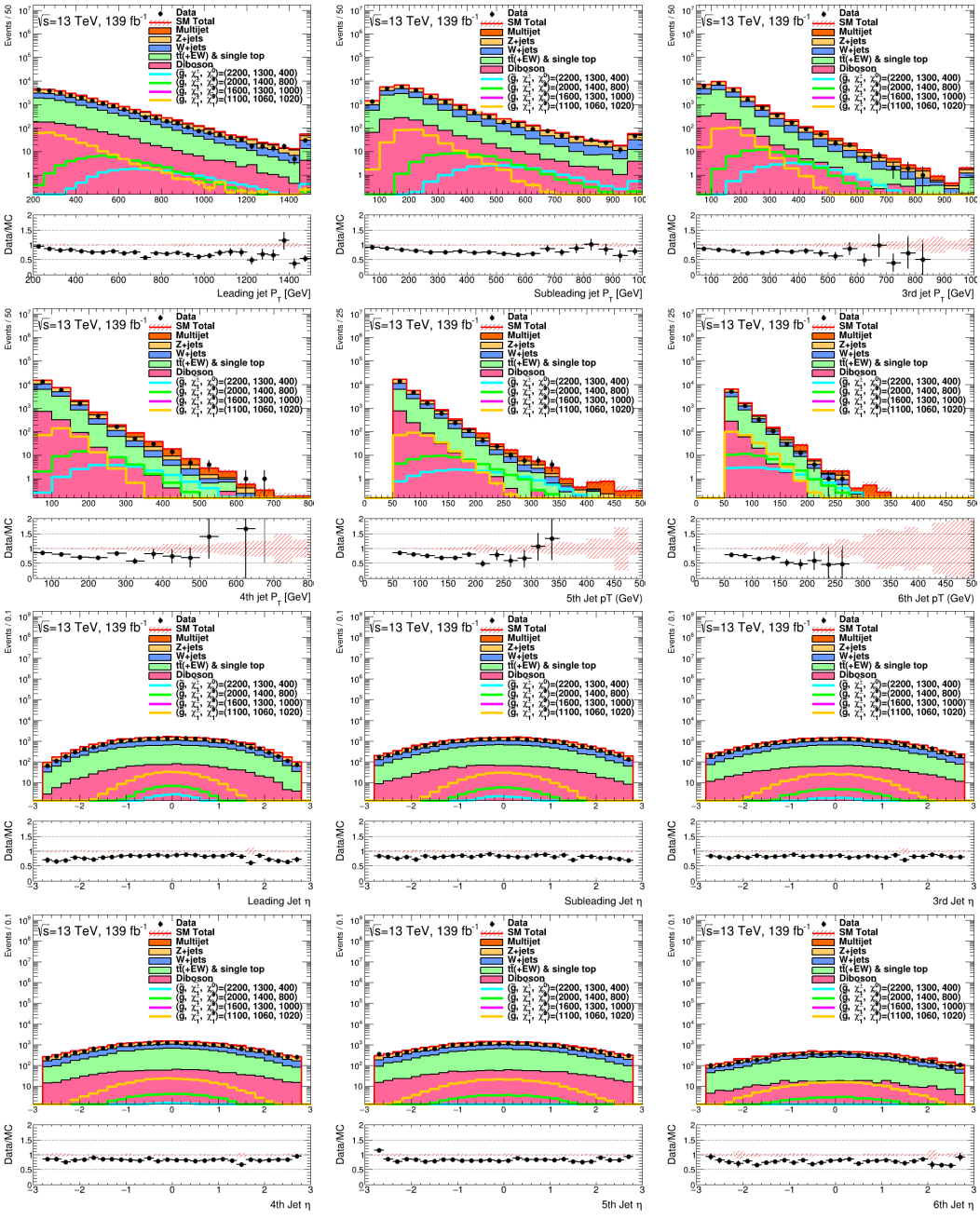

Figure A.3: Distribution of leading jet to 6th jet p_{T} and η with the preselection cut and $N_j \geq 5$. This signals in the plot are gluino one-step decay via W boson. The last bin includes the overflow. The hatched red error bands indicate the MC statistical uncertainties. The bottom panel is the ratio of the observed data and the MC simulation.

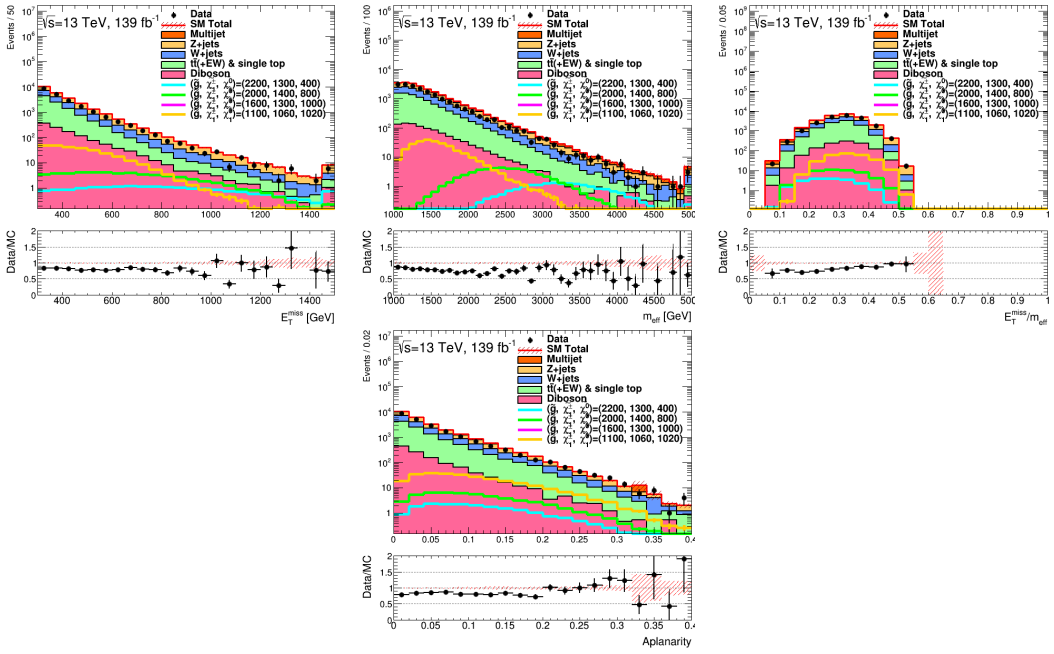

Figure A.4: Distribution of $E_{\mathrm{T}}^{\mathrm{miss}}$, m_{eff}, $E_{\mathrm{T}}^{\mathrm{miss}}/E_{\mathrm{T}}^{\mathrm{miss}}$ and aplanarity with the preselection cut and $N_j \geq 5$. This signals in the plot are gluino one-step decay via W boson. The last bin includes the overflow. The hatched red error bands indicate the MC statistical uncertainties. The bottom panel is the ratio of the observed data and the MC simulation.

B Input variable distribution

Figures B.1,B.2 and B.3 show pre-fit BDT score distributions in CRs for all training categories. The distributions in CRY and CRW is well-modelled by MC simulation, but the mismodelling is observed in CRT.

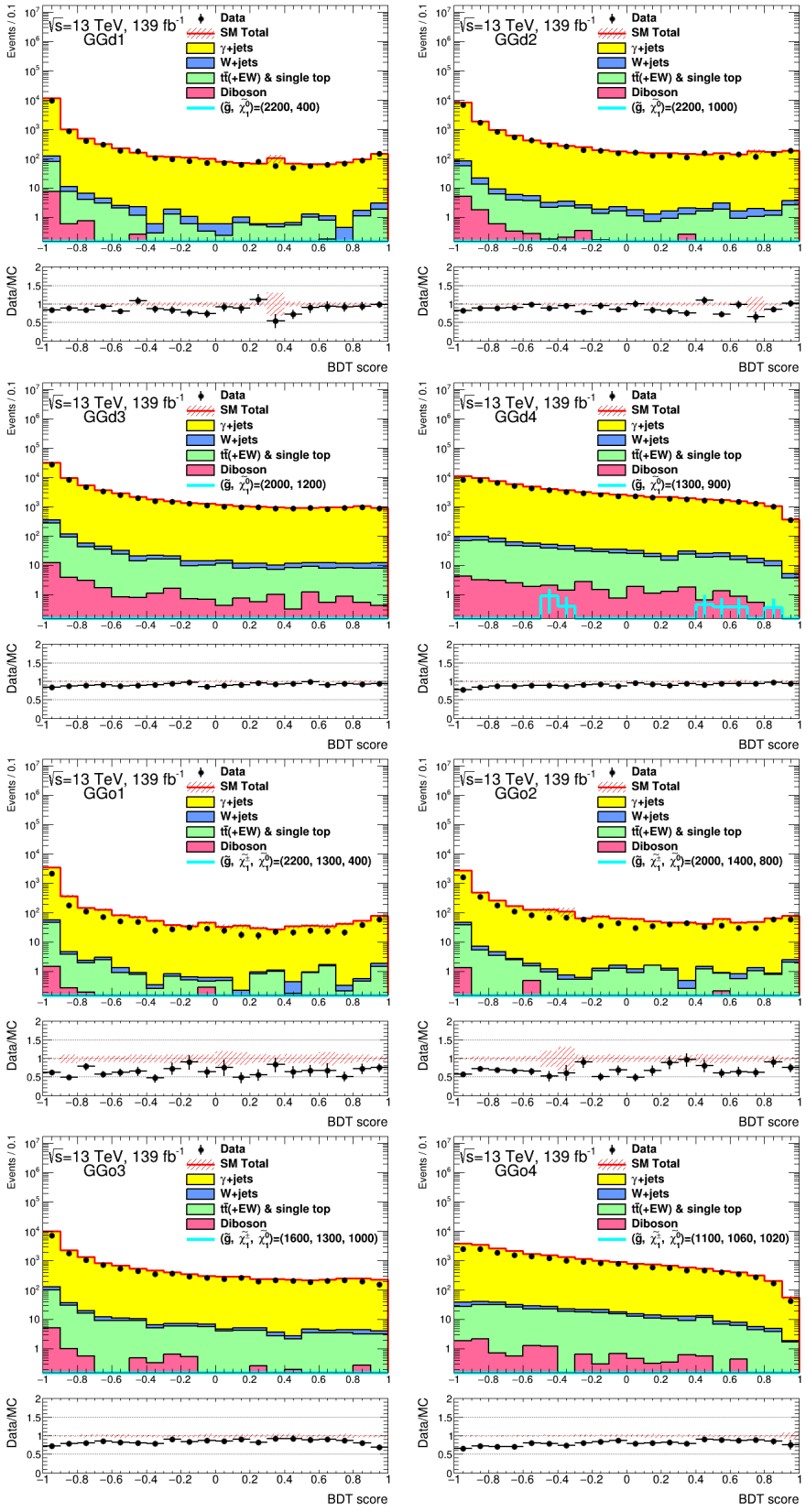

Figure B.1: BDT score distributions in CRY for all training categories. The hatched red error bands indicate the MC statistical uncertainties. The bottom panel is the ratio of the observed data and the MC simulation.

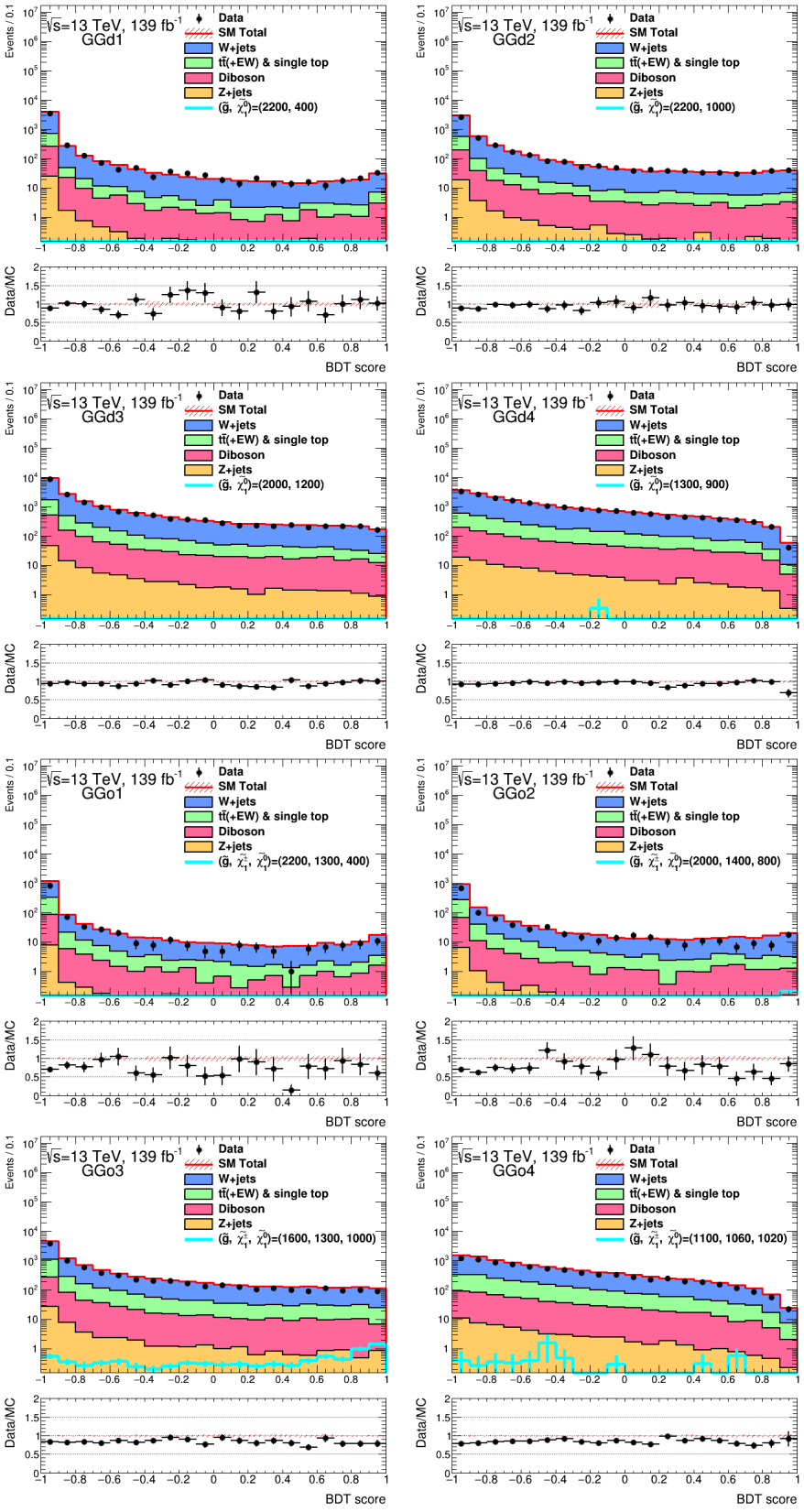

Figure B.2: BDT score distributions in CRW for all training categories. The hatched red error bands indicate the MC statistical uncertainties. The bottom panel is the ratio of the observed data and the MC simulation.

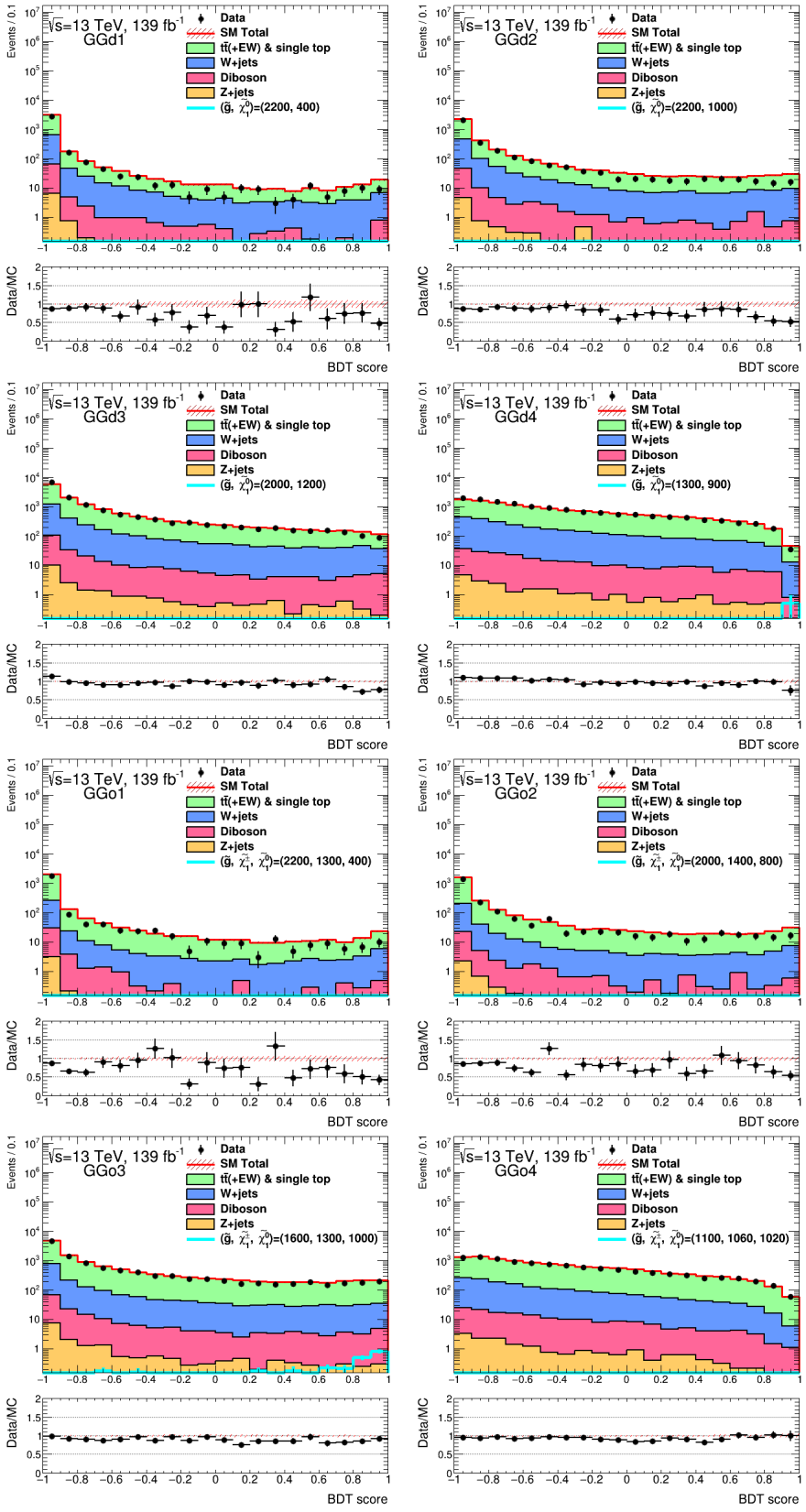

Figure B.3: BDT score distributions in CRT for all training categories. The hatched red error bands indicate the MC statistical uncertainties. The bottom panel is the ratio of the observed data and the MC simulation.

C Trigger readout electronics upgrade of the LAr calorimeter

In addition to the gluino search, an upgrade of trigger readout electronics of the LAr calorimeter has been worked in order to enhance the sensitivity in the search of SUSY particles. This section explains the electronic upgrade in details, which is based on Ref. [132, 133].

C.1 LAr calorimeter upgrade at Run 3 experiment

Run 3 experiment is expected to have two times higher instantaneous luminosity, L =3.0×10^{34} cm $^{-2}$s^{-1} than in Run 2. In order to perform the experiment under the high luminosity environment, the upgrade of LHC and subdetectors is planned for the long shutdown (2019-2020) [134]. For the LAr calorimeter, a trigger readout upgrade is planned to improve the L1 trigger performance, because the limitation of L1 trigger rate. The trigger rate of electron and photon object (L1 EM object) is determined to be 20 kHz in Run 3 experiment. In the current trigger readout scheme, the transverse momentum threshold has to be about 34 GeV as shown in Figure C.1 in order to keep the trigger rate. It leads to drop on the acquisition efficiency of W/Z boson, which decays to $W \rightarrow e\nu$ or $Z \rightarrow ee$. In order to reduce the threshold, the shower shape information of object is used to separate the EM object and jet. By utilizing the shower shape information, the trigger rate can be reduced while the transverse momentum threshold keeps the same level as Run 2 experiment (20 kHz) as shown inFigure C.1. Hence, the trigger readout scheme is upgraded to use the shower shape information.

C.2 New trigger readout scheme

As explained in Section 2.2, the LAr calorimeter has four layers, which are segmented in pseudo-rapidity η and azimuth ϕ directions. The current trigger readout, where the unit of the readout segment is shown in Figure C.2 and it is called a "Trigger Tower". The readout makes analog sums over cells of the four layers in a range of $\Delta\eta \times \Delta\phi = 0.1 \times 0.1$ at the frontend electronics. Then, the summed analog signals are transmitted via coaxial cables to the backend electronics, which digitizes at 40 MHz. The new trigger readout is shown in Figure C.2 and is called "Super Cells". The summed analog signals are digitized for each layer separately in the frontend electronics. In order to utilize the shower shape information, the range of the summation for the first and middle layers is changed to be finer, $\Delta\eta \times \Delta\phi = 0.025 \times 0.1$. These signals are transmitted to the backend electronics via optical fibers. As a result, one Trigger Tower corresponds to ten Super Cells.

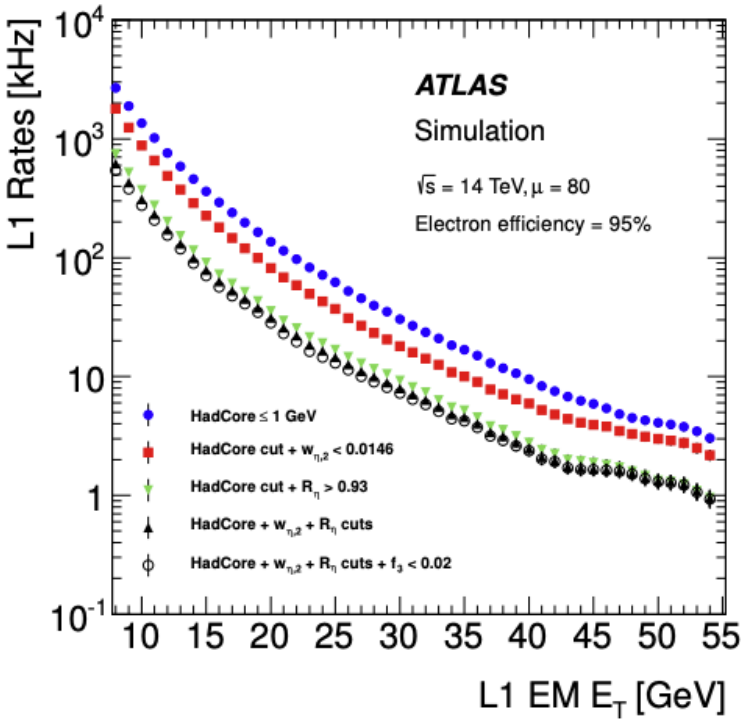

Figure C.1: L1 Trigger rate as a function of transverse momentum threshold with EM object (L1 EM E_T) [134]. It assumes that the electron efficiency is 95%. The blue point indicates the current trigger readout scheme. The red, green, black and white point indicate the new trigger readout scheme for Run 3 experiment with different selection criteria.

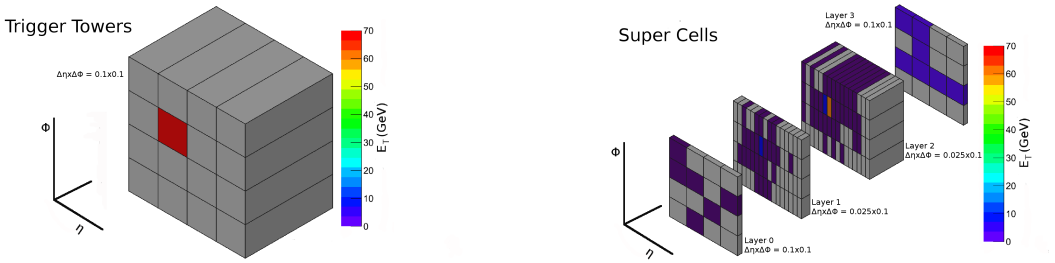

Figure C.2: The readout scheme of the current trigger readout, which is called Trigger Tower (left) and new trigger readout, which is called Super Cells (right) [134]. These colors indicate the energy deposit for 70 GeV electron.

In order to change the trigger readout scheme, a frontend and backend electronics are upgraded. The frontened electronics digitizes the information of Super Cells at 40 MHz to 12 bits and transmits it into the backend electronics. The backend electronics computes each transverse energy and the bunch crossing where the EM object is deposited to the Super Cells by using a Field Programmable gate array (FPGA) and transmits it into the L1 trigger system.

Bibliography

[1] M. K. Gaillard, P. D. Grannis, and F. J. Sciulli, *The standard model of particle physics*, Reviews of Modern Physics **71** (1999) S96, ISSN: 1539-0756, URL: http://dx.doi.org/10.1103/RevModPhys.71.S96 (cit. on p. 9).

[2] G. 't Hooft, *Naturalness, chiral symmetry, and spontaneous chiral symmetry breaking*, NATO Sci. Ser. B **59** (1980) 135 (cit. on pp. 9, 10).

[3] *Particle Physics Standard Model Elementary Particle*, URL: https://favpng.com/png_view/field-particle-physics-standard-model-elementary-particle-higgs-boson-png/JwgQnwMF (cit. on p. 9).

[4] G. Aad et al., *Observation of a new particle in the search for the Standard Model Higgs boson with the ATLAS detector at the LHC*, Physics Letters B **716** (2012) 1, ISSN: 0370-2693, URL: http://dx.doi.org/10.1016/j.physletb.2012.08.020 (cit. on p. 9).

[5] S. Chatrchyan et al., *Observation of a new boson at a mass of 125 GeV with the CMS experiment at the LHC*, Physics Letters B **716** (2012) 30, ISSN: 0370-2693, URL: http://dx.doi.org/10.1016/j.physletb.2012.08.021 (cit. on p. 9).

[6] C.-N. Yang and R. L. Mills, *Isotopic spin conservation and a generalized gauge invariance*, (1954) (cit. on p. 10).

[7] R. Ball, *Chiral gauge theory*, Physics Reports **182** (1989) 1, ISSN: 0370-1573, URL: http://www.sciencedirect.com/science/article/pii/0370157389900276 (cit. on p. 10).

[8] S. Weinberg, *Implications of dynamical symmetry breaking*, Phys. Rev. D **13** (4 1976) 974, URL: https://link.aps.org/doi/10.1103/PhysRevD.13.974 (cit. on p. 10).

[9] E. Corbelli and P. Salucci, *The extended rotation curve and the dark matter halo of M33*, Monthly Notices of the Royal Astronomical Society **311** (2000) 441, ISSN: 1365-2966, URL: http://dx.doi.org/10.1046/j.1365-8711.2000.03075.x (cit. on pp. 10, 11).

[10] V. N. Aseev et al., *Upper limit on the electron antineutrino mass from the Troitsk experiment*, Physical Review D **84** (2011), ISSN: 1550-2368, URL: http://dx.doi.org/10.1103/PhysRevD.84.112003 (cit. on p. 11).

[11] P. Serra, F. Zalamea, A. Cooray, G. Mangano, and A. Melchiorri, *Constraints on neutrino – dark matter interactions from cosmic microwave background and large scale structure data*, 2009, arXiv: 0911.4411 [astro-ph.CO] (cit. on p. 11).

[12] Y. A. Golfand and E. P. Likhtman, *Extension of the Algebra of Poincare Group Generators and Violation of p Invariance*, JETP Lett. **13** (1971) 323, Pisma Zh. Eksp. Teor. Fiz.13,452(1971) (cit. on p. 11).

[13] D. Volkov and V. Akulov, *Is the neutrino a goldstone particle?*, Physics Letters B **46** (1973) 109, ISSN: 0370-2693, URL: http://www.sciencedirect.com/science/article/pii/0370269373904905 (cit. on p. 11).

[14] J. Wess and B. Zumino, *Supergauge transformations in four dimensions*, Nuclear Physics B **70** (1974) 39, ISSN: 0550-3213, URL: http://www.sciencedirect.com/science/article/pii/0550321374903551 (cit. on p. 11).

[15] J. Wess and B. Zumino, *Supergauge invariant extension of quantum electrodynamics*, Nuclear Physics B **78** (1974) 1, ISSN: 0550-3213, URL: http://www.sciencedirect.com/science/article/pii/0550321374901126 (cit. on p. 11).

[16] S. Ferrara and B. Zumino, *Supergauge invariant Yang-Mills theories*, Nuclear Physics B **79** (1974) 413, ISSN: 0550-3213, URL: http://www.sciencedirect.com/science/article/pii/0550321374905598 (cit. on p. 11).

[17] A. Salam and J. Strathdee, *Super-symmetry and non-Abelian gauges*, Physics Letters B **51** (1974) 353, ISSN: 0370-2693, URL: http://www.sciencedirect.com/science/article/pii/0370269374902263 (cit. on p. 11).

[18] P. Fayet, *Supersymmetry and weak, electromagnetic and strong interactions*, Physics Letters B **64** (1976) 159, ISSN: 0370-2693, URL: http://www.sciencedirect.com/science/article/pii/0370269376903191 (cit. on pp. 11, 13).

[19] P. Fayet, *Spontaneously broken supersymmetric theories of weak, electromagnetic and strong interactions*, Physics Letters B **69** (1977) 489, ISSN: 0370-2693, URL: http://www.sciencedirect.com/science/article/pii/0370269377908528 (cit. on pp. 11, 13).

[20] W. d. Boer, *Perspectives on the detection of supersymmetric Dark Matter*, EPJ Web of Conferences **182** (2018) 02034, ed. by Y. Aharonov, L. Bravina, and S. Kabana, ISSN: 2100-014X, URL: http://dx.doi.org/10.1051/epjconf/201818202034 (cit. on p. 12).

[21] L. Girardello and M. T. Grisaru, *Soft Breaking of Supersymmetry*, Nucl. Phys. **B194** (1982) 65 (cit. on p. 12).

[22] G. R. Farrar and P. Fayet, *Phenomenology of the production, decay, and detection of new hadronic states associated with supersymmetry*, Physics Letters B **76** (1978) 575, ISSN: 0370-2693, URL: http://www.sciencedirect.com/science/article/pii/0370269378908584 (cit. on p. 13).

[23] K. Abe et al., *Search for proton decay via $p \to e^+\pi^0$ and $p \to \mu^+\pi^0$ in 0.31 megaton · years exposure of the Super-Kamiokande water Cherenkov detector*, Phys. Rev. D **95** (1 2017) 012004, URL: https://link.aps.org/doi/10.1103/PhysRevD.95.012004 (cit. on p. 13).

[24] L. J. Hall, D. Pinner, and J. T. Ruderman, *A natural SUSY Higgs near 125 GeV*, Journal of High Energy Physics **2012** (2012), ISSN: 1029-8479, URL: http://dx.doi.org/10.1007/JHEP04(2012)131 (cit. on pp. 13, 14).

[25] A. Djouadi, J.-L. Kneur, and G. Moultaka, *SuSpect: A Fortran code for the Supersymmetric and Higgs particle spectrum in the MSSM*, Computer Physics Communications **176** (2007) 426, ISSN: 0010-4655, URL: http://dx.doi.org/10.1016/j.cpc.2006.11.009 (cit. on p. 14).

[26] M. Frank et al., *The Higgs boson masses and mixings of the complex MSSM in the Feynman-diagrammatic approach*, Journal of High Energy Physics **2007** (2007) 047, ISSN: 1029-8479, URL: http://dx.doi.org/10.1088/1126-6708/2007/02/047 (cit. on p. 14).

[27] S. P. MARTIN, *A SUPERSYMMETRY PRIMER*, Advanced Series on Directions in High Energy Physics (1998) 1, ISSN: 1793-1339, URL: http://dx.doi.org/10.1142/9789812839657_0001 (cit. on p. 14).

[28] M. Ciuchini et al., *Delta MK and epsilonK in SUSY at the next-to-leading order*, Journal of High Energy Physics **1998** (1998) 008, ISSN: 1029-8479, URL: http://dx.doi.org/10.1088/1126-6708/1998/10/008 (cit. on p. 14).

[29] C. Beskidt et al., *Constraints on Supersymmetry from relic density compared with future Higgs searches at the LHC*, Physics Letters B **695** (2011) 143, ISSN: 0370-2693, URL: http://dx.doi.org/10.1016/j.physletb.2010.10.048 (cit. on p. 15).

[30] N. Aghanim et al., *Planck 2018 results. VI. Cosmological parameters*, 2018, arXiv: 1807.06209 [astro-ph.CO] (cit. on p. 15).

[31] G. Aad et al., *Summary of the ATLAS experiment's sensitivity to supersymmetry after LHC Run 1 — interpreted in the phenomenological MSSM*, Journal of High Energy Physics **2015** (2015), ISSN: 1029-8479, URL: http://dx.doi.org/10.1007/JHEP10(2015)134 (cit. on pp. 15, 16).

[32] A. Djouadi et al., *The Minimal supersymmetric standard model: Group summary report*, 1998, arXiv: hep-ph/9901246 (cit. on p. 16).

[33] C. F. Berger, J. S. Gainer, J. L. Hewett, and T. G. Rizzo, *Supersymmetry Without Prejudice*, JHEP **02** (2009) 023, arXiv: 0812.0980 [hep-ph] (cit. on p. 16).

[34] M. Aaboud, G. Aad, B. Abbott, and et.all, *Search for squarks and gluinos in final states with jets and missing transverse momentum using 36fb^{-1} of $\sqrt{s}$ =13 TeV pp collision data with the ATLAS detector*, Phys. Rev. D **97** (11 2018) 112001, URL: https://link.aps.org/doi/10.1103/PhysRevD.97.112001 (cit. on pp. 16, 17, 20, 35, 67, 69, 126–131).

[35] M. Aaboud et al., *Search for a scalar partner of the top quark in the jets plus missing transverse momentum final state at $\sqrt{s}$ =13 TeV with the ATLAS detector*, Journal of High Energy Physics **2017** (2017) 85, ISSN: 1029-8479, URL: https://doi.org/10.1007/JHEP12(2017)085 (cit. on pp. 16, 17).

[36] M. Aaboud et al., *Search for electroweak production of supersymmetric particles in final states with two or three leptons at $\sqrt{s}$ =13 TeV with the ATLAS detector*, The European Physical Journal C **78** (2018) 995, ISSN: 1434-6052, URL: https://doi.org/10.1140/epjc/s10052-018-6423-7 (cit. on pp. 16, 17).

[37] *LHC SUSY Cross Section Working Group*, URL: ttps://twiki.cern.ch/twiki/bin/view/LHCPhysics/SUSYCrossSections (cit. on pp. 19, 114).

[38] L. Evans and P. Bryant, *LHC Machine*, Journal of Instrumentation **3** (2008) S08001 (cit. on p. 21).

[39] T. A. Collaboration, *The ATLAS Experiment at the CERN Large Hadron Collider*, Journal of Instrumentation **3** (2008) S08003 (cit. on pp. 21, 23, 24).

[40] S. Chatrchyan et al., *The CMS experiment at the CERN LHC*, Journal of Instrumentation **3** (2008) S08004 (cit. on p. 21).

[41] A. A. Alves Jr. et al., *The LHCb Detector at the LHC*, Journal of Instrumentation **3** (2008) S08005 (cit. on p. 21).

[42] K. Aamodt et al., *The ALICE experiment at the CERN LHC*, Journal of Instrumentation **3** (2008) S08002 (cit. on p. 21).

[43] E. Mobs, *The CERN accelerator complex - August 2018.*, (2018), General Photo, URL: https://cds.cern.ch/record/2636343 (cit. on p. 21).

[44] G. Aad et al., *ATLAS data quality operations and performance for 2015-2018 data-taking*, 2019, arXiv: 1911.04632 [physics.ins-det] (cit. on pp. 22, 23, 31).

[45] G. Avoni et al., *The new LUCID-2 detector for luminosity measurement and monitoring in ATLAS*, JINST **13** (2018) P07017 (cit. on pp. 23, 31, 110).

[46] *CERN Archive Photo*, URL: https://mediaarchive.cern.ch/MediaArchive/Photo/Public/2008/0803014/0803014_01/0803014_01-A5-at-72-dpi.jpg (cit. on p. 25).

[47] *ATLAS Insertable B-Layer Technical Design Report Addendum*, tech. rep. CERN-LHCC-2012-009. ATLAS-TDR-19-ADD-1, Addendum to CERN-LHCC-2010-013, ATLAS-TDR-019, 2012, URL: https://cds.cern.ch/record/1451888 (cit. on p. 24).

[48] B. Abbott et al., *Production and integration of the ATLAS Insertable B-Layer*, Journal of Instrumentation **13** (2018) T05008, ISSN: 1748-0221, URL: http://dx.doi.org/10.1088/1748-0221/13/05/T05008 (cit. on p. 24).

[49] E. Abat et al., *The ATLAS TRT Barrel Detector*, Journal of Instrumentation **3** (2008) P02014, URL: https://doi.org/10.1088%2F1748-0221%2F3%2F02%2Fp02014 (cit. on p. 25).

[50] *ATLAS liquid-argon calorimeter: Technical Design Report*, Technical Design Report ATLAS, CERN, 1996, URL: https://cds.cern.ch/record/331061 (cit. on pp. 26, 27).

[51] *2015 start-up trigger menu and initial performance assessment of the ATLAS trigger using Run-2 data*, 2016, URL: https://cds.cern.ch/record/2136007 (cit. on pp. 28, 29, 31).

[52] *Trigger Menu in 2016*, 2017, URL: https://cds.cern.ch/record/2242069 (cit. on pp. 28, 31).

[53] *Trigger Menu in 2017*, 2018, URL: https://cds.cern.ch/record/2625986 (cit. on pp. 28, 31).

[54] *Trigger menu in 2018*, 2019, URL: https://cds.cern.ch/record/2693402 (cit. on pp. 28, 31).

[55] *Luminosity determination in pp collisions at $\sqrt{s}$ = 13 TeV using the ATLAS detector at the LHC*, 2019, URL: https://cds.cern.ch/record/2677054 (cit. on pp. 31, 110).

[56] E. Bothmann et al., *Event generation with Sherpa 2.2*, SciPost Physics **7** (2019), ISSN: 2542-4653, URL: http://dx.doi.org/10.21468/SciPostPhys.7.3.034 (cit. on pp. 33, 34).

[57] R. Gavin, Y. Li, F. Petriello and S. Quackenbush, *FEWZ 2.0: A code for hadronic Z production at next-to-next-to-leading order*, Comput. Phys. Commun. **182** (2011) 2388, arXiv: 1011.3540 [hep-ph] (cit. on p. 33).

[58] R. D. Ball et al., *Parton distributions for the LHC Run II*, JHEP **04** (2015) 040, arXiv: 1410.8849 [hep-ph] (cit. on pp. 33, 34).

[59] T. Gleisberg and S. Höche, *Comix, a new matrix element generator*, Journal of High Energy Physics **2008** (2008) 039, ISSN: 1029-8479, URL: http://dx.doi.org/10.1088/1126-6708/2008/12/039 (cit. on p. 33).

[60] F. Cascioli, P. Maierhöfer, and S. Pozzorini, *Scattering Amplitudes with Open Loops*, Physical Review Letters **108** (2012), ISSN: 1079-7114, URL: http://dx.doi.org/10.1103/PhysRevLett.108.111601 (cit. on p. 33).

[61] A. Denner, S. Dittmaier, and L. Hofer, *Collier: A fortran-based complex one-loop library in extended regularizations*, Computer Physics Communications **212** (2017) 220, ISSN: 0010-4655, URL: http://dx.doi.org/10.1016/j.cpc.2016.10.013 (cit. on p. 33).

[62] S. Schumann and F. Krauss, *A parton shower algorithm based on Catani-Seymour dipole factorisation*, Journal of High Energy Physics **2008** (2008) 038, ISSN: 1029-8479, URL: http://dx.doi.org/10.1088/1126-6708/2008/03/038 (cit. on pp. 33, 34).

[63] S. Höche, F. Krauss, M. Schönherr, and F. Siegert, *A critical appraisal of NLO+PS matching methods*, Journal of High Energy Physics **2012** (2012), ISSN: 1029-8479, URL: http://dx.doi.org/10.1007/JHEP09(2012)049 (cit. on p. 33).

[64] S. Höche, F. Krauss, M. Schönherr, and F. Siegert, *QCD matrix elements + parton showers. The NLO case*, Journal of High Energy Physics **2013** (2013), ISSN: 1029-8479, URL: http://dx.doi.org/10.1007/JHEP04(2013)027 (cit. on p. 33).

[65] S. Catani, F. Krauss, B. R. Webber, and R. Kuhn, *QCD Matrix Elements + Parton Showers*, Journal of High Energy Physics **2001** (2001) 063, ISSN: 1029-8479, URL: http://dx.doi.org/10.1088/1126-6708/2001/11/063 (cit. on pp. 33, 111).

[66] S. Frixione, P. Nason, and G. Ridolfi, *A positive-weight next-to-leading-order Monte Carlo for heavy flavour hadroproduction*, JHEP **09** (2007) 126, arXiv: 0707.3088 [hep-ph] (cit. on p. 34).

[67] P. Nason, *A new method for combining NLO QCD with shower Monte Carlo algorithms*, JHEP **11** (2004) 040, arXiv: hep-ph/0409146 (cit. on p. 34).

[68] S. Frixione, P. Nason, and C. Oleari, *Matching NLO QCD computations with Parton Shower simulations: the POWHEG method*, JHEP **11** (2007) 070, arXiv: 0709.2092 [hep-ph] (cit. on p. 34).

[69] S. Alioli, P. Nason, C. Oleari, and E. Re, *A general framework for implementing NLO calculations in shower Monte Carlo programs: the POWHEG BOX*, JHEP **06** (2010) 043, arXiv: 1002.2581 [hep-ph] (cit. on p. 34).

[70] *Studies on top-quark Monte Carlo modelling for Top2016*, 2016, URL: http://cds.cern.ch/record/2216168 (cit. on p. 34).

[71] *Studies on top-quark Monte Carlo modelling with Sherpa and MG5 aMC@NLO*, 2017, URL: http://cds.cern.ch/record/2261938 (cit. on p. 34).

[72] T. Sjöstrand et al., *An Introduction to PYTHIA 8.2*, Comput. Phys. Commun. **191** (2015) 159, arXiv: 1410.3012 [hep-ph] (cit. on p. 34).

[73] ATLAS Collaboration, *ATLAS Pythia 8 tunes to 7 TeV data*, ATL-PHYS-PUB-2014-021, 2014, URL: https://cds.cern.ch/record/1966419 (cit. on p. 34).

[74] M. Beneke, P. Falgari, S. Klein, and C. Schwinn, *Hadronic top-quark pair production with NNLL threshold resummation*, Nucl. Phys. B **855** (2012) 695, arXiv: 1109.1536 [hep-ph] (cit. on p. 34).

[75] M. Cacciari, M. Czakon, M. Mangano, A. Mitov, and P. Nason, *Top-pair production at hadron colliders with next-to-next-to-leading logarithmic soft-gluon resummation*, Phys. Lett. B **710** (2012) 612, arXiv: 1111.5869 [hep-ph] (cit. on p. 34).

[76] P. Bärnreuther, M. Czakon, and A. Mitov, *Percent-Level-Precision Physics at the Tevatron: Next-to-Next-to-Leading Order QCD Corrections to $q\bar{q} \to t\bar{t} + X$*, Phys. Rev. Lett. **109** (2012) 132001, arXiv: 1204.5201 [hep-ph] (cit. on p. 34).

[77] M. Czakon and A. Mitov, *NNLO corrections to top-pair production at hadron colliders: the all-fermionic scattering channels*, JHEP **12** (2012) 054, arXiv: 1207.0236 [hep-ph] (cit. on p. 34).

[78] M. Czakon and A. Mitov, *NNLO corrections to top pair production at hadron colliders: the quark-gluon reaction*, JHEP **01** (2013) 080, arXiv: 1210.6832 [hep-ph] (cit. on p. 34).

[79] M. Czakon, P. Fiedler, and A. Mitov, *Total Top-Quark Pair-Production Cross Section at Hadron Colliders Through $O(\alpha_S^4)$*, Phys. Rev. Lett. **110** (2013) 252004, arXiv: 1303.6254 [hep-ph] (cit. on p. 34).

[80] M. Czakon and A. Mitov, *Top++: A Program for the Calculation of the Top-Pair Cross-Section at Hadron Colliders*, Comput. Phys. Commun. **185** (2014) 2930, arXiv: 1112.5675 [hep-ph] (cit. on p. 34).

[81] R. Frederix, E. Re, and P. Torrielli, *Single-top t-channel hadroproduction in the four-flavour scheme with POWHEG and aMC@NLO*, Journal of High Energy Physics **2012** (2012), ISSN: 1029-8479, URL: http://dx.doi.org/10.1007/JHEP09(2012)130 (cit. on p. 34).

[82] J. Alwall et al., *The automated computation of tree-level and next-to-leading order differential cross sections, and their matching to parton shower simulations*, JHEP **07** (2014) 079, arXiv: 1405.0301 [hep-ph] (cit. on pp. 34, 35, 113).

[83] S. Frixione, E. Laenen, P. Motylinski, and B. R. Webber, *Angular correlations of lepton pairs from vector boson and top quark decays in Monte Carlo simulations*, JHEP **04** (2007) 081, arXiv: hep-ph/0702198 (cit. on p. 34).

[84] P. Artoisenet, R. Frederix, O. Mattelaer, and R. Rietkerk, *Automatic spin-entangled decays of heavy resonances in Monte Carlo simulations*, Journal of High Energy Physics **2013** (2013), ISSN: 1029-8479, URL: http://dx.doi.org/10.1007/JHEP03(2013)015 (cit. on p. 34).

[85] D. J. Lange, *The EvtGen particle decay simulation package*, Nuclear Instruments and Methods in Physics Research Section A: Accelerators, Spectrometers, Detectors and Associated Equipment **462** (2001) 152, BEAUTY2000, Proceedings of the 7th Int. Conf. on B-Physics at Hadron Machines, ISSN: 0168-9002, URL: http://www.sciencedirect.com/science/article/pii/S0168900201000894 (cit. on p. 34).

[86] J. Alwall, M.-P. Le, M. Lisanti, and J. G. Wacker, *Searching for directly decaying gluinos at the Tevatron*, Physics Letters B **666** (2008) 34, ISSN: 0370-2693, URL: http://dx.doi.org/10.1016/j.physletb.2008.06.065 (cit. on p. 35).

[87] J. Alwall, P. C. Schuster, and N. Toro, *Simplified models for a first characterization of new physics at the LHC*, Physical Review D **79** (2009), ISSN: 1550-2368, URL: http://dx.doi.org/10.1103/PhysRevD.79.075020 (cit. on p. 35).

[88] D. Alves et al., *Simplified models for LHC new physics searches*, Journal of Physics G: Nuclear and Particle Physics **39** (2012) 105005, ISSN: 1361-6471, URL: http://dx.doi.org/10.1088/0954-3899/39/10/105005 (cit. on p. 35).

[89] K. Hamaguchi and K. Ishikawa, *Prospects for Higgs- andZ-resonant neutralino dark matter*, Physical Review D **93** (2016), ISSN: 2470-0029, URL: http://dx.doi.org/10.1103/PhysRevD.93.055009 (cit. on pp. 35, 126).

[90] G. Aad et al., *The ATLAS Simulation Infrastructure*, Eur. Phys. J. C **70** (2010) 823, arXiv: 1005.4568 [physics.ins-det] (cit. on p. 36).

[91] S. Agostinelli et al., *GEANT4: A simulation toolkit*, Nucl. Instrum. Meth. A **506** (2003) 250 (cit. on p. 36).

[92] *The simulation principle and performance of the ATLAS fast calorimeter simulation FastCaloSim*, 2010, URL: http://cds.cern.ch/record/1300517 (cit. on p. 36).

[93] A. Rosenfeld and J. L. Pfaltz, *Sequential Operations in Digital Picture Processing*, J. ACM **13** (1966) 471 (cit. on p. 39).

[94] R. Fruhwirth, *Application of Kalman filtering to track and vertex fitting*, Nuclear Instruments and Methods in Physics Research Section A: Accelerators, Spectrometers, Detectors and Associated Equipment **262** (1987) 444, ISSN: 0168-9002, URL: http://www.sciencedirect.com/science/article/pii/0168900287908874 (cit. on p. 39).

[95] M. Aaboud et al., *Performance of the ATLAS track reconstruction algorithms in dense environments in LHC Run 2*, The European Physical Journal C **77** (2017), ISSN: 1434-6052, URL: http://dx.doi.org/10.1140/epjc/s10052-017-5225-7 (cit. on p. 39).

[96] M. Aaboud et al., *Reconstruction of primary vertices at the ATLAS experiment in Run 1 proton–proton collisions at the LHC*, The European Physical Journal C **77** (2017), ISSN: 1434-6052, URL: http://dx.doi.org/10.1140/epjc/s10052-017-4887-5 (cit. on p. 39).

[97] G. Aad et al., *Topological cell clustering in the ATLAS calorimeters and its performance in LHC Run 1*, The European Physical Journal C **77** (2017), ISSN: 1434-6052, URL: http://dx.doi.org/10.1140/epjc/s10052-017-5004-5 (cit. on p. 39).

[98] Matteo Cacciari and Gavin P Salam and Gregory Soyez, *The anti-ktjet clustering algorithm*, Journal of High Energy Physics **2008** (2008) 063 (cit. on pp. 39, 40).

[99] Cacciari, Matteo and Salam, Gavin P. and Soyez, Gregory, *FastJet user manual*, The European Physical Journal C **72** (2012) 1896, ISSN: 1434-6052, URL: https://doi.org/10.1140/epjc/s10052-012-1896-2 (cit. on p. 39).

[100] M. Aaboud et al., *Jet energy scale measurements and their systematic uncertainties in proton-proton collisions at* $\sqrt{s}$ = 13TeV *with the ATLAS detector*, Phys. Rev. D **96** (7 2017) 072002, URL: https://link.aps.org/doi/10.1103/PhysRevD.96.072002 (cit. on pp. 40–43, 110).

[101] G. P. Salam, *Towards jetography*, The European Physical Journal C **67** (2010) 637, ISSN: 1434-6052, URL: http://dx.doi.org/10.1140/epjc/s10052-010-1314-6 (cit. on p. 41).

[102] *Jet energy scale and uncertainties in 2015-2017 data and simulation*, URL: https://atlas.web.cern.ch/Atlas/GROUPS/PHYSICS/PLOTS/JETM-2018-006/ (cit. on p. 43).

[103] *Tagging and suppression of pileup jets with the ATLAS detector*, tech. rep. ATLAS-CONF-2014-018, CERN, 2014, URL: https://cds.cern.ch/record/1700870 (cit. on pp. 44, 45).

[104] *Optimisation of the ATLAS b-tagging performance for the 2016 LHC Run*, tech. rep. ATL-PHYS-PUB-2016-012, CERN, 2016, URL: https://cds.cern.ch/record/2160731 (cit. on pp. 45, 46, 110).

[105] *Performance ofb-jet identification in the ATLAS experiment*, Journal of Instrumentation **11** (2016) P04008, ISSN: 1748-0221, URL: http://dx.doi.org/10.1088/1748-0221/11/04/P04008 (cit. on pp. 45, 46, 110).

[106] M. Aaboud et al., *Electron reconstruction and identification in the ATLAS experiment using the 2015 and 2016 LHC proton-proton collision data at* $\sqrt{s}$ *= 13 TeV*, 2019, arXiv: 1902.04655 [physics.ins-det] (cit. on pp. 47, 48, 110).

[107] M. Aaboud et al., *Electron efficiency measurements with the ATLAS detector using 2012 LHC proton–proton collision data*, The European Physical Journal C **77** (2017), ISSN: 1434-6052, URL: http://dx.doi.org/10.1140/epjc/s10052-017-4756-2 (cit. on pp. 47, 48, 110).

[108] G. Aad et al., *Muon reconstruction performance of the ATLAS detector in proton–proton collision data at* $\sqrt{s}$*=13 TeV*, The European Physical Journal C **76** (2016), ISSN: 1434-6052, URL: http://dx.doi.org/10.1140/epjc/s10052-016-4120-y (cit. on pp. 48, 49, 110).

[109] M. Aaboud, *Performance of missing transverse momentum reconstruction with the ATLAS detector using proton-proton collisions at $\sqrt{s}$ =13 TeV*, The European Physical Journal C **78** (2018) 903, ISSN: 1434-6052, URL: https://doi.org/10.1140/epjc/s10052-018-6288-9 (cit. on pp. 49, 50, 110).

[110] *Selection of jets produced in 13TeV proton-proton collisions with the ATLAS detector*, tech. rep. ATLAS-CONF-2015-029, CERN, 2015, URL: http://cds.cern.ch/record/2037702 (cit. on p. 53).

[111] J. D. Bjorken and S. J. Brodsky, *Statistical Model for Electron-Positron Annihilation into Hadrons*, Phys. Rev. D **1** (5 1970) 1416, URL: https://link.aps.org/doi/10.1103/PhysRevD.1.1416 (cit. on p. 60).

[112] P. Speckmayer, A. Hocker, J. Stelzer, and H. Voss, *The Toolkit for Multivariate Data Analysis, TMVA 4*, Journal of Physics: Conference Series, v.219, 3, 1-11 (2010) **219** (2010) (cit. on p. 63).

[113] A. Hoecker et al., *TMVA - Toolkit for Multivariate Data Analysis*, 2007, arXiv: physics/0703039 [physics.data-an] (cit. on pp. 63, 64, 97).

[114] *Search for squarks and gluinos in final states with jets and missing transverse momentum using 139 fb^{-1} of $\sqrt{s}$ =13 TeV pp collision data with the ATLAS detector*, tech. rep. ATLAS-CONF-2019-040, CERN, 2019, URL: https://cds.cern.ch/record/2686254 (cit. on p. 65).

[115] R. D. Cousins, J. T. Linnemann, and J. Tucker, *Evaluation of three methods for calculating statistical significance when incorporating a systematic uncertainty into a test of the background-only hypothesis for a Poisson process*, Nuclear Instruments and Methods in Physics Research Section A: Accelerators, Spectrometers, Detectors and Associated Equipment **595** (2008) 480, ISSN: 0168-9002, URL: http://www.sciencedirect.com/science/article/pii/S0168900208010255 (cit. on p. 69).

[116] M. Czakon et al., *Top-pair production at the LHC through NNLO QCD and NLO EW*, Journal of High Energy Physics **2017** (2017), ISSN: 1029-8479, URL: http://dx.doi.org/10.1007/JHEP10(2017)186 (cit. on pp. 92, 113).

[117] M. Baak et al., *HistFitter software framework for statistical data analysis*, The European Physical Journal C **75** (2015), ISSN: 1434-6052, URL: http://dx.doi.org/10.1140/epjc/s10052-015-3327-7 (cit. on p. 107).

[118] G. Cowan, K. Cranmer, E. Gross, and O. Vitells, *Asymptotic formulae for likelihood-based tests of new physics*, The European Physical Journal C **71** (2011), ISSN: 1434-6052, URL: http://dx.doi.org/10.1140/epjc/s10052-011-1554-0 (cit. on pp. 108, 109).

[119] A. L. Read, *Presentation of search results: theCLstechnique*, Journal of Physics G: Nuclear and Particle Physics **28** (2002) 2693 (cit. on p. 109).

[120] A. Buckley et al., *General-purpose event generators for LHC physics*, Physics Reports **504** (2011) 145, ISSN: 0370-1573, URL: http://dx.doi.org/10.1016/j.physrep.2011.03.005 (cit. on pp. 110, 111).

[121] P. Skands, *QCD for Collider Physics*, 2011, arXiv: 1104.2863 [hep-ph] (cit. on p. 110).

[122] J. C. Collins, D. E. Soper, and G. Sterman, *Factorization of Hard Processes in QCD*, 2004, arXiv: hep-ph/0409313 [hep-ph] (cit. on p. 111).

[123] J. Bellm et al., *Herwig 7.0/Herwig++ 3.0 release note*, The European Physical Journal C **76** (2016), ISSN: 1434-6052, URL: http://dx.doi.org/10.1140/epjc/s10052-016-4018-8 (cit. on p. 113).

[124] M. Aaboud et al., *Search for new phenomena using the invariant mass distribution of same-flavour opposite-sign dilepton pairs in events with missing transverse momentum in $\sqrt{s}$ =13 TeV pp collisions with the ATLAS detector*, Eur. Phys. J. **C78** (2018) 625, arXiv: 1805.11381 [hep-ex] (cit. on pp. 126, 127).

[125] *Search for supersymmetry in final states with missing transverse momentum and multiple b-jets in proton-proton collisions at $\sqrt{s}$ = 13 TeV with the ATLAS detector*, tech. rep. ATLAS-CONF-2018-041, CERN, 2018, URL: https://cds.cern.ch/record/2632347 (cit. on p. 127).

[126] A. M. Sirunyan et al., *Search for supersymmetry in proton-proton collisions at 13 TeV in final states with jets and missing transverse momentum*, Journal of High Energy Physics **2019** (2019), ISSN: 1029-8479, URL: http://dx.doi.org/10.1007/JHEP10(2019)244 (cit. on pp. 131, 132).

[127] L. Randall and R. Sundrum, *Out of this world supersymmetry breaking*, Nuclear Physics B **557** (1999) 79, ISSN: 0550-3213, URL: http://www.sciencedirect.com/science/article/pii/S0550321399003594 (cit. on p. 132).

[128] H. Nilles, *Supersymmetry, supergravity and particle physics*, Physics Reports **110** (1984) 1, ISSN: 0370-1573, URL: http://www.sciencedirect.com/science/article/pii/0370157384900085 (cit. on p. 132).

[129] H. Haber and G. Kane, *The search for supersymmetry: Probing physics beyond the standard model*, Physics Reports **117** (1985) 75, ISSN: 0370-1573, URL: http://www.sciencedirect.com/science/article/pii/0370157385900511 (cit. on p. 132).

[130] M. Carena, J. Espinosa, M. Quirós, and C. Wagner, *Analytical expressions for radiatively corrected Higgs masses and couplings in the MSSM*, Physics Letters B **355** (1995) 209, ISSN: 0370-2693, URL: http://dx.doi.org/10.1016/0370-2693(95)00694-G (cit. on p. 132).

[131] M. Papucci, J. T. Ruderman, and A. Weiler, *Natural SUSY endures*, Journal of High Energy Physics **2012** (2012), ISSN: 1029-8479, URL: http://dx.doi.org/10.1007/JHEP09(2012)035 (cit. on p. 132).

[132] K. Uno, *Firmware Development for the first level trigger of ATLAS LAr Calorimeter*, PoS **KMI2017** (2017) 64 (cit. on p. 145).

[133] K. Uno, *The Phase-I Trigger Readout Electronics Upgrade of the ATLAS Liquid Argon Calorimeters*, PoS **TWEPP2018** (2019) 128 (cit. on p. 145).

[134] *ATLAS Liquid Argon Calorimeter Phase-I Upgrade Technical Design Report*, tech. rep. CERN-LHCC-2013-017. ATLAS-TDR-022, Final version presented to December 2013 LHCC., 2013, URL: https://cds.cern.ch/record/1602230 (cit. on pp. 145, 146).